The University of Queensland

Development of a Parallel Adaptive Cartesian Cell Code to Simulate Blast in Complex Geometries

By
Joseph Tang
B.E. (Mechanical and Space)

A thesis submitted for the degree of
Doctor of Philosophy at
The University of Queensland in June 2008

Principal Supervisor: *Doctor Peter Jacobs*
Associate Supervisor: *Doctor Michael Macrossan*

Division of Mechanical Engineering,
School of Engineering,
The University of Queensland,
Australia.

Statement of Originality

Joseph Tang

Publications

Published Works by the Author Incorporated into the Thesis

Tang, J. "Another alternative method for blast wave simulation in complex geometries using Virtual Cell Embedding", *10th International Workshop on Shock-Tube Technology*, Brisbane, Australia, 2006. Partially incorporated in Chapters 2, 11, 8 and 11.

Tang, J. "A simple axisymmetric extension to virtual cell embedding", *International Journal for Numerical Methods in Fluids*, Vol. 55, No. 8, 2007, pp. 785–791. Partially incorporated in Chapter 6 and Appendix D.

Tang, J. "A simple parallel adaptive mesh CFD method suitable for small engineering workstations", submitted to *Parallel Processing Letters*, 2008. Partially incorporated in Chapters 5 and 14.

Tang, J. "CFD simulation of blast in an internal geometry using a cartesian cell code", *16th Australasian Fluid Mechanics Conference*, Gold Coast, Australia, 2007. Partially incorporated in Chapters 14 and 15.

Tang, J. "Free-field blast parameter errors from cartesian cell representations of bursting sphere-type charges". *Shock Waves*, Vol. 18, pp. 11–20. Incorporated in Chapter 10.

Tang, J. "Theory manual to OctVCE – a cartesian cell CFD code with special application to blast wave problems", Report 2007/12, Department of Mechanical Engineering, University of Queensland, 2007. Partially incorporated in Chapter 4.

Published Works by the Author Relevant to the Thesis but not Forming Part of it

Tang, J. "User guide for shock and blast simulation with the OctVCE code (version 3.5+)", Report 2007/13, Department of Mechanical Engineering, University of Queensland, 2007.

Acknowledgements

I would firstly like to thank the Australian Government for the Australian Postgraduate Research Award and the Mechanical Engineering Department for the Research Scholarship.

I am grateful to my supervisor Peter Jacobs for his guidance and very helpful advice, who encouraged and enlightened me on numerous occasions when I felt hindered in my progress. I am very thankful to have had such a gentle and friendly supervisor. I also thank my fellow postgraduates Brendan O'Flaherty and especially Rowan Gollan for their assistance and fruitful discussions on many topics. I also appreciate the help of Martin Nicholls for his help in answering my questions about the computing facilties used for this thesis. Without the help of these people, my research would have been much more daunting.

I am indebted to and grateful to my parents and sister for their love, encouragement and support during this period. Their presence has helped make this time of my life far more tolerable than it would have been.

Lastly, but most importantly, I thank my Lord and Saviour, Jesus Christ, for being with me throughout this period and giving me the strength to arrive at this point, for "much study wearies the body" (Eccl 12:12). He is my ultimate Supervisor, for I know that "whatever you do, work at it with all your heart, as working for the Lord ... it is the Lord Christ you are serving" (Col 3:24-25).

Abstract

The modelling of blast propagation in urban environments generated by explosions allows prediction of blast loading on structures, which in turn has useful applications like damage assessment and improvement of structural design. However such an exercise is often realizable only with Computational Fluid Dynamics simulations, which can be difficult to perform because of the geometric complexity of the blast environment.

This thesis describes the development of the code `OctVCE` designed especially for modelling shock and blast effects in complex structural geometries. This code is designed for practical engineering use where high resolution is unnecessary. It uses a finite-volume formulation of the unsteady Euler equations with second-order explicit Runge-Kutta timestepping and linear interpolation with a minmod-based limiter. Flux solvers used are the Advection Upwind Splitting Method variant (AUSMDV) and the Equilibrium Flux Method (EFM). No fluid-structure coupling or chemical reactions are modelled, and gas models can be perfect gas or the real-gas JWL model.

The code uses the Virtual Cell Embedding (VCE) Cartesian cell method to automatically generate grids in complex geometries. This method is chosen because of its simplicity, robustness and generality. Additional efficiency in computational performance and memory usage is obtained by implementing an octree-based mesh adaptation scheme in the code. The parallel implementation of the code using the shared-memory OpenMP paradigm is also described.

The code is verified to establish reliability of the numerical implementation via test cases like the method of manufactured solutions, an ideal shock tube problem, supersonic flow over wedge and cone geometries and a supersonic vortex problem. The code is then validated to demonstrate its reliability and usefulness in simulating more realistic shock and blast problems. Test cases presented increase in geometric complexity and include unsteady shock interaction with wedge and cylinder geometries and blast interaction with barriers, axisymmetric containers, simple arrangements of cuboidal structures and complex cityscape buildings.

As part of a design exercise for the development of a static-firing test facility, `OctVCE` is applied to modelling internal blast in a shipping container geometry. It is found that very large amplification of pressures and impulse exists within the structure (by at least a factor of ten) due to blast confinement. It was not always easy to demonstrate convergence, especially along edges and corners of the geometry, due to the coarseness of the grids employed in the simulations. However, the impulse could still be computed with fairly low error.

The serial and parallel performance of the code is measured for some of these cases. The performance profiles indicate that substantial savings in storage and execution time is achieved on adaptive meshes compared to equivalent uniform meshes. Execution time is also considerably shortened through the use of parallel processing. However, code performance can still be significantly enhanced, and several aspects of the code are identified in the last chapter in which improvements can be made in future work. These include more efficient parallel implementation, better adaptation indicators, less conservative timestepping and importantly reduction of memory usage.

Keywords and Australian and New Zealand Standard Research Classifications

Keywords

Blast, numerical simulation, Cartesian cell, virtual cell embedding, complex geometry

Australian and New Zealand Standard Research Classifications (ANZSRC)

091501 100%

Contents

List of Tables

List of Figures

Nomenclature

a	Sound speed (m/s)
A	Area (m^2)
AUSMDV	Advection Upwind Splitting Method with flux difference and vector splitting
α	Angle
b	Barrier portion
β	Barrier fraction
CFL	Courant, Friedrichs, Lewy
C_p, C_v	Specific heat J/(kg.K)
DSM	Distributed-Shared Memory
e	Experimentally determined serial fraction, intensive internal energy (J/kg)
E	Elapsed time, total intensive energy (J/kg), error
EFM	Equilibrium Flux Method
ϵ	Error, indicator, serial fraction
f	Solution, mass fraction
F	Face, Force
$\mathbf{F}$	Flux
GCI	Grid Convergence Index
γ	Ratio of specific heats
h	Specific enthalpy (J/kg)
H	Halfline, Height, Total enthalpy (J/kg)
$\mathbf{i}, \mathbf{j}, \mathbf{k}$	Unit vectors
JWL	Jones-Wilkins-Lee
l, L	Length (m), level
L_2	L_2 norm
m	Gradient, Mass (kg)
M	Mach number
n	Problem size
$\widehat{\mathbf{n}}$	Normal vector
N	Number

NUMA	Non-Uniform Memory Access
`OctVCE`	Octree Virtual Cell Embedding
ω	Overhead fraction
p	Order of accuracy, number of processors
$\mathbf{p}$	Point
P	Pressure (Pa), number or processors
PPM	Piecewise parabolic method
ϕ	Parallel portion of a code
Φ	Limiter value
Q	Source term, any quantity
r	Grid refinement factor, radius (m)
R	Distance (m), Gas constant, J/(kg.K)
ρ	Density (kg/m^3)
s	Distance (m), entropy
S	Sum
S_p	Speedup
σ	Serial portion of a code
t	Time (s)
T	Temperature (K)
u	Velocity (m/s)
$\mathbf{u}, \mathbf{v}$	Velocity vector
$\mathbf{U}$	State vector
v	Velocity (m/s), Specific volume (m^3/kg)
$\widetilde{v}$	Relative volume of explosion products
V	Volume (m^3)
VCE	Virtual Cell Embedding
w	Velocity (m/s)
W	Charge mass (kg)
x, y, z	Co-ordinate directions

Subscripts

∞	Freestream conditions
0	Ambient conditions, solid conditions
a	Ambient conditions
avg	Average
c	Child, Centre
$\mathbf{c}$	Centroid
i	Interface, cell centre index, species index
$i \pm \frac{1}{2}$	Cell interface index
if	Interface
l, L	Left
min	Minimum
n	Neighbour, Normal
o	Parallel overhead
p	Parent, Explosion products
r, R	Right
s	Subcell, entropy, surface
w	Wall
x, y, z	Co-ordinate directions

Superscripts

L	Left
n	Number
R	Right

Chapter 1

Introduction

The reliable prediction of blast loading in urban environments has become an important goal due to the heightened awareness of terrorism in recent times, which usually take the form of external bomb attacks in the presence of nearby buildings forming street geometries [159]. Such predictions help in assessing damage, estimating safety distances and even improving structural design by providing insight into factors that contribute to the blast resistance of structures [160]. However, this can be a challenging exercise as many urban geometries can have a complex profile, requiring Computational Fluid Dynamics (CFD) simulations to obtain the required predictions.

To address this problem, this thesis describes the development and testing of the Octree Virtual Cell Embedding (`OctVCE`) code, a CFD code written in the C programming language designed especially for modelling blast propagation in complex geometries. Important objectives behind the development of the code include using simple numerical methods (to reduce development time and help with code maintainability) and implementing automated mesh generation, mesh adaptation and parallel processing technology (to increase time and storage efficiency of computations). It is developed to be suitable for other shock propagation problems and also with a view to making it available in the CFCFD group's codes in the University of Queensland, as this is the first code in the group that has explored adaptive gridding technology in three dimensions.

This chapter first describes in Section 1.1 why CFD simulations are important for blast propagation problems in complex geometries. A review of previous commercial and research codes used for such problems is also given in Section 1.1.1. Some general background information into the major characteristics of explosion-generated blast is provided in Section 1.2.

1.1 The Need for Numerical Simulation

In recent years CFD simulation has become more prominent as a means of investigating the blast environment in a complex geometry environment [194]. Estimation of blast pressure histories is a complex problem as it depends on many factors including charge size, distance, and the shape, size, orientation and spacing of obstacles. The blast loading of a structure is also the result of shielding, focussing and amplification effects taking place within the blast environment [39, 45, 175] which sometimes occur in counterintuitive locations.

It has been found that for even simple street geometries the formulation of simple rules to predict blast resultants is a difficult task [173] and in many experimental and numerical investigations the channeling and amplification due to confinement of the blast wave along a street can be very significant, with overpressures being as much as give times the unobstructed reflected pressure value [160, 172, 173, 191, 195, 194]. Numerical simulations can also account for the varying topography of the ground terrain [212] and are often the only alternative in cases where it is difficult to perform experiments or extract the required design information from them.

There are also some disadvantages in performing scaled experiments and the recording of surface pressures on structures near a high explosive detonation can be difficult due to the sensitivity of gauges to stress, heat and light [107, 171]. Errors in recording can result from finite response time, spatial averaging or transducer orientation [156], and transducer vibration (occasionally due to fast-moving stress waves through the ground or structure) often increases observed peak pressure [165].

Sensors might indicate a finite overpressure well after the event due to shifting of the record baseline [107, 171], which can affect measurement of the negative phase of the blast. The experiment must be performed several times to ensure statistical repeatability of results and to minimize errors resulting from incomplete detonation [171]. This must be repeated for each case, which may be costly and tedious especially if pressure fields over multiple surfaces in a complex geometry environment are desired.

Simple semiempirical methods [19, 25, 43, 89, 92, 119, 192] combine the results of experiments with an analytic component. The structures analyzed are usually limited to simple rectangular shapes, and usually only ideal one-dimensional blast parameter curves are used. The structure may be modelled as a simple mass-spring system, and usually only the positive phase is considered (represented by a triangular shape) with the assumption of uniform loading.

These methods also consider the angle of incidence and reflection of the blast wave. The empirical approach might also use correlations determined from a database of experiments [103, 213], making the extension to scenarios not corresponding to the database difficult [175]. The blast interaction with other structures (which can have a significant effect) is difficult to incorporate.

Examples of semiempirical software include the Eblast software [70] which relies on an empirical database. It does not calculate reflections and diffractions from buildings and accounts for channeling via enhancement factors. The Antiterrorist Planner software [13] uses scaled blast parameters with empirical shielding algorithms to provide structural damage evaluations. More recent attempts include useage of a large experimental database to train artificial neural networks to predict the blast environment behind blast barriers [161] much faster than CFD could. A series of numerical simulations was also performed to provide empiricial formulae to predict reflected pressure and impulse in blast wave interaction with standalone columns [186]. These are useful and fast design tools, but limited in application and would not model the blast environment in general complex geometry adequately.

Another more sophisticated semiempirical method are the Low Altitude Multiple Burst (LAMB) shock addition rules [94]. These rules require path lengths for rays along which waves travel. The ray paths describing multiple reflections are calculated and the pressure history from each ray is superposed. The LAMB rules are used by the BLASTX code [33], the ASLAR code [117] and Needham's code [139]. All these codes are much faster than CFD and rely to an extent on empirical formulae and/or CFD calculations, limiting their applicability to certain classes of simple geometry. It is still difficult to model multiple complex building blast wave interactions [139, 171], which is why CFD is the preferred option for such problems.

1.1.1 Previous CFD Approaches to Blast Modelling

This section gives a brief overview of prominent CFD codes used to model blast in complex geometries. Codes employing unstructured grids have been quite popular due to automatic grid generation capability. A popular unstructured commercial code is AUTODYN [104], designed especially for blast propagation problems from high explosive sources. It employs both finite-element and finite-volume solvers and can model full fluid-structure interaction.

It also employs a time-saving method where a one-dimensional spherical analysis between the explosive centre and nearest surface is performed before remapping the solution to higher dimensions, removing the requirement for highly resolved multidimensional grids early in the simulation. AUTODYN has been used to model a variety of blast propagation problems in complex external and internal geometries [7, 48, 74, 159]. Another commerical unstructured code implementing the remapping capability is Chinook [165] which has been used to model blast in urban scenarios.

A well known research code is Löhner's unstructured finite element FEM-FCT code [131], which can also model coupled fluid-structure interaction. This is a sophisticated code which has been previously used to model explosions in very complex geometries like tanks and underground carparks and airplanes [21, 22, 23]. A similar research code has been developed by Timofeev *et al* [211, 212, 220] which uses finite-volume unstructured meshes. This has been used to compute blast wave propagation over complex terrains generated by high explosives and volcanic blasts.

The SHAMRC code is a Cartesian cell Eulerian finite-difference code designed specially for the calculation of airblast propagation [12]. Rigid boundaries are assumed for structural surfaces and it appears to allow only grid-oriented obstacles. It has been used to calculate blast loads on office buildings and in internal room detonations [138]. Another well known Eulerian mesh code is CTH [93], which can simulate complex problems involving fluid-structure interaction like penetration, perforation and explosive detonation. It does not appear to have been used to model blast propagation in complex geometries.

Cieslak *et al* [54] developed a cut-cell Cartesian cell code to simulate blast propagation for geometries like gun attenuators. The CEBAM code [56, 57] has been used to simulate blast from gas explosions and solid explosives in complex geometries like offshore installations. It uses a finite volume formulation within a structured, curvilinear framework to solve the conservation laws, but does not explicitly represent sub-grid scale structures, implementing a porosity model to account for the effect of these obstacles.

The code which has the most features in common with `OctVCE` is `Air3d` developed by Rose [171]. It is quite memory-efficient and fast compared to AUTODYN, and uses Cartesian cells with the assumption of rigid surfaces, originally only handling grid-aligned structures. It was further extended concurrently with `OctVCE` to incorporate more general complex geometries and adaptive octree meshing in the `ftt_air3d` code[1] [174, 177]. `Air3d` and `ftt_air3d` has been used extensively to model blast propagation problems in a variety of simple and complex urban building environments [160, 171, 172, 173, 174, 175, 178, 193, 194]. The development of `ftt_air3d` and `OctVCE` has been independent and has resulted in a number of different design decisions being made. Sections 14.2 and 16.1 compare some differences between the `ftt_air3d` and `OctVCE` codes.

1.2 Characteristics of Explosive Blasts

This section gives an overview of the main characteristics of blasts from explosive charges. Fuller treatment of this subject can be found in many texts [19, 92, 119, 192]. An explosion is the phenomenon resulting from a rapid release of energy, usually of such strength and occuring in such a small volume as to produce an audible pressure

[1] http://gow.epsrc.ac.uk/ViewGrant.aspx?GrantRef=GR/S04109/01, accessed May 2008

wave [19, 119]. For high explosives, the energy release is caused by chemical detonation which is nearly all transferred to the blast wave [92, 192], and initially consists mostly of internal (rather than kinetic) energy [41].

The detonation products (commonly referred to as the explosive fireball) are quite complex and formed by various processes including dissociation and ionization [119]. Very quickly the density in this fireball becomes lower than the surrounding air due to a partial vacuum being created from the outward momentum of the air induced by the primary blast wave. Under the influence of gravity the fireball rises and draws debris into its centre, forming the well known 'mushroom cloud'.

Accurate modelling of these products require modelling chemical reactions, but this is outside the scope of this thesis (see Chapter 4). Many chemical explosives are oxygen-deficient [101]; the energy release does not all occur at detonation because of insufficient oxygen to achieve complete oxidization, but also occurs later in combustion of the explosive products as they mix with air (afterburning). TNT has a significant oxygen-deficiency of 75% [101] but the effect of afterburning on the incident shock is small [120]. However, afterburning can affect flow speed and thus later parts of the blast wave.

It is well known that all blast waves quickly develop a spherical profile [19, 119, 120], even for non-spherical charges. As long as energy release is sufficiently rapid the same general configuration of the blast wave will result. The contact surface between the detonation products and ambient gas usually becomes irregular with a high level of mixing [25], but the uniformity of the spherical shock is not affected greatly (even with afterburning). An analytical solution to the free-field wave structure (i.e. without any obstacles) is difficult to obtain [25], although early attempts were made for both the near- and far-field [19]. A numerical solution to the spherically symmetric conservation equations is the preferred method, and was first attempted by Brode [40].

The blast wave is the dominant damage mechanism when the explosion occurs in the vicinity of structures. Important features of this wave are shown in Figure 1.1 which shows the overpressure history at a point in space away from the explosion. This figure only characterizes free-field burst because numerous reflections and shock wave interactions are expected for a blast environment comprising of structures.

The severity of blast loading is usually characterized by the peak overpressure. However, damage is usually caused only if the positive phase duration is long relative to the period of natural vibration of the structure [89]. Hence the peak impulse (the maximum value of the pressure integral over time) is also an equally (if not more) important blast parameter [171, 195]. The peak overpressure is usually of the order of gigapascals at the explosion but decreases rapidly as the shock propagates outward, being quite well described by the ideal gas law [119], and usually being too weak for structural engineering

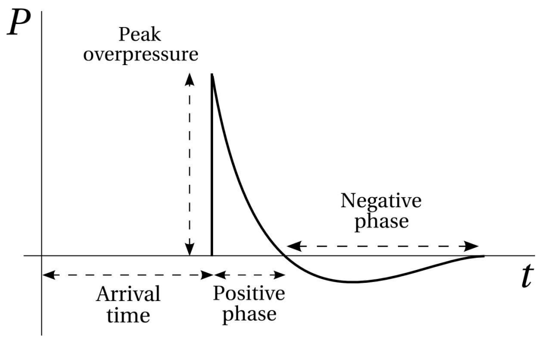

Figure 1.1: Typical blast wave profile

considerations after a scaled distance of 30 m/kg$^{1/3}$ [171] (scaled distances are explained on page 7).

A negative phase occurs due to a partial vacuum being created surrounding the explosion. Eventually the displaced atmosphere will rush inward to fill this volume, thus creating a suction phase in the explosion process. The negative phase lasts up to three times as long as the positive phase but is usually less damaging than the positive phase, and thus ignored [19, 119]. In some cases it can be a significant loading mechanism, although measuring it experimentally can be difficult [172]. But it is the cause of much broken glass being blown onto the streets in an urban environment blast.

The relationship with distance of blast parameters like peak overpressure, impulse etc. for a free-field TNT burst has been measured empirically and documented in many sources, sometimes supplied with curve fits [19, 25, 92, 103, 119, 192]. These curves can also be developed from numerical simulation [41, 171] and correlations exist even for differently shaped charges [43]. These relationships have also been documented for hemispherical bursts on the ground, which are different from free-field burst because realistic surfaces are not perfectly reflecting [201].

The profile in Figure 1.1 is not entirely accurate as a weaker secondary shock is also produced after the explosion, which may have some contribution to the positive impulse [25, 41, 92]. The deceleration of the contact surface produces an outward moving rarefaction wave and an imploding secondary shock, which may be initially swept outward. After implosion this shock expands outward and partially reflects off the contact surface again, further imploding and repeating the process, although each time the shock decreases in intensity. Thus only the secondary shock is usually seen, and it does not usually catch up to the incident shock. Because the secondary shock is much weaker than the incident shock, it is usually ignored [171].

In a height-of-burst scenario when the charge is detonated above the ground the blast wave will reflect from the ground, as shown in Figure 1.2. There are three types of reflections – normal reflection (directly underneath the burst), oblique reflection (angle of incidence less than 40 degrees) and Mach stem reflection for larger angles of incidence. The overpressure in reflected waves may be much greater than the incident shock, especially behind the Mach stem [19, 193].

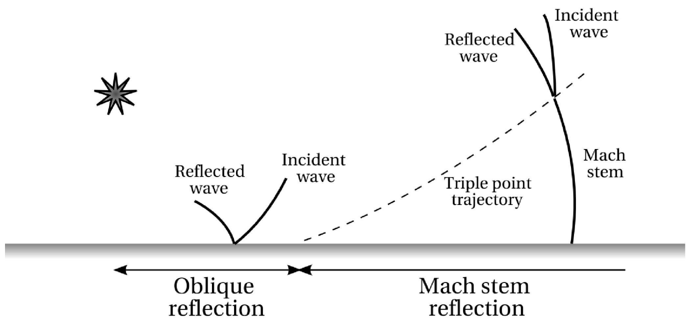

Figure 1.2: Height-of-burst scenario

1.2.1 Scaling Laws

When two spherical charges made of the same explosive are detonated in the same atmosphere and have the same geometry but are of different scales, Hopkinson 'cube-root' scaling applies [119, 120]. This scaling law is based on fundamentals of geometrical similarity, and can eliminate charge mass as a parameter in describing blast wave properties. These two charges will exhibit the same property Q behind the primary shock (e.g. in overpressure) at the same scaled distance.

The scaled distance is $Z = R/W^{1/3}$ where R is the distance from the centre of the explosion and W the mass of the explosive. Pressure history profiles will also be identical at the same scaled distance if time is also scaled i.e. $t_{sc} = t/W^{1/3}$. Impulse can be scaled either by a time scale (like positive phase duration) or by $W^{1/3}$. This scaling law is approximate when comparing the blast waves between two different types of explosives with different energy release rates that exhibit afterburning [120]. The scaling law does not apply if the flowfield is spherically asymmetric [120], but this is an acceptable limitation as departures from sphericity only occur close to the fireball.

It is also common to compare explosive blast effects in terms of equivalency to the burst from a spherical TNT charge, expressed as an equivalent mass of TNT. The simplest equivalency is comparison in terms of blast energy, but equivalencies can also be based on peak overpressure or impulse [213], which are not always equal (or parallel) due to factors like the oxygen deficiency [101]. Charge shape can also complicate the equivalency, and more complex scalings formulate TNT equivalence varying with scaled distance (looking at either pressure or impulse) [120, 201].

1.3 Scope of Thesis

Chapter 2 reviews different CFD methods used to model flows in complex geometries, concluding in Section 2.4 with a discussion of the Virtual Cell Embedding (VCE) method [124], a simple Cartesian cell method that automatically generates a mesh in arbitrary geometries. This thesis is thus also an application study into the suitability of the VCE gridding method in simulating blast propagation and loading in complex geometries. Chapter 3 describes the mesh adaptation procedure implemented by `OctVCE`, which uses a recursive octree data structure as its basis for refining and coarsening cells. This section discusses pseudocode of important adaptation routines, degeneracies encountered and adaptation indicators.

Chapter 4 reviews and describes various aspects involved in the numerical methodology of the code including the scope, governing equations, flux solvers, equations of state, initial and boundary conditions and point-inclusion queries. More detailed coverage of these aspects can also be found in the Appendix. Some discussion will centre on potential instabilities with the code resulting from the conjuction of the VCE gridding method with the numerical flow calculation methodology. Chapter 5 reviews parallel computing methods in general and describes the shared-memory parallel implementation of the `OctVCE` code in Section 5.5. While the work in this thesis was being done, the availability of multiple core processors became common. In the near-future all engineering workstations are expected to have multiple cores. Useful measures of parallel performance will also be discussed.

Chapter 6 presents four different verification test cases to demonstrate the reliability of the numerical implementation – the Method of Manufactured Solutions (Section 6.1), ideal shock tube problem, supersonic flow over wedges and cones and supersonic vortex flow. Chapters 7 to 14 cover validation test cases to determine the credibility and accuracy of the code in solving realistic blast and shock propagation problems. Examples are shock diffraction over wedges and cylinders (Chapters 7 to 8), explosive bursting sphere problems (Chapters 9 and 10), blast in axisymmetric containers and in environments comprising of simple rectangular prismatic geometries (Chapters 11 to 13), and blast in complex city scape geometries (Chapter 14).

Profiling of the code will also be performed for a number of these test cases to establish its performance in serial and parallel execution. Chapter 15 focusses on an application study of the code where an explosion in an internal geometry is modelled. This shows the code being used in a design process where the geometry, although somewhat simplified, had to retain its essentially complex features. Finally all results are summarized in Chapter 16 and some improvements to the code are also suggested.

Chapter 2

Meshes for Complex Geometries

The simulation of blast propagation in complex geometries usually requires the mesh to encompass the domain. This can be time-consuming if performed manually, and thus automated grid generation methods are preferred. To reduce code development and maintenance time, simple methods are also preferred over complex ones. This section gives an overview of the three main approaches (body-fitted, grid-free and cartesian grid methods) used to generate grids and perform numerical simulations in environments with complex surface geometry.

2.1 Body-fitted Grids

Structured grids basically consist of rectangular or hexahedral cells stored in an array, with neighbouring connectivities regularly determined by array indices [79]. They can be 'body-fitted' and may require metrics and transformations to map the physical grid into computational space where flow equations are solved. They are an efficient data structure as connectivity is fixed and not explicitly stored, and can be organized into blocks of structured grids when performing simulations in parallel.

Structured grids require some degree of user interaction in their construction, and can be tedious to create for complex geometries [79, 106]. Metric terms add some additional complexity to the code, and the fixed connectivity prevents implementation of h-refinement where cells are added or deleted. Chimera or overset grids [72] are popular for moving body problems and consist of overlapping patches of structured grids fitted around each body. Effort still has to be put into generating structured grids around each body [106] and there is the additional complexity of hole-cutting, stencil identification, interpolation coefficients and inter-grid communication associated with the chimera grid approach [72].

Unstructured grids are composed of an arbitrary collection of randomly oriented cells which do not typically have a repeatable topological structure. They are commonly composed of triangles or tetrahedral cells, which can be generated by Delaunay triangulation, advancing-front methods or tree-based techniques (where an initial Cartesian mesh adjusts boundary elements before undergoing tessellation) [29, 79]. All these methods allow a high degree of automation [45]. Unstructured grids can also be body-fitted, and for some grid construction algorithms like the advancing-front method a surface mesh composed of triangular panels may also be required.

Compared to structured grids, unstructured grids are much more taxing on memory and solution time [118], and can also be difficult and cumbersome to code. They are more inefficient at filling the domain [51] and have poorer shock-capturing ability [27] due to irregular numerical interfaces causing some refraction and scattering of waves [64]. Generating an appropriate surface mesh can also be challenging [1, 128], and may still require a degree of user-interactivity [140]. Research into generating quadrilateral or hexahedral unstructured grids has also been undertaken [29]. Hexahedral meshes have more regularity than tetrahedral meshes and are comparatively more accurate, time-efficient and memory-efficient [1, 27, 29, 30].

However, automated grid generation for unstructured hexahedral meshes has not reached as advanced a stage compared to tetrahedral meshes [29, 200]. Blacker [31] provides a good overview of various methods for hexahedral mesh generation, including use of primitives (applicable only to a class of specialized geometries), decomposition into recognizable primitive shapes, advancing-front techniques and overlay grids. Advancing-front techniques for hexahedral meshes include a whisker weaving scheme [207] and plastering scheme [32, 198]. These methods are still an active area of research and can be quite complex to implement and time intensive. A surface mesh also needs to be specified.

One of the more widely used hexahedral grid generation schemes is the overlay grid method [183]. The volume to be meshed is initially overlayed with a mesh of hexahedral cells and cell nodes on the body surfaces are adjusted to fit to the surface. Sometimes mixed cell types (tetrahedral and hexahedral) result due to degeneracies. Depending on the methods considered, the algorithmic complexity of the overlay grid method may still be higher than for some Cartesian cell methods.

2.2 Grid-free and Particle Methods

Another method to solve flows in complex geometry is the 'grid-free' approach [197]. This approach essentially solves the conservation equations using least squares fitting of nodes in the domain to approximate derivatives. This method is 'grid-free' in the sense that the nodes can be generated using any means [197]. However these methods do not guarantee global conservation and are slower than mesh-based counterparts, and need to introduce some artificial dissipation [132]. The least squares procedure can be complex, requiring inversion of geometric matricies and thus depends on the stencil of grid points chosen to prevent ill-conditioning. Other difficult degeneracies include insufficient nodal density, surface discontinuities and thin bodies.

Particle methods discretize the fluid (a Lagrangian approach) rather than the flow domain (Eulerian approach). These also can be meshed-based, like the popular Arbitrary Lagrangian-Eulerian (ALE) methods [134], and thus suffer from the disadvantages associated with unstructured grids. Lagrangian mesh-based approaches can result in severe mesh distortion and entangling and thus require remapping, but this introduces numerical diffusion [84].

A well-known gridless method is the Smoothed Particle Hydrodynamics (SPH) method [137] in which the fluid is represented by a collection of fluid pseduo-particles. This method, originally applied to astrophysical problems, is good for simulating flows where fluid interfaces are important, and has seen extension to other applications in recent times. However SPH is computationally expensive and offers lower resolution compared to contemporary finite-volume methods [38], also requiring artificial viscosity. Particle penetration problems associated for shocked flows exist and boundary conditions (even just reflecting boundaries) are more difficult to handle than with finite-volume methods [143]. At least for blast propagation problems, Eulerian methods are still preferrable, simpler to implement and more established.

Another particle method used to model blast propagation is the Direct Simulation Monte Carlo (DSMC) method of Sharma *et al* [184, 185]. This method is derived from kinetic theory and uses a statistically representative set of particles which are tracked in their collisions with each other and with boundaries. Sharma *et al* have modified the method to use a much larger timestep than the mean collision time. DSMC thus gives approximate results and is faster than continuum methods, but has lower resolution and statistical scatter. This method is promising but has not seen wider application and usage compared to finite-volume methods.

2.3 Cartesian Grid Methods

Cartesian grids are composed of axis-aligned hexahedral (often cubical) finite-volume cells which treat solid geometries as 'immersed' within the mesh. Cells that are completely obstructed or unobstructed are ignored or treated normally respectively. Various approaches exist to treat partially obstructed or intersected cells [4, 45, 65, 106, 121, 124, 128, 153, 174]. These methods vary in complexity and accuracy. Because the number of cells is usually a small fraction of all the cells, the additional calculations on intersected cells usually involve small overhead [224].

Problems with Cartesian grids usually relate to flaws in surface representation, thin bodies or very small cells. Very small intersected cells lead to ineffiencies as the global timestep needs to be drastically reduced to ensure stability of the flow update scheme for each and every cell. Various methods have been developed to circumvent this problem [77, 145] but an easy approach is simply to merge a small cell with a larger neighbouring cell [59, 153].

Cartesian grids have a high degree of automation, can incorporate mesh adaptation fairly easily. To an extent, they also have the benefits of the structured grids over unstructured grids like better efficiency and accuracy. They have been used for aerodynamics applications [1], incompressible flows [226] and blast propagation problems in urban geometries [177, 194]. The Cartesian grid approach is chosen for this thesis because of its past usage and advantages over other methods.

2.3.1 Cut Cells

As bodies are usually surface triangulated, each triangular facet might represent a wall interface for the Cartesian finite-volume cell intersected by that facet. Cut cell methods preserve with full fidelity the surface definition for each intersected cell [4, 50, 54]. However these methods are very complex, requiring tedious computational geometry routines to perform intersections and possible re-triangulations to extract the wetted body surface for each cell. Further work has to go into accounting for numerous geometrical degeneracies, which arise because of floating point representations of cell and vertex positions.

2.3.2 Curvature-Corrected Symmetry Technique

This method, developed by Dadone [64, 65], does not require the complex topological description of intersected cells, insteading relying on reflected ghost cells near surfaces. An assumed flow-field model represents the effect of the surface; this model satisfies the normal momentum equation and accounts for surface curvature effects, consisting of a vortex flow of constant entropy and total enthalpy. Surface values are obtained through interpolation. This method has been used to solve flows over circular objects and airfoil geometries. It may still be more complicated to implement than other Cartesian cell methods because it requires reflecting ghost nodes through a body and calculating body curvature.

2.3.3 Surface Approximation

This method has many variants (varying in complexity) but generally approximates the surface by representing the portion of the body in an intersected cell as a single planar surface. Some methods only admit certain types of intersected cells [66, 106, 128, 153]. By admitting more cell types, the body surface can be represented more accurately, but this can be a cumbersome exercise. Other methods allow the planar surface to be computed generally using computational geometry routines or empirical geometric formulae [121, 124, 145, 174, 224].

Another method, not really suitable here, is the Porosity/Distributed Resistance (PDR) approach [45, 56, 78] where all (or just small-scale) obstacles are not actually resolved, but their effect accounted for by introducing appropriate porosities and distributed resistances into the flow equations. This approach has been used to model heat exhanger geometries and gas explosions in petrochemical processing installations [45], and is really only suitable for predicting global flow effects. PDR parameters like resistance terms are often empirically derived (or calculated from high resolution simulations), and can be difficult and expensive to extend to more complex configurations.

2.4 The Virtual Cell Embedding Method

The Virtual Cell Embedding (VCE) method, developed by Landsberg *et al* [124, 125] is chosen for this thesis due to its simplicity and robustness. It is a general surface approximation method (Section 2.3.3) and is based purely on a point-inclusion test, being equally suitable for convex or concave bodies or surfaces given by an analytic or arbitrary polyhedral definition. The VCE method has been used for simulations of flows over ship superstructures [124], blasts in pressure vessels [129] and dispersion of contaminants over complex city geometries [37]. This thesis combines the VCE method with hierarchical grid refinement (Chapter 3) and will explore the suitability of the VCE to model blast propagation in complex geometries.

The first stage of VCE involves subdividing an intersected cell into a lattice of 'subcells' (Figure 2.1(a)) each with its associated centroid. A subcell is labelled as inside/outside a body if its centroid is inside/outside. In this manner a summation of subcell volumes will yield the approximate unobstructed cell volume. Each cell face is also divided into 'sub-areas' to determine the approximate unobstructed face area. These subcells are not stored in memory; they are simply counting aids to determine the proper cell face areas and volume. Clearly the more subcells are used the better the obstruction is approximated.

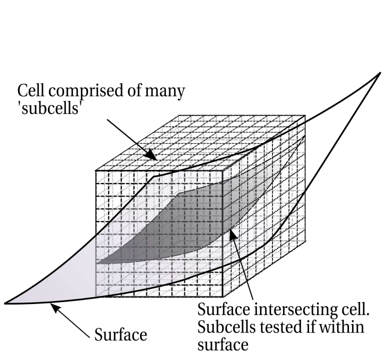
Cell comprised of many 'subcells'
Surface intersecting cell. Subcells tested if within surface
Surface

(a) 'Subcells' illustration

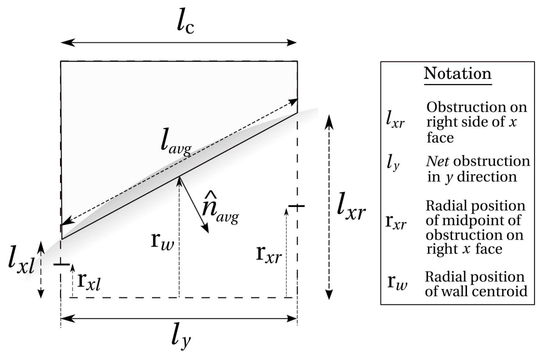
l_c
l_{avg}
$\widehat{n}_{avg}$
l_{xr}
l_{xl}
r_w
r_{xr}
r_{xl}
l_y
Notation
l_{xr} Obstruction on right side of x face
l_y Net obstruction in y direction
r_{xr} Radial position of midpoint of obstruction on right x face
r_w Radial position of wall centroid

(b) Computing surface properties

Figure 2.1: VCE method

In the second stage, the surface cutting through the cell is approximated as a single planar wall using the cell's obstructed areas. This is achieved by calculating the net obstructed face areas along each axis. For example, in Figure 2.1(b) the net obstructed area along the x axis is found by subtracting the 'left' obstructed area from the 'right' obstructed area i.e. $l_x = l_{xr} - l_{xl}$. The average wall surface normal $\mathbf{n}_{avg}$ is then

$$\mathbf{n}_{avg} = \sum_i \widehat{\mathbf{n}}_i l_i,\ i = x,\ y,\ z \tag{2.1}$$

$\widehat{\mathbf{n}}_\mathbf{i}$ is the unit vector along axis i. The corresponding wall surface area is

$$l_{avg} = ||\mathbf{n}_{avg}|| \tag{2.2}$$

and the unit surface normal is $\mathbf{n}_{avg}/l_{avg}$. Solid wall (i.e. reflection or symmetry) boundary conditions are then implemented for this surface. As the body representation has greater dependency on obstructed interface areas, normally more subcells are used on the face areas than the cell volume. Landsberg [124] commonly used 10^3 subcells for the cell volume and 20^2 subcells for each cell face, but this thesis usually uses 16^3 volume subcells and up to 64^2 face subcells.

2.4.1 VCE Resolution Issues

The VCE subcell subdivision potentially lets some cells that should be intersected go undetected in the presence of small-scale geometrical features (e.g. a knife edge penetrating into a cell). However for such cases, the inaccuracy would consistent with the grid resolution chosen, which would be too coarse in any case to resolve such fine features [124]. Another degeneracy occurs when all volume subcells are obstructed though a small part of the cell is outside a body. The whole cell should then be treated as if it were fully immersed (a ‘solid’ cell), and if any of its face areas are or were previously open, they are now closed.

A related degeneracy occurs when a thin wall might be contained within a cell. The VCE method does not ‘split’ cells, and thus flow can ‘leak’ across the wall as its interfaces are not properly obstructed. The simplest solution is to choose a cell size to ensure any walls in the domain are thicker than the longest length within a cell (from corner to corner) that would be used at surfaces (if cell sizes vary, as for adaptive meshes). This may require having finer cells at walls than elsewhere.

2.4.2 Dealing with Small Cells

As discussed earlier, very small cells are merged with larger cells to prevent excessively small timesteps. In `OctVCE` a cell is regarded as small if its fluid volume is 5–10% of its basis Cartesian cell volume. The cell merging algorithm searches a small cell’s neighbours for candidates to merge with into a larger ‘cluster’ cell (which stores the list of all such cells) treated as one cell by the flow solver. It searches preferentially for neighbouring large cells but if none are available recursively searches neighbouring small cells to form a cluster. The C pseudocode for the cell merging algorithm is given in Figure 2.2.

```
merge_cell(Cell C) {
  Search neighbours for unmerged
   large cell ULC to merge with
  if successful {
    Add C and ULC to merged cluster list
    return(TRUE)
  }

  Search neighbours for merged
   large cell MLC to merge with
  if successful {
    Add C to MLC's merged cluster list
    return(TRUE)
  }

  Search neighbours for small cell SC
   not already marked to merge with
  if successful {
    Mark C /*Prevent returning to this cell*/
    if merge_cell(SC) is TRUE {
      Add C to SC's merged cluster list
      return(TRUE)
    }
  }

  /*C cannot be in any merged cluster of
   sufficiently large cells*/
  Make C solid cell
  return(FALSE)
}
```

Figure 2.2: Pseudocode of cell merging algorithm

2.4.3 VCE Staircased Representation

A VCE ‘staircased’ surface representation is also possible, as in Figure 2.3. In this case each subcell comprising the ‘wetted’ staircase is a cell interface where solid boundary conditions are set. But as the flux through each subcell interface is the same in each direction, the total flow through the solid portion in that direction is

$$\sum_{subcells} (\mathbf{F_{wall}} \cdot \widehat{n}\Delta A) = (\mathbf{F_{wall}} \cdot \widehat{n}) \sum_{subcells} \Delta A \tag{2.3}$$

where $\sum \Delta A$ is simply the net obstructed area normal to the axis normal $\widehat{n}$; in Figure 2.3 it is $\Delta A = A^+ - A^-$.

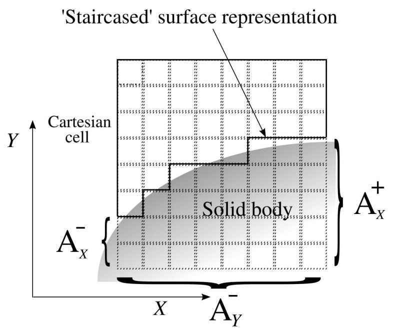

Figure 2.3: Staircased VCE representation

The staircased representation is generally inferior to the planar wall approximation of Figure 2.1(b) as it will result in low flow velocities near surfaces. This is shown in Figure 2.4 where Mach 4 flow over a wedge is simulated. There are about 100 cells along the wedge surface. Note that the flow over the staircased surface produces a thicker shock layer which noticeably deviates from the analytical shock angle (upper black line), and has low flow velocity at the surface.

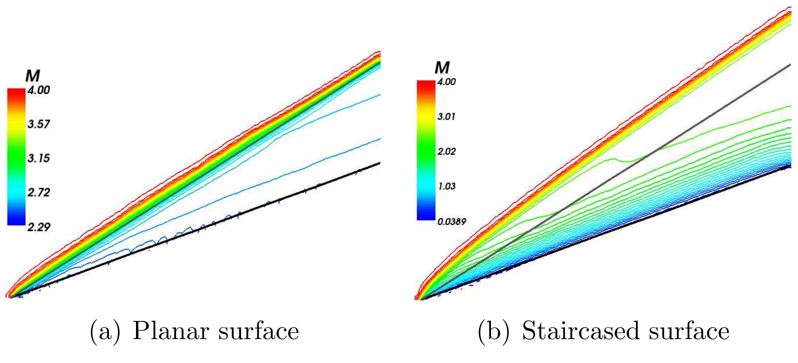

(a) Planar surface (b) Staircased surface

Figure 2.4: Comparison of planar and staircased VCE flow over a wedge

2.4.4 VCE Surface Noise

Note from Figure 2.4(a) the flow-field is not entirely uniform behind the shock. This is as the approximated surface normal in each intersected cell does not always align with the actual surface or with the surface normals of other intersected cells. This essentially numerically ‘roughens’ the surface, which produces some noise there. This noise can be seen in Figure 2.5 where pressure contours for the same Mach 4 flow problem over a wedge is shown, and the data limits adjusted to better show the generated noise at the surface. This spurious effect is studied numerically in more detail in Section 6.3.2. The results of Chapters 6 to 14 indicate that shock and blast propagation problems in complex geometry can still be simulated with reasonable accuracy despite this degeneracy.

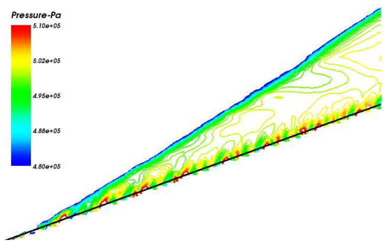

Figure 2.5: VCE-generated surface noise for supersonic wedge flow

2.4.5 Geometric Evaluations

Depending on the grid resolution, the VCE method requires the evaluation of potentially $O(10^5)$ to $O(10^6)$ point-inclusion tests for every subcell centroid. This may seem expensive, but the number of intersected cells is generally quite small relative to the entire grid [124]. Also, these geometric computations need only be done once at startup if cells at surfaces are not adapted, which is a small fraction of the total execution time. Tree-based adaptive meshes also allow propagation of geometrical properties from parent cells to children (e.g. unobstructed parents imply unobstructed children) and vice versa, which can save time as point-inclusion tests need not be performed for many newly created cells.

To improve the speed of geometric evaluations (especially for large multi-faceted bodies), the bounding boxes of all component bodies and their associated surface panels in the domain are also pre-processed and sorted into Alternating Digital Tree (ADT) structures [36] (see Appendix I). Then cells which are candidates for intersection are identified, undergoing subcell division to calculate volume and face obstructions. The point-inclusion algorithm is detailed in Section 4.9.

2.4.6 Example VCE-generated Mesh

An early demonstration of the versatility and robustness of the VCE method in generating grids over very complex geometries was given in Reference [202] and repeated in Figure 2.6. In this example the geometry corresponds to the buildings near the Mechanical Engineering building in the University of Queensland, and an explosion is initiated near this building. The square plan layout is about 200 m along the edge, with the highest building about 45 m. The geometry was built using CAD in the STL format (consisting of triangles, Figure 2.6(b)). Grids were adapted to the finest level at building surfaces, Figure 2.6(c).

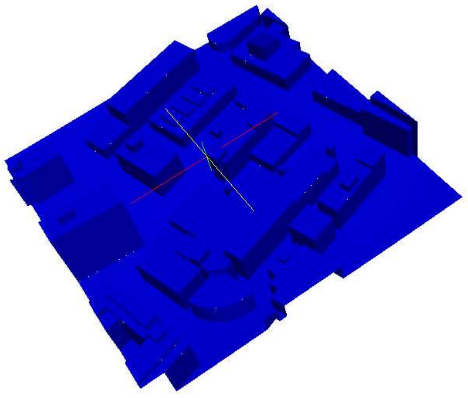
(a) Geometry

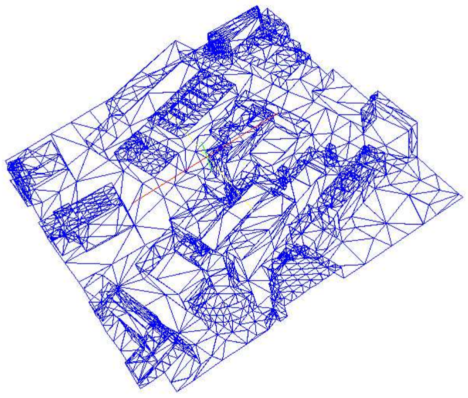
(b) Geometry (showing triangulation)

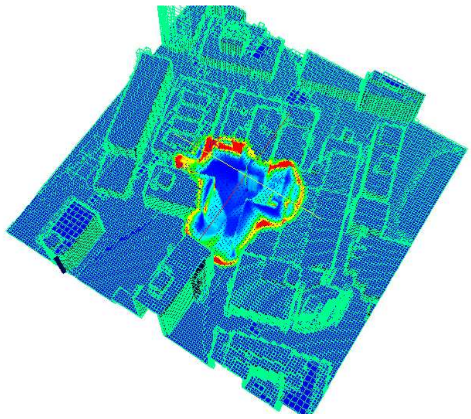
(c) Grid

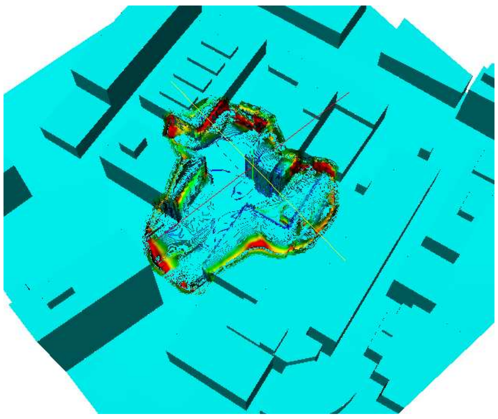
(d) Surface pressure contours

Figure 2.6: Gridding UQ geometry

Chapter 3

Mesh Adaptation

Mesh adaptation is a feature that adapts the grid to important flow features, allowing more accurate solutions to be obtained with fewer cells, resulting in significant savings in execution time [174]. One method of mesh adaptation, r-refinement, involves redistributing a fixed number of cells. For Cartesian cell approahces, this method is not as popular as h-refinement [26] where cells are added or deleted appropriately (and the width h of a cell is divided) because the grid distortion can be complicated to manage [228], and in many cases a grid redistribution will not resolve important features as well as h-refinement [59].

This thesis implements isotropic refinement where only one type of refined cell is created. Anisotropic refinement allows different types of cells to be created depending on the state of the local flow. This approach can result in even greater savings in cells [3, 50] where flow is predominantly unidirectional, but blast propagation in complex geometries is a more multidirectional problem which is suited to isotropic refinement [79]. Anisotropic refinement will also involve complicated data structures which would be more tedious to implement.

The Adaptive Mesh Refinement (AMR) method developed by Berger [24, 26] relies on adding or deleting entire patches of block-structured meshes rather than refining or coarsening individual cells (a tree-based method). Different timesteps are used on different patches (but are appropriately subcycled and interleaved to preserve time accuracy), and adaptation is guided by error estimation based on Richardson extrapolation. Because entire patches are added, about 30% of added cells are usually unnecessary [1, 118] which might lead to large memory requirements [177].

AMR might still be more memory efficient and faster than tree-based approaches because of structured mesh usage, which avoids the slower indirect addressing (pointers) common in tree-based meshes [24]. However, the AMR method is not used for this thesis due to its complexity [72, 81] in managing a dynamically changing collection of meshes, which need periodic rebuilding as the solution evolves over time [118].

`OctVCE` thesis implements the octree structure [51, 181] for mesh adaptation. This involves an isotropic division of a parent cubical cell undergoing refinement to yield eight children cells (and vice versa for the coarsening process), as shown in Figure 3.1.

The two-dimensional analogue is the quadtree. A cell corresponds to a tree *node*, and are *leaf* cells (being a part of the mesh used in the numerical solution) if they have no children. The creation of new children results in a new *level* in the tree (higher level nodes mean smaller children cells for this case). The *root* cell is the initial cell (without a parent) that undergoes division. Parent cells are not deallocated from memory during refinement so they can be quickly recovered during a coarsening phase.

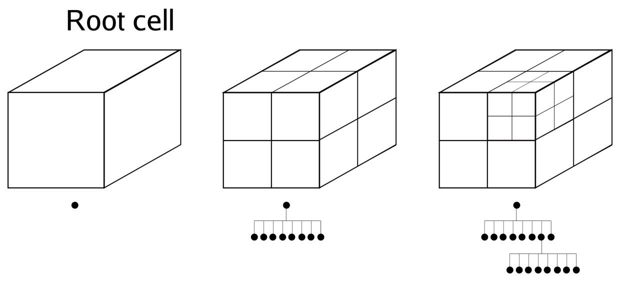

Figure 3.1: Refining an octree

It is a simple data structure to implement, but about 25% of the computing time is devoted to finding neighbour cells if mesh connectivity is not explicitly stored [66], and there can be substantial memory overhead to maintain the tree structure [118]. Sections 3.1 to 3.5 discuss various aspects of this adaptation procedure as implemented in `OctVCE`. More information on how to set up an adaptive mesh simulation with the code can be found in the user manual [205].

3.1 Explicit Storage

Because of the overhead from mesh traversal in determining cell neighbour relationships and the frequency with which these neighbours need to be accessed, a decision was made in the early stages of code development for each cell to explicitly store all face-adjacent neighbour cells. The sacrificing of memory for speed felt justified in lieu of the rapid growth in memory of workstation class machines over the past few years. Also, the main computing facility used for simulations in this thesis is the Altix supercomputer at the University of Queensland, which has a very large amount of memory (120 GB).

Geometric cell properties like centroids, which can be inferred from the tree structure, are also stored explicitly. To further minimize mesh traversal, all current leaf cells are stored on a dynamically linked list structure (Appendix K). This approach is quite memory-intensive and perhaps not feasible for smaller scale computing facilities.

A more memory-efficient tree structure is the Fully Threaded Tree (FTT) structure [118] where cells point to parents of neighbours, thus requiring no extra alteration when neighbours are coarsened. Because of the better memory efficiency, this approach may be ultimately more efficient than an explicit storage of all neighbours, and it has been implemented in Rose's `ftt_air3d` code [174, 177] (using about 0.25 kilobytes per cell).

3.2 Enforcement of Grid Regularity

Grid regularity is enforced when the level difference between cell neighbours is no more than one. This is to prevent too great a disparity amongst neighbouring cell sizes and minimize resultant noise. Mesh adaptation produces noise in the flow to a degree, particularly in the case of a shock passing from a coarse to a fine mesh [58, 118, 152], due to local errors in numerical fluxes in the vicinity of a strong shock. For octree cells this means a cell interface can have at most 4 neighbours.

However, the grid regularity is relaxed when adjacent neighbours are separated by a body like a solid wall, as in Figure 3.2. This prevents necessary refinement, especially for cells completely immersed within bodies. Cells store at most 4 neighbours per face, meaning that during refinement or coarsening downward or upward mesh traversal is still required for connectivities to be updated.

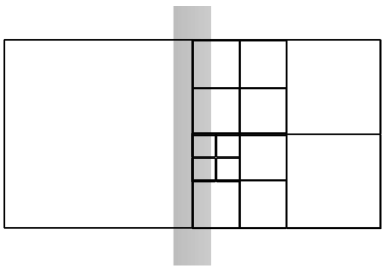

Figure 3.2: Cell with multiple neighbours

3.3 Cell Refinement and Coarsening Method

The cell refinement (and mesh traversal) process can be performed recursively, as shown in the pseudocode of Figure 3.3. Note that neighbour cells might require recursive refinement to satisfy grid regularity constraints (Section 3.2). The cell refinement step is done first during the adaptation phase by traversing the list of leaf cells and refining appropriate cells with this algorithm.

The cell coarsening step is then performed by traversing through the list of leaf cells again and marking their parents for coarsening if permissible. The list is re-traversed and parent cells are further checked against grid regularity constraints. This step is

```
refine/visit(cell) {
  if(refining this cell) {
    if(any neighbour needs refinement)
      refine(neighbour)

    Allocate children to cell's pointers
    Update grid topology and children's
      geometric properties
  }

  if(need to refine/visit a child)
    refine/visit(child)
}
```

Figure 3.3: Cell refining pseudocode

performed recursively as sometimes neighbouring cells of different levels can be coarsened, despite the list of leaf cells being traversed sequentially and the grid regularity constraints being temporarily violated whilst cells are coarsened. The pseudocode for this checking algorithm is shown in Figure 3.4. Coarsening parent cells can then be performed quite easily, as shown in the cell coarsening pseudocode in Figure 3.5.

```
check_for_coarsen(parent_cell) {
  if any children cells are not leaf cells
    return FALSE

  if any child flagged for refinement
    return FALSE

  Cycle through child cell neighbours {
    if neighbour too high level {
      if check_for_coarsen(neighbour's parent) FALSE
        return FALSE
    }
    else if neighbour flagged for refinement
      return FALSE
  }

  flag parent_cell for genuine coarsening
  return TRUE
}
```

Figure 3.4: Cell coarsen checking pseudocode

```
coarsen(parent_cell) {
  Delete children from list of leaf cells
  Add parent_cell to list of leaf cells
  Update mesh connectivities
  Reconstruct parent_cell state vector
  Deallocate children cells from memory

  return(TRUE)
}
```

Figure 3.5: Cell coarsening pseudocode

When cells are adapted, conservation in mass, momentum and energy should be preserved. When parent cells are coarsened, this is simple; its flow state is the volume-weighted average of its children [200, 228]. When parent cells are refined, the parent cell-centered flow state is interpolated to children cell centres using the conservativity-preserving interpolation procedure [200, 228] of Section 4.3 . The cell pressure is then calculated via the equation of state.

To enforce conservation of a quantity Q for partially obstructed parental cells p

undergoing refinement, the quantity Δ is calculated which represents the degree of non-conservation where

$$\Delta = Q_p V_p - \sum_{c=1}^{n} Q_c V_c \tag{3.1}$$

V_p is the parent cell volume, and V_c is the child cell volume; summing over n children cells $V_p = \sum_{c=1}^{n} V_c$. Q_c is the interpolated value of Q to child cell c from the reconstruction procedure of Section 4.3. To preserve conservation, the proper value of Q for the child cell c is

$$Q = Q_c + \frac{\Delta}{nV_c} \tag{3.2}$$

Based on the conservative timestepping criterion in Equation 4.7 it takes at least 4 timesteps for a shock to cross a cell, so adaptation every 5 timesteps is sufficient to ensure adapted flow features never leave a fine mesh region and lose resolution [118]. Interleaved timestepping for different cell levels is not implemented. Cells adjacent to those cells that are actually flagged for refinement are also refined to the highest permissible level to act as a 'buffer' layer.

3.4 Degeneracies during Adaptation

During adaptation geometric properties between cells must be consistent and airtight. As cell geometric properties are derived from VCE subcell division (Section 2.4), parental cells (having larger subcells) will not compute areas or volumes as accurately as children cells, and this must be accounted for. If adaptation of partially obstructed cells is allowed, one degeneracy occurs during the refinement stage as shown in Figure 3.6.

Here an intersected parent cell is refined but as a result of obstruction, one of its children are made 'solid'. Thus an interface area on the parent which was previously unobstructed is now obstructed. This new information must be remembered if the parent is coarsened and thus geometric information from children should be used during coarsening. Adaptation can also break up merged cell clusters that were formed because of the small cell degeneracy discussed in Section 2.4.2. When this occurs, pointers and associated data structures must be deallocated properly, and should small cells still exist after adaptation, re-merging with new cells should be done at this stage.

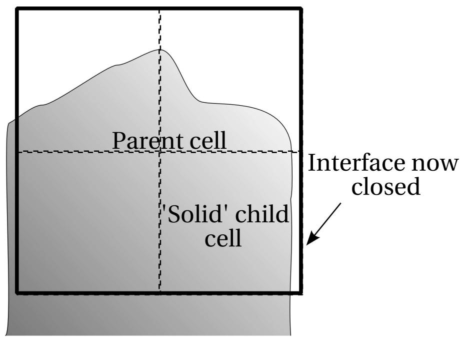

Figure 3.6: Solid cell refinement degeneracy

3.5 Adaptation Indicators

Adaptation indicators used in this thesis are gradient-based due to their simplicity and effectiveness [141], especially for blast propagation problems [118, 155, 174, 211]. The first indicator only detects shocks. It takes advantage of the fact that the velocity gradient through a shock is always negative irrespective of the direction of shock propagation –

$$\epsilon_1 = L\frac{\partial u_i/\partial x_i}{a_{min}}, \quad i = 1, 2, 3 \tag{3.3}$$

L is a length scale, typically the cell's edge length, and a_{min} is the minimum sound speed from the cell and its neighbours. Typically if ϵ_1 is smaller than -0.01 in any direction i the cell can be refined, or else it can be coarsened (by default).

The other indicator is based on Löhner's indicator [148, 155] and uses the second derivative of density and a noise filter term (based on the local mean density) to prevent needless refining around oscillations in the solution. A similar form of this indicator is also used in the unstructured code by Timofeev *et al* [211, 212, 220]. It can refine about contact surfaces and also smoother flow regions like the positive phase behind a blast, which might be important. It uses density differences along each axis i –

$$\epsilon_2 = \frac{\sum_i |2\rho_c - \rho_+ - \rho_-|}{\sum_i (|\rho_c - \rho_-| + |\rho_+ - \rho_c|) + \alpha \sum_i (\rho_- + 2\rho_c + \rho_+)} \tag{3.4}$$

where ρ_c, ρ_+ and ρ_- are the average densities at the cell centre, its right neighbour(s), and its left neighbour(s) respectively. The user must set thresholds on ϵ_2 for refinement and coarsening and also for the noise filter α.

Sometimes the indicators ϵ_1 and ϵ_2 are used jointly as the ϵ_1 indicator refines fewer cells (resulting in faster solutions), but the ϵ_2 indicator might be more important in the earlier stages of the explosion. A simple pressure difference indicator (that can be non-dimensionalized) can also be used [118], but this has not been implemented due to its similarity with the ϵ_1 indicator. Adaptation ‘regions’, which allow one to switch off mesh adaptation in some regions of the solution domain (implemented in the `ftt_air3d` code [177]), is not implemented here.

Chapter 4

Flow Simulation Algorithm

This section reviews and describes various important aspects in the numerical methodology behind `OctVCE`, including the governing equations, time integration scheme, flux solvers used, equations of state, implementation of initial and boundary conditions, interpolation or reconstruction method and point-inclusion query algorithm. It will be useful first to make some general comments as to the scope of the methodology.

Firstly, where possible, simple methods or methods already implemented in the `MB_CNS` code [109] (developed here at the University of Queensland) will be used. This will help streamline the process of eventually incorporating `OctVCE` as a submodule of `MB_CNS`, and also cuts down on code development time. Viscous effects can be ignored [160, 185] as blast propagation and loading problems are dominated by convection processes. The code will thus solve the unsteady Euler (compressible, inviscid) flow equations (Section 4.1).

Very accurate modelling of blast interaction with structures would require modelling fluid-structure interaction and multi-material shock physics, which can be challenging and tedious to code. This thesis considers only those class of blast propagation problems where structures are considered rigid and non-deforming and the pressure load is desired at some point(s) in space. This is a good assumption to hold in many cases even when buildings are subjected to intense loading because of the strength of modern-day reinforced concrete or steel-framed structures [160, 193]. The most significant damage to buildings usually occur at glazed areas like windows, and transfer of momentum to the building is small, justifying rigid boundary condition implementation and decoupling blast-structure interaction.

Chemical reactions are not modelled as this is computationally expensive and really only needed for accurate modelling of the explosive fireball, which is not the focus of this thesis. It has been demonstrated in numerous blast propagation simulations [160, 174, 211, 212] that accurate chemical modelling of detonation is not required for good results in the mid- to far-field (see Sections 1.2 and 1.1.1). The most important quantity is the energy released [19, 171, 211].

Due to the adoption of the VCE Cartesian grid method (Section 2.3) a finite-volume scheme [96] is favored for the discretization of the flow equations, as almost all Cartesian grid methods are formulated on a finite-volume approach. Compared to other methods, the finite-volume scheme is also simple to implement, inherently conservative and can capture shocks well. Other discretization methods, like the finite difference [9, 96], finite element [53, 96], spectral [102] and the more recent CESE method [229] are not as flexible or evolved as finite-volume methods, may require reliance on unstructured grids (thus subject to the disadvantages discussed in Section 2.1) or be difficult to implement in complex geometry.

4.1 Governing Equations

The three-dimensional Euler equations in integral form can be expressed as

$$\frac{\partial}{\partial t}\int\int\int_V \mathbf{U}dV + \int\int_S \mathbf{F}\cdot\widehat{\mathbf{n}}dS = \mathbf{0} \tag{4.1}$$

where $\mathbf{U}$ is the vector of conserved quantities (per unit volume) $\mathbf{U} = [\rho, \rho u, \rho v, \rho w, \rho E, \rho_p]^T$ (in three dimensions), t is the time dimension, ρ and ρ_p are the total density and explosive products (thus at most two gas species are tracked) density, u, v and w are velocity components in the x, y and z directions respectively. If ρ_a is the density of the ambient gas (typically air), the total density is $\rho = \rho_p + \rho_a$.

E is the total intensive energy where $E = e + \rho\left(u^2 + v^2 + w^2\right)/2$, e is the intensive (internal) energy. $\widehat{\mathbf{n}}$ is the outward unit normal on the surface S which bounds the control volume V. In two dimensions the z components are neglected. The vector of fluxes is

$$\mathbf{F} = \begin{bmatrix} \rho u \\ \rho u^2 + P \\ \rho uv \\ \rho uw \\ \rho Eu + Pu \\ \rho_p u \end{bmatrix}\widehat{\mathbf{i}} + \begin{bmatrix} \rho v \\ \rho uv \\ \rho v^2 + P \\ \rho vw \\ \rho Ev + Pv \\ \rho_p v \end{bmatrix}\widehat{\mathbf{j}} + \begin{bmatrix} \rho w \\ \rho uw \\ \rho vw \\ \rho w^2 + P \\ \rho Ew + Pw \\ \rho_p w \end{bmatrix}\widehat{\mathbf{k}} \tag{4.2}$$

where P is the absolute static pressure. The equation of state provides pressure in terms of energy and density, $P = P(\rho, e)$.

It is also intended for the code to solve for flows in two dimensions with complex planar and axisymmetric geometry. The planar case uses the same form of the Euler equations (Equation 4.1) but without the third dimension (or any quantity associated with it); the axisymmetric Euler equations require some modification and in integral form are expressed as

$$\frac{\partial}{\partial t}\int_A \mathbf{U} dA + \int_l r\mathbf{F}\cdot\widehat{\mathbf{n}} dl = \int_V \mathbf{Q} dA \tag{4.3}$$

where $\mathbf{U} = [\rho, \rho u, \rho v, \rho E, \rho_p]^T$ and $\mathbf{F}$ are the same quantities (but without the third dimension) in Equation 4.1. This time, $\widehat{\mathbf{n}}$ is the outward unit normal on the surface l which bounds the control volume A, which is a volume per radian. If the x axis is the symmetry axis and y axis the radial axis, then r is the radial co-ordinate at an interface and the source term $\mathbf{Q} = [0, 0, P/r, 0, 0]^T$ where P is the pressure in the cell.

4.2 Finite-Volume Discretization

A cell-centered finite-volume discretization of the Euler Equations (Equation 4.1) is given by

$$\frac{d\mathbf{U}_c}{dt} = -\frac{1}{V_c}\sum_{if}\mathbf{F}_{if}\cdot\widehat{\mathbf{n}}_{if}A_{if} \tag{4.4}$$

where the subscript if stands for interface, V_c is the cell volume, and $\mathbf{U}_c$ is the cell-centered state vector. The interface fluxes $\mathbf{F}_{if}$ are calculated from the procedures described in Sections 4.3 to 4.4

These equations are marched forward in time using an explicit scheme (in which the solution at the next time step depends only on previous solution values). Explicit schemes are simple to code, easier to parallelize and generally less memory intensive than implicit schemes [9]. The classical second-order Runge-Kutta [82] method, consistent with the code's second-order spatial accuracy (Section 4.3) is used to advance all cells in time –

$$\mathbf{U}_c^{n+\frac{1}{2}} = \mathbf{U}_c^n - \frac{\Delta t}{2V_c}\sum_{if}\mathbf{F}_{if}^n\cdot\widehat{\mathbf{n}}_{if}A_{if} \tag{4.5}$$

$$\mathbf{U}_c^{n+1} = \mathbf{U}_c^n - \frac{\Delta t}{V_c}\sum_{if}\mathbf{F}_{if}^{n+\frac{1}{2}}\cdot\widehat{\mathbf{n}}_{if}A_{if} \tag{4.6}$$

This requires storage of the cell flow state at both time n and $n+1/2$ to obtain the cell state at the next time $n+1$. It is possible for different timesteps to be taken for different cell levels in the adaptive mesh [118] in an interleaved manner to preserve time accuracy. For reasons of simplicity and issues with integration of `OctVCE` into the `MB_CNS` code, this approach is not taken here.

To prevent instability in the solution the timestep must be chosen to be smaller than the minimum time taken for physical processes operating in the solution domain, which in this case is the crossing of an acoustic wave signal across a cell [62]. A conservative timestep [50] for each cell c is

$$\frac{\Delta t_c}{V} = \frac{\text{CFL}}{\sum_{if} A_{if}(a + |\mathbf{u} \cdot \widehat{n}_{if}|)} \tag{4.7}$$

where the CFL number [62] CFL ≤ 1 (typically 0.5), a is the soundspeed in the cell and $\mathbf{u}$ the fluid velocity. A_{if} is the interface area for a face of the cell, which varies for Cartesian cells. It is quite conservative, taking into account intersected cells which might have smaller volumes and interface areas than unobstructed cells, and requires at least 4 timesteps for a wave to cross an unobstructed cell. The global timestep for the whole solution with n cells would be

$$\min_n (\Delta t_1, \Delta t_2, ..., \Delta t_n)$$

4.2.1 Axisymmetric VCE Method

For the axisymmetric Euler equations (Equation 4.3), the cell-centered finite-volume discretization is given by

$$\frac{d\mathbf{U}_c}{dt} = -\frac{1}{A_c}\sum_{if} r_{if}\mathbf{F}_{if} \cdot \widehat{\mathbf{n}}_{if} l_{if} + \mathbf{Q} \tag{4.8}$$

where the volume per radian $A_c = Ar_c$, A is the cell area and r_c the cell's average radial co-ordinate. An axisymmetric extension to VCE has been developed as part of this thesis [204] and is repeated in Appendix D.

4.3 Reconstruction

In finite-volume methods, the values of the flow variables in the vector of fluxes $\mathbf{F}_{if}$ in Equation 4.4 are usually interpolated from the cell centre to the cell interface to establish greater than first order spatial accuracy. The interpolation process is limited for flows containing strong gradients or discontinuities as it can overshoot, causing high frequency noise and even instability and failure in the flow solution [97]. In regions with high gradients the limiter should cause the interpolation to revert to first order and in regions of smooth flow should allow normal interpolation to proceed.

Limiters must satisfy the Total Variation Diminishing (TVD) constraints [14, 97], which is a minimum requirement for many CFD codes [171]. TVD schemes prohibit the generation of new extrema, are monotonicity preserving [97] and are generally restricted to second-order accuracy [14]. However, because TVD schemes suppress noise in solutions, they may sometimes cause of loss of genuine extrema [14, 110]. The process of interpolation and limiting is termed *reconstruction* and in this code is multidimensional in nature [218] as the Cartesian cells are not always aligned with the flow direction.

4.3.1 Interpolation

The most common interpolation procedure is linear interpolation of flow variables ρ, $\mathbf{u}$ and e from the cell centre to cell interfaces, which achieves second-order spatial accuracy. This requires computation of flow gradients, which can be an expensive step. Gradients can be computed using the Green-Gauss approach [5, 66, 80] or least squares approach [5, 20]. Both these approaches require a cloud of neighbouring points (usually values at nearby cell centres) around the cell centre.

The least squares gradient calculation is chosen due to its reliability and somewhat easier implementation [5]. This scheme, also detailed in [50], is as follows. For each cell c, over all its neighbours n (h-refined cells may have more than one neighbour on each interface), the difference in centroidal co-ordinates is summed and placed in the inverse (symmetric) *reconstruction matrix* –

$$\mathbf{R}^{-1} = \begin{bmatrix} \sum_n (\Delta x)^2 & \sum_n (\Delta x \Delta y) & \sum_n (\Delta x \Delta z) \\ \sum_n (\Delta y \Delta x) & \sum_n (\Delta y)^2 & \sum_n (\Delta y \Delta z) \\ \sum_n (\Delta z \Delta x) & \sum_n (\Delta z \Delta y) & \sum_n (\Delta z)^2 \end{bmatrix} \tag{4.9}$$

where $\Delta\{\,\cdot\,\} = \{\,\cdot\,\}_n - \{\,\cdot\,\}_c$. If two-dimensional flow is simulated the third row and column of this matrix is ignored. If the gradient of a flow quantity Q is desired, the 3×1 vector $\mathbf{r}$ is calculated as

$$\mathbf{r} = \sum_n (\mathbf{c}_n - \mathbf{c}_c)\left((Q)_n - (Q)_c\right) \tag{4.10}$$

where $\mathbf{c}$ stands for a cell centroid and subscript c denotes the cell centre. Then the cell-centered gradient vector of Q would be

$$\nabla (Q_c) = \mathbf{R}\mathbf{r} \tag{4.11}$$

The flow quantity Q can now be interpolated to any point $\mathbf{p}$ within the cell using the expression

$$Q(\mathbf{p}) = \Phi \cdot \nabla (Q_c) \cdot (\mathbf{p} - \mathbf{c}_c) \tag{4.12}$$

Now Φ is a limiter value that ensures no new extrema are created and prevents spurious oscillations in the numerical solution. It is determined according to the procedure described in Section 4.3.2.

For reasons of simplicity and efficiency, interpolation to the centre of cell interfaces is performed and only face-adjacent neighbours are chosen for the reconstruction matrix (Equation 4.9); neighbours which only share edge or corner connectivity are ignored. This means that the least squares calculation collapses to one-dimensional differencing to obtain the gradients for uniform Cartesian cells.

4.3.2 Limiting

Whilst there exist several ways by which the limiter Φ can be determined [218], the multidimensional min-mod type limiter of Barth [20] is chosen for its simplicity. This type of limiter is also used in Rose's `Air3d` code and has proven to be useful for many blast simulations [171, 176]. This is a non-differentiable limiter which may hamper convergence of steady state solutions [218] but is adequate when modelling unsteady blast waves.

For a flow quantitiy Q and looking over all a cell's neighbours n, let

$$Q^{\min} = \min_n (Q_c, Q_n) \tag{4.13}$$

and

$$Q^{\max} = \max_n (Q_c, Q_n) \tag{4.14}$$

where subscript c denotes the cell-centred value. Then the unlimited value of Q is interpolated to a point $\mathbf{p}$ coinciding with each cell corner j –

$$Q_j = Q_c + \nabla (Q_c) \cdot (\mathbf{p}_j - \mathbf{c}_c) \tag{4.15}$$

The limiter value for the flow quantity q at cell corner j is thus ϕ_j^Q and is determined by

$$\phi_j^Q = \begin{cases} \min\left(1, \frac{Q^{\max} - Q_c}{Q_j - Q_c}\right) & \text{, if } Q_j - Q_c > 0 \\ \min\left(1, \frac{Q^{\min} - Q_c}{Q_j - Q_c}\right) & \text{, if } Q_j - Q_c < 0 \\ 1 & \text{, if } Q_j - Q_c = 0 \end{cases} \tag{4.16}$$

The global limiter (for a cubical cell there are 8 corners) for this cell is finally

$$\Phi = \min\left(\phi_1^Q, \phi_2^Q, ..., \phi_8^Q\right) \tag{4.17}$$

It is possible to have multiple limiters for each flow variable, or a single limiter from the minimum of each limiters, though it has been found that the extreme gradients at the start of a explosion simulation will cause the code to fail unless a single limiter is used. After a while multiple limiters can be used safely.

4.3.3 No Reconstruction for Intersected Cells

Because the VCE method (Section 2.4) does not actually store position vectors of partially obstructed cell interfaces for intersected cells, interpolation cannot be performed to the wall surface. An averaging procedure, much like in axisymmetric VCE extension of Section 4.2.1 can be developed to compute the position vectors of the interfaces but this is difficult and potentially expensive to apply to the wall surface itself in three dimensions. Thus for simplicity and efficiency, no reconstruction is performed at intersected cells, although the scheme is still globally second-order accurate. This may also be preferrable since the VCE method can generate spurious noise at surfaces (Section 2.4.4) which can be damped to an extent by reverting to a first-order scheme there.

4.4 Flux Solvers

Once the flow variables are reconstructed appropriately to the interface, the vector of fluxes $\mathbf{F}_{if}$ (Equation 4.2) is calculated with a flux solver. The most common flux solvers are one-dimensional, where the flux convection speed is independent of the tangential interfacial velocity and fluxes are computed through each interface independently. This approach has worked well in practice [97, 170] and is adopted here because of its widespread usage and simplicity. Many flux solvers are upwind schemes which account for the physically correct manner in which information propagates between cells [199].

Upwind schemes broadly include difference splitting schemes which solve the exact or approximate Riemann problem [85, 154, 214], vector splitting schemes with the flux combining of forward and backward vectors [217], kinetic theory based [150] methods or the very popular Advection Upwind Splitting Method (AUSM) type schemes [221] which use different splittings for convective and pressure terms. These methods vary in computational expense and accuracy. Exact Riemann solvers are accurate but expensive, approximate Riemann solvers are cheaper but require some fixes and suffer from odd-even decoupling [154], kinetic theory methods are quite dissipative and AUSM-based methods are fairly cheap, nearly as good as difference splitting schemes, but can have pressure oscillations.

The main flux solver used in this thesis is the AUSMDV scheme [221]. This scheme resolves shock waves accurately without excessive dissipation and is also the solver of choice in the `MB_CNS` code [109]. AUSM-based schemes are also less dependent on fluid thermodynamics, which is useful in this thesis as real gas models can be incorporated (Section 4.5). It is quite simple to code, fairly efficient, and found to be suitable for blast propagation problems in the `Air3d` code [171].

The kinetic theory based Equilibrium Flux Method (EFM) [150] is also implemented. This flux solver is especially useful at shocks to damp oscillations, which can lead to odd-even decoupling (in which perturbations at a shock are aphysically amplified, leading to flow instability) even for the AUSMDV method [110, 154]. An adaptive flux solver (switching from AUSMDV to EFM at shocks) is also employed by the `MB_CNS` code [109]. The AUSMDV and EFM flux solvers are covered in greater detail in Appendix F.

4.5 Equations of State

In the code, the ambient gas (usually initially at atmospheric conditions) is modelled as an ideal, calorically perfect gas, and the detonation products can be modelled either as an ideal gas or with the real gas JWL equation of state [127]. Despite the significant non-ideal effects near the fireball, using an ideal gas for both the explosive products and ambient gas is computationally faster and adequate for many blast effects problems in which the main objective is the determination of blast loads [41, 144, 166, 174, 211].

4.5.1 Ideal Gas Equation of State

The ideal gas equation of state is $P = P(\rho, e) = \rho e(\gamma - 1)$ where P is static pressure, ρ density and e intensive energy, and γ is the ratio of specific heats C_p/C_v. It is assumed the gas is calorically perfect with constant specific heats and internal energy $e = C_vT$. Thus the temperature-dependent form is $P = P(\rho, T) = \rho RT$ where the gas constant $R = C_v(\gamma - 1)$. If there is a mixture of ambient gas and explosion products, the mixture specific heat is given by the mass fraction-weighted expression $C_v = f_aC_{v,a} + f_pC_{v,p}$ where f_a and f_p are the mass fractions of the ambient gas and explosive products, $f_a = 1 - f_p$. A similar expression for C_p can be found for the mixture and thus γ for the equation of state.

4.5.2 JWL Equation of State

The JWL equation of state [127] is a popular real gas equation of state used to model explosive detonation. It is an empirical equation of state calibrated based on the cylinder expansion test and has been extensively used to model other applications of explosives [146]. Being empirical, it already takes into account (to some extent) afterburning effects [101]. The JWLB equation of state [17] is a more advanced version which better describes the gas behaviour in other states not close to adiabatic expansion e.g. if the detonation products are re-shocked. The JWL equation of state for the explosion products is

$$P_p = P_p\left(\rho_p, e_p\right) = A\left(1 - \frac{\omega}{R_1\widetilde{v}}\right)e^{-R_1\widetilde{v}} + B\left(1 - \frac{\omega}{R_2\widetilde{v}}\right)e^{-R_2\widetilde{v}} + \omega\rho_p e_p \tag{4.18}$$

where $\widetilde{v}$ is the relative volume of the explosion products $\widetilde{v} = \rho_{0,p}/\rho_p$ and $\rho_{0,p}$ is the initial undetonated density of the explosive. e_p is the specific internal energy of the explosive products, and A, B, R_1, R_2 and ω are expermentally-determined constants. All these values (including $\rho_{0,p}$ and e_p) can be found in References [126, 127].

A temperature-dependent form has been developed by Baker [17, 18] originally for the JWLB equation of state, but applicable to the JWL form if the additional JWLB terms are discounted –

$$P_p = P_p\left(\rho_p, T\right) = Ae^{-R_1\widetilde{v}} + Be^{-R_2\widetilde{v}} + \rho_p\omega C_{v,p}T \tag{4.19}$$

$$e_p = e_p\left(\rho_p, T\right) = \frac{A}{R_1\rho_{0,p}}e^{-R_1\widetilde{v}} + \frac{B}{R_2\rho_{0,p}}e^{-R_2\widetilde{v}} + C_{v,p}T \tag{4.20}$$

The specific heat of the explosion products $C_{v,p}$ is assumed constant, and is usually a derived value (from Equation 4.19) if temperature and pressure at a given condition is known (usually the initial explosive condition, like the Chapman-Jouguet condition). Mader [133] provides initial detonation temperatures for some explosives. If the JWL equation of state is used in simulations, a combined JWL-ideal gas equation of state may be required near the fireball where there is some mixing of detonation products and ambient gas. The derivation is left to Appendix G and G.1.

4.6 Initial Conditions

In `OctVCE` the charge or bomb is represented by a group of high pressure and temperature cells tuned to give the correct blast energy which approximate the charge shape, known as the ‘balloon analogue’ or ‘isothermal bursting sphere’ model [144, 166, 174, 211]. This approach has been found to be a simple and adequate initial condition to use for the mid- to far-field regimes, as the dominant variable affecting the primary shock intensity is the initial energy released [19, 41, 144, 166, 171, 211]. This approach has produced very good correlation with experimental TNT blast distance curves from as close as 0.3 m/kg$^{1/3}$ to the charge [171], even using ideal gas for the charge. Afterburning also affects the blast intensity [166], and the negative phase and secondary shock are more sensitive to initial conditions [166], but these effects are not so significant for many realistic blast loading problems [171, 174].

The initial charge shape can be adjusted, which has an effect on the early blast wave [40, 211], although a spherical blast wave pattern develops fairly close to the charge (see Section 1.2). To enable better resolution of the early stages of the explosion on expensive multi-dimensional meshes, a remapping strategy can be used which maps a highly resolved one-dimensional spherically symmetric solution to higher dimensions before the blast passes any surface [104, 171, 174]. This requires some effort to implement, is inapplicable for non-spherical charges, and may be difficult to perform if geometry is close to the charge. There is also some loss in resolution when solutions are remapped to lower resolution meshes. Chapters 10 to 14 explore the accuracy of blast propagation simulations where remapping is not performed.

4.6.1 Calculating Correct Conditions

To ensure correct blast energy and charge mass, the density of the charge is set to $\rho = m/V$ where V is the volume of the cells representing the charge and m the charge mass. The balloon gas intensive energy is equal to the intensive blast energy. The pressure is then calculated via the equation of state. For the JWL equation of state (Section 4.5.2), the value $\rho_{0,p}$ can be adjusted to this value of ρ, although this is not necessary. This is a simplistic use of the JWL equation as no simulation of finite-rate burning of the explosive material is performed, but this initial condition would correspond roughly to the final state of the detonation products following a confined explosion. In axisymmetric geometry, the volume V and mass m are expressed as a volume and mass per radian respectively. The volume per radian of any axisymmetric volume V is $V/(2\pi)$. The mass per radian is obtained using the expression ρV. The volume per radian of a Cartesian cell is Ar_c where A is the cell's area and r_c the cell's average radial co-ordinate.

4.7 Boundary Conditions

As only rigid structures are considered in this thesis, allowable boundary conditions are wall and inflow/outflow boundary conditions. All these boundary conditions are implemented by fabricating appropriate state vector values $\mathbf{U}_b$ at a given cell's interface.

4.7.1 Wall Boundary Condition

Solid surfaces in intersected cells are represented as a cell interface with an outward normal vector $\widehat{\mathbf{n}}$ (see Section 2.4). This wall boundary condition $\mathbf{U}_b$ (which is identical to the symmetry boundary condition) has the same state of flow at the interface but with a reversed normal velocity component to ensure zero mass flux. Thus if $\mathbf{u}$ is the flow velocity at the cell interface $\mathbf{U}_b = \left[\rho, \rho\left(\mathbf{u} - 2\left(\mathbf{u}\cdot\widehat{\mathbf{n}}\right)\widehat{\mathbf{n}}\right), \rho E, \rho_p\right]^T$.

4.7.2 Inflow/Outflow Boundary Conditions

Inflow/outflow boundary conditions are implemented at the boundaries of the computational domain where flow is permitted to flow in or out. In the code, individual flow variables can be set to fixed or extrapolated values. Usually the domain is sufficiently large to encompass the entire blast environment and the exiting blast typically induces outflow. If the flow is supersonic, all variables can be extrapolated [9] as characteristics all point outward.

Problems with boundary specification arise when the outflow is subsonic. For such cases, non-reflecting boundary conditions might be implemented which attempt to minimize boundary effects from influencing the solution within the domain. This topic has been a subject of much research [61, 216]. Many non-reflecting boundary conditions involve linearization at the boundary about uniform conditions and setting all incoming wave amplitudes to zero [61]. Popular non-reflecting boundary conditions are based on characteristic analysis [61], like the Thompson boundary conditions [209, 210]. These methods are usually developed (and possibly exact) for one-dimensional problems and in multidimensions usually prescribe a predominant direction of wave propagation, typically normal to the boundary. Some reflections will occur for outgoing non-isentropic or oblique waves [116, 216].

More advanced approaches use buffer zones or absorbing layers near boundaries where some filtering or numerical damping is usually performed [61, 162]. This can be done by introducing artificial dissipation, increasing physical viscosity or adding a linear friction coefficient to the governing equations. The solution would be aphysical in this region, and more complicated formulations of this damping (typically called Perfectly Matched Layers) can be implemented which minimize the reflectivity of the absorbing layer itself [61, 88]. These methods can be *ad hoc* and involve parameters which require manual tuning like the buffer zone size.

As many of these methods are computationally expensive and complicated to implement, only Thompson's [210] non-reflecting boundary conditions are implemented in `OctVCE`. This method is simple and proven to be quite robust [61], and performs best when the outgoing wave is normal to the boundary. The selection of non-reflecting boundary conditions is not so crucial in any case; sufficiently large numerical domains can usually be set up because mesh adaptation allows coarser (thus fewer) cells near boundaries [211]. The implementation of the Thompson boundary conditions is described in Appendix H. In the code, numerical oscillations at boundaries are further suppressed by using the more dissipative EFM flux solver at border cells and cells adjacent to border cells.

4.8 Numerical Instabilities

4.8.1 CFL cut-back Procedure

Numerical instability or even failure of the solution can result in simulations of strong explosions, due to the extreme discontinuities and conditions near the explosion core [116, 211]; the pressure in this region can vary from about 5×10^5 atmospheres to near-vacuum levels [133]. This can be prevented by keeping fine grids or simply using a first-order scheme there e.g. Rose proposes a 'switching-time' strategy [171] where no reconstruction is performed until a scaled time of about 1.2×10^{-3} s/kg$^{1/3}$ after the explosion.

A CFL cut-back procedure can also be implemented, which reduces the CFL number to limit the maximum relative change in density and pressure each timestep. This procedure, originally developed for aerodynamic simulations [58], can be used in conjunction with the switching-time strategy. At timestep k, first let the minimum timestep be found for the maximum allowable Courant number CFL_{max}, and the values of the density and pressure after the first Runge-Kutta step k^* is found. Then let

$$\epsilon_\rho = \frac{|\rho_{k^*} - \rho_k|}{\rho_k} \tag{4.21}$$

$$\epsilon_P = \frac{|P_{k^*} - P_k|}{P_k} \tag{4.22}$$

Then an acceptable CFL can be found for some cut-back fraction ϵ_{cut} using

$$C = \frac{\epsilon_{cut}}{max\left(\epsilon_\rho, \epsilon_P\right)}$$

$$\text{CFL} = \min\left(C, \text{CFL}_{max}\right) \tag{4.23}$$

$\epsilon_{cut} = 0.1$ is usually a good default value. The CFL cut-back procedure is usually required at the beginning of an explosion, but afterwards the CFL gradually ramps back up to CFL_{max}.

4.8.2 Axisymmetric Numerical Jetting

Aphysical numerical jetting along the symmetry axis can occur for axisymmetric blast simulations, as in Figure 4.1 where the density contours are shown. This results from the axisymmetric correction term for degenerate cells along the axis of symmetry [44, 148]. Using an adaptive mesh would amplify the jetting. This glitch can be fixed if a small core of cells around the axis is removed or the grid is radially stretched, but using a dissipative flux solver like EFM (Section 4.4) at the shock has also worked for this case.

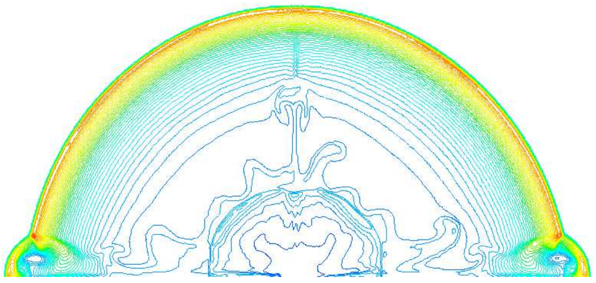

Figure 4.1: Example of numerical jetting for 2D axisymmetric blast simulation

4.9 Point-inclusion Queries

The VCE method is based on a point-inclusion query which determines the location of subcell centroids relative to solid objects. In `OctVCE` a polyhedral representation of geometries is chosen because point-inclusion queries for surfaces defined by non-linear representations are difficult and time-consuming. Moreover, many methods have been developed for polygonal and polyhedral point-inclusion tests.

Point-inclusion tests are usually based on (or conceptually related to) variants of the ray-casting approach [100]. Assuming the point is reasonably close to the polygonal/polyhedral body, if a ray beginning at the point is cast in any direction to a sufficiently large distance, it will be inside the body if it intersects it (i.e. pierces the body's boundary) an odd number of times, and outside if it never intersects or intersects an even number of times. Degeneracies need to be accounted for e.g. ray intersection with an edge of vertex of the body. Many point-in-polyhedron tests also require performing point-in-polygon tests.

Review articles on various point-in-polygon algorithms can be found in [98, 100]. Other point-in-polygon algorithms include the sum-of-angles method, sum-of-area method (similar to sum-of-angles, but for convex polygons only), swath method (ray intersection-based), sign-of-offset method, orientation method (like sum-of-area, but without area calculation) and wedge method (similar to swath method, but only for convex polygons). Generally those methods that are based on routine computation of trigonometric quantities are less efficient, which is why the ray casting method is still a popular and efficient method [130, 223].

There have also been numerous point-in-polyhedron algorithms developed [75, 99, 111], which can vary in complexity. Many methods reduce dimensionality of the problem by projecting planar images of the polyhedral facets along with an image of the point being tested. This thesis implements the simple polyhedral point-inclusion test by Linhart [130] which is also a ray intersection-based projection method. Degeneracies are resolved by associating with each point of intersection a certain positive or negative weight. Linhart's method is also applicable for the point-in-polygon test, which needs to be performed for polyhedron queries. This method is described in Appendix J.

Chapter 5

Parallel Computing

Simulating blast propagation in three dimensions can involve large meshes, which usually mean long execution times. More computing power can be achieved if processors are combined in parallel to solve a single problem. Another motivation for parallel solutions is the increased memory resources of a multi-processor system, which might be necessary for large simulations.

Ideally the parallelization strategy should be fairly portable and scale proportionally with the number of processors. However parallel computing methods can be complicated to implement, as can determining the theoretical code performance [95]. As most of the computing time is usually spent in a relatively small portion of the code [147], the optimal parallelization method requires insight into the underlying algorithms. Scaling to more processors usually results in scaling in memory resources which can have an adverse effect on performance; efficient use of memory is also an important consideration for parallel solutions.

The most common way of solution parallelization in CFD problems is through domain decomposition, where the same code is executed on different sections of the numerical domain. A brief survey of popular domain decomposition methods will be given in Section 5.1. Section 5.2 outlines parallel computing architectures, and Sections 5.3 and 5.4 respectively discuss parallel programming methods and parallel performance measures. Finally Section 5.5 describes the shared-memory parallelization strategy for the `OctVCE` code in particular.

5.1 Domain Decomposition Methods

Domain decomposition is a challenging problem which involves partitioning the mesh and assigning each portion to a separate processor. Twin goals are achieving a good load balance (equal amount of computational work per processor) and minimizing the edge-cut or interprocessor communication. This is a large field of research, and journals devoted to domain decomposition methods and other aspects of parallel computing include *Concurrency*, *Journal of Parallel and Distributed Computing* and *Parallel Computing*. A number of review articles have also been written [69, 215]. In many cases, different methods perform best for different problems [215].

A number of methods varying in sophistication have been developed. One of the more simple and popular methods is the recursive co-ordinate bisection method [187, 215] and its variations. This method performs well for small numbers of processors [215] (eight or less) and when the mesh is evenly spread over a simple domain [69]. It basically partitions the domain according to the co-ordinates of the verticies perpendicular to the co-ordinate direction to achieve an equal load on either side of the cut [215]. This process is repeated recursively on each subdomain until the required number of subdomains is obtained. This method can generate decompositions efficiently [69] but does not minimize the edge-cut as well as other methods. The edge-cut is important for distributed-memory parallelism because it determines the amount of communication required between processors.

Other methods involve mapping the mesh into an octree structure and basing the partition on the octree representation [76]. Recursive bisection can also be applied to this representation [135]. Octree partitioning involves traversals of the tree structure to accumulate octants or subtrees into successive partitions. Like the recursive bisection method, it is incremental in its dynamic load balancing; small changes in the mesh (through mesh adaptation) produce small changes in the partitions, resulting in little migration or data movement between processors. This is an important goal of iterative dynamic load balancing techniques [219] as overheads involved with moving application data can be high [69].

Other more complicated methods are graph-based, like the recursive spectral (or eigenvalue) [187], multilevel [91] or diffusive [63] methods. These methods often produce the best quality partitions for mesh-based partial differential equation simulations [69]. The mesh is seen as a graph where verticies represent data to be partitioned. The goal of graph partitioning is to assign equal total vertex weight to partitions while minimizing the weight of cut edges [69]. Well known mesh partitioning tools include METIS [114, 115] and JOSTLE [222] which use multilevel iterative partitioning algorithms. These libraries are very sophisticated, can be implemented in parallel and seek to minimize data redistribution times during dynamic load balancing.

Another popular mesh partitioning method is the space-filling curve (SFC) method [69, 149]. This approach maps the multi-dimensional data to one dimension along the SFC. An object's co-ordinates are converted to a key representing its position along the SFC through a physical domain; sorting the keys orders the objects which are assigned into weighted pieces for each processor [69]. Like recursive bisection methods, SFC methods generally incur higher communication costs than graph partitioners, but these methods are also dynamically incremental.

5.2 Popular Parallel Architectures

This section briefly overviews popular computer architectures used for parallel computing. A more extensive survey of supercomputing methods can be found in References [47, 73, 84, 151]. Many parallel programs execute on shared-memory systems where multiple processes (or threads) run by different processors occupy a single shared address space. Communication and coherency of elements in the data set are often done implicitly via reads/writes of shared variables.

Symmetric Multi-Processor (SMP) systems are one such shared-memory system in which processors are connected to the memory through a high speed bus and crossbar switch [84]. All processors have equally fast access to the shared memory, but these systems have limited scalability due to limited memory bandwidth capability [47]. On the other extreme are distributed-memory systems like clusters, which are essentially arrays of networked computers. The memory is distributed and not directly accessible to all processors, necessitating broadcasting or message passing of data through the interconnection network. These systems are highly scalable and easy to assemble but hard to use and have long latencies [157].

Distributed-Shared-Memory (DSM) systems [47] are a combination of the distributed and shared-memory approaches (Figure 5.1). These systems, which can be scalable to thousands of processors, create a shared-memory system image but with differing speed of access to the memory due to its physical distribution. The main computing facility used for the simulations in this thesis is the SGI Altix 3700 [105] which is a DSM system. Such systems are also usually called Cache-Coherent Non-Uniform Memory-Access (CC-NUMA) systems due to the differing memory access speed and the need for coherence of data across each processor's cache when processors write different copies of variables to one another. Highly scalable code must be written exploiting locality of memory to attain top performance on these systems [47].

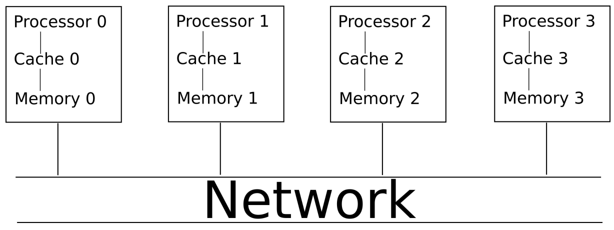

Figure 5.1: Non-Uniform Memory Access architecture

5.3 Parallel Programming

The Message Passing Interface (MPI) standard [87, 112, 151] and the OpenMP standard [34, 47, 112, 151] are popular application programming interfaces for explicit parallelization (where the user controls the parallelization) on distributed and shared-memory systems respectively. They consist of a set of compiler directives, library functions and environment variables. In MPI, processes can communicate with other processes by sending and receiving messages. The parallel implementation using OpenMP of the `OctVCE` code is discussed in greater detail in Section 5.5, but OpenMP will be described in some more detail below.

An advantage with OpenMP (and shared-memory parallel programming in general) is its ability to support incremental parallelism where an application can be parallelized in stages and usually require little modification to the source code [47, 151]. Parallel regions like loops are specified through the use of compiler directives which can be ignored when the code is executed in serial. It uses a fork/join model of parallelism where a master thread (or process) is forked into a team of threads of execution when a parallel construct is created, and the threads synchronized and joined again at the end of the section. However due to limited floating-point representations, operations like reductions may not yield precisely the same result in parallel as those in serial [47].

Each thread usually corresponds to a processor and executes within the same shared address space as the serial program, but it can have its own stack and copy of the variables. Co-ordination of the threads is important (under both shared and distributed-memory models) when they access shared variables as they may simultaneously modify/read the same variable, resulting in a *race condition* and incorrect values of the variables. Race conditions can be removed by restructuring the code or using explicit synchronization of threads (a point where each thread must wait for all others to arrive). Synchronizations require communication between threads, and along with their forking and joining can have high overhead [28, 47].

5.4 Parallel Performance Measures

In most parallel applications the speedup scales less than linearly with the number of processors because some portions of the code have not been parallelized and there are additional overheads like communication time, thread-related overheads like barriers and syncrhonization and load balancing [47]. Amdahl's law [8] is a simple but useful formula that sets limits on the speedup. Let the inherently serial portion of the code be $\sigma(n)$ and $\phi(n)$ the parallel portion of the code for problem size n. Assuming the serial percentage of the code $\epsilon = \frac{\sigma(n)}{\sigma(n)+\phi(n)}$, and remaining percentage $1-\epsilon$ can be parallelized, and neglecting other overheads like memory contention, latencies etc. Amdahl's law states

$$S_p \leq \frac{1}{\epsilon + \frac{1-\epsilon}{p}} \tag{5.1}$$

where S_p is the maximum speedup and p is the number of processors. This expression shows the large effect of even a small serial portion in the code; even if 90% of the code can be parallelized, the speedup will be no larger than 4.7 for an 8 processor simulation.

This derivation assumes ϵ is independent of the problem size, but it has been observed occasionally that on some cache-friendly codes ϵ decreases as a function of problem size [73, 112], increasing the upper bound on S_p. This can sometimes lead to linear speedup, and superlinear speedup ($S_p > p$) can be occasionally observed, although this is usually due to poor memory access or cache mismanagement on a single processor. Amdahl's law ignores parallel overheads, which can be large, especially for memory-intensive applications due to more communication time [73]. A more realistic limit to the speedup thus requires knowledge of the overhead time, which can be difficult to ascertain. However, usually time spent in overhead has lower complexity than time spent in execution (the Amdahl effect [151]).

The inverse of Amdahl's law can be used to estimate the experimentally determined serial fraction of a code (serial portion plus parallel overhead) when it is run on p processors. This is a very useful formula and is often termed the Karp-Flatt metric [113], which states that given a parallel computation exhibiting speedup S_p on p processors where $p > 1$, the experimentally determined serial fraction e is

$$e = \frac{1/S_p - 1/p}{1 - 1/p} \tag{5.2}$$

Now $e = (\sigma(n) + t_o) / (\sigma(n) + \phi(n))$ where t_o is the overhead time. This e would be an upper bound to the actual serial code fraction, and if the same simulation is performed in parallel for increasing number of processors p, an increasing e can give an indication of the magnitude and increase of parallel overhead. Alternatively, it might be possible to extrapolate the e versus p graph back to a 1 processor result to estimate the true serial fraction ϵ. More discussion on the Karp-Flatt metric is also found in Section 7.3 where it is also used to profile the parallel performance of the code.

5.5 Parallel Implementation

The parallel method of `OctVCE` implements domain decomposition and OpenMP [34, 47, 151] for shared-memory parallelism. This approach is chosen as it more fully utilizes the capabilities of the main supercomputer at the University of Queensland, an SGI Altix 3700, which is a shared-memory NUMA machine. There are also some advantages that shared-memory parallelism has over distributed-memory parallelism [131]. Distributed memory systems require extra development effort, debugging time and file structures to manage the inter-processor data communication. Inefficiencies also result from load imbalances requiring complex mesh redistribution techniques, which can be tedious to code, debug and maintain, and introduce overhead. Finally, the limited size for most simulations limits the useful number of processors.

The parallelism implemented here is particularly simple, but not optimized for efficiency. Although still conforming to the octree structure, all the leaf cells (more precisely, pointers to the leaf cells) are placed on a list which is then subdivided into smaller 'sub-lists' each of which is assigned to its processor or thread to work on, as shown in Figure 5.2. These 'sub-lists' correspond to numerical sub-domains. Each of these smaller lists has its own local head and tail.

This method is slightly similar to octree partitioning [76] except that the tree structure is not traversed as only leaf cells are considered for partitioning. This simple approach is also adopted in the unstructured code by Timofeev *et al* [220] where cells are uniformly distributed under a shared-memory paradigm. Some overhead exists during the forking, joining and synchronization of threads at the end of parallel sections, but this decreases for larger problem sizes.

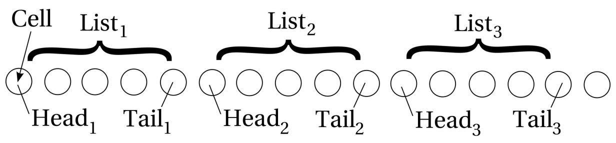

Figure 5.2: Domain decomposition from cell list

In OpenMP this is implemented by a `parallel` region construct attached to the body of code that is to be executed concurrently by multiple threads. The number of threads is specified by using the runtime library routine `omp_set_num_threads()`. An example C code using this OpenMP directive is shown in Figure 5.3. A list of all local heads and tails for each sub-list is stored in the arrays `List_of_heads` and `List_of_tails`. Details of the list and cell data structures are shown in Appendix K. Each list node has a pointer back to the cell which also points to its list node.

Within the `pragma omp parallel` clause thread-private variables are declared for each list – the `Head`, `Tail` `thread_num` and the cell pointer `C`. This `thread_num` variable is assigned the actual thread number to specify which sub-list the thread will be operating on (denoted by its `Head` and `Tail`), which utilizes the OpenMP runtime library function `omp_get_thread_num()`. This list is then traversed from head to tail using the standard `while` loop and the required operation is performed on the cell.

```
struct list * Head;
struct list * Tail;
struct list * node;
struct cart_cell * C;
int thread_num;

#pragma omp parallel private (Head, Tail, thread_num, node, C)
{
   # ifdef _OPENMP
   thread_num = omp_get_thread_num();
   # endif

   Head = List_of_heads[thread_num];
   Tail = List_of_tails[thread_num];

   node = Head;

   while (1) {
     C = node -> cell;
     Perform_operation (C);

     if(node == Tail)
       break;
     else node = node -> next;
   }
}
```

Figure 5.3: Example code for OpenMP parallel implementation

Note in the case of serial execution the above body of code need not be changed. The OpenMP directives will simply be ignored and the lists' head and tail become the head and tail of the list of all cells. This illustrates the effectiveness and simplicity of the incremental shared memory approach in OpenMP where the same block of code (with some modification) can be used in both serial and parallel execution [47].

In some cases the parallel work has to be partitioned into several sections to avoid race conditions e.g. if multiple threads compute interface fluxes and time-integrate their respective cell sub-lists. If threads finish flux computation at separate times and one thread proceeds to integrate its cells in time, some interfacial flux values from the previous timestep (assigned to an adjacent thread) may not have yet been fully updated. Parallel sections are declared by `barrier` directives, which synchronizes all threads at the barrier point.

5.5.1 Parallel Flow Solution and Output

There are three places in the solution computation process that can be readily parallelized without danger of race condition. In these sections the code implementation is very similar to the generic code fragment in Figure 5.3. These sections are (1) Computing the minimum timestep (2) Gradient and limiter computation and (3) Computing the adaptation criterion. These computations can be executed concurrently without race condition as there is no change in cell flow states or connectivity. The other major sections of the code are the flux calculation and time integration stage, which are at risk of race condition if performed within the same parallel section.

Flux computation

As fluxes are shared between cell interfaces the fluxes need only be calculated in one direction per axis per cell. Thus during traversal of the ‘sub-list’ cells assigned to each thread, the flux calculation stage consists of –

1. Computing wall flux (if the cell is intersected by a solid object)
2. Computing domain boundary flux (if the cell is a boundary cell)
3. Computing inter-cell interfacial fluxes in east, north and upper direction

Time integration

The time integration stage involves simply summing the fluxes (stored at cell interfaces which have been previously updated) and updating the current cell state vector from each thread. A code fragment of this process (for one Runge-Kutta step) including the relevant OpenMP directives is shown in Figure 5.4.

```
struct list * Head;
struct list * Tail;
int thread_num;

#pragma omp parallel private (Head, Tail, thread_num)
{
   # ifdef _OPENMP
   thread_num = omp_get_thread_num();
   # endif

   Head = List_of_heads[thread_num];
   Tail = List_of_tails[thread_num];

   calculate_flux_vectors(Head, Tail);
   # pragma omp barrier

   integrate_in_time(Head, Tail);
   # pragma omp barrier

   compute_gradients(Head, Tail);
   compute_limiters(Head, Tail);
}
```

Figure 5.4: Example code for OpenMP parallel flow update stage

Solution output

The parallel solution output methodology depends on the file format required by the grid visualizer. In this case the VTK file format is used [15] where a unique listing of cell verticies also need to be output. The necessitated the use of the `vertex` data structure (shown in Appendix K) which stores pointers to all leaf cells sharing the vertex (and which is also pointed to by these cells). The verticies are stored in a global list and are uniquely numbered for each cell sub-domain in which they reside. All verticies belonging to the sub-domain are first written into the corresponding file. As each cell in the sub-domain also points to these numbered verticies the mesh connectivity information for them is then written as the code traverses each sub-list. Finally the required flow quantities are reconstructed to each vertex, averaged and written.

5.5.2 Parallel Mesh Adaptation

The mesh adaptation process requires significant 'house-keeping' code to manage the changing grid e.g. updating intefacial and vertex connectivities, flux vectors etc. Implementing this in parallel requires even more code, and additional measures must be adopted to avoid race conditions. Thus it is more difficult to straightforwardly use the same serial adaptation code. Race conditions will exist as cell connectivity might be read and written to concurrently.

That the cell merging process is performed in serial for simplicity as it may potentially require cells from across separate domains. Any cells that require adaptation are no longer members of the large merged cell cluster, and only after adaptation will cell merging proceed for remaining small cells and newly adapted cells. This section gives an overview of the parallel mesh adaptation process.

Adding cells to sub-lists in parallel

With the addition or deletion of cells in each sub-domain (or sub-list), the newly formed children cells or parent cell are inserted into the sub-list at the location where the original parent or children cells were respectively. This is done to ensure sub-domains attain a measure of contiguity which would not occur if new cells are placed at the front or back of the list. Given the cell numbering scheme, in some cases sub-domains will only be diagonally contiguous and can occasionally be spatially separated.

After adaptation these sub-lists are all joined into the global list of cells which is repartitioned to yield an equal number of cells for each sub-domain. This is done via a simple counting technique. An example of the numerical sub-domains for the blast in a complex cityscape problem (Section 14) is shown in Figure 5.5. The simulation is performed using 4 processors, meaning 4 sub-domains. It can be seen that the domains (cell clouds) are fairly contiguous.

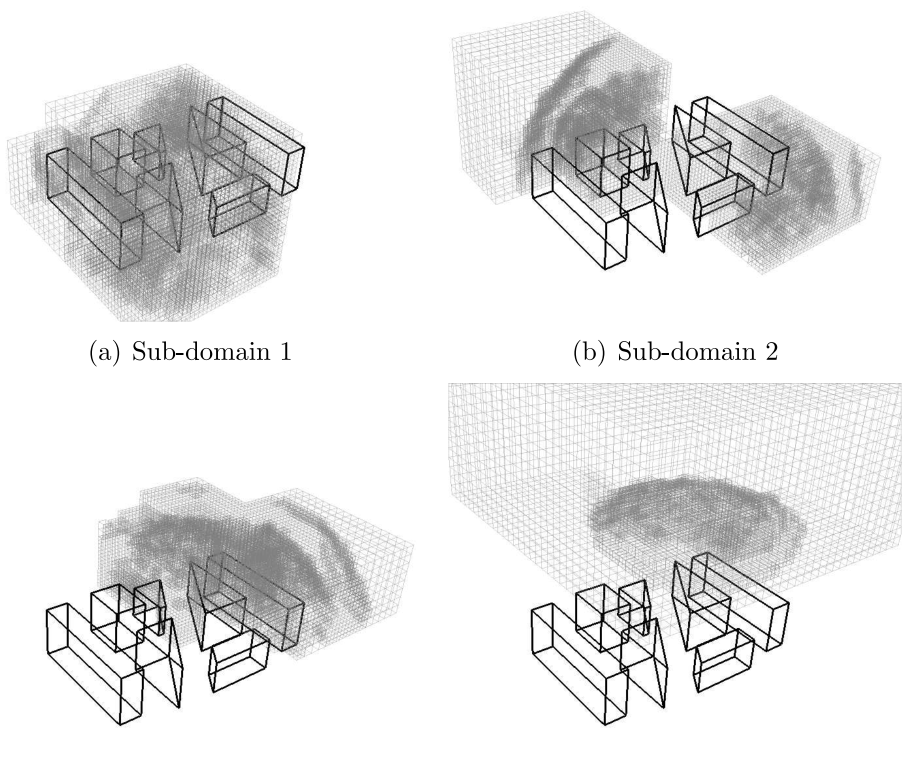
(a) Sub-domain 1 (b) Sub-domain 2

(c) Sub-domain 3 (d) Sub-domain 4

Figure 5.5: Numerical sub-domains for blast in cityscape problem

Flagging cells for adaptation in parallel

The cells in each sub-list (Figure 5.2) are first traversed, and the adaptation indicators (Section 3.5) computed and the relevant cells flagged for refinement or coarsening. However, some cells not flagged for refinement still require refinement because of mesh smoothness constraints. Therefore, sub-lists are traversed again and cells flagged for refinement recursively flag their neighbours for refinement if required. Recursive checks may require visitation of neighbour cells not within the sub-domain in which the program was originally executed, so there is some redundancy in this stage. The cell refinement flagging stage is performed first as some cells tagged for coarsening might no longer be suitable for it after this stage.

Sub-lists are then traversed and parent cells checked for coarsening eligibility. This algorithm is essentially the same as Figure 3.4, which is recursive. This ensures that the cell coarsening process itself can be performed in one step rather than a number of stages. As mentioned in Section 3.2 this requires the code to handle adjacency of cells of very disparate levels, as mesh smoothness will only be ultimately enforced when all cells are finished coarsening.

Updating mesh connectivities in parallel

The mesh connectivity update has to be performed in stages to avoid race conditions. Hence, interface connectivity updates must be performed on per-interface basis. As the domain decomposition is on a per-cell basis, interface connectivities should first be performed in one direction per axis per cell in one stage, then in the opposite directions in the next stage. This is similar to the parallel flux calculation routine in Section 5.5.1, and ensures all interfaces are 'visited' by one thread at a time. An example of this two-stage directional interface connectivity update is shown in Figure 5.6.

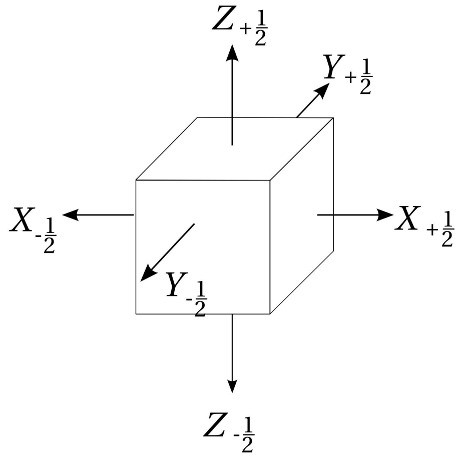

Stage 1: Update connectivities on
$X_{+\frac{1}{2}}, Y_{+\frac{1}{2}}, Z_{+\frac{1}{2}}$ faces
Stage 2: Update connectivities on
$X_{-\frac{1}{2}}, Y_{-\frac{1}{2}}, Z_{-\frac{1}{2}}$ faces

Figure 5.6: Interface connectivity update for parallel adaptation

For vertex connectivity it is important to select groups of verticies belonging to leaf cells so that at each parallel stage, each thread will uniquely visit this group of verticies belonging to the cell during sub-list traversal. An adapted octree parent cell (whether newly coarsened or refined) has potentially 27 verticies, as shown in Figure 5.7. These cell verticies can be placed into 4 unique groups which will only be visited by one thread at a time. Hence the vertex connectivity update stage consists of 4 stages.

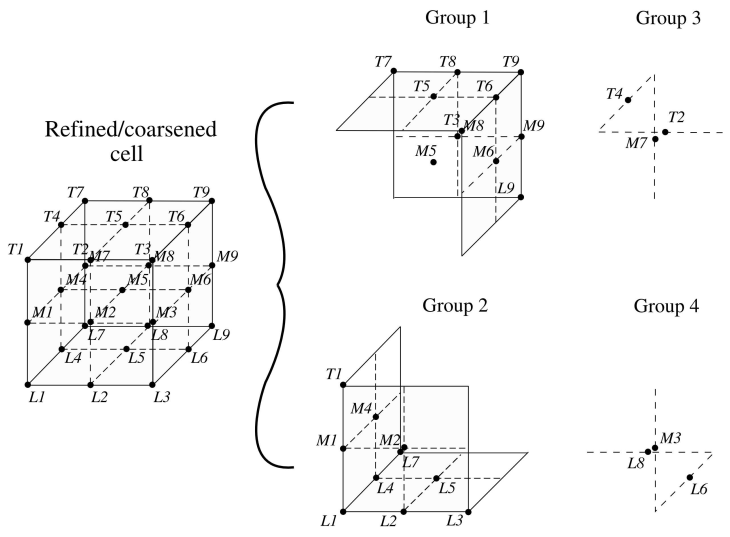

Figure 5.7: Vertex groups for parallel adaptation

Parallel refinement stages

Given the necessary steps for parallel connectivity update, the parallel refinement stages are enumerated below. Each of these stages end in a synchronization barrier.

1. Allocate memory to children cells and set their state vectors accordingly
2. Update interface connectivities in east, north, upper directions, and vertex connectivities for group 1 verticies (from Figure 5.7)
3. Update interface connectivities in west, south, lower directions, and vertex connectivities for group 2 verticies
4. Update vertex connectivities for group 3 verticies (Figure 5.7)
5. Update vertex connectivities for group 4 verticies

Parallel coarsening stages

Similar to (but performed after) the refinement stage, the parallel coarsening stages are enumerated below. Each of these stages end in a synchronization barrier. Also, sub-lists are slightly modified prior to this step so that sibling leaf cells are not spread across different sub-lists.

1. Set parent state vector, update interface connectivities in east, north and upper directions, and vertex connectivities for group 1 verticies (from Figure 5.7)

2. Update interface connectivities in west, south and lower directions, and vertex connectivities for group 2 verticies
3. Update vertex connectivities for group 3 verticies
4. Update vertex connectivities for group 4 verticies, de-allocate children cells

Code fragment for parallel adaptation process

A code fragment of the adaptation process described above including relevant OpenMP directives is shown in Figure 5.8. Note the `pragma omp single` directive which specifies that one thread only unmerges cells to be adapted and modifies the sub-lists so that parallel coarsening can be performed.

```
struct list * Head;
struct list * Tail;
int thread_num;

#pragma omp parallel private (Head, Tail, thread_num)
{
   #ifdef _OPENMP
   thread_num = omp_get_thread_num();
   #endif

   Head = List_of_heads[thread_num];
   Tail = List_of_tails[thread_num];

   compute_adaptation_parameters(Head, Tail);
   # pragma omp barrier

   flag_for_refinement(Head, Tail);
   # pragma omp barrier

   flag_for_coarsening(Head, Tail);
   # pragma omp barrier

   # pragma omp single
   {
     umerge_cells_to_be_adapted();
     modify_lists_for_adaptation(List_of_heads,
       List_of_tails);
   }

   parallel_refine_stage_1(Head, Tail);
   # pragma omp barrier
   .
   .
   .
   parallel_refine_stage_5(Head, Tail);
   # pragma omp barrier

   parallel_coarsen_stage_1(Head, Tail);
   # pragma omp barrier
   .
   .
   .
   parallel_coarsen_stage_4(Head, Tail);
}

remerge_cells();
compute_new_list_heads_and_tails();
```

Figure 5.8: Example code for OpenMP parallel adaptation

5.5.3 Problems with the Parallel Method

On NUMA machines like the SGI Altix, locality of data is important for good performance [47]. Recalling the discussion in Section 5.2, NUMA systems have a shared-memory address space to all processors but memory access times are substantially faster if a data element is on a node's cache or in nearby memory. A well-structured code exploits locality so that the majority of requests are to data residing on a node's local memory and thus the majority of references are cache hits. Communication overheads for referencing memory not connected to the node can be quite high[1], as much as 20-50%.

The parallel adaptation method does allocate cells to reside on the local memory of each node of the cpuset. If the adaptation process were not parallelized there would be a less uniform distribution of data across nodes, leading to increased communication overhead. This also means a smaller parallel code fraction, further limiting the theoretical speedup from Amdahl's law (Equation 5.1). However, the mesh repartitioning strategy implemented via simple cell counting does not always lead to good locality as it is problem-depedent; some sub-domains may undergo more refinement and cells allocated by one thread may be assigned to remote threads that will need frequent access to the data. A further complication is thread migration from processor to processor, leading to a higher degree of remote access. The `dplace` command can help tie threads to processors, and the `numactl` command allows interleaved (round-robin) memory allocation to prevent bottlenecks. These will only partly increase efficiency.

The code also makes significant storage demands (see Appendix K for the cell data structure), requiring at a minimum 988 bytes per cell, and a nominal operational storage of 3 kB per cell (which includes other data structures like lists and pointers). This leads to performance inefficiencies with more cache misses and longer communication time. In some cases cpusets consisting of several nodes needed to be requested just for the memory, even if a single processor simulation was performed.

The parallel method relies on partitioning parallel sections into several stages via synchronization barriers, which can be quite expensive [47] and cause the parallelism to become somewhat fine-grained and thus inefficient. Sections 10.4.1, 14.2 and 7.3 display parallel performance statistics of the code for different simulations. They indicate that considerable overhead does exist for parallel simulations, but this occurs mainly from communication and not barrier overheads. The results encouragingly suggest a fairly high parallel fraction of the code. `OctVCE` is likely to perform better on SMP systems but this has not been investigated. Further work would focus on reducing storage and using a more effective domain decomposition method exploiting locality on NUMA machines.

[1]http://nf.apac.edu.au/facilities/userguide/, accessed June 2008

Chapter 6

Verification and Validation

To establish the credibility of the `OctVCE` code it must be verified and validated for a range of test cases. Verification is generally understood to be the activity of establishing the reliability and accuracy of the numerical methodology i.e. solving the equations right [168, 169]. It typically involves evaluating the discretization error against a known solution (typically analytic) and establishing the order of accuracy through a grid convergence study. Validation, which is usually done after verification, is demonstrating how well the mathematical model actually represents the physical system i.e. solving the right equations [168].

Verification can help demonstrate the stability and robustness of the numerical scheme and provide good confidence that no programming errors in the code exist [142, 180], although it cannot identify errors that result in a loss of efficiency [168]. The test cases used in the verification process, having generally analytic solutions, are usually geometrically simple and not related to problems that the code is normally designed for (in this case blast propagation), and the observed order of accuracy can be problem-specific [168] and influenced to an extent by boundary conditions [142]. For CFD problems, verification test cases usually involve smooth flows as analytic solutions for shocked flows are rare or do not exercise all terms in the numerical scheme.

Validation test cases are typically those problems for which the code is designed, and usually involve comparison to experimental or previously verified numerical data [169]. Better confidence in the code's predictive ability for such problems will be generally established if a larger number and varied range of such test cases are chosen. In simulations of validation cases and other complex problems a popular method of estimating the error is through Richardson extrapolation [163, 164], which is a technique for combining solutions from two different grids to give a more accurate estimate for the exact solution. If f_1 is the fine-grid solution and f_2 the coarser-grid solution, the exact (grid-independent) result can be estimated as

$$f_{exact} = f_1 + \frac{f_1 - f_2}{r^p - 1} \tag{6.1}$$

where r is the refinement factor (which would be 2 if the grid is doubled in each direction) and p the order of accuracy. This equation is generally $p+1$-order accurate for upwind methods [168]. The estimated fractional error to the fine grid solution is thus

$$E = (f_1 - f_2) / (f_1 (r^p - 1)) \tag{6.2}$$

which is usually a good approximation if $E << 1$.

Richardson extrapolation may not consistenly work in some situations and is generally used with caution at those places where the solution is not smooth e.g. peak overpressure at a shock and in the presence of non-linear flux limiters [168]. It can also be difficult to determine a value of r for non-uniformly refined meshes [167]. A consistently decreasing value of E (as grids are refined) demonstrates a convergence (the asymptotic range of solution convergence having been attained) and thus at least three differently-refined grids need to be employed to ascertain asymptoticity. The quantity

$$\text{GCI} = 3\,|E| \tag{6.3}$$

is the Grid Convergence Index (GCI) proprosed by Roache [168, 179] which provides an error band where a safety factor of 3 (and the absolute value) is used for conservatism. If the observed order of accuracy matches the formal order (typically for fine-grid solutions), the safety factor can be reduced to 1.25.

Sections 6.1 to 6.4 of this chapter present four different verification test cases. In Chapters 7 to 14, a number of different validation test cases will be presented. Not all of these are blast propagation problems from charge detonations; some (like Chapters 7 and 8) are more mundane shock propagation problems to demonstrate the versatility and accuracy of the VCE method for different flow problems. As mesh-convergent solutions can be quite difficult to obtain, especially for three-dimensional blast propagation problems [171], many of these validation cases will use Richardson extrapolation to test for convergence trends and estimate the magnitude and sign of errors. Profiling of the code will also be done for some simulations to establish its performance in serial and parallel executions.

6.1 Verification via the Method of Manufactured Solutions

The first verification exercise uses the Method of Manufactured Solutions, which is a general and quite robust verification methodology that allows all terms in the governing equations to be exercised [142, 168, 180]. An analytic solution is chosen (or 'manufactured') and passed through the flow equations, generating source terms as a result. These source terms are input into the solution procedure and compared with the analytic solution for code verification. This process is repeated on a series of uniformly refined grids to obtain an order of accuracy.

The analytic solution bears no relation to any physical problem but is simply used for verification purposes. It requires the code to specify arbitrary source terms and boundary conditions, which can be difficult to implement [83]. Guidelines for appropriate choice of manufactured solutions include generality (so that all terms can be exercised), smoothness, ensuring no derivatives vanish, and ensuring no predominance of any one particular term in the governing equations [180]. This method cannot be used to detect code deficiencies affecting efficiency or robustness; its only purpose is to highlight any spatial discretization errors. Also, it relies on uniform refinement of the grid to properly obtain the order of accuracy.

The global discretization error for all mesh points can be given by the L_2 or 'root mean square' norm –

$$L_2 = \left(\frac{\sum_{n=1}^{N} |Q_{num,n} - Q_{exact,n}|}{N} \right)^{\frac{1}{2}} \tag{6.4}$$

where N is the total number of cells, Q_{num} is the computed solution (e.g. in density or energy) and Q_{exact} the exact solution. The order of accuracy p calculated from two mesh levels k and $k+1$ is then

$$p = ln\left(\frac{L_{k+1}}{L_k}\right)/ln\left(r\right) \tag{6.5}$$

Alternatively, if a series of L_2 norms are obtained for several different mesh levels, p can be obtained by a power-law fit (in the form of $L = c_1 + c_2 r^p$, c_1 and c_2 being constants) to the curve in the L_2 versus r graph (c_1 should be theoretically zero). The observed order of accuracy is compared with the formal order of accuracy, which for the code is $p = 2$ due to implementation of reconstruction (Section 4.3).

The steps for the method of manufactured solutions are thus summarized below –

1. Choose form of governing equations
2. Choose form of manufactured solution
3. Derive modified governing equations, source terms and analytic boundary conditions
4. Solve discrete form of modified governing equations on multiple meshes
5. Evaluate global discretization error in numerical solution
6. Calculate order of accuracy

6.1.1 Manufactured Solution for Two-Dimensional Geometry

Verification will first be conducted in two-dimensional geometry. This is easily achieved with the code by constructing a single 'layer' of cells and preventing out-of-plane flow. The manufactured solution chosen for this section follows the solution chosen by Roy *et al* in their own verification work [180], and has the following steady-state form –

$$\begin{aligned}
\rho\left(x,y\right) &= \rho_0 + \rho_x \sin\left(a_{\rho x}\pi x\right) + \rho_y \cos\left(a_{\rho y}\pi y\right) \\
u\left(x,y\right) &= u_0 + u_x \sin\left(a_{ux}\pi x\right) + u_y \cos\left(a_{uy}\pi y\right) \\
v\left(x,y\right) &= v_0 + v_x \cos\left(a_{vx}\pi x\right) + v_y \sin\left(a_{vy}\pi y\right) \\
p\left(x,y\right) &= p_0 + p_x \cos\left(a_{px}\pi x\right) + p_y \sin\left(a_{py}\pi y\right) \qquad (6.6)
\end{aligned}$$

The constants ϕ_0, ϕ_x, ϕ_y and ϕ_{xy} where ϕ is the variable ρ, u, v or p are given in Table 6.1. The analytic solutions for density, velocity and pressure of Equation 6.6 are

Table 6.1: Table of constants for 2D manufactured solution

Equation, ϕ	ϕ_0	ϕ_x	ϕ_y	$a_{\phi x}$	$a_{\phi y}$
ρ (kg/m^2)	1.0	0.15	-0.1	1.0	0.5
u (m/s)	800.0	50.0	-30.0	1.5	0.6
v (m/s)	800.0	-75.0	40.0	0.5	2/3
p (Pa)	1.0×10^5	0.2×10^5	0.5×10^5	2.0	1.0

substituted into the governing Euler equations (Equation 6.7) to generate the source terms f_m, f_x, f_y and f_E. The energy is obained via the equation of state assuming calorically perfect gas ($\gamma = 1.4$, $R = 287$ J/(kgK)) as $E = P/\left(\rho\left(\gamma-1\right)\right) + \left(u^2+v^2\right)/2$.

$$\begin{aligned}
\frac{\partial \rho}{\partial t}+\frac{\partial(\rho u)}{\partial x}+\frac{\partial(\rho v)}{\partial y} &= f_m \\
\frac{\partial(\rho u)}{\partial t}+\frac{\partial(\rho u^2+p)}{\partial x}+\frac{\partial(\rho u v)}{\partial y} &= f_x \\
\frac{\partial(\rho v)}{\partial t}+\frac{\partial(\rho v u)}{\partial x}+\frac{\partial(\rho v^2+p)}{\partial y} &= f_y \\
\frac{\partial(\rho E)}{\partial t}+\frac{\partial(\rho u E+p u)}{\partial x}+\frac{\partial(\rho v E+p v)}{\partial y} &= f_E \qquad (6.7)
\end{aligned}$$

The source terms can be extremely lengthy to derive by hand and for this exercise were generated using the symbolic mathematical manipulation tool `maxima` [68]. This problem is solved on a square domain on the series of meshes listed in Table 6.2. The density field for the manufactured solution is shown in Figure 6.1.

Table 6.2: Meshes for 2D manufactured solution

Mesh	No. cells
1	8 × 8
2	16 × 16
3	32 × 32
4	64 × 64
5	128 × 128

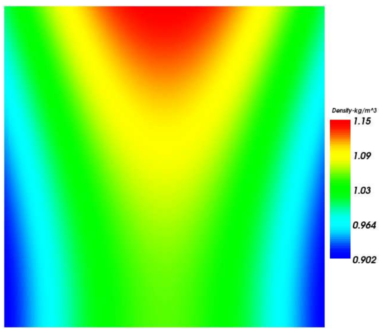

Figure 6.1: Analytic density field of 2D manufactured solution

Simple extrapolated outflow boundary conditions are used on the north and east boundaries of the domain as the solution is supersonic there, whilst the analytic boundary conditions are used on the west and south boundaries (using Equation 6.6). Initial conditions correspond to column one of Table 6.1 (the ϕ_0 values), with the solution marched into time from these conditions until steady-state conditions are reached i.e. when L_2 values appear constant.

6.1.2 Results from Two-Dimensional Method of Manufactured Solution

A comparison of the computed density fields on different grids with the analytic solution can be seen in Figure 6.2. These solutions were computed with the AUSMDV flux solver. The trend of increasing agreement with the analytic solution as mesh resolution is increased can be observed.

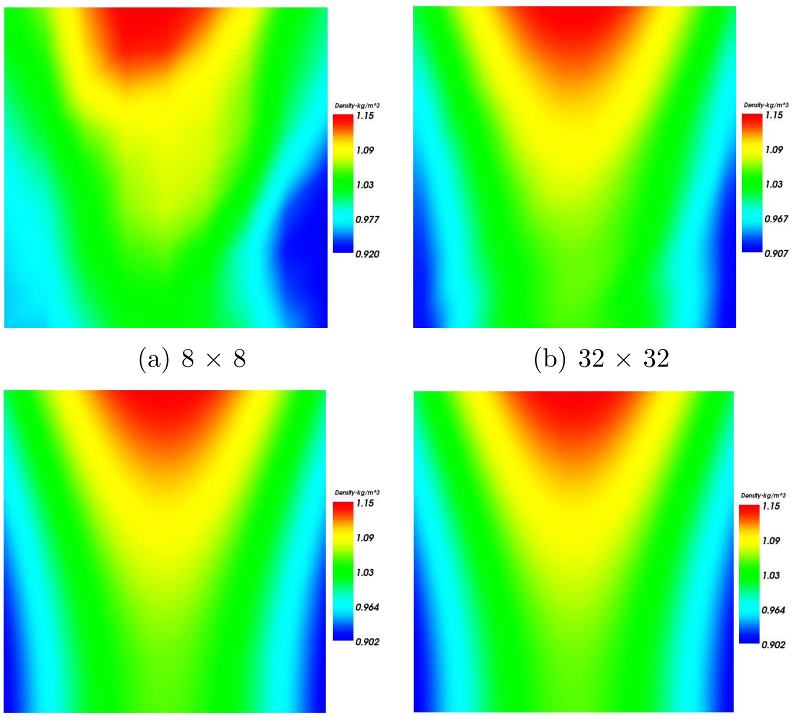

(a) 8×8 (b) 32×32

(c) 128×128 (d) Analytic solution

Figure 6.2: Comparison of density fields for 2D manufactured solution

The solutions are determined to be steady state by observing when the L_2 norm no longer changes with time, as in Figure 6.3(a) where the L_2 versus time curves for various mesh resolutions are plotted. The trend of decreasing error (i.e. smaller L_2 values) with increasing mesh resolution is observed. These steady-state L_2 norms are plotted against grid resolution in Figure 6.3(b) to obtain the order of accuracy p. This figure plots the norms from a low order (no reconstruction) and high order (with reconstruction) solution for both the AUSMDV and EFM flux solvers.

As expected, the slope of the low-order curves are shallower than than the higher-order curves, indicating lower order of accuracy. The order of accuracy for the L_2 norms in Figure 6.3(b) has been tabulated in the first and second columns of Table 6.3. It is apparent that the low order solution exhibit orders of accuracy lower than 1, and high order solutions have orders of accuracy greater than 1 but substantially less than 2.

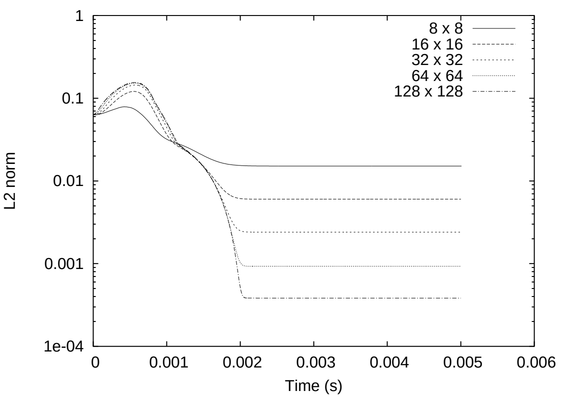

(a) Versus time

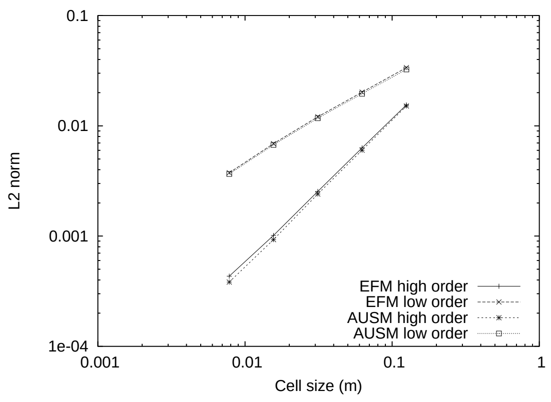

(b) Versus grid resolution

Figure 6.3: L2 density norms

The mismatch between the observed and formal orders of accuracy is strange given the linear graphs in Figure 6.3(b).

Better solution convergence was attempted using two further strategies. Firstly, as it is known that limiters (especially of the min-mod variety) can inhibit convergence [50, 110, 218], a high order AUSMDV solution was run without limiters. Secondly, a different reconstruction procedure – the piecewise-parabolic-method (PPM) – was used. This method, used in the MB_CNS code [109], implements quadratic interpolation and a modified van Albada limiter [110] and should be third order accurate. This approach was chosen as it could be compared with a previous verification study [83] identically on this problem using the MB_CNS code. The resulting orders of accuracy can be seen in columns 3 and 4 of Table 6.3.

Table 6.3: Order of accuracy for 2D manufactured solution

Flux solver	Low order	High order	High order, unlimited	High order, PPM
EFM	0.697632	1.29777	-	1.55609
AUSMDV	0.690081	1.32844	1.33298	1.53493

Interestingly, the elimination of limiters from the high order solution only slightly improved the solution order, whilst the PPM method improved the convergence order to slightly greater than 1.5. In either case the orders of accuracy are still significantly lower than 2 for the high order solutions. These figures are fairly consistent with those obtained from the MB_CNS code in the same verification exercise [83] where for the AUSM scheme the low order solution had a value of 0.71 and higher order solution was 1.62. The PPM reconstruction scheme did demonstrate third-order accuracy when tested on a sine wave profile, and without the van Albada limiter exhibited a convergence order of 1.9. Although this is still substantially less than 3, the single-point quadrature of the fluxes in the solution integration scheme (Section 4.2) implies truncation orders of 2 at best [82].

It will be shown in Sections 6.1.4 and 6.4 that better matches between observed and formal orders of accuracy result for different verification problems. As mentioned previously, observed orders of accuracy seem quite dependent on both the nature of the problem and the solution procedure [168].

6.1.3 Manufactured Solution for Three-Dimensional Geometry

The manufactured solution in Equation 6.6 will now be extended to fully test all terms in the formulation of the three-dimensional Euler equations. In steady-state form, the solution has the form –

$$\begin{aligned}
\rho(x,y,z) &= \rho_0 + \rho_x \sin(a_{\rho x}\pi x) + \rho_y \cos(a_{\rho y}\pi y) + \rho_z \cos(a_{\rho z}\pi z) \\
u(x,y,z) &= u_0 + u_x \sin(a_{ux}\pi x) + u_y \cos(a_{uy}\pi y) + u_z \cos(a_{uz}\pi z) \\
v(x,y,z) &= v_0 + v_x \cos(a_{vx}\pi x) + v_y \sin(a_{vy}\pi y) + v_z \sin(a_{vz}\pi z) \\
w(x,y,z) &= w_0 + w_x \cos(a_{wx}\pi x) + w_y \sin(a_{wy}\pi y) + w_z \sin(a_{wz}\pi z) \\
p(x,y,z) &= p_0 + p_x \cos(a_{px}\pi x) + p_y \sin(a_{py}\pi y) + p_z \sin(a_{pz}\pi z)
\end{aligned} \tag{6.8}$$

The constants for this solution are given in Table 6.4. Note that these values in two dimensions are identical to those in Table 6.1 with additional values provided for the third dimensional component. Like in Section 6.1.1, the source terms are generated by substituting the analytic solution into the Euler equations.

Table 6.4: Table of constants for 3D manufactured solution

Equation, ϕ	ϕ_0	ϕ_x	ϕ_y	ϕ_z	$a_{\phi x}$	$a_{\phi y}$	$a_{\phi z}$
ρ (kg/m^2)	1	0.15	-0.1	0.12	1	1.5	2
u (m/s)	800	50	-30	20	1.5	0.6	0.5
v (m/s)	800	-75	40	-25	0.5	2/3	1
w (m/s)	800	40	-40	20	0.3	0.5	2
p (Pa)	1.0×10^5	0.2×10^5	0.5×10^5	0.25×10^5	2.0	1.0	0.5

The solution methodology is identical to the two-dimensional verification exercise in Section 6.1.1. However, due to the large number of cells that would be required in a three-dimensional solution, only three mesh resolutions are considered, which are tabulated in Table 6.5.

Table 6.5: Meshes for 3D manufactured solution

Mesh	No. cells
1	$8 \times 8 \times 8$
2	$16 \times 16 \times 16$
3	$32 \times 32 \times 32$

6.1.4 Results from Three-Dimensional Method of Manufactured Solution

L_2 norms were computed in both density and total energy for the AUSMDV and EFM flux solvers. The PPM reconstruction scheme was also used to observe the increase in order of accuracy when used with the AUSMDV scheme. The orders of accuracy are shown in Tables 6.6 and 6.7 respectively.

Table 6.6: Density-based order of accuracy for 3D Method of Manufactured Solution

Flux solver	Low order	High order	High order, PPM
EFM	0.820488	1.42164	-
AUSM	0.813862	1.43043	1.46816

Table 6.7: Energy-based order of accuracy for 3D Method of Manufactured Solution

Flux solver	Low order	High order	High order, PPM
EFM	0.874216	1.34335	-
AUSM	0.865135	1.35793	1.42389

The computed order of accuracy also varies depending on the variable under consideration, although the differences are not large. The convergence orders for both reconstruction-off and reconstruction-on are higher than with the 2D verification exercise (Table 6.3), and thus closer to ideal behaviour. The PPM-based order of accuracy is interestingly lower than the values in Table 6.3, and its improvement over the linear reconstruction values is less pronounced.

6.1.5 Performance of the Method of Manufactured Solutions

The total number of cells in a square mesh undergoing uniform refinement scales by ${n_x}^2$, where n_x is the number of cells along one side. As the allowable time step per cell decreases proportional to cell size, a scaling of ${n_x}^3$ in two dimensions is expected. The scaling for a three-dimensional cubical mesh is ${n_x}^4$. Alternatively if the total number of cells is N, the scaling will go according to $N^{3/2}$ for two dimensions and $N^{4/3}$ for three dimensions.

Graphs of total execution time versus n_x for the two- and three-dimensional verification exercise of this section are shown in log-log plots respectively in Figures 6.4(a) and 6.4(b). Power-law curve fits are also shown. The linear nature of these graphs (at least for larger n_x values) and the values of their gradients are well predicted by the scaling principle. Other aspects of the code execution e.g. geometry interrogation, file output etc. may account for any non-linearities.

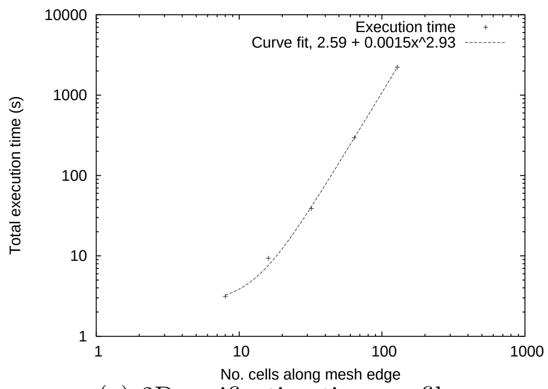

(a) 2D verification time profile

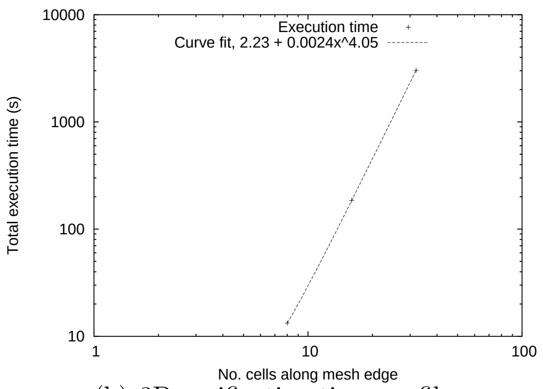

(b) 3D verification time profile

Figure 6.4: Execution time vs mesh size for Method of Manufactured Solutions

The GNU compiler `gprof` profiler tool was used to ascertain the relative time spent in executing reconstruction-related operations (e.g. computing gradients, limiters and reconstruction). The percentage of execution time spent in this process is plotted with respect to n_x in Figures 6.5(a) and 6.5(b) for the two- and three-dimensional problem respectively. Also plotted is the percentage of execution time spent in simply advancing the solution (computing fluxes, time integration).

These results indicate that nearly *half* of the time spent executing the code is used in reconstruction-related operations, whilst around 30% is actually spent on flux computation and time integration. The cost of reconstruction might be lowered for this problem if one-dimensional interpolation is used as opposed to the generalized multi-dimensional interpolation scheme implemented in the code (Section 4.3).

6.1.6 Concluding Remarks

As the results from the two- and three-dimensional tests indicate convergence, it is reasonable to assume `OctVCE` has passed this verification test case. A convergence order

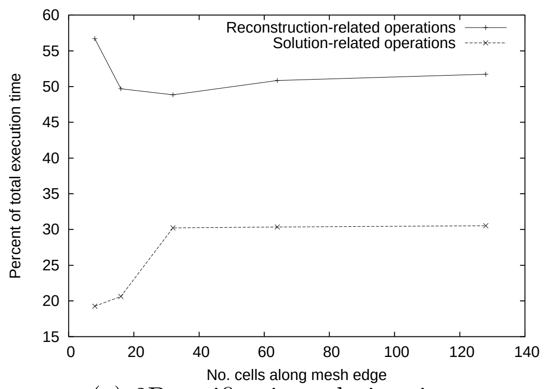

(a) 2D verification relative time

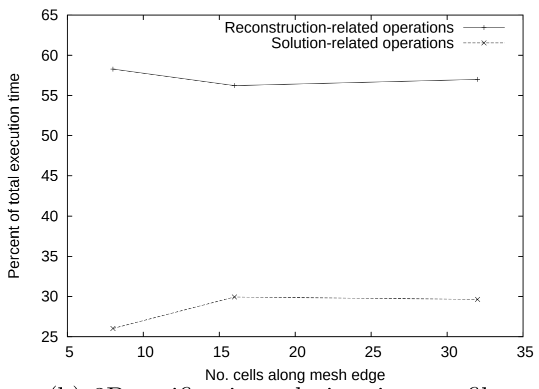

(b) 3D verification relative time profile

Figure 6.5: Relative execution time vs mesh size for Method of Manufactured Solutions

lower than first-order was observed without reconstruction, and an order of accuracy greater than 1 (but considerably less than 2) was seen with reconstruction. The sub-optimal performance could in part be due to flow non-uniformities and misalignments with mesh edges [148]. Similar figures for these convergence orders have been reported for similar verification problems of the two-dimensional Euler equations on formally second-order codes [50, 110, 148]. Removing the limiter, or using smoother limiters (as investigated in Section 6.1.2) did not always improve the convergence order drastically. Future work should also be given to reducing the cost of solution reconstruction, given that it is the largest part of the computational effort.

6.2 Verification with Sod's Shock Tube Problem

In this section the ideal shock tube problem based on Sod's initial conditions [196] will be simulated. This relatively simple, unsteady, one-dimensional problem has a well-known analytic solution that can be computed using iterative techniques (see for example Reference [10]). The code can thus be compared against this solution and also run in two-dimensional, three-dimensional, adaptive mesh and axisymmetric modes as the solutions should all be equivalent.

The shock tube has a length of 1.0 m, and the high-pressure conditions to the left of the imaginary diaphragm at $x = 0.5$ m are

$$u = 0, \rho = 1.0 \text{ kg/m}^3, P = 10^5 \text{ Pa}, x \leq 0.5$$

and the conditions to the right are

$$u = 0, \rho = 0.125 \text{ kg/m}^3, P = 10^4 \text{ Pa}, x \geq 0.5$$

For the two-dimensional simulations, the domain is a rectangle of 128 cells length-wise and 3 cells height-wise (totalling 348 cells) as shown in Figure 6.6. The three-dimensional simulation has 3 additional cells width-wise (thus 1152 cells). The gas is calorically perfect air ($\gamma = 1.4$), and solid wall boundary conditions apply to shock tube walls. Only AUSMDV will be used in this example.

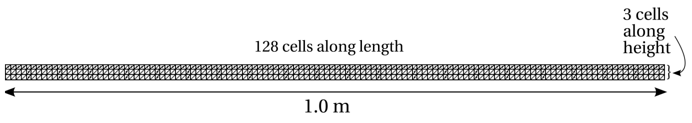

Figure 6.6: Uniform grid for 2D Sod shock tube problem

The adaptive mesh simulation (done in two dimensions) has 3 working levels (levels 7, 8 and 9) corresponding to cell sizes 7.8125×10^{-3}, 3.90625×10^{-3} and 1.953125×10^{-3} m. The density-based adaptation indicator (Equation 3.4) was used with refinement threshold, coarsening threshold, and noise filter values of 0.08, 0.05 and 0.01.

This shock tube problem also provides a good testing ground for the effectiveness of the Thompson non-reflecting boundary conditions (Appendix H) which are applied at the tube ends. The left end of the tube allows applies the subsonic inflow boundary conditions after the expansion wave exits the domain, and the right end applies the subsonic outflow boundary conditions following exit of the shock. This test was also performed by Thompson [209] in which errors of less than 1% reflection following the outgoing shock were reported.

6.2.1 Results for Sod's Shock Tube Problem

The density solution at time 0.6 ms is displayed in Figure 6.7 where the two-dimensional solutions in planar and axisymmetric geometry are displayed. Both higher-order planar and axisymmetric calculations have better resolution of discontinuities and the expansion fan compared to the first-order solution.

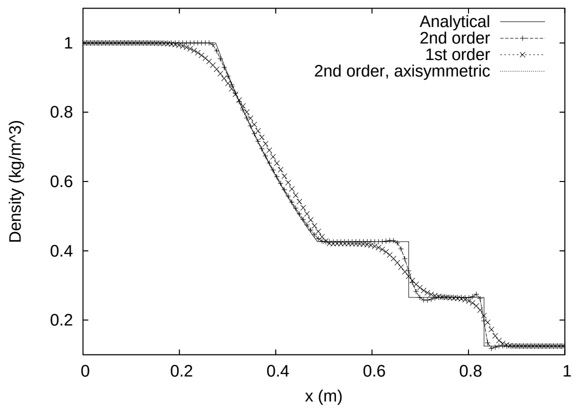

Figure 6.7: Two-dimensional shock tube results (0.6 ms)

A comparison of the planar two- and three-dimensional higher order solutions at $t = 0.6$ ms is shown in Figure 6.8. There is very good agreement between both solutions, which is expected.

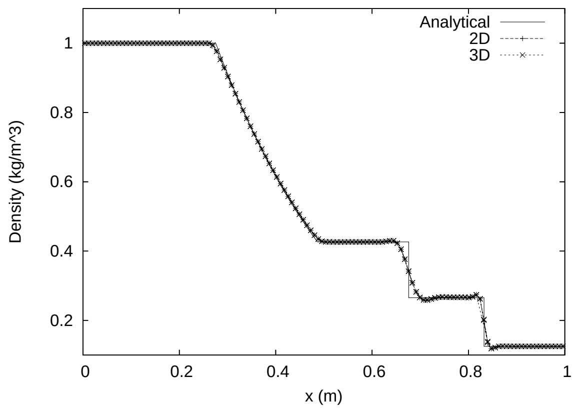

Figure 6.8: Two- and three-dimensional shock tube results (0.6 ms)

A final comparison at 0.6 ms is between an adaptive mesh solution and an equivalent uniform grid solution with cells at the minimum cell size of the adaptive mesh solution (i.e. at 1.953125×10^{-3} m), shown in Figure 6.9. The resolution of discontinuities with these solutions is even sharper than previous graphs (e.g. Figure 6.8, and both solutions are very similar (the uniform mesh actually has slightly oscilliatory behaviour at the contact surface which is not evident with the adaptive mesh solution).

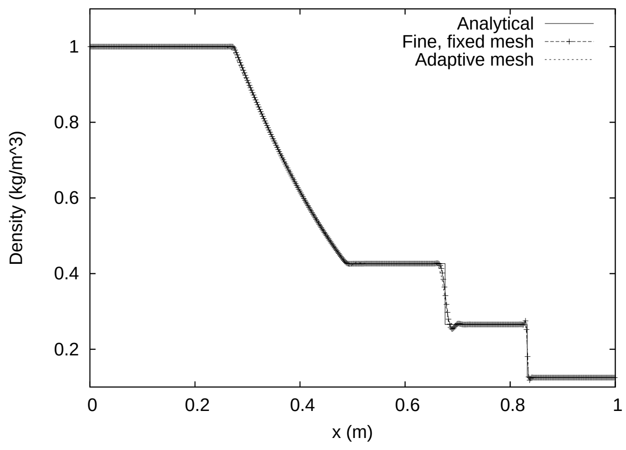

Figure 6.9: Adapted mesh and equivalent uniform mesh shock tube result (0.6 ms)

Performance statistics for the uniform and adaptive mesh solutions are shown in Table 6.8. The adaptive mesh solution has time and space savings of around a factor of 3 and 3.4 respectively. As mentioned in Section 6.3.4, time savings are typically smaller than storage savings as additional work needs to be implemented to manage the adaptation e.g. managing connectivities, computing adaptation indicators etc. Savings for this problem should be more significant with finer adaptation levels and/or extension to three-dimensional flow.

Table 6.8: Performance statistics for shock tube problem on uniform and adapted mesh

	Uniform grid	Adaptive mesh
Max cells	6144	1815
Solution time (s)	457.595	153.517

To test the non-reflecting boundary condition implementation, the solution at $t = 1.3$ ms is output. This corresponds to a time after the shock has exited the right boundary but just before the expansion fan reaches the left boundary. The solutions for the uniform two- and three-dimensional results and adaptive mesh solution are shown in Figures 6.10(a) and 6.10(b). It is evident that the subsonic outflow boundary condition seems to be working well with minimal reflection there.

At 2.0 ms both the contact surface and expansion fan have exited the domain, providing further opportunity to test both subsonic inflow and outflow boundary conditions. Solutions are shown in Figure 6.11. In Figure 6.11(a) there is a slight reflection at the subsonic outlet end which is of the order of observed by Thompson [209]. The non-reflecting subsonic inflow boundary condition appears to work well with hardly any observable reflections.

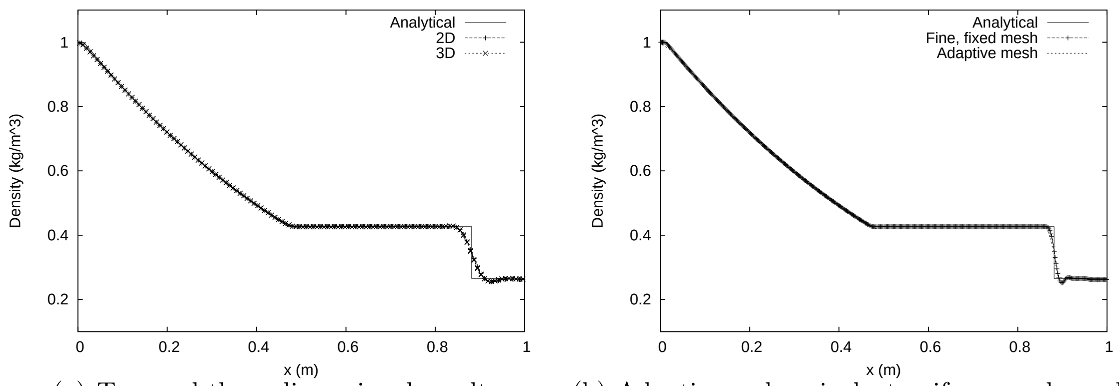

(a) Two and three dimensional results (b) Adaptive and equivalent uniform mesh results

Figure 6.10: Shock tube results at 1.3 ms

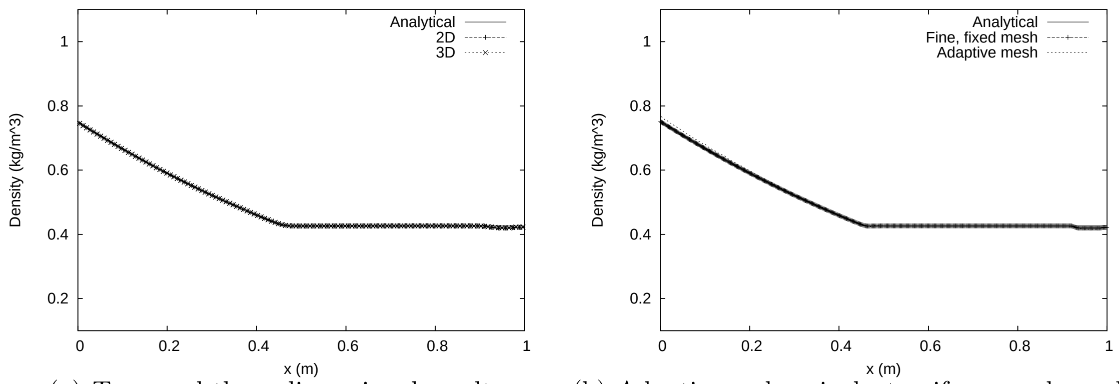

(a) Two- and three-dimensional results (b) Adaptive and equivalent uniform mesh results

Figure 6.11: Shock tube results at 2.0 ms

The adaptive mesh and equivalent uniform mesh (Figure 6.11(b)) likewise displays a disturbance at the outflow end that appears to be more noticeable (though still small) than the coarser grid solutions. Coarser grids are more dissipative and thus tend to damp these oscillations. At the subsonic inlet end, there are no reflections but the adaptive mesh solution overpredicts slightly the density whilst the uniform grid solution performs as well as the coarser, uniform grid solutions in Figure 6.10(a).

The actual non-reflecting implementation as described in Appendix H involves limited extrapolation, and switch to the more dissipative EFM at border cells (and cells beside border cells) to damp oscilliatory behaviour. The linear extrapolation on different sized cells under an adaptive scheme may not be as smooth at the inflow end compared to a uniform grid. Limiters may also degrade the extrapolation slightly. In any case the non-reflecting boundary conditions still perform quite well, and in real explosion modelling the predominant non-reflecting boundary condition should be subsonic outflow.

6.3 Verification of Supersonic Wedge and Conical Flow

In this section supersonic flow over a wedge and cone geometry will be computed. This is an important exercise for two reasons. Firstly, analytic solutions to these problems exist, and thus they constitute a more realistic verification test case than the Method of Manufactured Solutions (Section 6.1). However, the simplicity of these solutions, especially for wedge flow, may not exercise all terms of the code. Secondly, a convergence study can be performed to observe the effect of the VCE surface representation when both subcell and mesh density are varied. As shown in Section 2.4.4, the VCE method effectively ‘numerically roughens’ surfaces. Appendix E.1 also demonstrates that further noise can occur for the axisymmetric VCE method. Measuring the solution errors at the surface as the grid and subcell resolution is increased can help ascertain the severity of these surface effects.

The test case here simulates steady-state flow of freestream Mach number $M_\infty = 2.5$ over a 20° half-wedge or half-cone. Analytic solutions to the post-shock flow for the wedge case can be derived from the oblique shock relations, and for conical flow can be computed from the method of Taylor and Maccoll [208] (in the steady-state limit, constant property lines are generators from the cone vertex). Published tables of supersonic conical flow solutions [188] can also be used.

Initial conditions are freestream values, which are $P_\infty = 10^4$ Pa and $\rho_\infty = 0.1$ kg/m^3. The solution is advanced in time until all errors appear constant. Simple extrapolated supersonic boundary conditions are used for the outlet. Analytic surface values for the wedge and conical flow cases are given in Table 6.9.

Table 6.9: Analytic solution for supersonic flow past wedge and cone

	Wedge	Cone
Shock angle	42.89°	32.581°
P_s/P_∞	3.211	2.309
ρ_s/ρ_∞	2.2	1.802

6.3.1 Program of Simulations

Only the density and pressure solution on the surface of the wedge or cone will be monitored, as errors are likely greatest here due to the VCE surface effects. Also a convergence study of the global solution error may not be so useful as the presence of an embedded shock will lower the convergence order to at most first-order accuracy [179].

A dimensionless root mean square error norm (the L_2 norm) is computed to quantify the error over the whole surface –

$$L_2 = \sqrt{\frac{1}{N}\sum_{n=1}^{N}\left(\frac{Q_{num,n} - Q_{theory,n}}{Q_{theory,n}}\right)^2} \tag{6.9}$$

where N is the number of cells along the surface, Q_{num} the computed solution and Q_{theory} the analytic solution.

Simulations will be performed for three different mesh resolutions (levels 6, 7 and 8) and also for three different subcell resolutions (32, 64 and 128 subcells along the cell edge). Mesh levels 6, 7 and 8 correspond to a basis Cartesian cell length of 0.015625, 0.0078125 and 0.00390625 m respectively. Computational limits prevent more mesh or subcell density, although a level 9 mesh just for the 64 subcell case will also be used.

An adaptive mesh simulation for 64 subcells with three working levels (levels 6 to 8) is also performed. The mesh is adapted to the finest level at the surface. The density-based adaptation indicator (Equation 3.4) is used with refinement threshold, coarsening threshold, and noise filter values of 0.3, 0.1 and 0.05 respectively for wedge solutions, and 0.2, 0.1 and 0.02 respectively for cone solutions. These values were judged from trial runs to be sufficient at capturing the shock. A low-order, reconstruction-off mesh refinement study will be also run, just for the 64 subcell case.

Only those cells sufficiently far from the wedge or cone apex will be used to compute the error norm in Equation 6.9 as the shock is initially smeared over a few cells, giving high error for cells close to the apex. This is seen in Figure 6.12, which plots the pressure distribution over the cone surface for the three subcell resolutions and also the analytic surface pressure. Note the oscillatory nature of the computed distribution due to the numerical surface roughening, and the finite distance over which the surface pressure rises before leveling near the analytic value. Also note that the error at a cell can be abnormally high if the surface normal is computed quite inaccurately there e.g. if the cell is only slightly intersected. Only those cells greater than a distance of 0.25 m will be used.

It will also be interesting to measure errors in the evaluation of the integrated force along the cone surface, since the oscillating noise on the surface may to some extent ‘cancel’ the errors occuring from overly high or low pressure values. Thus force errors may actually be lower than other errors or even stay roughly constant, which is a favourable result for practical engineering purposes. The force is calculated according to the procedure in Appendix E. The error measure for force will simply be the absolute relative error i.e. $\left|F_{num} - F_{theory}\right| / F_{theory}$.

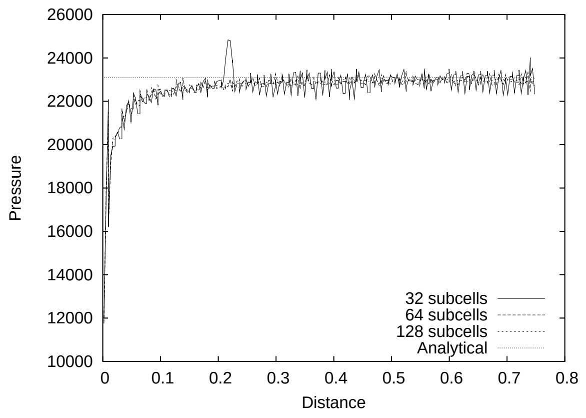

Figure 6.12: Pressure distribution over cone surface

6.3.2 Results for Supersonic Flow past Wedge

Higher-order wedge solutions for various grids (for the 64 subcell case) are shown in Figure 6.13. Also shown are outlines of the meshes, with the wedge surface and theoretical shock angle demarcated by the thicker and thinner black lines respectively. The diagonal elements in each cell are an artifcat of the grid visualizer Paraview [90].

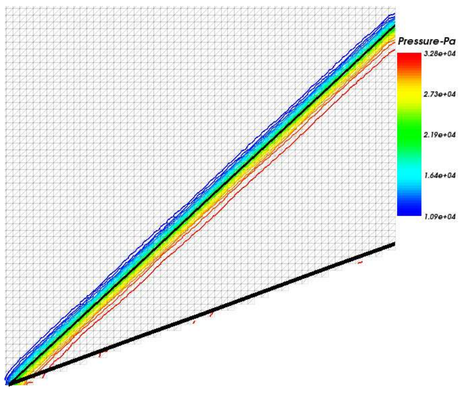

(a) Level 6 mesh

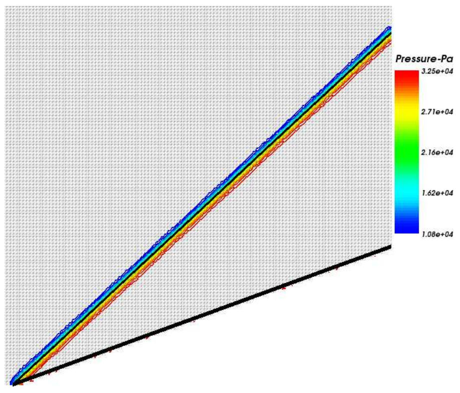

(b) Level 7 mesh

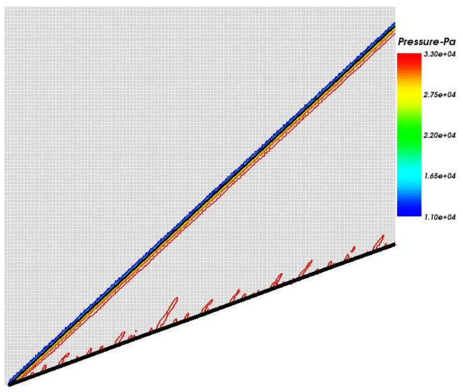

(c) Level 8 mesh

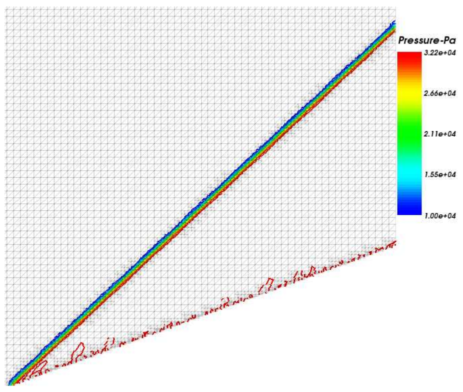

(d) Adaptive mesh, level 6-8

Figure 6.13: Wedge pressure contours for various grids, 64 subcells

The agreement with the theoretical shock angle for all solutions is quite good, and the increasing shock resolution with finer meshes is obvious. The surface 'noise' arising from inexact surface representation can also be seen. Because of the lack of a length scale on this problem (the flow is essentially uniform before and after the shock), a finer mesh can be thought to simply yield the same solution on a coarser mesh but over a larger distance of the surface, which could explain why the noise (a finer scale flow structure) is better observed for finer meshes (or larger domains). The shock resolution on the adaptive solution appears just as sharp as the fully uniform level 8 solution, whilst decreasing the number of cells used by more than a factor of ten.

Error versus uniform grid resolution

The solution error versus uniform grid spacing for the three different subcell resolutions is shown in Figure 6.14. Grid-convergent behaviour is not always expected here as only solution errors at the surface are considered. As metioned above, a finer grid yields the same solution only at a larger scale, so the surface noise for this problem will decrease only with better subcell, not grid, resolution (see Figure 6.15).

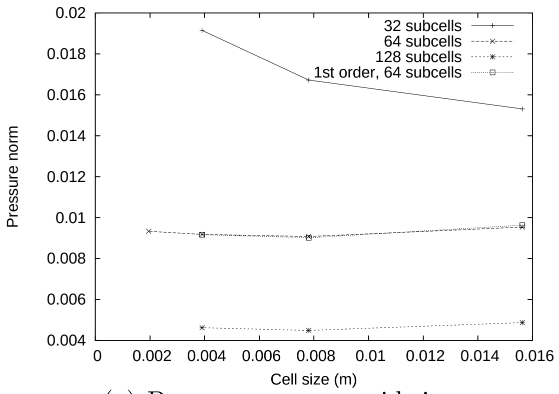

(a) Pressure norm vs grid size

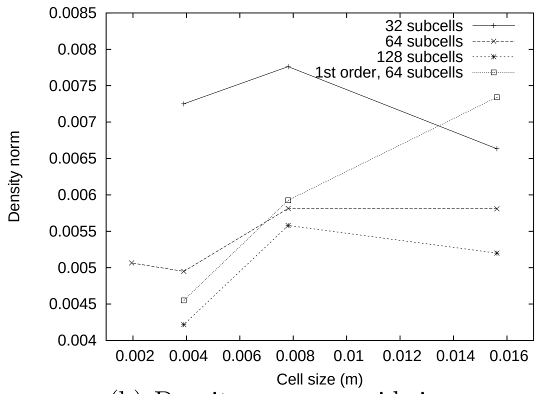

(b) Density norm vs grid size

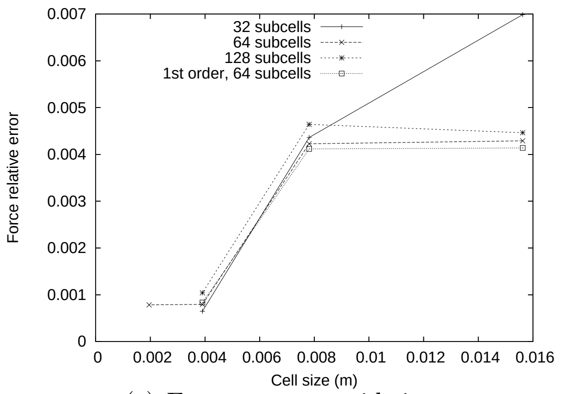

(c) Force error vs grid size

Figure 6.14: Wedge solution error vs grid size for various subcells

Note in Figure 6.14(a) the surface pressure norm is seen to *increase* slightly for finer grids using 32 subcells, whilst for finer subcell resolutions the norms remain somewhat constant. The low-order density norm is also lower than the higher-order value at one point (Figure 6.14(b)). These counter-intuitive results might be expected, as depending on how the surface intersects the mesh, it is possible that coarser mesh or subcell resolutions actually perform better for a given test case. The low-order pressure solution closely coincides with the higher-order result; this may be expected given the absence of reconstruction at surfaces (Section 4.3.3). However, it does not always coincide (e.g. in the density or force solution) due to the presence of reconstruction away from the surface. All these errors are fairly low, typically much less than 2%.

The force errors (Figure 6.14(c)) seem to generally decrease for finer meshes. For nearly all mesh resolutions, these errors do not seem so dependent on subcell resolution compared to the pressure or density norm. The force errors do not exceed 0.7% even for the coarsest mesh. This result is quite encouraging, suggesting that obtaining a quite accurate force value does not require a high grid or subcell resolution.

Error vs subcell resolution

This time the solution errors versus the inverse of the number of subcells are plotted for the three main uniform grid levels in Figure 6.15. Also shown are adaptive mesh errors, just for the 64 subcell case. As better subcell resolution means better surface representation, it should be expected that these graphs show decreasing error for more subcells.

The fairly linear decrease of the pressure surface norm with increasing subcell resolution (for all meshes) can be seen in Figure 6.15(a). The adaptive pressure error is very close to the finest 64 subcell uniform grid result. The apparently superlinear decrease of density surface norm with increasing subcell resolution is also observed in Figure 6.15(b). However, the adaptive density error is significantly lower than the 64 subcell uniform grid result.

The force errors (Figure 6.15(c)) do not seem to display subcell-convergent behaviour and seem to stay roughly constant. This is probably due to the partial cancellation of surface pressure noise as described in Section 6.3.1. However, the errors seem to increase slightly for the 128 subcell case, but this may simply be the accidental result of the numerical surface roughening described above. The adaptive solution error again is lower than the finest uniform mesh result (it just may be that cancellation is not so good for this subcell value).

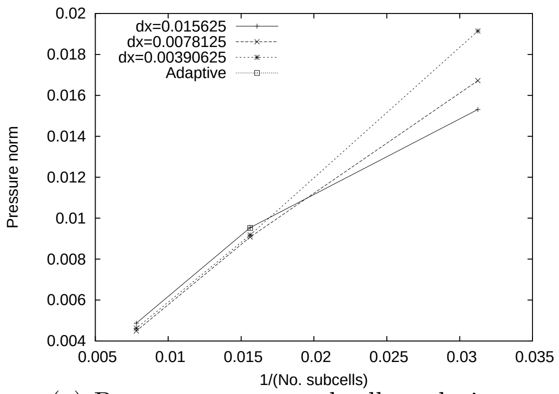

(a) Pressure norm vs subcell resolution

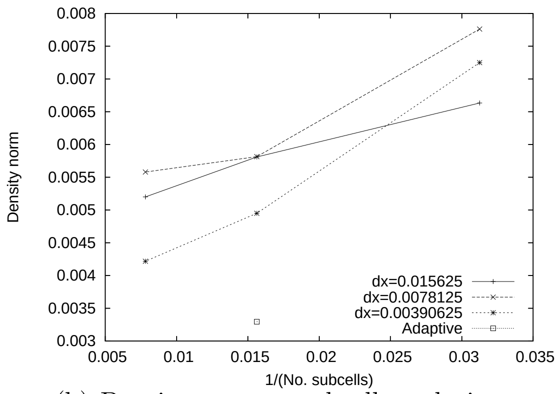

(b) Density norm vs subcell resolution

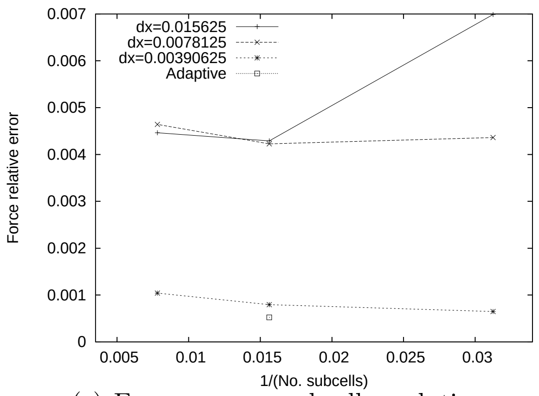

(c) Force error vs subcell resolution

Figure 6.15: Wedge solution error vs subcell resolution for various grids

Conclusions

The surface errors for this subcell and mesh refinement study are shown to be quite low despite the presence of surface noise, showing that the VCE method does not result in an excessively numerically roughened surface. It is encouraging to see that solutions generally display fairly good convergent behaviour (at least for surface values) for increasing subcell resolution. The force errors seem to stay roughly constant as subcell resolution is increased, due to partial cancellation of the pressure noise. The adaptive mesh solution consistently gave errors as low (or lower than) the finest uniform mesh, illustrating the effectiveness of adaptive meshes in producing accurate solutions with fewer computational resources.

6.3.3 Results for Supersonic Flow Past Cone

Higher-order cone solutions for various grids (for the 64 subcell case) are shown in Figure 6.16. Like the wedge solutions of Section 6.3.2, agreement with the theoretical shock angle for all solutions and increasing shock resolution with finer meshes is readily observed. Surface noise arising from VCE surface effects can be seen again. The adaptive solution seems to produce a solution of comparable quality to the finest uniform grid.

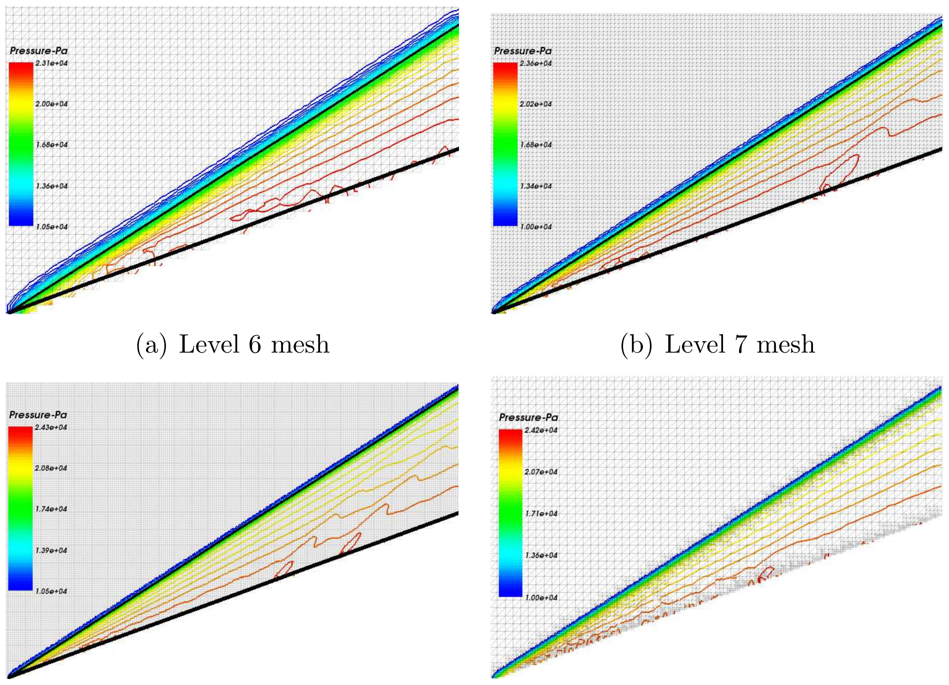

(a) Level 6 mesh

(b) Level 7 mesh

(c) Level 8 mesh

(d) Adaptive mesh, level 6-8

Figure 6.16: Cone pressure contours for various grids, 64 subcells

Error versus grid resolution

The solution error versus uniform grid spacing for the three different subcell resolutions is shown in Figure 6.17. Unlike the wedge solutions in Section 6.3.2, grid-convergence for surface errors should expected here because finer grids have cells closer to the cone surface, and the solution here does vary between the shock and the surface. Nonetheless, occasional counter-intuitive results arising from the VCE surface effects (described in Section 6.3.2) may occur.

In Figure 6.17(a) the somewhat linear decrease of pressure error with cell size can be seen, which may be a result of the nominally first-order solution scheme at the surface (Section 4.3.3). The first-order error is nearly the same magnitude as the higher-order error (for 64 subcells) for finer cell sizes. Pressure errors are all smaller than 4%. Figure 6.17(b) plots the density norm, which generally decrease with finer cell size. This time the first-order solution has a consistently higher error. Errors are all smaller than 2%.

The force errors (Figure 6.17(c)) display superlinear grid convergence. However, the error behaves linearly for the first-order solution. Power law fits of the higher-order

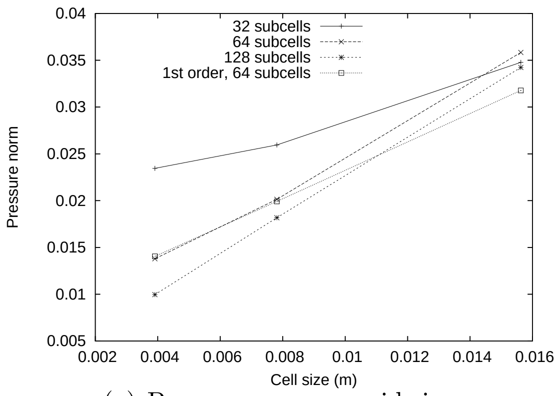

(a) Pressure norm vs grid size

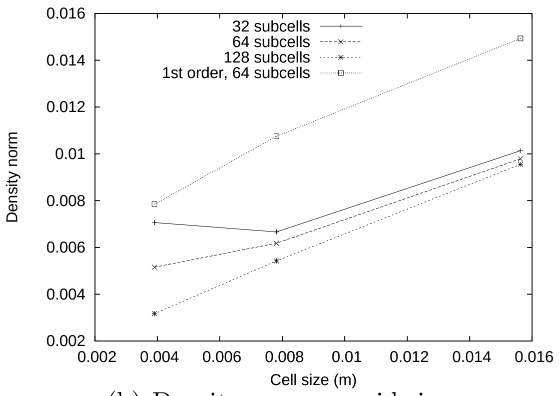

(b) Density norm vs grid size

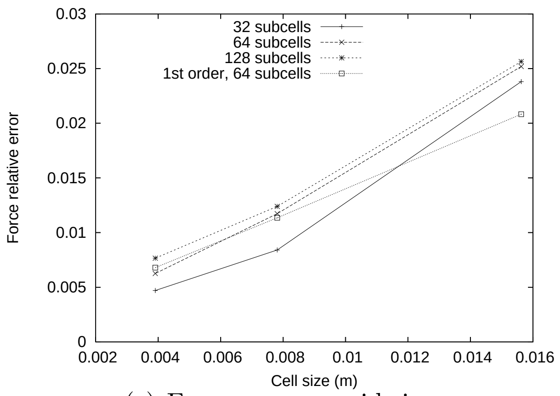

(c) Force error vs grid size

Figure 6.17: Cone solution error vs grid size for various subcells

curves give convergence orders between 1 and 2. This example shows an interesting reverse trend that *lower* subcell resolutions give a more accurate force result. The force errors here are significantly higher than the wedge case (Figure 6.14(c)), although they still are lower than 3%.

Error vs subcell resolution

The results of a previous study [204] are repeated here which show the decrease of solution noise with increasing subcell resolution in Figure 6.18. The surface noise can be qualitatively seen to decrease as subcell resolution is increased. The graphs of solution error versus the inverse of the number of subcells are shown in Figure 6.19. Also shown are adaptive mesh errors, just for the 64 subcell case.

Pressure norms for finer meshes seem to decrease fairly linearly with increasing subcell resolution (Figure 6.19(a)) although they are nearly constant for the coarsest mesh. The adaptive 64 subcell pressure error is very close to the equivalent finest mesh 64 subcell error. Decreasing values of the density surface norm are also shown in Figure 6.19(b). The density error on the adaptive 64 subcell solution is lower than the

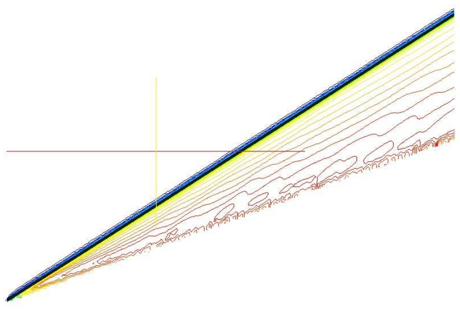
(a) 32 subcells

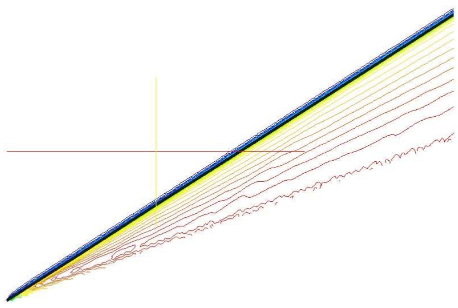
(b) 64 subcells

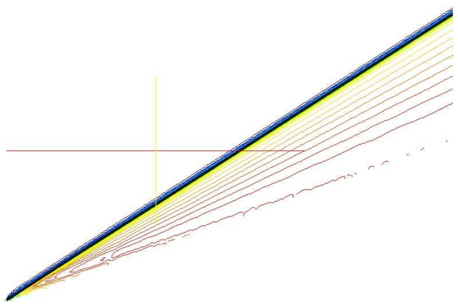
(c) 128 subcells

Figure 6.18: Cone density contours for various subcells, level 8 mesh (from [204])

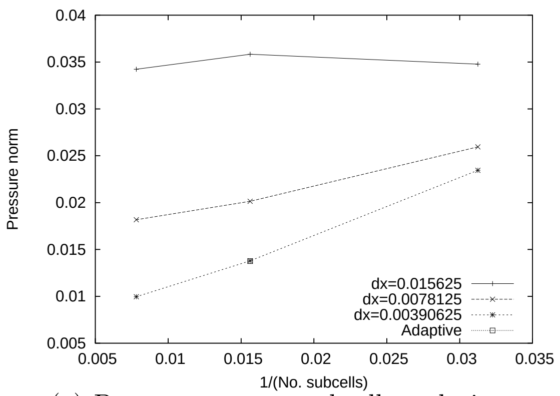

(a) Pressure norm vs subcell resolution

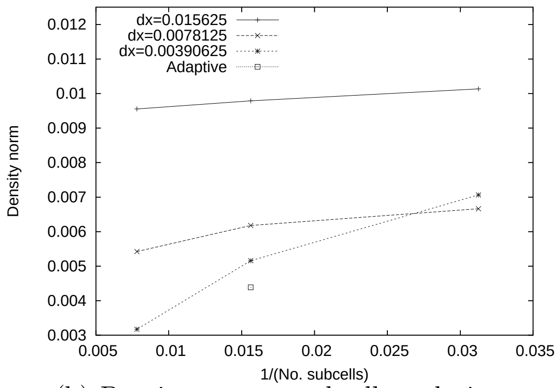

(b) Density norm vs subcell resolution

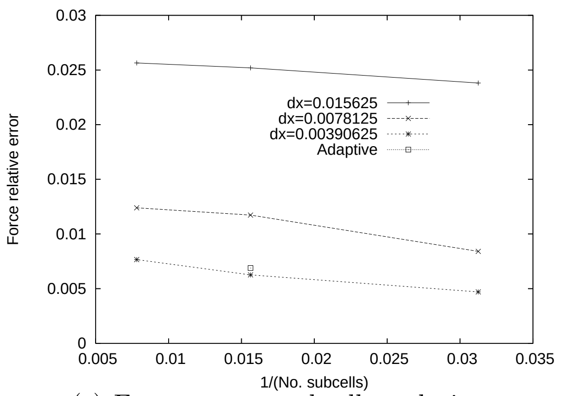

(c) Force error vs subcell resolution

Figure 6.19: Cone solution error vs subcell resolution for various grids

equivalent finest mesh 64 subcell error.

The force errors (Figure 6.19(c)) apparently do not display subcell-convergent behaviour. There is a slight increase of error with finer subcell resolution. The considerations of Section 6.3.2 would seem to apply, namely, that this could be an accidental product of the numerical VCE surface roughening. In [204] a similar subcell convergence study was performed, this time by recording the *maximum* values in pressure and density relative error over the surface (rather than the root mean square error). An additional subcell value of 256 was included in the study. The resulting graph is shown in Figure 6.20.

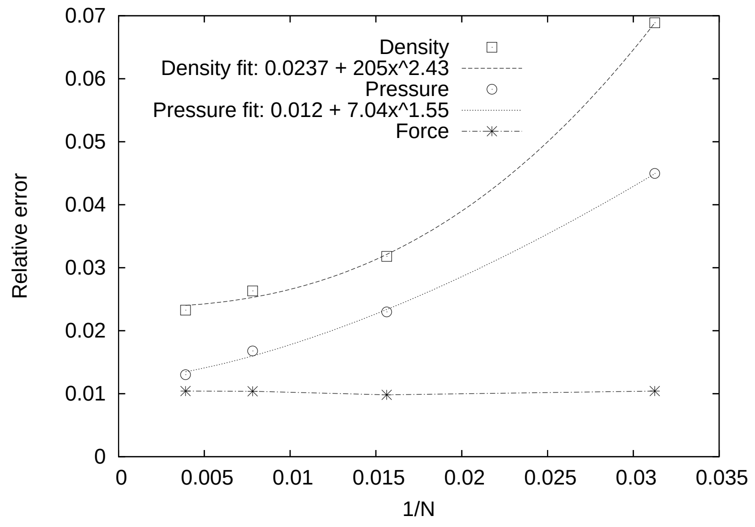

Figure 6.20: Maximum errors vs subcell resolution for cone (From [204])

In this example, the integrated force relative error does stay roughly constant with subcell resolution, demonstrating that despite greater noise at lower resolutions, cancellation between positive and negative pressure amplitudes does occur. The force error is quite low at around 1%. Power-law curve fits for the pressure and density errors have also been attempted to calculate an approximate 'convergence order' for subcell resolutions. These convergence orders are 2.43 and 1.55 for the density and pressure errors respectively, which is encouraging given that the underlying flow solver also has greater than first-order accuracy.

Conclusions

Like with the wedge study of Section 6.3.2, surface errors are quite low despite the presence of surface noise and additional axisymmetric complications (Appendix E.1). Nevertheless, there is still observable subcell- and mesh-convergent behaviour. The decreases in error as both subcell and mesh resolution are successively doubled (Figures 6.17 and 6.19) seem to be of similar magnitude. The adaptive mesh solution for the 64 subcell case likewise consistently gave errors as low (or lower than) the equivalent finest uniform mesh. The VCE method appears to produce quite satisfactory results when very high resolution solutions are not required e.g. for practical engineering design purposes say where the integrated pressure forces are required.

6.3.4 Performance of Wedge and Conical Flow Solution

The solution time versus total number of cells (in turn related to mesh level) for the wedge and cone simulations is plotted in Figure 6.21. This is done for the 64 subcell case only as the curve can be directly compared with the adaptive grid solutions which were also performed with 64 subcells. All solutions were marched from the same initial condition and terminated at the same flow time.

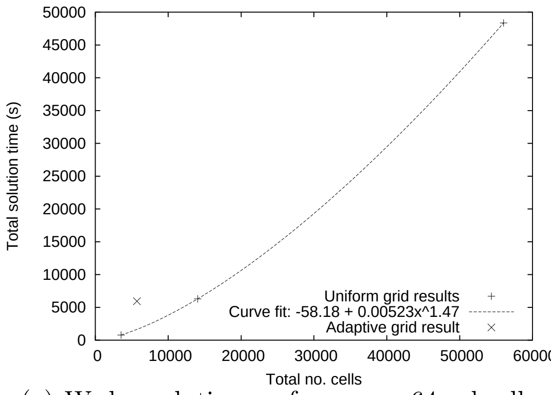

(a) Wedge solution performance, 64 subcells

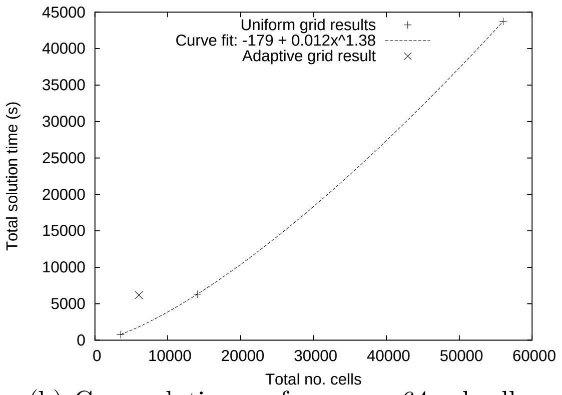

(b) Cone solution performance, 64 subcells

Figure 6.21: Performance of wedge and cone solutions on 64 subcells

A power-law curve fit through the uniform grid results is also seen, with the solution time scaling with the grid size according to a power of 1.47 and 1.38 for the wedge and cone simulations respectively. These figures are close to the theoretical scaling of 1.5 on a square, uniform mesh (Section 6.1.5), but due to the presence of the wedge or cone geometry the mesh here is not a perfect square.

The performance of the adaptive solution is also shown on these graphs, where the final (and maximum) number of cells for the adaptive simulation is reported. For the wedge solution, the number of cells in the adaptive mesh is decreased by nearly a factor of 10 over the uniform grid, with time savings of a factor of 8.14. For the cone case, the savings in storage and solution time are 9.3 and 7.1 respectively. These are significant savings in both time and storage, and adaptive mesh results are at least as accurate as the equivalent finest level mesh. In three dimensions, the time and storage savings should be even greater.

6.4 Verification of Supersonic Vortex Flow

This two-dimensional test case is an inviscid supersonic vortex bounded by two circular, ninety-degree arcs, and is chosen because it has a smooth, analytic solution [6] and can be compared with previous solutions [110, 148]. This test case is also worth performing as a global order of convergence can be computed, and this problem has a slightly more complex geometry compared to the wedge and cone study of Section 6.3. The flow conditions are chosen to be identical to those of References [6, 110, 148].

The initial flow condition chosen for the domain is

$$\rho = 1.0, P = 1.0, u = v = 0$$

The inner arc radius is at $r_i = 1$ and the outer arc radius at $r_o = 1.384$. The analytic density as a function of radius r for this flowfield is

$$\rho\left(r\right) = \rho_i \left[1 + \frac{\gamma - 1}{2} {M_i}^2 \left(1 - \left(\frac{r_i}{r}\right)^2\right)\right]^{\frac{1}{\gamma-1}} \tag{6.10}$$

where the inlet Mach number at the inner radius is $M_i = 2.25$ and density $\rho_i = 1$. The pressure $P_i = 1/\gamma$ and it varies throughout the flowfield according to the isentropic relation $P = P_i \rho^\gamma$. The inflow (at $x = 0$) is distributed inversely proportional to the radius i.e. $\mathbf{u_i} = (M_i/r)\,\widehat{\mathbf{i}}$.

The global discretization error is computed two different ways, a dimensionless L_1 norm representing 'average' error (Equation 6.11) –

$$L_1 = \frac{1}{N} \sum \left| \frac{Q_{num} - Q_{exact}}{Q_{exact}} \right| \tag{6.11}$$

where N is the number of cells, Q_{num} is the computed numerical solution (in this case it will be density) and Q_{exact} the exact solution. Another error measure is the dimensionless root mean square norm already enunciated in Equation 6.9.

Like Section 6.1, the grid convergence order is obtained from simulations on three successivly-refined uniform grids. They are mesh levels 5, 6, and 7 corresponding to cell sizes of 0.04325, 0.021625, and 0.0108125 m respectively. Three different subcell resolutions are also used (32, 64, and 128 subcells) to observe error behavior with subcell refinement.

The flux solvers are AUSMDV and EFM, and a first-order (no reconstruction) grid convergence study will also be performed with AUSMDV. As the circular walls are represented by polygons, care was taken to position the points along the arc circumference such that their distance was at least five times smaller than the smallest cell size, to minimize errors from the geometry representation itself.

6.4.1 Results for the Supersonic Vortex Problem

The nine pressure solutions (3 mesh levels, 3 subcell resolutions) with overlayed Cartesian grid outlines are shown in Figure 6.22. The noisy behaviour at the surface is obvious on coarser meshes. Due to grid coarseness and the flow visualizer behaviour, contours can sometimes appear outside walls.

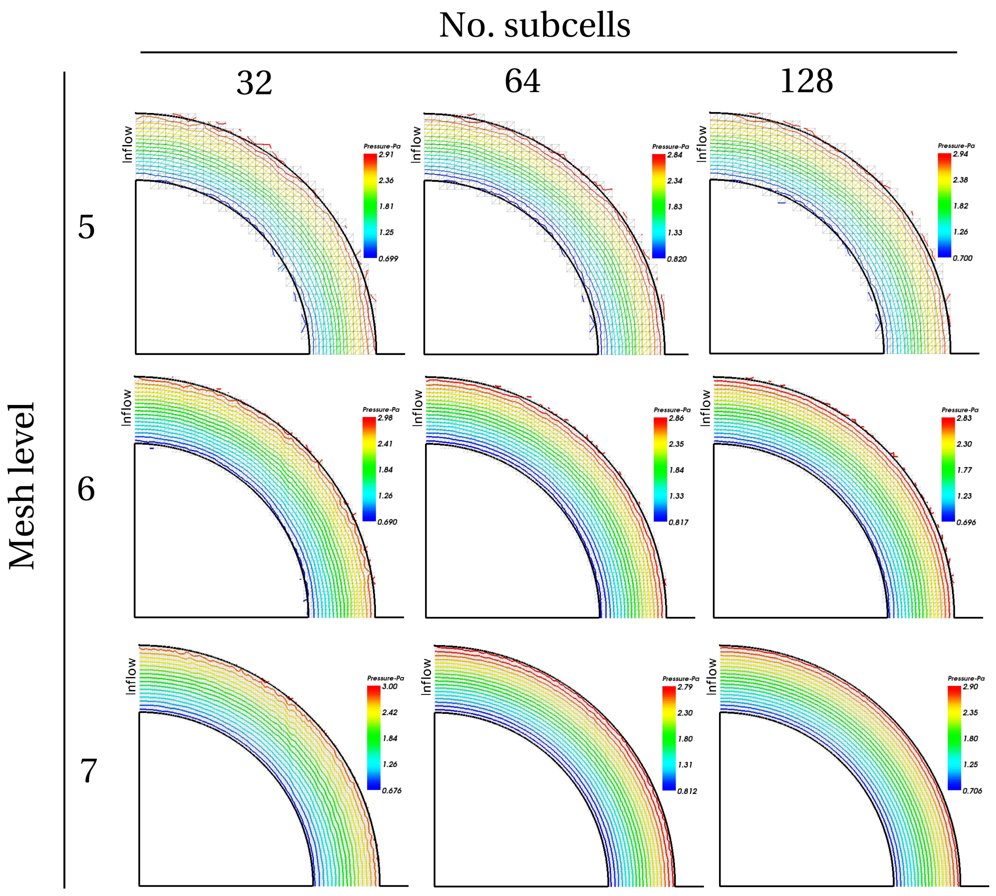

Figure 6.22: Pressure contours for supersonic vortex simulations

Nonetheless, the general smoothness of the solution shows that VCE does represent the surface fairly well. The smoothness becomes more evident with increasing mesh refinement. However, the improvement in quality is not as obvious for a fixed mesh level and increasing subcell resolution.

Grid convergence

The AUSMDV convergence orders are shown in Table 6.10. An additional simulation was performed where errors only from surface cells were computed, to test convergence for the locally 'noisier' flow there. This simulation, and the first-order one, is performed only for 64 subcells.

Table 6.10: AUSMDV grid convergence orders for supersonic vortex problem

	No. subcells		
Norms	32	64	128
First-order, L_1	-	1.04416	-
First-order, L_2	-	1.20606	-
L_1	1.69724	1.72636	1.99776
L_2	1.85416	1.90352	2.10717
Surface L_1	-	1.63797	-
Surface L_2	-	1.73622	-

The convergence orders are even better than reported body-fitted grid values [110, 148], and are comparable to previous Cartesian grid values [2] of 1.82 to 2.11. Wall boundary representations might improve much better on Cartesian grids undergoing refinement compared with body-fitted grids, partially explaining why these convergence orders are so high.

These values are also considerably better than the observed orders in Sections 6.1.2 and 6.1.4 (despite the smoothness of both solutions), confirming again the problem-dependent nature of convergence orders, and deflating the suspicion that the poorer convergence behaviour in previous verification studies is the result of coding error. There is also an apparent trend that convergence order increases for higher subcell resolution. The convergence is also good even when only surface values are observed, demonstrating good VCE representation of the curved surface. The EFM convergence orders are shown in Table 6.11, and the values are comparable with those in Table 6.10.

Table 6.11: EFM grid convergence orders for supersonic vortex problem

	No. subcells		
Norms	32	64	128
L_1	1.58489	1.89283	1.97694
L_2	1.75611	1.98967	2.0864

Subcell convergence

Alternatively 'subcell convergence' orders can be obtained from curves that plot error norm with respect to the inverse of the number of subcells (for a fixed mesh resolution), like in Figure 6.23 for the AUSMDV solution. Figure 6.23 shows the decreasing error for increasing subcell resolution for a given mesh. All error norms are fairly low, less than 2.5%.

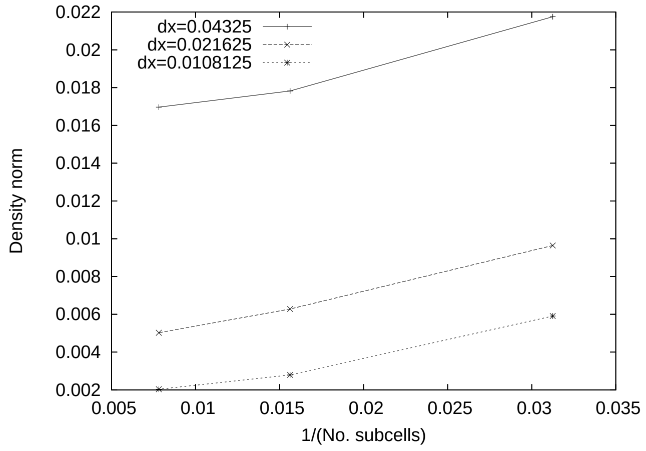

Figure 6.23: Solution norm vs subcell resolution for supersonic vortex problem (AUSMDV)

The subcell ‘convergence orders’ are shown in Tables 6.12 and 6.13. It is encouraging to see these convergence orders are similar in magnitude to the formal order of accuracy for the numerical method, and that for this problem the solutions converge consistently and roughly equally in both subcell and grid resolution.

Table 6.12: AUSMDV subcell convergence orders for supersonic vortex problem

	Mesh level		
Norms	5	6	7
L_1	2.19552	1.42058	2.0398
L_2	2.45689	1.71389	2.71342

Table 6.13: EFM subcell convergence orders for supersonic vortex problem

	Mesh level		
Norms	5	6	7
L_1	1.56195	1.99705	2.12797
L_2	1.51753	2.21202	2.86945

Chapter 7

Validation - Shock Diffraction Over Wedge

The unsteady diffraction of a Mach 1.3 shock wave over a 55° wedge will be simulated. These results can be compared with the simulations of Sivier *et al* [189] (which used Löhner's FEM-FCT code [131]) and can also be compared with Schardin's experimental work [182], and is thus a validation test case.

Figure 7.1(a) shows Sivier's [189] density contours some time after the initial shock has diffracted over the wedge. Several flowfield features can be observed – shocks, reflected shocks, a slip layer, Mach stems, expansion fan, vortex and entropy layer. There also exists shock-vortex interaction. Figure 7.1(b) gives a schematic of flow measurements associated with these features. These measurements include –

1. **x** – horizontal distance from the back of the wedge to the primary shock
2. **a** – horizontal distance from wedge nose to primary reflected shock (feature '**B**' in Figure 7.1(a))
3. **r** – vertical distance from wedge midline to highest point of primary reflected shock (**B**)
4. **b** – horizontal distance from the back of the wedge to triple point formed at the intersection of diffracted Mach stem (**D**) and its reflected shock (**H**)
5. **c** – horizontal distance from the back of the wedge to the intersection of the diffracted Mach stem's reflected shock (**H**) and the slip layer (**C**)
6. **d** – horizontal distance from wedge midline to the highest point of the shock (**I**)
7. **vcx** – horizontal distance from back of the wedge to the geometric centre of the vortex (**F**)
8. **vcy** – vertical distance from wedge midline to the geometric centre of the vortex (**F**)

A goal of this validation exercise is to match frame by frame the results of Sivier *et al* and demonstrate good agreement in results. This is done by extracting their shock

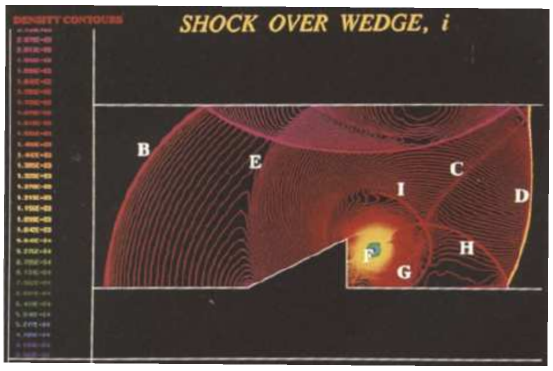

(a) Sivier's density contours at frame 11

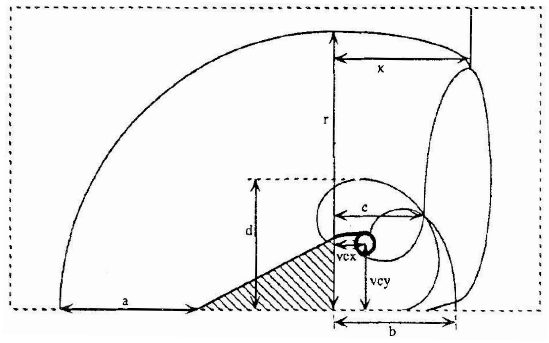

(b) Diagram of measured flow features

Figure 7.1: Flow features in shock diffraction over wedge problem (from [189])

speed, frame rate and initial shock location [189]. The Rankine-Hugoniot relations [10] can then be used to calculate the post-shock pressure and density ratios and flow speed. Nonetheless, it is impossible to fully replicate the simulations of Sivier *et al* [189] as they use a finite element scheme and unstructured grids. The ambient atmospheric and post-shock conditions are given in Table 7.1. The present simulations assume perfect gas air ($\gamma = 1.4$) and will use the AUSMDV flux solver.

Table 7.1: Initial flow conditions for shock diffraction problem

	Ambient	Post-shock
ρ	1.145144 kg/m^3	1.73569 kg/m^3
P	10^5 Pa	1.805×10^5 Pa
U	0	154.653 m/s

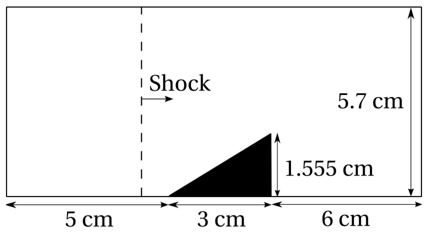

Figure 7.2: Numerical domain for shock diffraction over wedge study

In this study the computation domain is shown in Figure 7.2. Two different adaptive meshes will be used to test grid dependence. For the first case, five working mesh levels (levels 5 to 10) corresponding to cell sizes ranging from 4.38×10^{-3} to 1.37×10^{-4} m will be used. In the higher resolved case, grid levels 6 to 11 will be used, corresponding to cell sizes from 2.19×10^{-3} to 6.84×10^{-5} m. Note the minimum cell size of Sivier *et al* is 2.8×10^{-5} m [189], so their results might be more resolved, but the goal of this validation exercise is to demonstrate good agreement, not exact correspondence. The density-based adaptation indicator (Equation 3.4) is used with 0.063, 0.035 and 0.004 for the refinement, coarsening and noise filter thresholds respectively; Sivier *et al* [189] also use the same indicator, but their choice of values was inappropriate for this methodology as it resulted in excessive cell refinement. The number of subcells are 64 and 10 for the cell area and volume respectively.

7.1 Results for the Shock Diffraction Over Wedge

In this section the computed densities at different frames are presented (the results are from the higher resolution solution). The flowfield corresponding to frame 2 of Sivier *et al* [189] is shown in Figure 7.3. The current results seem to lag very slightly behind the results of Schardin [182] and Sivier *et al* [189]. This is unfortunate, but the initial conditions are based on a best estimate on the initial incident shock location in Sivier's paper [189]. However, general good agreement with previous results can be seen. The slip layer can be clearly observed and very close to the wedge surface there appears to be slight solution noise arising from the VCE approximate surface representation (Section 2.4.4), but this is relatively small.

The adapted mesh in Figure 7.3(b) also superimposes the schileren image of the flowfield; note the diagonal lines in the mesh outlines are an artifact of the grid visualizer. The grid has adapted well to all major flow features, however not all cells along the slip layer are at maximum level; an additional entropy indicator, as recommended by Sivier *et al* [189], would improve the adaptation there.

Figure 7.4 shows the results at Frame 4. Agreement with Sivier's results is quite good, but the curled-up entropy fan is not as well resolved. This could be due to their finer minimum cell size and entropy adaptation indicator. Some contours upstream of the expansion fan exhibit more noisy behaviour compared to Sivier's result; this could be due to the less dissipative AUSMDV scheme being used compared to the FEM-FCT scheme with artificial viscosity and partly also from the numerically roughened surface. Also, the mesh is coarser in these regions (from Figure 7.4(b)) and the contours pass through different sized cells, which makes for uneven visualization.

In Figure 7.5 (frame 6) the diffracted Mach stem has reflected from the bottom wall (equivalent to the crossing of the Mach stems with a symmetric boundary condition). Both the still-deforming slip layer and the curled-up entropy fan are moving closer to each other, in agreement with Sivier's result. Agreement in all major flowfield features with experimental and numerical results is quite good (although the computed results seem to lag slightly in time, as discussed above).

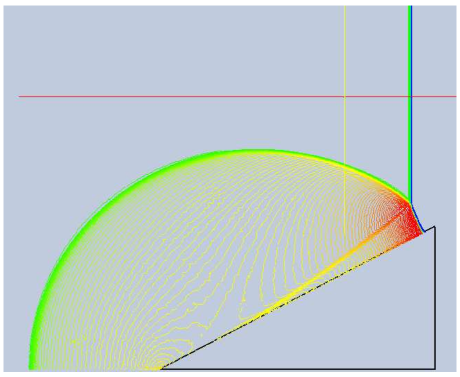
(a) Density contours for frame 2

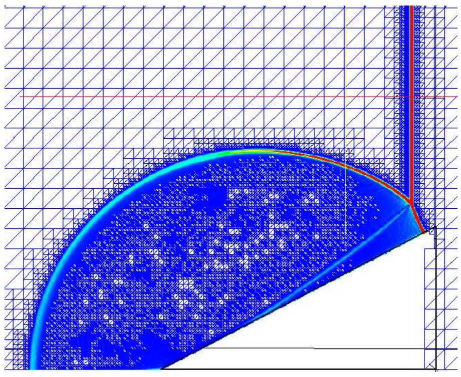
(b) Grid and schlieren for frame 2

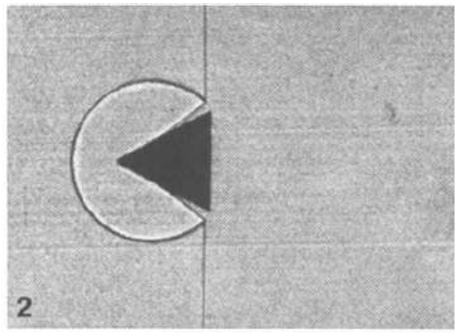

(c) Schardin frame 2 (from [182])

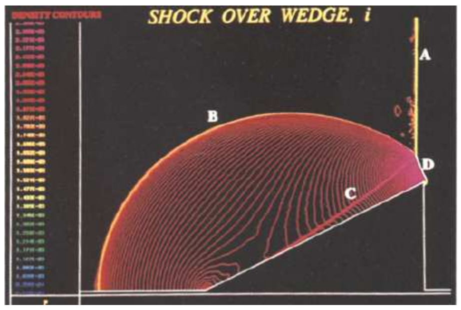

(d) Sivier frame 2 (from [189])

Figure 7.3: Frame 2 results for shock diffraction over wedge study

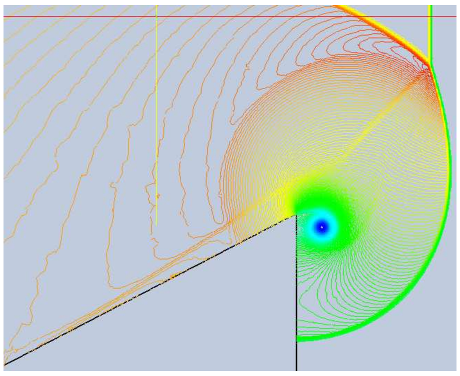
(a) Density contours for frame 4

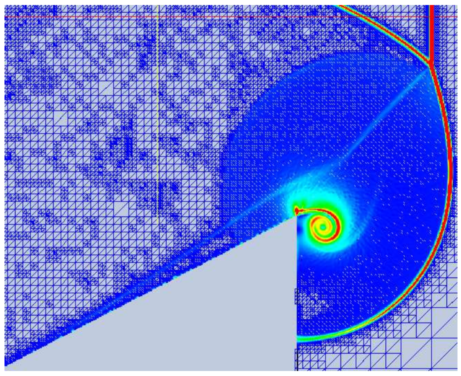
(b) Grid and schlieren for frame 4

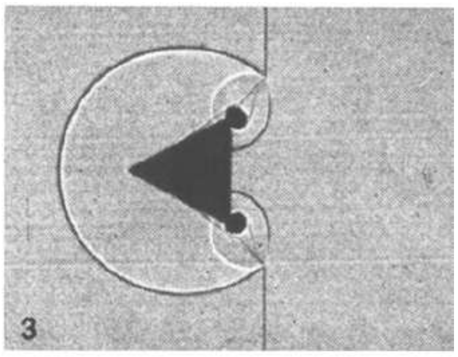

(c) Schardin frame 4 (from [182])

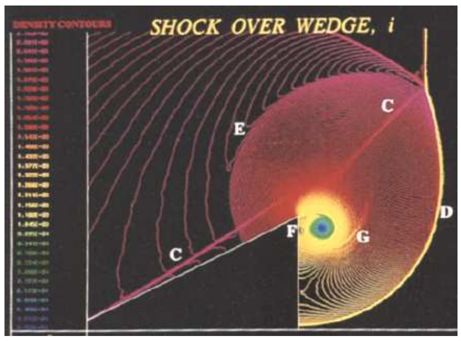

(d) Sivier frame 4 (from [189])

Figure 7.4: Frame 4 results for shock diffraction over wedge study

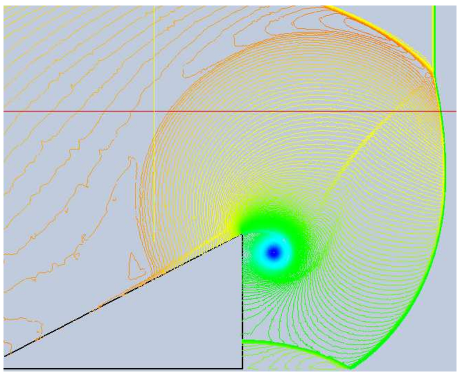
(a) Density contours for frame 6

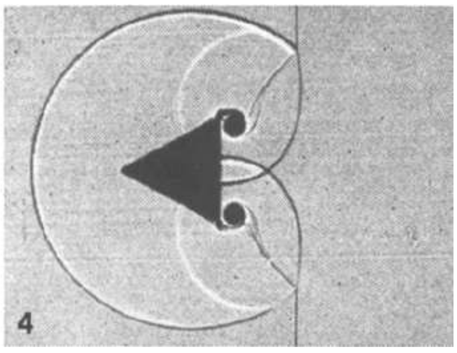

(b) Schardin frame 6 (from [182])

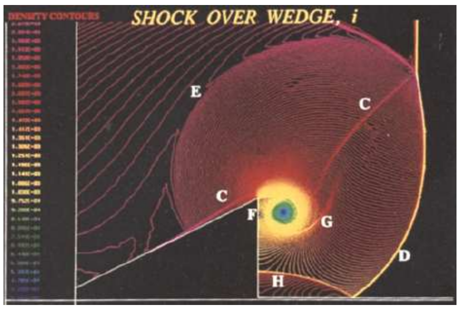

(c) Sivier frame 6 (from [189])

Figure 7.5: Frame 6 results for shock diffraction over wedge study

In Figure 7.6 (frame 8) the reflected Mach stem (**H**) has been broken in two by the vortex. The accelerated end of this shock (**I**) extends from the back wedge face to the vortex, and the remnant of the reflected Mach stem (**H**) is decelerated below the vortex. The slip layer and entropy layer continue to move closer to each other, but these features are not as sharply resolved as Sivier's [189]. Unlike Sivier's simulation, Kelvin-Helmholtz instabilities arising from the interaction of shocks **I** and **H** with the vortex are not present, although they do develop at later times. This may be due to the coarser grid resolution and the associated numerical diffusion because Kelvin-Helmholtz is sensitive to diffusive effects. In all other respects the results agree quite well with the previous work.

In frame 9 (Figure 7.7) the shock (**I**) has passed through the vortex layer and is growing into a cylindrical configuration. What appears to be the beginnings of a Kelvin-Helmholtz instability in the vortex layer can be seen near the wedge corner. There also appears to be a triple point arising from interaction with the reflected Mach stem (**H**) and the vortex (also visible in Sivier's simulation).

The flowfield results for the final frame, frame 11, are shown in Figure 7.8. All major flow features present in Figure 7.8(b) agree well with Sivier's simulation (Figure 7.8(d)). The entropy layer (**G**) is more visible here than at other frames, and the shock (**I**) is

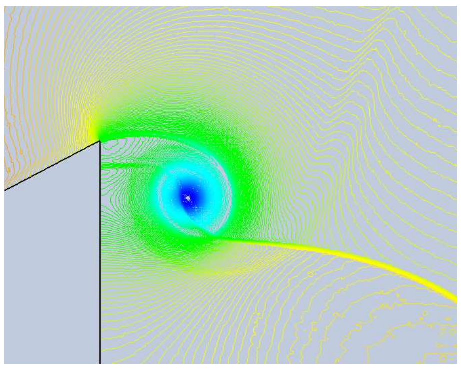
(a) Density contours for frame 8

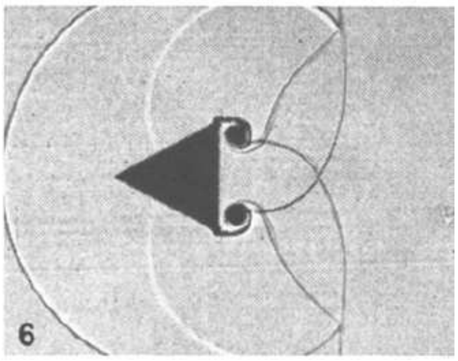

(b) Schardin frame 8 (from [182])

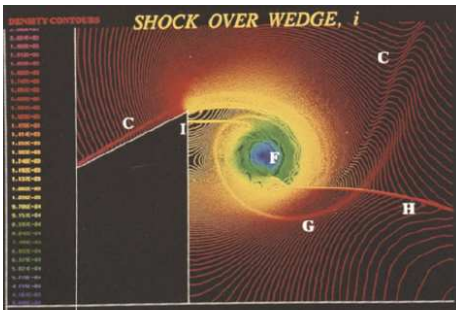

(c) Sivier frame 8 (from [189])

Figure 7.6: Frame 8 results for shock diffraction over wedge study

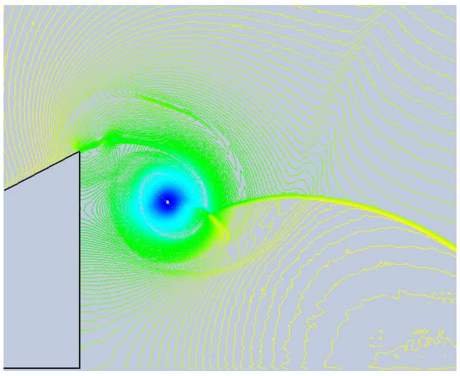
(a) Density contours for frame 9

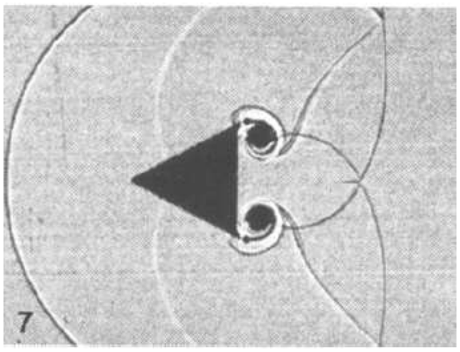

(b) Schardin frame 9 (from [182])

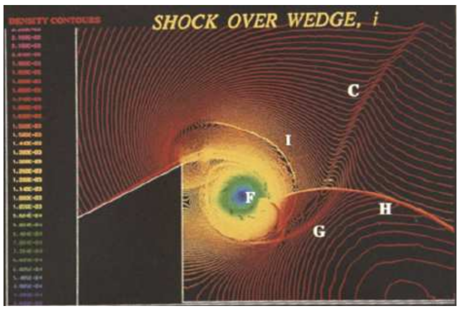

(c) Sivier frame 9 (from [189])

Figure 7.7: Frame 9 results for shock diffraction over wedge study

now much more sharply resolved than in Figure 7.7(a). Also present (and observable in Sivier's results) is the formation of a triple point at the intersection of the diffracted Mach stem (**D**) and reflected Mach stem (**H**).

The adapted mesh (with overlaid flowfile schlieren) is shown in Figure 7.8(c) and it is clear that it continues to refine over discontinuities. There seems to be some spurious refinement at the top wall upstream of the reflected shock (**B**) whose cause is not exactly known. However, given that the top wall is not exactly flush with the grid boundary and the suppression of reconstruction for intersected cells, it is possible that slightly aphysical disturbances arise that trigger adaptation.

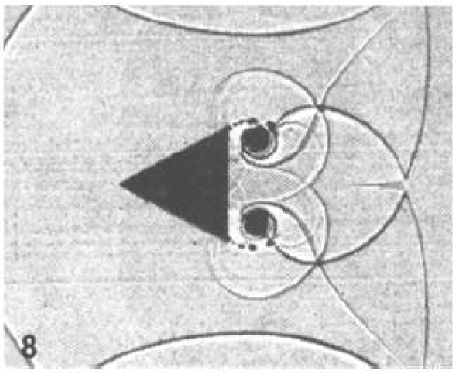

(a) Schardin frame 11 (from [182])

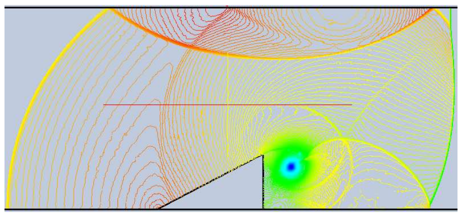
(b) Density contours for frame 11

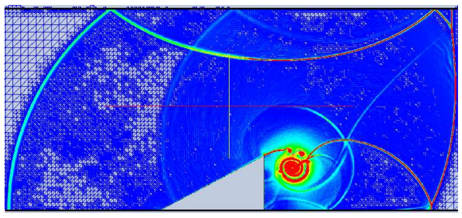
(c) Grid and schlieren for frame 11

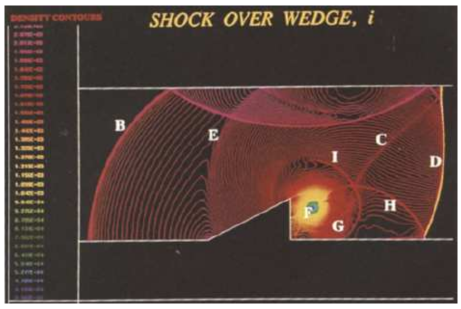

(d) Sivier frame 11 (from [189])

Figure 7.8: Frame 11 results for shock diffraction over wedge study

Most notably the schlieren in Figure 7.8(c) shows a more developed Kelvin-Helmholtz instability in the vortex layer. This is also observable from the experimental results in Figure 7.8(a) and is more clearly seen in a closeup of the flowfield at the vortex in Figure 7.9. The coarser and finer mesh resolution is displayed to compare how well this instability is captured. It is obvious that the dissipation inherent in the coarser mesh simulation suppressed the generation of the secondary vorticies (evident in the finer mesh simulation), although the vortex layer is nonetheless slightly unstable and perturbed. This demonstrates again the highly grid-dependent nature of these instabilities [16, 84].

Quantitative flowfield measurements from the flow features described in Figure 7.1(b)

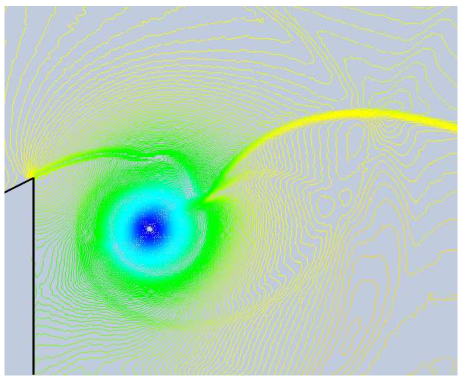
(a) Frame 11 closeup (coarser resolution)

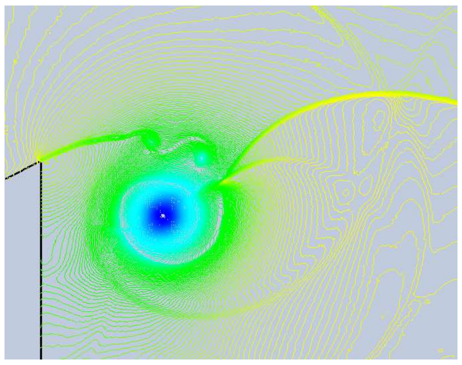
(b) Frame 11 closeup (finer resolution)

Figure 7.9: Frame 11 closeup of Kelvin-Helmholtz instability

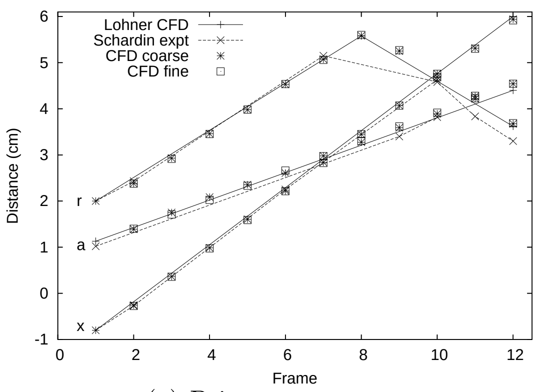

(a) Primary structures

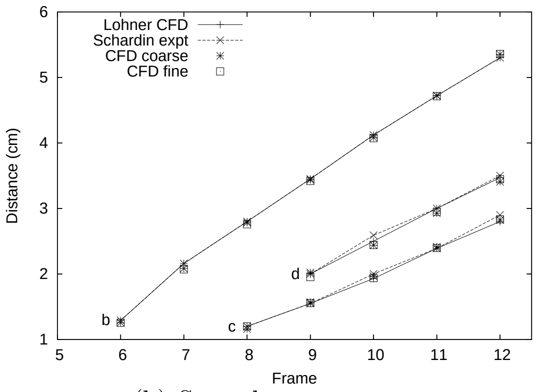

(b) Secondary structures

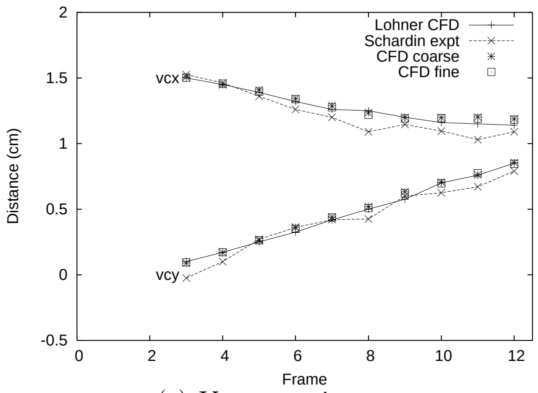

(c) Vortex trajectory

Figure 7.10: Flowfield measurements for shock diffraction over wedge study

are plotted in Figure 7.10, where results from the two grid resolutions are shown to observe grid dependence. The primary flow structures (**a**, **r** and **x**) and the secondary flow structures (**b**, **c** and **d**) are plotted in Figures 7.10(a) and 7.10(b) respectively. Agreement with previous results is quite good, with nearly grid-independent behaviour.

In Figure 7.10(c) the vortex position (**vcx** and **vcy**) is plotted. Agreement with Sivier's result is quite good, and possible explanations of discrepancies with Schardin's experiments include the difficulty of locating the vortex and the complex interaction of the reflected Mach stem with the vortex [189]. These results demonstrate that `OctVCE`, despite the issues with flow noise at surfaces (Section 2.4.4), has the ability to provide an accurate and fairly well-resolved simulation of this problem. Along with Sivier *et al* [189], it is reasonable to assert that surface wedge pressures would also be estimated well.

7.2 Serial Performance

The serial performance of the simulations is profiled using the GNU profiler `gprof`. The relative percentages of time spent in important portions of the code are shown in Table 7.2 for the two different resolution simulations. The important sections of the code are –

1. Reconstruction-related operations – computing gradients, limiters, reconstruction
2. Solution advancement – computing fluxes, timesteps, boundary conditions, time integration
3. Adaptation – computing adaptation indicators, refining and coarsening the mesh
4. Geometric operations – point-inclusion tests, calculating cell geometric properties
5. Connectivity management – updating mesh connectivity, list operations
6. Output – writing solutions to output files

It is clear that reconstruction-related operations are a large fraction of the computation time, and the relative difference between these operations and solution advancement is quite similar to the performance figures in Section 6.1.5. It might be worthwhile for future work to investigate more efficient ways to perform reconstruction. There appears to be good efficiency in the adaptation process, but connectivity management is a necessary overhead on an adaptive scheme, meaning a net overhead of around 10% for the entire adaptation process. This is actually a fairly significant figure that can

Table 7.2: Serial performance for shock diffraction over wedge simulations (reported values in percentages)

Code portion	Coarser resolution	Finer resolution
Reconstruction-related	47.65	49.77
Solution advancement	27.66	32.46
Adaptation	3.36	3.86
Geometric operations	14	9.1
Connectivity management	7.13	4.55
Output	0.2	0.26
Solution run time (hrs)	9.5	44.7
Max. no. cells	1.3×10^5	2.83×10^5

further limit the Amdahl speedup (Section 5.4), so parallelizing adaptation might be a worthwhile goal. There is very low cost associated with solution output, but this is dependent on the file output frequency.

Currently with `OctVCE` the parallelization of adaptation, geometric operations and connectivity management for two-dimensional problems is not performed. Also, the relatively high cost of geometric operations in Table 7.2 would probably be lower in three-dimensional simulations as there is some redundancy in geometric calculations in two-dimensional simulations. It seems that geometric and connectivity management operations reduce for the higher resolution simulation, showing that as grids become finer more time is spent in solving the actual flow equations.

7.3 Parallel Performance

The parallel performance of this problem on 2 and 4 processors is measured, and the observed speedups in execution time for the coarser and finer resolution simulations are shown in Table 7.3. These simulations were run on the University of Queensland owned SGI Altix 3700 supercomputing facility. It is clear that the speedup performance is not very good, indicating a large serial code fraction and/or high parallel overheads.

Table 7.3: Observed speedups for shock diffraction over wedge simulations

	2 processors	4 processors
Coarser resolution	1.69	1.9
Finer resolution	1.59	2.05

The Karp-Flatt Metric [113] (Equation 5.2) can calculate an 'effective' serial fraction e given the speedup. This effective fraction incorporates both the actual serial and parallel overhead code fractions ϵ and ω respectively. Using the Intel compiler with the `openmp-profile` option also permits a degree of parallel code profiling, but although total time spent in serial and parallel regions is reported, these implicitly include overheads and so an accurate value of $\epsilon(n)$ cannot be computed. Nonetheless, other useful reported measures are the per-thread time spent in barrier (synchronization) regions $b\,(n,p)$ and the cumulative imbalance time (the total sum in the course of the simulation of the time difference between threads for each entry to the region). Only the maximum values of the barrier and imbalance times will be reported, and these values should ideally be low.

Using the terminology of Section 5.4 for problem size n let $t_o\,(n,p)$ be the parallel overhead given p processors; the important quantities are

$$\begin{aligned}
\beta\,(n,p) &= b\,(n,p) \,/\, (\sigma\,(n) + \phi\,(n)) \\
e\,(n,p) &= (\sigma\,(n) + t_o\,(n,p)) \,/\, (\sigma\,(n) + \phi\,(n)) \\
\epsilon\,(n) &= \sigma\,(n) \,/\, (\sigma\,(n) + \phi\,(n)) \\
\omega\,(n,p) &= t_o\,(n,p) \,/\, (\sigma\,(n) + \phi\,(n)) \\
E\,(n,p) &= \sigma\,(n) + \phi\,(n)\,/p + t_o\,(n,p) \qquad (7.1)
\end{aligned}$$

$\beta(n,p)$ can be thought of as a barrier fraction of the code, and $E\,(n,p)$ is the total elapsed time of the simulation. As mentioned in Section 5.4 the Karp-Flatt metric can be used to plot the behaviour of $e\,(n,p)$ for different numbers of processors p, and extrapolated to yield an estimate of $e\,(n,1) \simeq \epsilon\,(n)$ (no parallel overheads exist for serial execution). In many cases, it is difficult to determine the actual value of $\epsilon(n)$ due to code complexity and this extrapolation is the simplest way. It is thus possible also to obtain an estimate to ω i.e. $\omega\,(n,p) = e\,(n,p) - e\,(n,1)$. As a measure of the extrapolation's validity, the elapsed time on p processors can be estimated and compared with the measured elapsed time using the formula

$$E' = [e(n,1) + (1 - e(n,1))\,/p + \omega(n,p)]\, t_1(n) \qquad (7.2)$$

where $t_1(n)$ is the measured serial elapsed time ($t_1(n) \equiv \sigma(n) + \phi(n)$) and $e(n,1)$ is the extrapolated serial fraction. The performance statistics discussed above are reported in Table 7.4, which reports these statistics for the 1, 2 and 4 processor simulations for the coarser and finer resolutions. The fraction of overhead spent in synchronizations (or barriers), β/ω is also shown.

A discussion of each performance statistic is given below. Firstly, the effective serial fraction e for both coarse and fine resolutions is quite significant given the more limited

Table 7.4: Parallel performance statistics for shock diffraction over wedge simulations

	1 processor		2 processors		4 processors	
	Coarse	Finer	Coarse	Finer	Coarse	Finer
Single processor time (s) t_1	34237	160903				
'Effective' serial fraction e			0.183	0.26	0.367	0.316
Extrapolated serial fraction $e(n, 1)$	0.0915	0.231				
Overhead fraction ω			0.0919	0.028	0.276	0.0854
Barrier fraction β			0.009	0.0087	0.0793	0.0154
Barrier/overhead β/ω			0.104	0.306	0.288	0.18
Imbalance time/elapsed time			0.0033	0.0029	0.0563	0.0106
Estimated elapsed time (s) E'			21831	103623	20347	81847
Measured elapsed time (s) E			20232	101364	17978	78402

parallelization of the two-dimensional code discussed in Section 7.2, and it increases for more processors due to parallel overhead (time spent in process startup, communication or synchronization). The increase (between 2 and 4 processors) is 0.184 and 0.056 for the coarser and finer grid results respectively. The increase is smaller for the finer grid result, probably due to the Amdahl effect [151] (Section 5.4) where the parallel overhead fraction typically decreases for larger problem sizes as t_o has a lower complexity than ϕ.

The extrapolated serial fraction $e(n, 1) \simeq \epsilon$ appears to be smaller for the coarser grid result. Perhaps one cause of this stems from the longer execution time in some serial operations for larger problem sizes like list traversals which utilize indirect addressing. However the value of $e(n, 1)$ is an estimate and the serial fraction ϵ may be different if executed using the resources of more processors.

The overhead fractions ω are based on extrapolated ϵ values and for the coarser grid result are very signficant, being *larger* than its extrapolated serial fraction, and increasing by about a factor of 3 between 2 and 4 processors. The overheads for the finer grid result are consistently smaller (the Amdahl effect) by about 70% and also increase by about a factor of 3. They are also smaller than its extrapolated serial fraction. The barrier fractions β are smaller than the overhead fractions as expected, and are generally smaller for the finer resolution simulation. The predominant parallel overheads appear to consist of communication overheads.

Imbalance times are quite small (demonstrating good load balancing), and appear to increase for more processors, and is less significant for the finer resolution, indicating better performance in parallel regions. Estimated elapsed times E' also compare quite well with actual elapsed times E (indicating a reasonably sound extrapolation of $e(n, 1)$), but are somewhat larger. Thus could be due to the conservatism in the ω estimates. Also, the elapsed 1 processor time $t_1(n)$ used to compute E' in Equation 7.2 may have been smaller if it were run with the increased memory resources of a parallel simulation.

The performance statistics suggest a fairly large fraction of the code remains serial for this problem, limiting parallel efficiency. Moreover, parallel overheads are also quite significant, and increase considerably with more processors. Synchronization times also form a significant portion of these overheads, although communication time is apparently the dominant factor. This behaviour is expected for a NUMA machine like the Altix and the minimal exploitation of locality of storage (and large memory requirements) of the code as described in Section 5.5.3.

Chapter 8

Validation – Shock Diffraction Over Cylinder

This two-dimensional validation test case simulates inviscid shock wave diffraction over a circular cylinder, and was also presented in References [202, 203]. Notable experimental work on this problem was performed by Bryson and Gross [42] and past numerical work included inviscid simulations on finite difference [225], body-fitted structured [16, 230] and adaptive Cartesian [153] grids.

The shock speed is Mach 2.81, and the pre- and post-shock gas conditions are shown in Table 8.1. The post-shock conditions were obtained from the Rankine-Hugoniot relations. Perfect gas air ($\gamma = 1.4$) is assumed. The domain size is similar to Quirk's domain [153]. The numerical results here will also compare solution contours with Quirk's adaptive Cartesian code [153] because of similarity in methodology and because Quirk's solution, which uses finer grids, is more resolved.

Table 8.1: Initial flow conditions for shock over cylinder problem

	Ambient	Post-shock
ρ	0.1 kg/m^3	0.3674 kg/m^3
P	10^4 Pa	9.04545×10^4 Pa
U	0	765.21 m/s

Two different adaptive meshes are used to observe grid dependence. In the coarser grid simulation, five working mesh levels (level 5 to 10) corresponding to cell sizes ranging from $0.2188r$ to $6.836 \times 10^{-3}r$ will be used, where r is the cylinder radius. In the finer grid simulation, grid levels 6 to 11 will be used. These might be compared with Zóltak's body-fitted structured grid [16, 230], where the smallest circumferential cell was $0.01304r$, and Quirk's Cartesian grid [153], where the smallest cell was about $2.552 \times 10^{-3}r$.

All simulations use the density-based adaptation indicator (Equation 3.4) of 0.07, 0.04 and 0.0175 for the refinement, coarsening and noise filter thresholds respectively. The number of subcells are 64 and 16 for the cell area and volume respectively. The adaptive flux solver is implemented (Section 4.4) where EFM operates at shocks and AUSMDV is used elsewhere.

Pressure traces are recorded at locations around the cylinder corresponding to angles $\phi = 0°$, $30°$, $40°$, $60°$, $90°$, $120°$, $150°$ and $180°$. The traces record surface pressure normalized by ambient pressure against nondimensional time tu/r where t, r and u are the time, cylinder radius and incident shock velocity respectively.

8.1 Results for Shock Diffraction Over Cylinder

Figure 8.1 compares density contours from the finer grid simulation with Quirk's contours [153]. The comparison is quite good, and all important flow features are resolved well (the shock, contact discontinuity, vortex and vortex stem).

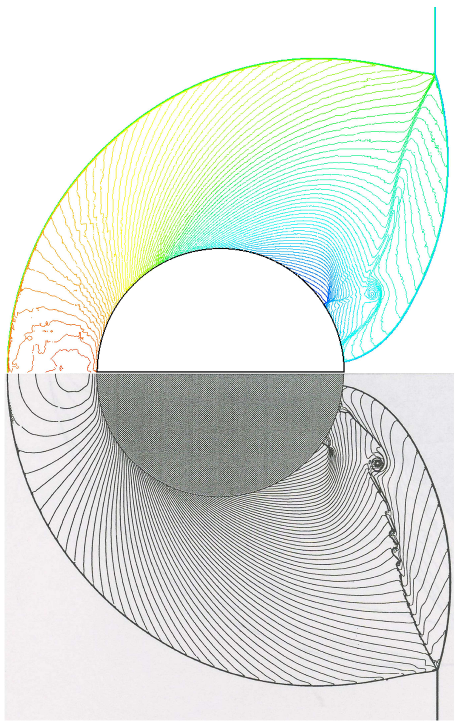

Figure 8.1: Shock cylinder density contours. Top figure – current results, bottom figure – Quirk's [153]

However, contours behind the bow shock are not smooth and exhibit noticeable noise, which could be due to noise being generated at the shock (AUSMDV is used in most of the flow). This results from a discretized stepped representation of the curved bow shock, creating artifical shear layers which stream into the stagnation region. Also Figure 8.2, which shows the corresponding grid, has a less uniform distribution of mesh levels near this region, which makes for a noisier visualization of contours.

The current results also do not exhibit the developing Kelvin-Helmholtz instability seen in Quirk's result [153] at the contact discontinuity, perhaps because the grids are coarser and/or a more dissipative flux solver than Quirk's (who uses a Riemann solver). However the original experimental results [42] also did not seem to show this instability well. As diffusion regulates the rollup of Kelvin-Helmholtz instabilities and Quirk only performs an inviscid simulation, it is possible Quirk's simulation does not contain the full physics for the shear layers.

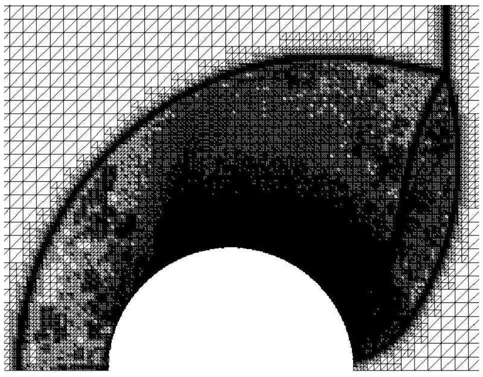

Figure 8.2: Adapted grid for shock over a cylinder

Figure 8.3 plots the computed pressure histories at various points along the cylinder surface and compares it with previous work [225, 230]. Agreement is generally very good, especially for those positions at the cylinder front (smaller than 90°), and traces from the two different mesh resolutions show high similarity and thus grid independence to an extent. There are some minor differences at those points at the back of the cylinder.

Some grid-dependence in the post-shock pressure history at the separation point (150°) can be observed in Figure 8.3(f) where the initial pulse agrees well with previous results, but differs more noticeably at later times. The peak pressures at the back stagnation point (Figure 8.3(g)) are also computed to be higher than the structured-grid simulations, but this appears to also be the case with Zóltak's adaptive mesh simulation [230] which consistently gives higher peak pressures (probably because of the better resolution) especially for the second half of the cylinder. In general, the current results agree well with previous work on this problem in spite of the VCE surface approximation.

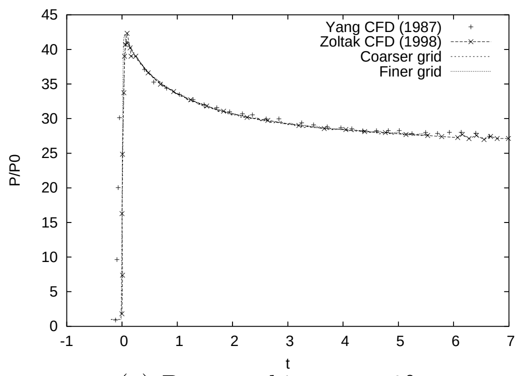

(a) Pressure history at 0°

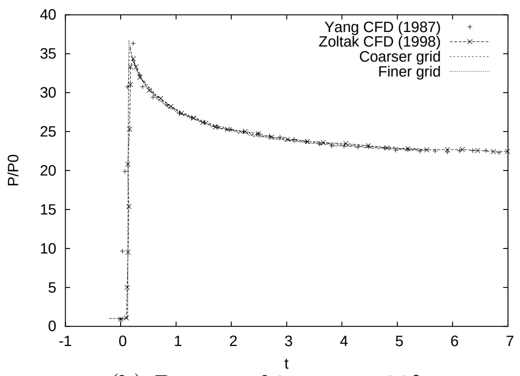

(b) Pressure history at 30°

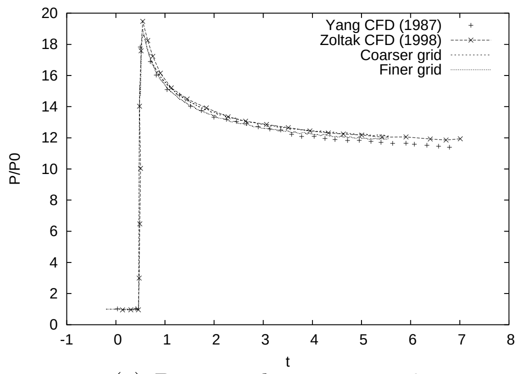

(c) Pressure history at 60°

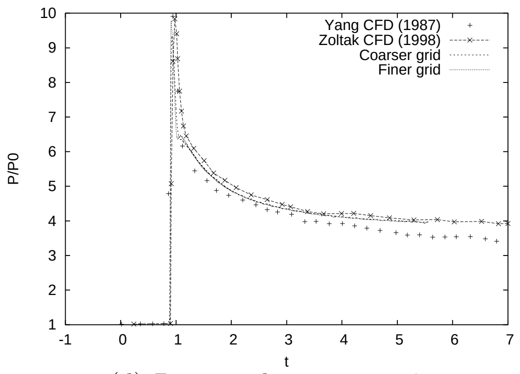

(d) Pressure history at 90°

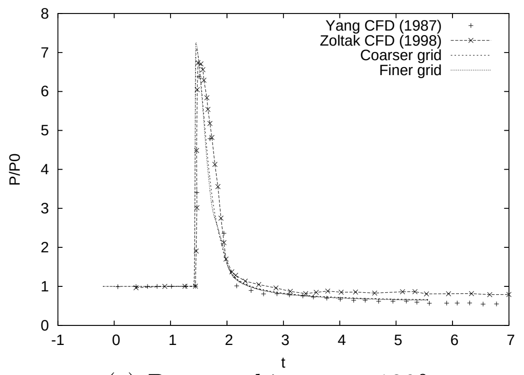

(e) Pressure history at 120°

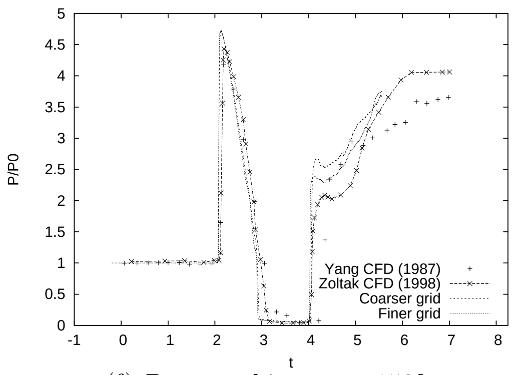

(f) Pressure history at 150°

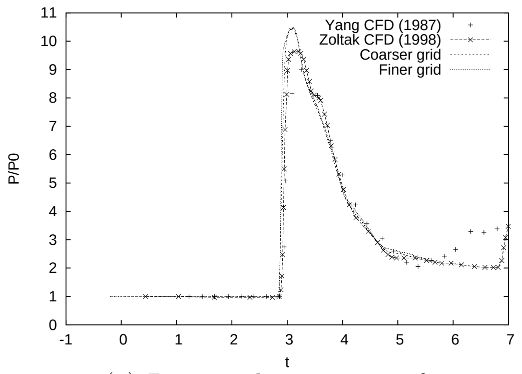

(g) Pressure history at 180°

Figure 8.3: Shock cylinder pressure histories

Chapter 9

Validation - One-Dimensional Spherical Blast Waves

This section simulates spherical blast waves using the second-order one-dimensional code to solve the unsteady Euler equations in one-dimensional spherical geometry (described in Appendix B). This will help establish the validity of results obtained from the one-dimensional code which, in turn, is used to verify `OctVCE`. The test case will be compared with the numerical results of Ritzel and Matthews [166], who investigated the use of the "balloon analogue" model (Section 4.6) to initiate explosions.

9.1 Description of Simulations

The initial charge or balloon conditions are a pressure of 30,000 atmospheres and temperature of 3600 K for the helium gas. The energy of the charge is equivalent to 0.25 kg of Pentolite with a specific energy of 6.55 MJ/kg [166]. The blast energy is related to the balloon gas pressure and volume via the ideal gas relation

$$E = \frac{(P - P_0)\,V}{\gamma - 1} \tag{9.1}$$

where E is the total blast energy, P the initial gas pressure, P_0 ambident pressure, V volume and γ ratio of specific heats. Using Equation 9.1, the initial charge radius and density of around 0.0441 m and 406.24 kg/m^3 are calculated respectively ($\gamma = 1.667$). Assumed ambient conditions for the air are $P_0 = 101.325$ kPa and $\rho_0 = 1.2$ kg/m^3.

Ritzel and Matthews used a flux-corrected transport (FCT) scheme with an element size of 5 mm [166]. To obtain exact correspondence in energy the number of cells within the charge must be an integer multiple of its radius and the closest cell size to Ritzel's that can be used is around 4.9 mm (9 cells in the charge). Further simulations are also performed assuming the same blast energy but different charge conditions –

1. A first-order simulation without reconstruction, to demonstrate increased accuracy of the second-order scheme.

2. A second-order simulation using the TNT explosive and the JWL equation of state (Section 4.5.2), also initiated using the balloon analogue model described in Section 4.6. This tests what effect the different initial condition and implementation of the JWL equation has on the solution. JWL parameters for TNT are taken from Reference [127], where the initial density and energy density are 1630 kg/m^3 and 7×10^9 J/m^3 respectively. An initial pressure of 8.384×10^9 Pa is calculated from the JWL equation of state, and a charge radius of 0.03822 m is computed; the closest cell size to Ritzel's values is 4.778 mm (8 cells in the charge).

3. A second-order simulation also using the JWL equation of state with TNT JWL parameters, but now with the same initial charge volume and density as the helium charge, and hence the energy density for this balloon gas is not 7×10^9 J/m^3. This soley tests the effect of the JWL equation on the solution. The pressure is calculated to be 7.651×10^9 Pa and C_v is backward-calculated using Equation 4.20. This initial condition is more academic than practical and is beyond the normal limits of applicability of the JWL equation; the 'solution order switching time' strategy (Section 4.8.1) was required to keep this simulation stable.

9.2 Results

9.2.1 Comparison of Helium Charge Solutions

Figure 9.1 shows the computed pressure histories at two sensor locations for the helium charge. The computed arrival time, peak overpressure and positive-phase behaviour is in very good agreement with the results of Ritzel and Matthews [166]. The arrival time and magnitude of the secondary shock is also in good agreement.

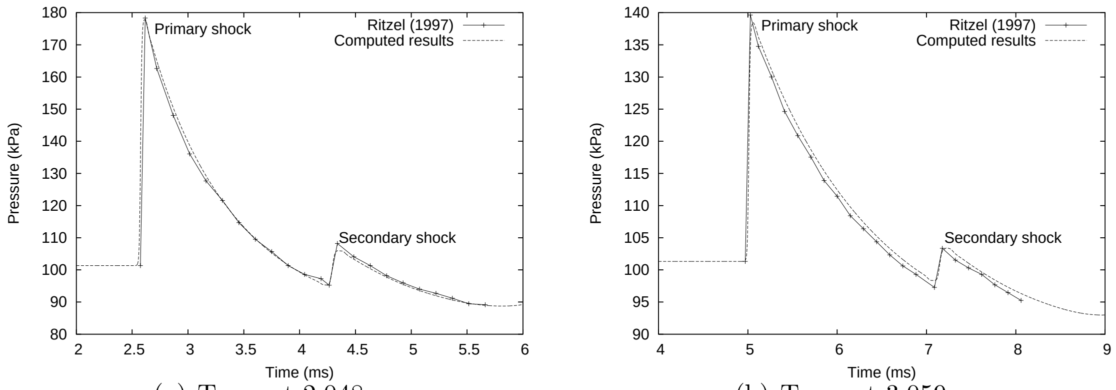

(a) Trace at 2.048 m (b) Trace at 3.059 m

Figure 9.1: Comparison of computed traces of one-dimensional blast simulation

The wave diagram comparing trajectories of primary and secondary shocks and the contact surface is shown in Figure 9.2. Note for the spherical shock problem the contact surface's position is roughly constant [25]. Very good agreement between current and past results can be observed. The results give good confidence in the simple spherical one-dimensional code.

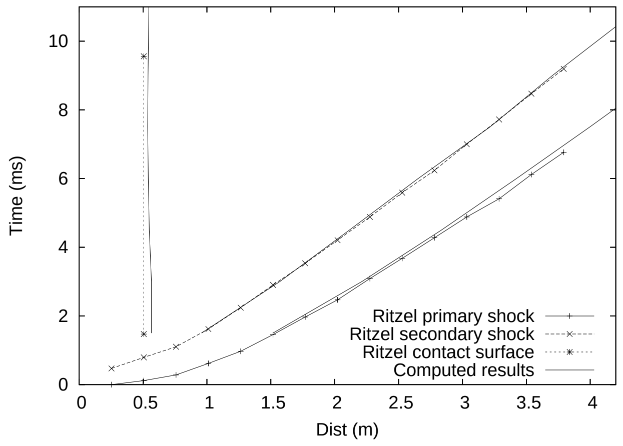

Figure 9.2: Comparison of computed trajectories of one-dimensional blast simulation

9.2.2 Comparison of Different Charge Solutions

The second-order helium, first-order helium and two JWL solutions are compared at different times in this section. The solutions at an early time of 1.5 ms are shown in Figure 9.3. Note the "JWL altered TNT equiv" line corresponds to the simulation where the "altered" JWL equation of state is used but on a gas with the same volume and density as the helium balloon gas, as opposed to the "proper" TNT solution (with more realistic TNT initial conditions), labelled as the "JWL TNT equiv" line.

As expected the first-order solution more poorly resolves the primary and secondary shocks, and consequently underestimates the peak overpressure. The primary shock strength and positive phase wave behaviour between all solutions are quite similar, although primary shocks of the TNT solutions seem to lag in arrival time slightly. The main difference in solutions occur after the positive phase; the proper TNT solution exhibits a much larger and delayed secondary shock and even reverse flow. It would seem this is mainly caused by the different initial condition of the proper TNT solution, since the altered TNT solution also uses the JWL equation but is much more similar to the helium solution.

Figure 9.4 shows the solutions at 3 ms. The poorer resolution of the first-order solution is evident, especially of the secondary shock. The agreement between all solutions

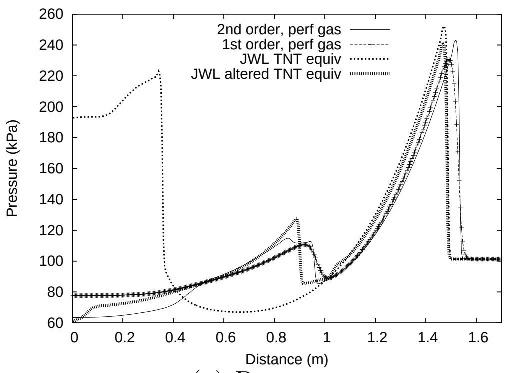

(a) Pressure

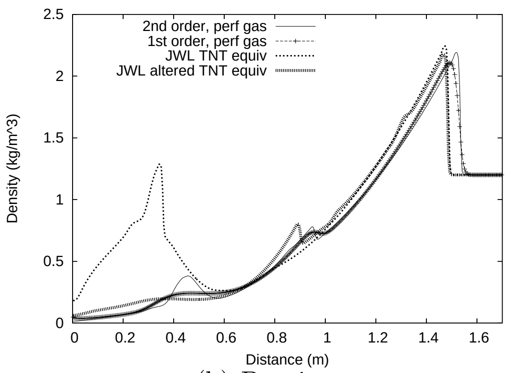

(b) Density

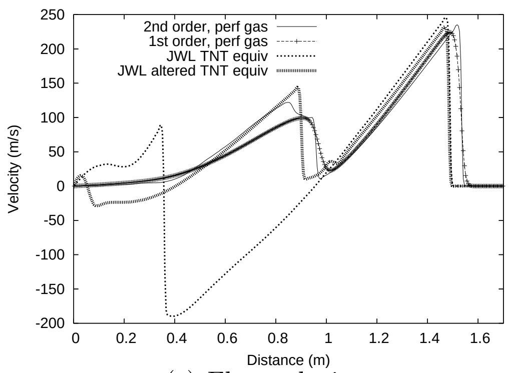

(c) Flow velocity

Figure 9.3: One-dimensional blast at 1.5 ms

in the positive phase is also more pronounced, and, as with Figure 9.3, the only significant difference occurs with the proper TNT solution after the positive phase, which as mentioned above is likely mainly due to its different initial condition. The altered TNT solution has an unusual discontinuity near the explosion core that may be a numerical artifact triggered by the sudden switching of the solution order.

The solutions at 7.5 ms are shown in Figure 9.5. At this time there is very close agreement with all solutions in the positive phase region. The pressure near the explosion core appears to be rising back to the ambient value at this time. The contact surfaces of the helium and proper TNT solutions are also visible at around $x = 0.5$ m. This surface is not captured well for the first-order or altered TNT solutions probably as a result of being run first-order at earlier times. The proper TNT solution also has apparently developed a tertiary shock, and its secondary shock continues to be larger in magnitude and lag behind the other solutions. The first-order solution can no longer represent the secondary shock effectively.

The wave diagram of all solutions is shown Figure 9.6. Wave trajectories amongst all solutions agree very well with each other except for the secondary shock trajectory of the proper TNT solution. It appears the main cause of this different secondary shock trajectory is due to the different initial condition rather than usage of the JWL

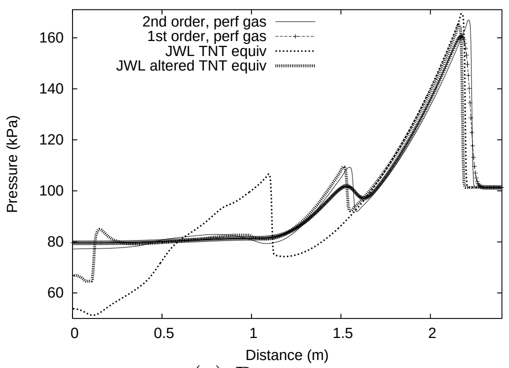

(a) Pressure

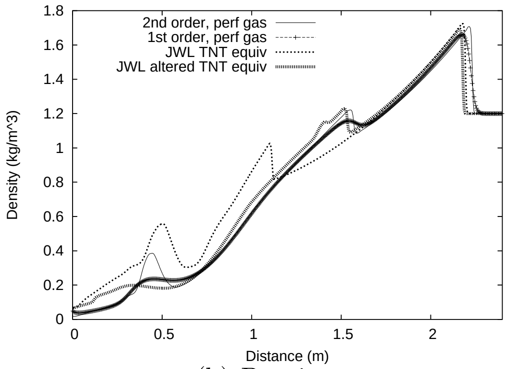

(b) Density

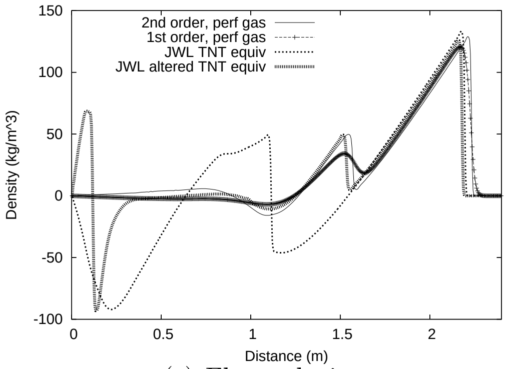

(c) Flow velocity

Figure 9.4: One-dimensional blast at 3 ms

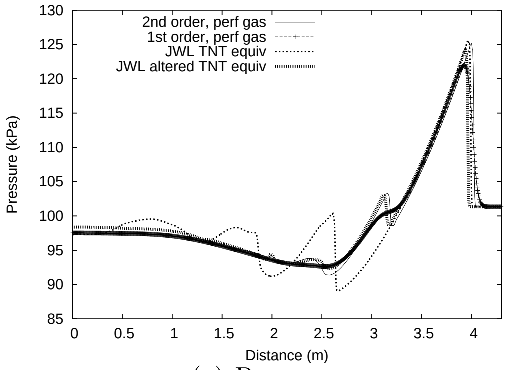

(a) Pressure

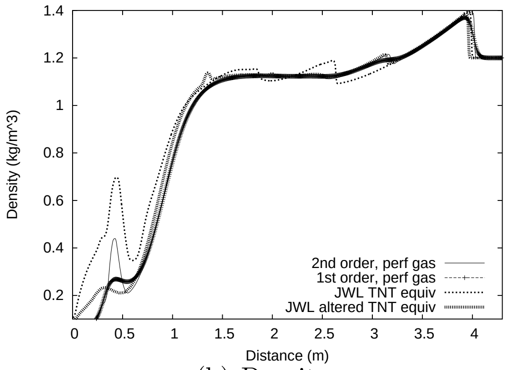

(b) Density

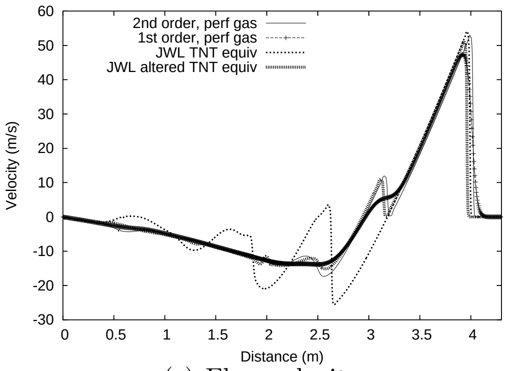

(c) Flow velocity

Figure 9.5: One-dimensional blast at 7.5 ms

equation of state. On this scale it is difficult to notice the small differences in primary shock arrival time between the helium and TNT solutions.

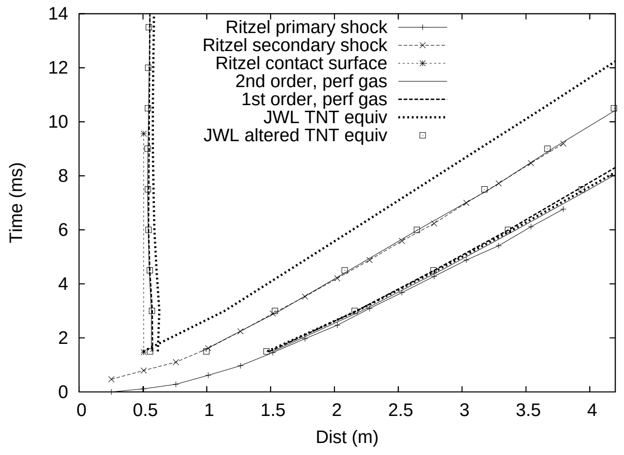

Figure 9.6: Computed trajectories for one-dimensional blast simulation

These results demonstrate that mid- to far-field behaviour of the positive-phase waveform is nearly independent of charge initial conditions or equation of state usage. They confirm that the dominant parameter determining primary shock intensity and positive phase impulse is the initial explosive energy (Section 4.6), and thus using a perfect gas balloon model is an acceptable approach for mid- to far-field regimes. Large differences occur in the negative phase, which are also corroborated by Ritzel's numerical experiments [166] which indicated that a denser balloon gas caused a more severe negative phase and stronger secondary shock.

9.3 Non-reflecting Boundary Condition Test

A final test case will investigate the performance of the non-reflecting outlet boundary condition (Appendix H) after the primary shock exits the domain. The helium solution is simulated on a truncated domain (8 m long) and compared with the solution on a longer domain using the same cell size. The solution at 19.5 ms is shown in Figure 9.7 after the primary shock has left the domain (but before the secondary shock). No reflections can be observed in pressure, density or velocity. Note the velocity in the positive phase is less than 20 m/s meaning subsonic flow.

The solution at 22.5 ms is shown in Figure 9.8, which is after the secondary shock has left the domain. The pressure and velocity (Figures 9.8(a) and 9.8(c) respectively) do not display reflections, but there exists some upstream influence of the boundary condition that causes the negative phase solution to deviate slightly.

The solution at 30 ms is shown in Figure 9.9 well after the negative phase has left

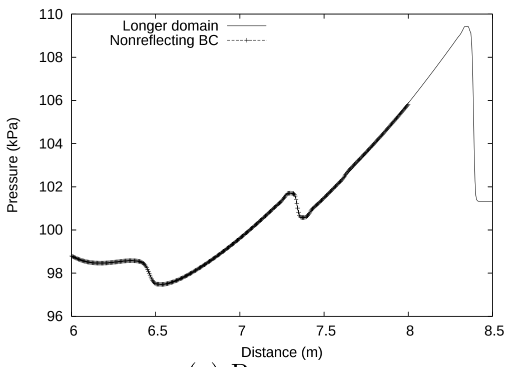

(a) Pressure

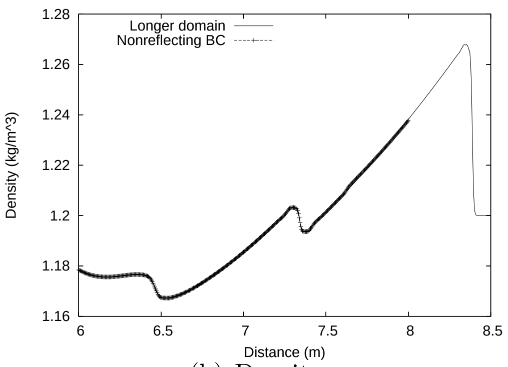

(b) Density

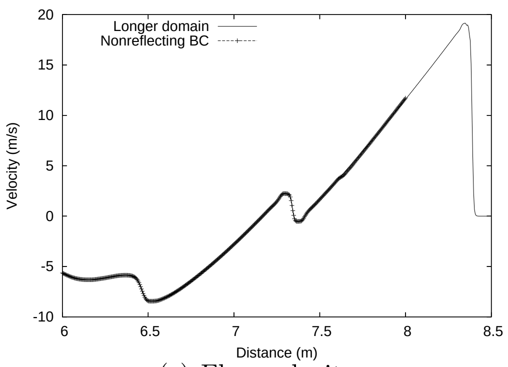

(c) Flow velocity

Figure 9.7: One-dimensional blast at 19.5 ms (non-reflecting test case)

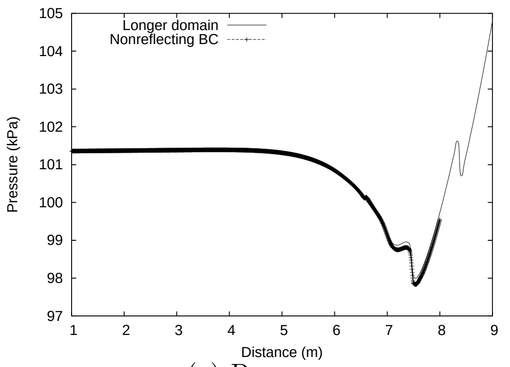

(a) Pressure

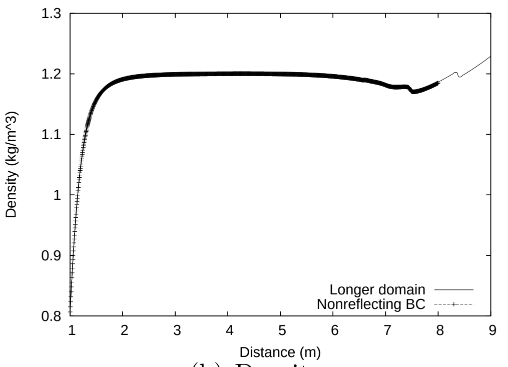

(b) Density

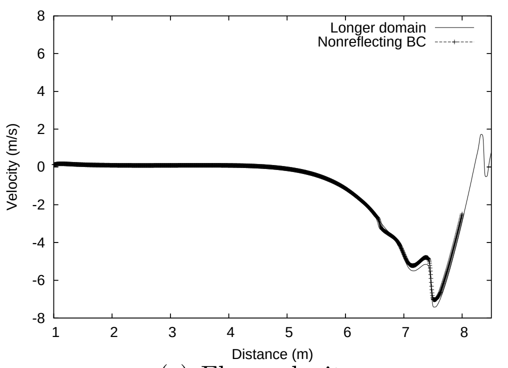

(c) Flow velocity

Figure 9.8: One-dimensional blast at 22.5 ms (non-reflecting test case)

the domain. This time the upstream influence from the boundary is more noticeable, which extends leftward until the small inward-moving reflection wave. The density solution (Figure 9.9(b)) still seems to display very good agreement with the longer domain solution. The subsonic outlet non-reflecting boundary condition seems to work quite well even some time after the secondary shock has exited the domain, although it performs more poorly at later times. Similar performance might be expected in multi-dimensional simulations when a wave parallel to the boundary exits the domain. For oblique exiting waves, there may be small reflections [116, 210].

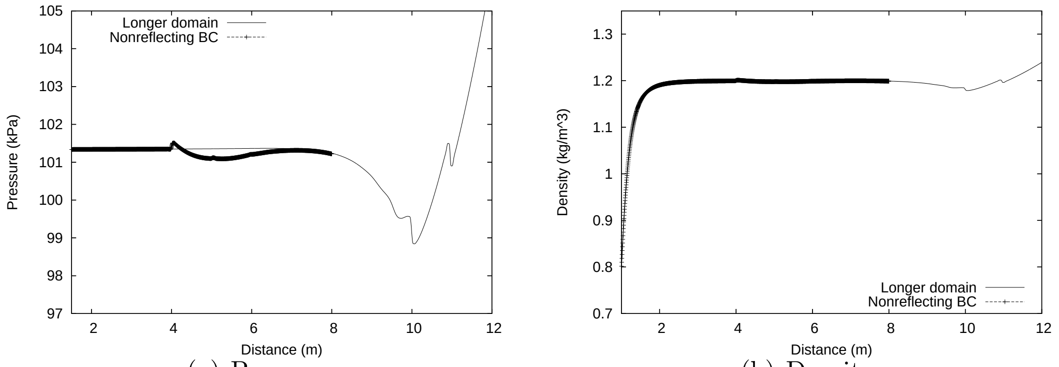

(a) Pressure (b) Density

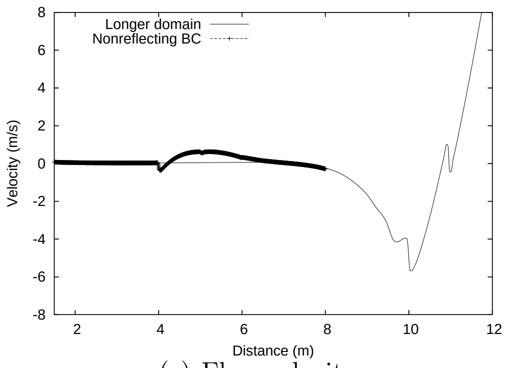

(c) Flow velocity

Figure 9.9: One-dimensional blast at 30 ms (non-reflecting test case)

Chapter 10

Validation – TNT Blast

The calculation of free-field blast parameters versus scaled distance following the explosion of a spherical TNT charge is an important test case for this code given the wealth of data on this problem [19, 25, 40, 119, 171, 192]. The material for this section appeared in Reference [206] by the author. Simulations are first performed with the one-dimensional spherical code and compared with data from the CONWEP program [103], Kinney's explosives text of [119] and the study by Cullis and Huntington-Thresher [101], and the explosions are initiated using the balloon gas approach like in Chapter 9.

Simulations are also performed in two and three dimensions and compared with the one-dimensional result. They should ideally be identical to the one-dimensional result, but this is not always attainable as the charge representation is asymmetrically 'discretized' in the radial direction by a Cartesian representation with the balloon gas or bursting sphere model (Section 4.6). The blast also does not usually propagate along the mesh direction and will give slightly different results depending on what direction one is looking. Multi-dimensional simulations are also usually quite expensive and use coarser grids that may give solutions that are not grid-independent.

The simulations use the JWL parameters for TNT taken from Reference [127], like in Section 9.1. A charge mass of 1 kg is used, thus all reported distances are also scaled values. Assumed ambient air conditions are $P_0 = 101.325$ kPa and $\rho_0 = 1.2$ kg/m^3.

10.1 One-Dimensional TNT Blast

The initial JWL TNT conditions in Section 9.1 are used here for the TNT charge, and an initial temperature of 2900 K is assumed [133]. A simulation is also performed where a mass- and energy-equivalent volume of perfect gas air is used for the balloon gas. The results are shown in Figure 10.1; note Cullis' results [101] were only reported to a distance of 8 m/kg$^{1/3}$. Grid-independence is virtually attained with 40 cells through the charge. The impulse is normalized by positive phase duration, and CONWEP data was not obtainable directly but extracted from Cullis' paper [101]. Error bars in Cullis' data series are used to cover their range of results and for the impulse plot the CONWEP result lies within this range.

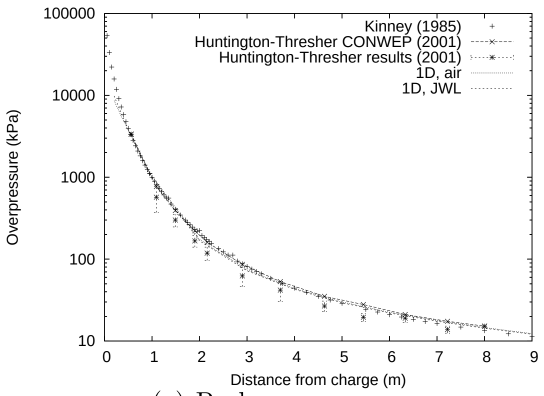

(a) Peak overpressure

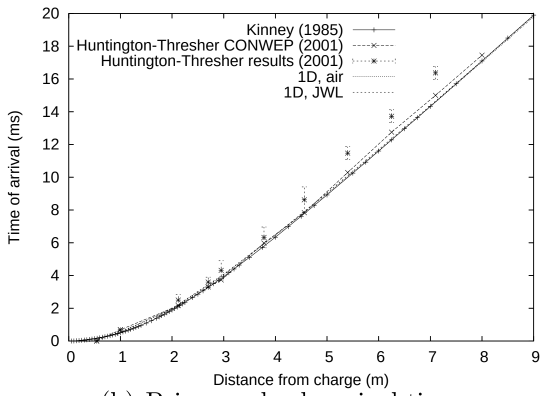

(b) Primary shock arrival time

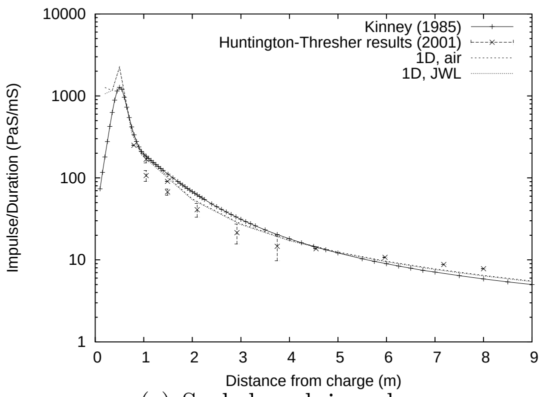

(c) Scaled peak impulse

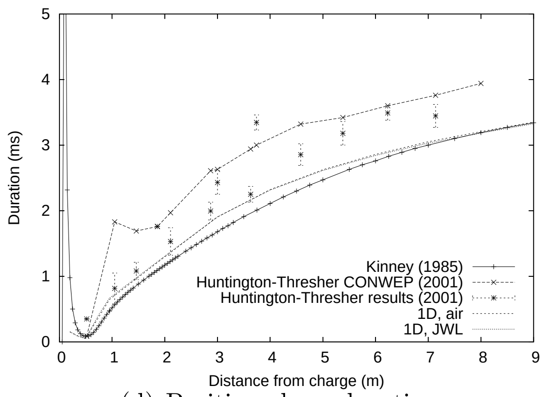

(d) Positive phase duration

Figure 10.1: One-dimensional TNT blast parameters

In general the results agree well with existing data, especially in pressure and impulse (often the most important quantities), and differences between the JWL and air solutions are very small. These results indicate that a perfect gas bursting sphere approach can produce good correlation with experimental data of important blast parameters from as close as 0.5 m/kg$^{1/3}$, which has also been observed by Rose [171]. The one-dimensional solution can thus be used to compute the error from multi-dimensional simulations (see Section 10.3).

Cullis and Huntington-Thresher mention that the finite gauge rise time may have caused their arrival time to be overpredicted slightly, as appears evident in Figure 10.1(b). The greatest discrepancies occur with the positive phase duration (Figure 10.1(d)), although the current results follow Kinney's line fairly closely. Positive phase duration appears to be a difficult quantity to measure, and has been known to vary by more than one order of magnitude in experimental results [146]. Poor agreement in computed results and CONWEP values was also observed by Rose [171]. Cullis suggests that CONWEP might overestimate this value due to afterburning effects [101].

10.2 Axisymmetric TNT Blast

Simulations are performed in two-dimensional axisymmetric geometry and with adaptive quadtree meshes with typically 4 working levels. To investigate convergence, five different meshes are used with minimum cell sizes of 0.1875, 9.375 $\times 10^{-2}$, 4.688 $\times 10^{-2}$, 2.344 $\times 10^{-2}$ and 1.172 $\times 10^{-2}$ m (successive grid doubling). The coarser of these grids can only represent the charge in one cell, and thus not all solutions may be in the asymptotic range of convergence (this is demonstrated below). The finest cell size is chosen to correspond roughly with a common fine cell size used by Rose *et al* [171, 175] in their three-dimensional simulations of blast interaction with buildings.

An example of an initial coarse Cartesian cell charge representation is shown in Figure 10.2. The curved line represents the spherical charge; cells intersected by or within that volume are initiated to the charge or balloon conditions (again, diagonal lines are an artifact of the grid visualizer Paraview [90]). A plane of symmetry at $x = 0$ is assumed. To save costs, smaller computational domains are used for finer grids. Domain sizes vary from 6 to 20 m; experience has shown these distances are sufficient for a blast wave profile to develop. Sensor locations are placed on the radial axis at around 0.2 m increments close to the charge, and around 1 m increments farther away.

Ideal gas air is used for the balloon gas. The density of this gas depends on the volume of the cells representing the charge and is adjusted for each grid (using the method in Section 4.6.1) such that the charge has a mass of 1 kg. The balloon gas pressure is adjusted to give the correct blast energy equivalent to a 1 kg TNT charge. An adaptive flux solver (Section 4.4) is used with EFM at shocks and AUSMDV elsewhere. The density-based adaptation indicator (Equation 3.4) is used and typical values for the refinement, coarsening and noise filter thresholds are 0.3, 0.02 and 0.008 respectively. However these thresholds are adjusted slightly for each mesh as the indicators perform differently for different mesh resolutions, and are chosen to give a good but not excessive degree of refinement in the region leading up to the primary shock.

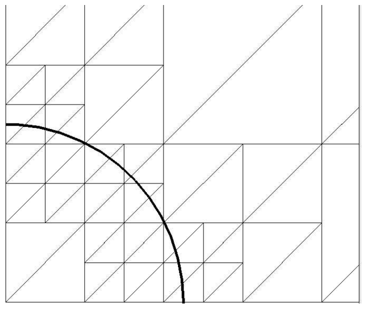

Figure 10.2: Initial grid for 2D axisymmetric TNT blast simulation

The calculated blast parameters are shown in Figure 10.3 and compared with the one-dimensional spherical result. The overpressure plot shows a trend of convergence toward the one-dimensional result as the cell size decreases, and coarser grids usually underpredict the overpressure. At distances less than about 1 m the differences between the solutions are not so consistent; this is probably a result of the near-field effect of the initial explosive shape, which has a significant effect on the blast waveform at this range [40, 211]. The scaled impulse plot also shows reasonable agreement between one-dimensional and axisymmetric solutions with finer grids generally giving a better result. However it is shown later that convergence is not so easy to demonstrate for (non-scaled) impulse. Arrival time is quite grid-independent, and positive phase duration seems to be the most grid-dependent parameter (but its convergence can still be observed).

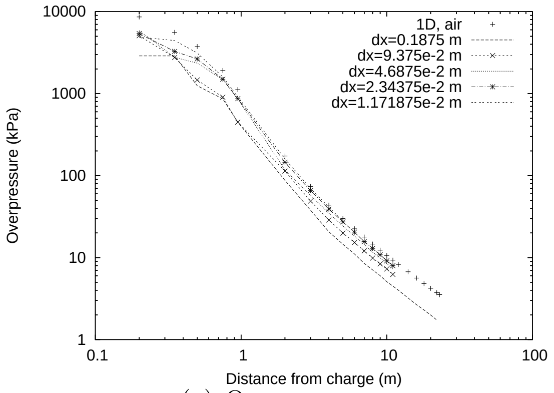

(a) Overpressure

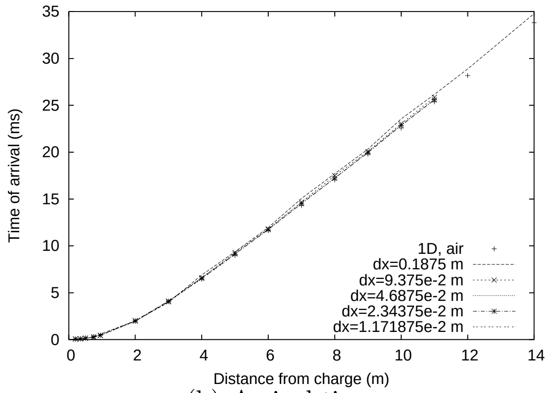

(b) Arrival time

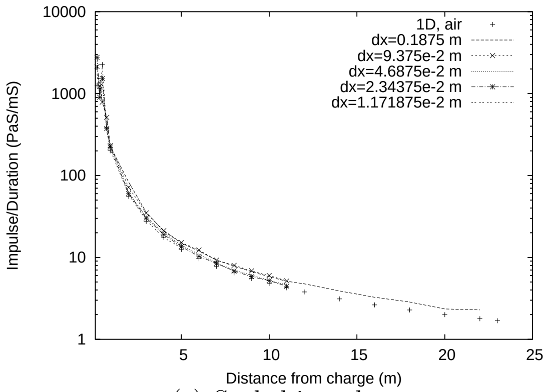

(c) Scaled impulse

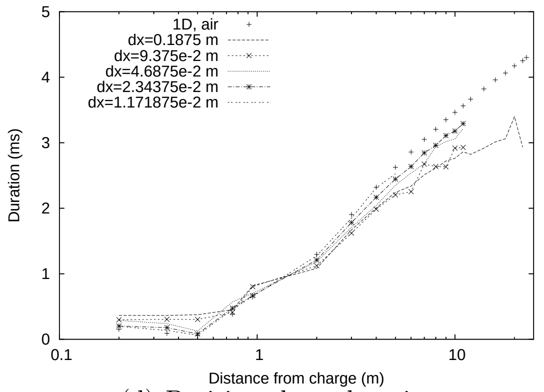

(d) Positive phase duration

Figure 10.3: Two-dimensional TNT blast parameters

An example pressure history at 11 m radial distance showing convergence of the axisymmetric solutions is shown in Figure 10.4. The differences between sucessive peaks become increasingly smaller and the positive phase waveform takes better shape. There is a noticeable finite rise time to peak overpressure on coarser grids because of the poorer shock resolution. The secondary shock is very difficult to resolve even on the fine grids, but this feature is not so important.

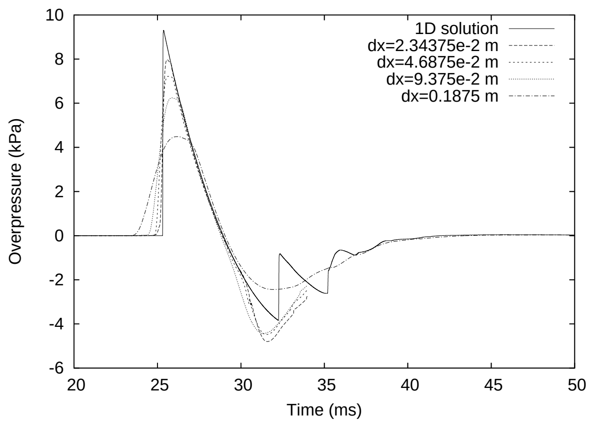

Figure 10.4: Example pressure history from TNT blast

10.3 Error Quantification in the Axisymmetric Solutions

This study takes the results of Section 10.2 and quantifies the differences between the axisymmetric result and the virtually grid-independent one-dimensional spherical result (Section 10.1) for the different axisymmetric grids[1]. As mentioned above, these errors result from grid coarseness and the discretization of the spherical charge volume into a 'staircased' Cartesian representation.

Only the peak overpressure and peak impulse parameters (versus distance) will be considered as these are the most important quantities from an engineering perspective. Pressure sensors are also placed along both radial and diagonal (parallel to $\widehat{\mathbf{i}}+\widehat{\mathbf{j}}$) directions. Diagonal sensors might be expected to yield least accurate results and suffer most from numerical diffusion as wave propagation is most misaligned to the mesh along the diagonal.

It is hoped that this study will provide both a guide to the magnitude of the errors at a given scaled distance and an assessment of the quality of error estimates computed from grid refinement studies, which are based on Richardson extrapolation (Equations 6.2 and 6.3). As a guide to the quality of an error estimate, it will be useful to produce statements like 'the estimated error has a $x\%$ chance of being too large/small, and (i) it will be too large/small by no more than value y 90% of the time, (ii) it will be too large/small by an average of $z\%$'. This study might then also be applicable for more complicated blast problems where fine grid resolution is too costly to attain. A study of the errors in the near-field may also help determine the scaled range below which the balloon gas charge representation (and estimated error) is unsuitable.

[1]This section is taken from Reference [206] and is a more condensed version of that paper.

10.3.1 Actual Errors

At every sensor point, the relative error in blast parameters is computed as $(f_e - f)/f_e$ where f_e is the 'exact' solution (the one-dimensional result) and f the axisymmetric solution. These errors are plotted in Figure 10.5 along both sensor lines (radial and diagonal). A discussion of the errors is given below.

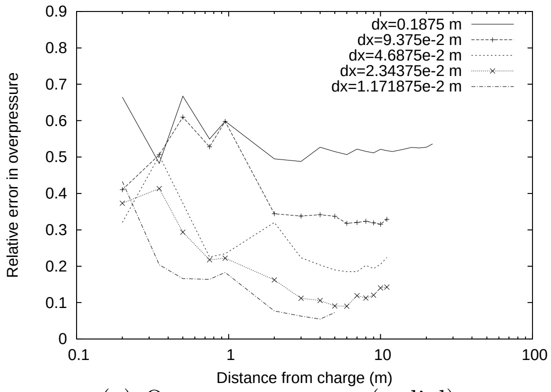

(a) Overpressure error (radial)

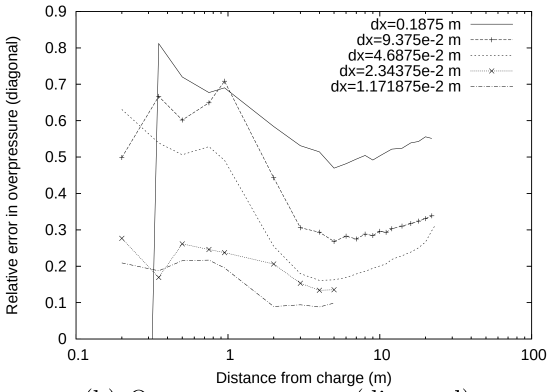

(b) Overpressure error (diagonal)

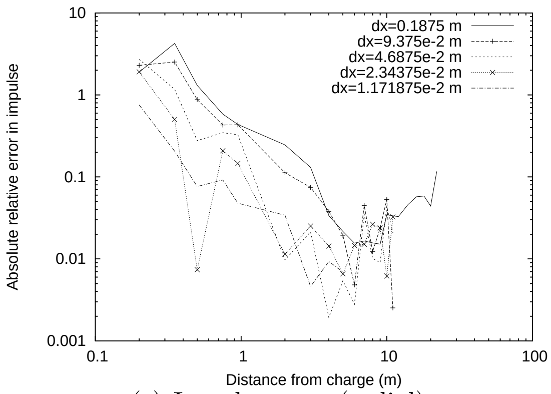

(c) Impulse error (radial)

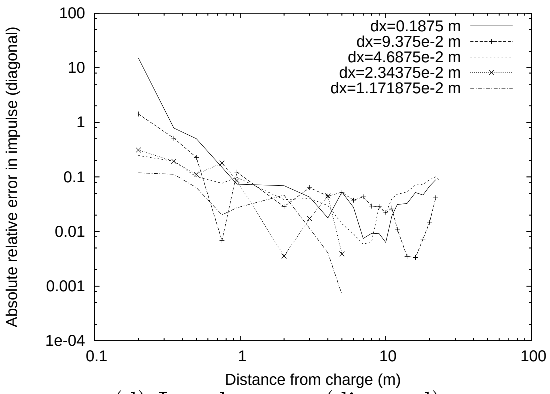

(d) Impulse error (diagonal)

Figure 10.5: Actual axisymmetric TNT parameter relative errors vs distance

Overpressure

It is clear from the graph of overpressure error along the radial axis (Figure 10.5(a)) that after about 1 m the solutions are converging. Coarser grids always tend to produce lower overpressures because of poorer shock resolution. Errors prior to 1 m are very large and do not behave so consistently because of the still-significant effect of the initial charge shape on the developing waveform which is forming into a more radially symmetric pattern. This suggests for this range of cell sizes a 'cut-off' distance of 1-2 m at which the balloon gas approach is appropriate when estimating error based on grid refinement studies. The curves are not always smooth, and increase slightly for larger distances probably because of numerical diffusion.

The errors along the diagonal direction (Figure 10.5(b)) are quite similar to those along the radial direction. Errors also do not behave consistently before about 1 m, and have steeper increase with distance after 1 m as numerical diffusion is more severe along this direction. Although the solutions are converging at these distances, the differences between errors for each grid are not always consistent, which will affect the Richardson extrapolation-based error estimator.

It is likely that this is at least partly due to the different adaptation indicators used. Although convergence to the one-dimensional waveform is still generally exhibited (Figure 10.4), different indicators are used for different grids, and these were adjusted (by trial and error) to be appropriate for that grid. If used on another grid it might result in excessive or inadequate refinement. Although the grid near the primary shock is usually refined, the region leading up to it (i.e. positive phase) does not always have the same degree of refinement, which ultimately has an effect on the solution.

Ideally in performing grid refinement studies the grid should be uniformly refined, or at least the same adaptation indicators used. But this can be computationally expensive for many multi-dimensional blast problems. This study focusses on the quality of the error estimation procedure in spite of this departure from ideality, and thus might be more relevant for practical purposes. It appears that a cell size of smaller than the finest cell (length 0.0117 m) is required to keep errors less than 10%.

Impulse

Convergent behaviour is difficult to observe with impulse (Figures 10.5(c) and 10.5(d)), and the curves are much less smooth than the overpressure error curves. The absolute value of the errors are taken because they are sometimes negative and a logarithmic scale is used for the ordinate to better show the errors. The errors are quite high within 1 m of the charge because of the effect of the initial charge shape, but within that range it is generally the case that finer grids do give lower errors.

It appears that the selected range of grid sizes is not within the range of convergence, but it is still interesting to see how well the Richardon extrapolation error estimators work. Impulse might be a more difficult quantity to converge (perhaps requiring very costly finer grids) as the area under the finite rise time to the peak pressure (as shown in Figure 10.4) may offset the loss in area resulting from a lower peak in coarser meshes. Despite the lack of convergent behaviour at larger distances, all errors for the different grids are around (or substantially less than) 10%, which is a much lower value than coarser-grid overpressure errors. This is an encouraging result as impulse is often the most important engineering quantity.

10.3.2 Estimated Errors

The estimated errors for overpressure and impulse for each grid are computed based on the GCI (Equation 6.3 p.g. 6) and compared with the actual error for every grid resolution and at every sensor point. This is done with each graph in Figure 10.5. Important summary statistics for each graph are the maximum over- and underestimation (the maximum values of how much larger/smaller the GCI is relative to the actual error), average values of over- and underestimation, 90th over- and under-estimation percentile (the value below which 90% of the over- and underestimation values fall) and fraction (out of all sensors) which overestimate. Overestimations are preferred due to conservatism in the design process.

The GCI error can be signed in the case of overpressure (i.e. $3E$ from Equation 6.3) as it is always underestimated but given the erratic impulse error behaviour (Figures 10.5(c) and 10.5(d)) should be taken as an absolute value for this quantity (i.e. $3|E|$, the standard definition of GCI). The assumed refinement factor $r = 2$, and $p = 1$ for overpressure (the scheme reverts to nominally first-order at shocks) and $p = 2$ for impulse errors (the flow is nominally second-order in the smooth positive phase). However only those sensors after 2 m from the charge are used, since it is found that this is the range where the error estimates start to be more consistently conservative.

The error statistics are shown in Tables 10.1 and 10.2. These tables also display the statistics for the $p = 1.5$ case, as it is proposed that this rounded figure may help the overpressure and impulse GCI to be slightly less and more conservative respectively (whilst still attaining a good fraction of overestimations). These tables will hopefully be a reasonable guide to the magnitude and probability of over- and underestimations that occur when estimating error from grid refinement (due to grid coarseness and the departure of the discretized charge from the ideal spherical shape).

Overpressure error summary

The overpressure error summary statistics are shown in Table 10.1 and are for the signed error. With $p = 1$ the fraction of overestimations is around 90%, but the average overestimation value is 30-40%, which might be excessively conservative. Taking $p = 1.5$ reduces the average overestimation (and its 90th percentile) by a factor of 2-4, whilst keeping average underestimation about the same. The overestimation fraction is not as high, especially along the diagonal direction at 60%, but this might still be preferred in lieu of the smaller overestimation magnitude. Because of the low number of underestimations, the 90th underestimation percentile is computed to be the same value as the maximum underestimation value.

Table 10.1: Overpressure error summary statistics

	Radial	Radial	Diagonal	Diagonal
	($p = 1$)	($p = 1.5$)	($p = 1$)	($p = 1.5$)
Maximum overestimation	0.587455	0.178413	0.676975	0.226954
Maximum underestimation	0.214859	0.262645	0.122117	0.201611
Average overestimation	0.303943	0.0798927	0.376296	0.152875
Average underestimation	0.114163	0.0802441	0.0480577	0.0665265
90th overestimation percentile	0.527328	0.147001	0.647733	0.220307
90th underestimation percentile	0.214859	0.262645	0.122117	0.122851
Fraction of overestimations	0.941176	0.882353	0.85	0.6

Table 10.2: Impulse error summary statistics

	Radial	Radial	Diagonal	Diagonal
	($p = 2$)	($p = 1.5$)	($p = 2$)	($p = 1.5$)
Maximum overestimation	0.092165	0.157443	0.0452596	0.0767958
Maximum underestimation	0.0338829	0.031263	0.0517206	0.0513935
Average overestimation	0.0246888	0.0427211	0.0215482	0.0433587
Average underestimation	0.0132443	0.0134597	0.021764	0.0202336
90th overestimation percentile	0.0573218	0.100296	0.0434746	0.0745365
90th underestimation percentile	0.0224399	0.031263	0.0439641	0.0513935
Fraction of overestimations	0.588235	0.764706	0.65	0.8

Impulse error summary

The impulse error summary statistics are shown in Table 10.2 and are for the absolute error. Over- and underestimation magnitudes are substantially smaller than for overpressure since impulse errors are lower. In some cases the error is reduced by nearly an order of magnitude from the equivalent overpressure result. If $p = 2$ the average overestimation is within 2.5%, and if $p = 1.5$ the average overestimation rises to within 4.5% (with similar underestimation values), but the fraction of overestimations also increases to close to 80% in both radial and diagonal directions.

10.3.3 Conclusions

Errors in blast parameters between the axisymmetric simulations and an equivalent one-dimensional result have been studied. The errors behave similarly along both radial and diagonal directions. Error estimates based on grid refinement studies have also been investigated. The absolute error should be taken for the impulse parameter because of difficulty in convergence of this quantity, but these errors are substantially lower than overpressure errors. Error estimation based on the GCI with a refinement factor of $r = 2$ and solution order of $p = 1.5$ seems to work reasonably well, and data on the quality of these estimations has been provided in terms of the probability and magnitude of error over- and underestimations. For this range of grid sizes, a near-field limit of around 2 m/kg$^{1/3}$ is chosen because of the unreliability of error estimates smaller than this distance. It remains to be seen if these results are also applicable for the much more expensive three-dimensional simulations.

10.4 Three-Dimensional TNT Blast

This problem will be finally simulated in three-dimensional geometry. It is performed only using one grid resolution as it is more computationally expensive than axisymmetric simulations, and the convergence results computed in Section 10.3 might applicable to this case too. The simulation has 4 mesh levels with the coarsest and finest grid sizes being 0.1875 and 2.344 $\times 10^2$ m respectively. 'Quarter-space' symmetry is used where the x, y and z planes all constitute symmetry planes. Figure 10.6 shows the solution some time after the initial burst; the left plane plots pressure contours, the right plane density contours and the bottom plane the grid with superimposed schlieren. There seems to be excessively dense refinement between the two shocks.

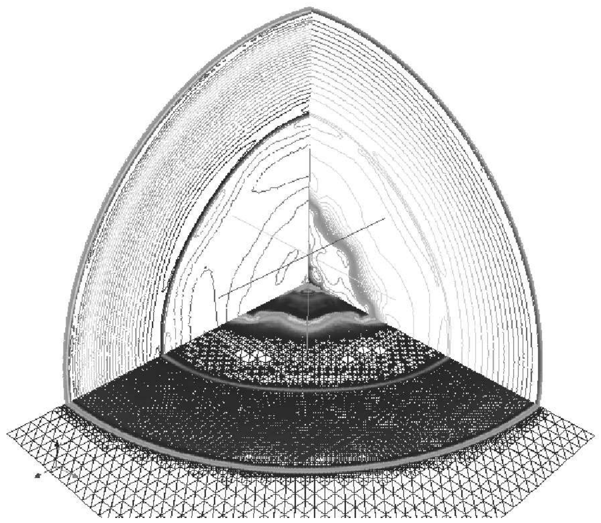

Figure 10.6: Contours for 3D TNT Blast simulation

The blast parameters are plotted in Figure 10.7. Results are plotted for traces along the vertical $[0, 0, 1]$ direction and the $[1, 1, 1]$ diagonal direction, and compared with the one-dimensional and axisymmetric solution (that used the same minimum cell size). Agreement with the equivalent axisymmetric solution is generally quite good; the variant trace readings often lie to either side of this result.

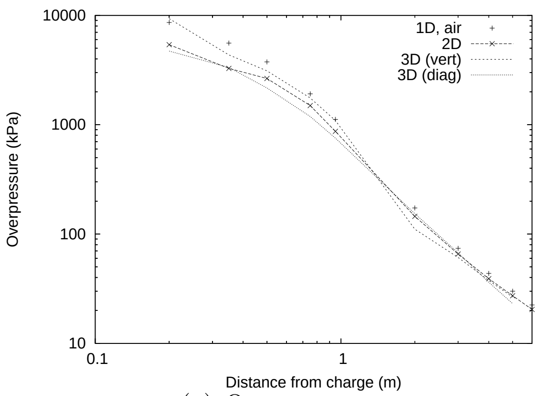

(a) Overpressure

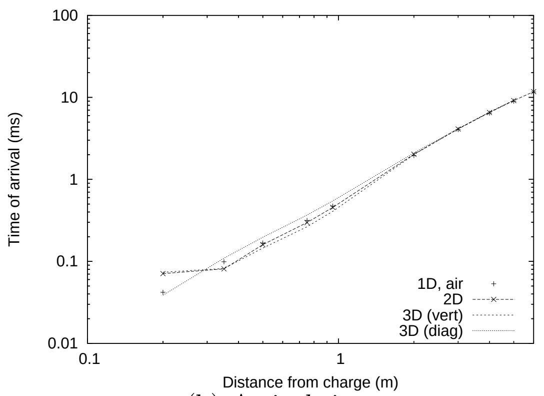

(b) Arrival time

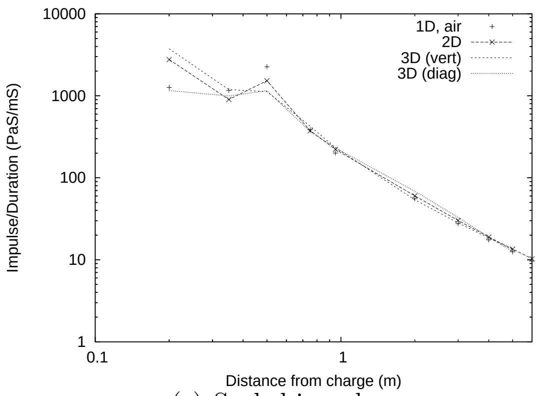

(c) Scaled impulse

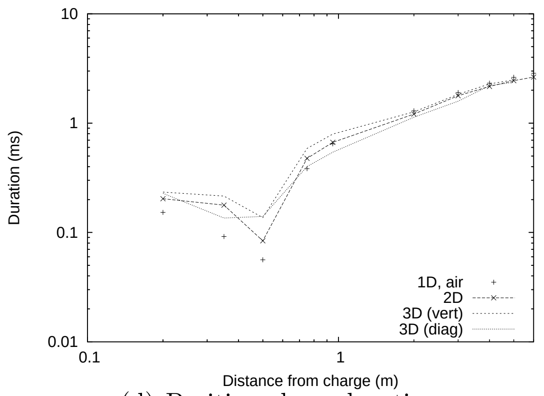

(d) Positive phase duration

Figure 10.7: Three-dimensional blast parameters for TNT blast

10.4.1 Parallel Performance of the Simulations

Like the test case in Section 7.3 the simulations were run on an SGI Altix 3700 to observe the parallel performance of the code for this problem. The three-dimensional simulation was performed on up to 8 processors. Measured speedups are shown in Figure 10.8. The three-dimensional solution displays overall better parallel performance than the axisymmetric solution, probably due to the Amdahl effect (Section 5.4) which states that parallel overhead decreases relative to the parallel code portion for larger problem sizes.

A table of performance statistics can be constructed similar to that in Table 7.4 in Section 7.3. Further parallel code profiling using the Intel compiler was not performed for these simulations. Performance statistics for the axisymmetric simulation are shown in Table 10.3 and are for the grid with minimum cell size 4.688 $\times 10^{-2}$ m. It is note-

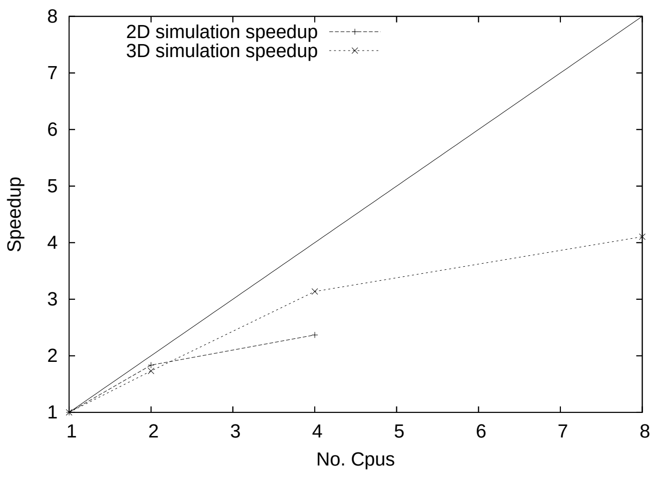

Figure 10.8: Parallel speedup for TNT blast simulations

Table 10.3: Parallel performance for axisymmetric TNT blast simulations

	1 processor	2 processors	4 processors
Single processor time (hrs)	1.988		
Max no. cells	4.2 $\times 10^4$		
'Effective' serial fraction		0.0896	0.2297
Extrapolated serial fraction	0.0195		
Overhead fraction		0.07	0.21
Estimated elapsed time (hrs)		1.153	0.9439
Measured elapsed time (hrs)		1.083	0.8394

worthy that the effective serial fractions computed from the Karp-Flatt metric [113] for all simulations are lower than those of Table 7.4, although there is a similar substantial increase in this value between 2 and 4 processors indicating significant overhead. The extrapolated serial fraction is quite low at 2%, but this may be an underestimate. However, relative differences between the columns of this table still indicates the large increase of overhead. The reasons for this high overhead are discussed in Section 5.5.3 and 7.3 and stem mainly from high communication cost on distributed-memory machines like the Altix.

The performance statistics for the three-dimensional simulation are shown in Table 10.4. It is obviously a much larger simulation with over 2 million cells. Unlike the axisymmetric simulation, parallelization of adaptation routines is performed (Section 7.2). Somewhat curiously the effective serial fraction does not increase uniformly with more processors. The reason for this behaviour might stem from the 4 processor simulation benefitting from increased computational resources (which is spread over

Table 10.4: Parallel performance for 3D TNT blast simulations

	1 processor	2 processors	4 processors	8 processors
Single processor time (hrs)	137.68			
Max no. cells	2.27 $\times 10^6$			
'Effective' serial fraction		0.155	0.0918	0.1356
Extrapolated serial fraction	0.0918			
Overhead fraction		0.0632*	0*	0.0438*
Estimated elapsed time (hrs)		83.86*	43.9*	34.3*
Measured elapsed time (hrs)		79.51	43.9	33.54

dual-processor nodes). Hence an extrapolation of the serial fraction cannot be performed, and the minimum effective fraction of 0.0918 is used. This represents an upper bound to the actual serial fraction, and is consistent with the axisymmetric result.

Because of this the overhead for the 4 processor job is by definition zero, and thus reported figures of overhead are relative to the 4 processor performance. The estimated elapsed time is thus equal with the actual elapsed time if the overhead is zero (henced the starred values). Relative increases in overhead are considerably smaller than the axisymmetric values in Table 10.3, which is due to the Amdahl effect and also perhaps the increased code parallelization.

The performance statistics show encouragingly that the code appears to be fairly well parallelized (less than 10% of operations are serial). Obviously, more work can still be done to increase performance efficiency. In terms of actual elapsed time the code can obtain results in an reasonable timeframe on 8 processors, although it would be advisable to do initial low resolution calculations if rapid hazard analysis is required.

Chapter 11

Validation - Blast Walls

Blast walls are a protective measure that reduce the severity of the blast environment behind the wall by reflecting back some of the incoming blast energy [161]. A typical blast wall configuration can be seen in Figure 11.1. The different factors which influence the loading on the structure include charge weight, height of burst, wall height, wall distance from charge, and distance of structures from the wall.

This problem has been the subject of past experimental and numerical studies [48, 49, 123, 144, 171], and despite the simplicity of the geometry, accurate prediction of airblast loads behind the wall is realizable only from three-dimensional numerical computations, due to the complex nature of the post-wall blast environment. To alleviate this lengthy computational cost, past research has focussed on investigating the predictive ability of a much cheaper axisymmetric simulation [123], and on the development of a fast neural network based tool constructed from a database of experiments [161]. However, in unique geometric arrangements, only full three-dimensional simulations (such as can be done by `OctVCE`) will be reliable.

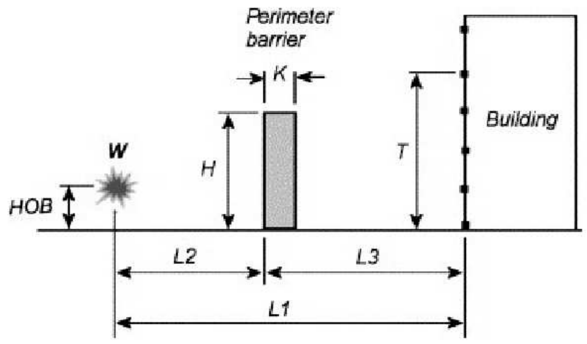

Figure 11.1: Blast wall configuration. Source [161]

As validation, `OctVCE` is used to simulate two different axisymmetric blast wall scenarios conducted by Chapman *et al* [48, 49] and Rice *et al* [123]. Both references used an axisymmetric code to model the blast environment, but also compared numerical with experimental results. The comparisons were favourable, indicating that despite the planar geometry of the experiment, good prediction of pressure histories with the axisymmetric code can still be obtained. These blast wall scenarios are –

1. Referring to Figure 11.1, in the scenario of Chapman *et al* [48, 49], the charge mass was the equivalent of 60 g of TNT, with a height of burst at 0.15 m, a distance to the structure $L1 = 1.05$ m and a distance to the wall $L2 = 0.6$ m. The wall height is 0.3 m and its thickness is 0.02 m. The only pressure transducer was located 0.3 m up the structure.

2. In the scenario of Rice *et al* [123], the charge mass was 0.513 g of PETN at a height of burst of 0.0134 m, a distance to the structure $L1 = 0.167$ m and a distance to the wall $L2 = 0.1$ m. The wall height was 0.0535 m, and its thickness is estimated to be about 0.01 m. Rice *et al* also performed a three-dimensional simulation, which yielded a similar solution to the axisymmetric result. Three pressure transducers were located at 0.04, 0.08 and 0.12 m up the structure.

Cell sizes were not specified in either of these references. In both cases, the computational domain stretches from the symmetry axis to the structure, as shown in Figure 11.2. This approach avoids the problem with axisymmetric obstructed corner cells (between the structure and the floor) as discussed in Appendix E.1, although corner cells exist at the junction of the blast barrier and the ground. A non-reflecting boundary condition is placed on the top boundary and its effectiveness will also be tested later. Standard air at atmospheric conditions is used for the ambient gas.

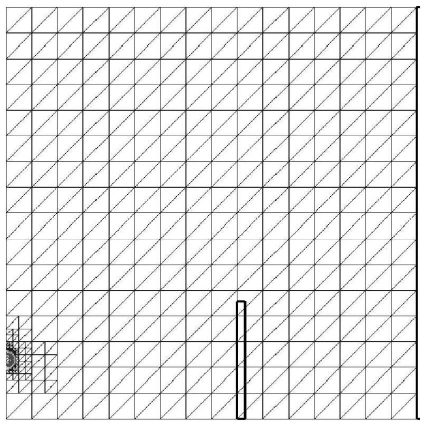
Figure 11.2: Initial grid for blast wall simulation

The JWL equation of state is used to simulate the explosion products. Explosive JWL parameters are taken from Reference [127]. However, given the balloon method of charge initialization (Sections 4.6 and 10.2), the charge balloon densities and pressures have to be modified somewhat to ensure correct blast energy and mass. For both scenarios, five working mesh levels (level 5 to level 9) are used, but a higher resolution simulation with level 10 cell sizes are also performed to observe grid dependence. Both simulations use the density-based adaptation indicator (Section 3.4) of 0.3, 0.1 for the refinement and coarsening thresholds respectively. In the first simulation, a noise filter threshold of 0.017 is used, and in the second simulation this value is 0.04. AUSMDV is used as the flux solver and 64 subcells are used.

11.1 Blast Wall Scenario 1

This section displays the solution to the blast wall problem of Chapman *et al* [48]. This test case was also performed by the author in Reference [202]. Density contours at various times are shown in Figure 11.3. Note at times some contours appear to pass through the blast barrier but this is due to the wall being so thin that no coarse cells are actually fully immersed in it.

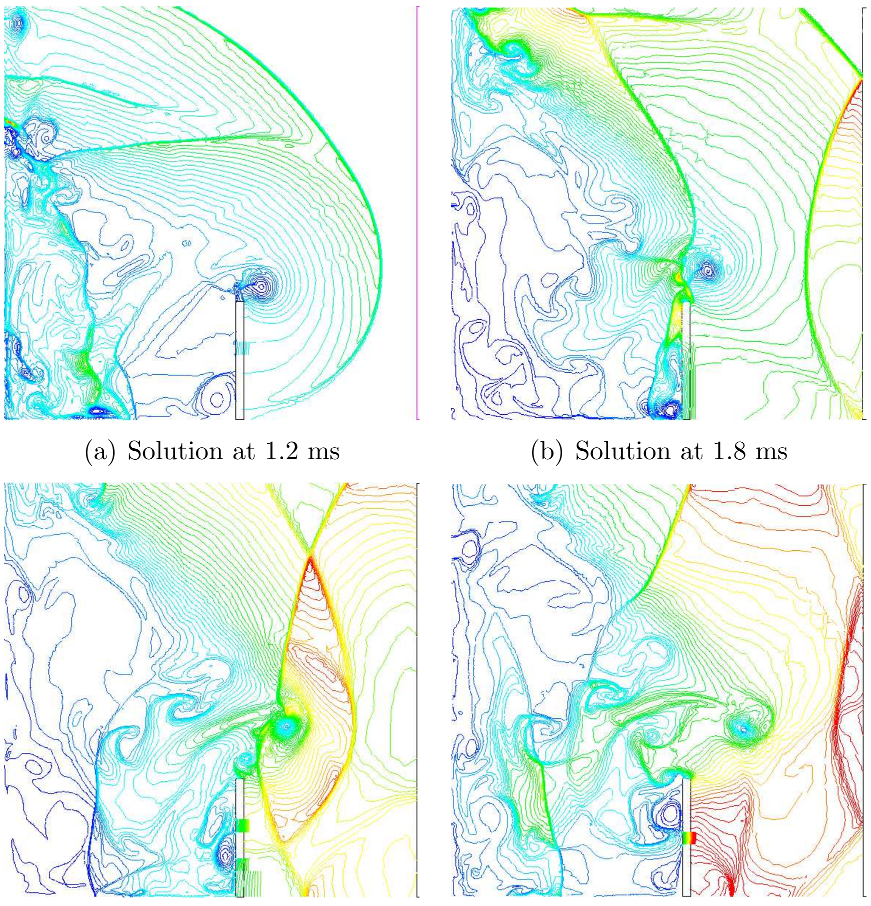
(a) Solution at 1.2 ms (b) Solution at 1.8 ms

(c) Solution at 2.4 ms (d) Solution at 3.0 ms

Figure 11.3: Solution to Chapman's [48] blast wall problem

To test the non-reflecting boundary condition, a simulation with the same minimum and maximum cell size is performed, but with the upper boundary extended. The solution on this extended boundary simulation is shown in Figure 11.4. There is very good agreement between the solutions in Figure 11.3 and 11.4.

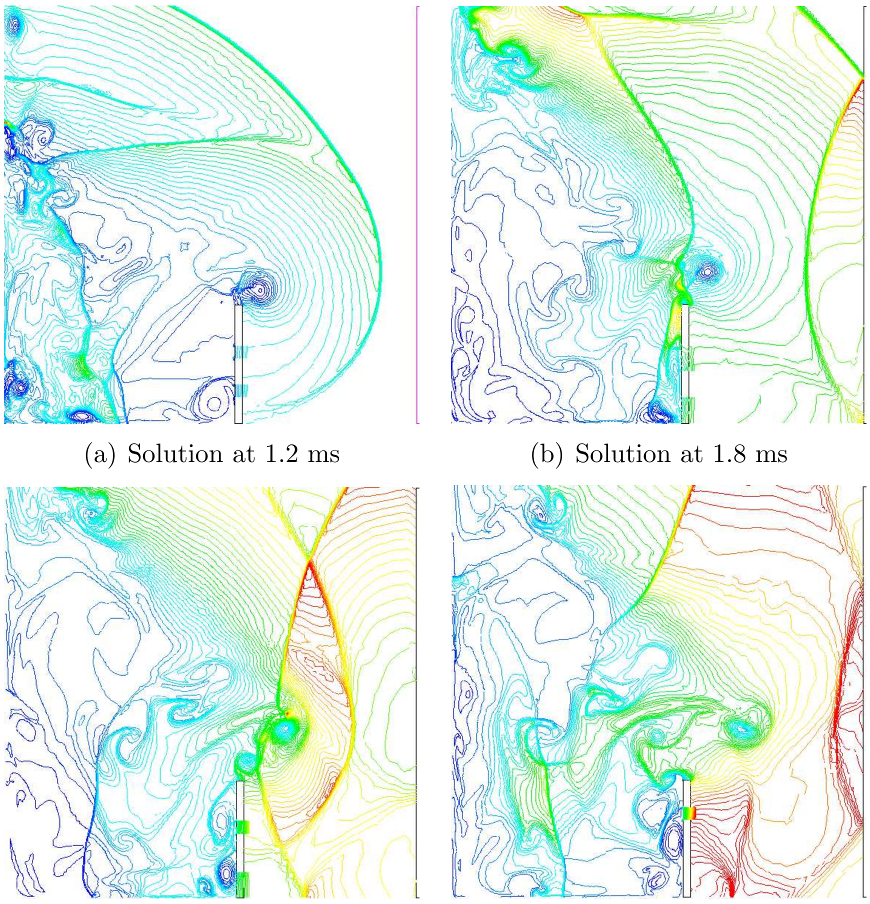

(a) Solution at 1.2 ms (b) Solution at 1.8 ms

(c) Solution at 2.4 ms (d) Solution at 3.0 ms

Figure 11.4: Solution to Chapman's [48] blast wall problem, longer domain

The pressure history is shown in Figure 11.5, and compared with Chapman's results [48]. There appears to be a discrepancy in primary wave arrival time, and it is too large to be accounted for by the detonation time of the charge if initiated from the centre. However peak pressures (especially for the finer resolution mesh) and positive phase behaviour agree well with past results. There is also a large reflection at around 2.8 ms not present in Chapman's result, but this is due to reflection from the symmetry axis which Chapman *et al* did not model.

It is not known why the discrepancy in arrival time is so large. Although Chapman *et al* [48] did not explicitly state the blast energy, there is sufficient agreement in peak overpressures and positive phase behaviour to suggest only a small discrepancy with their actual blast energy. Perhaps their results were somehow offset in time, but this was not specified. In any case, arrival time is not a particularly useful engineering quantity in blast wave modelling, so this problem is not very serious.

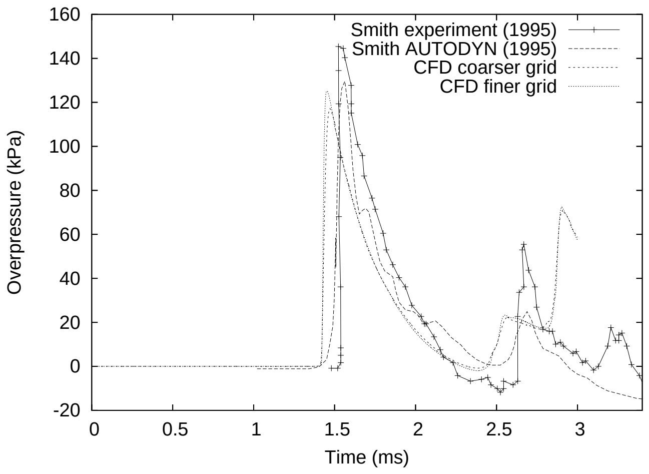

Figure 11.5: Pressure history for blast wall scenario 1

11.1.1 Performance of the Simulation

A uniform mesh simulation with all cells at the same size as the minimum cell size in the lower resolution adaptive mesh simulation was performed to see how significant the savings in solution time would be. Both were run on 1 processor. The uniform mesh simulation had 260830 cells with an elapsed time of 22.5 hours. The adaptive mesh simulation had a maximum of 55000 cells and took 4.9 hours. This means savings of a factor of 4.74 and 4.59 in storage and solution time respectively. With an increasing problem size in three-dimensional meshes, the savings would be expected to be even larger.

11.2 Blast Wall Scenario 2

This section displays the solution to the blast wall problem of Rice *et al* [123]. As Rice *et al* also performed a three-dimensional planar simulation, it also seems appropriate to perform one here. This simulation has four working mesh levels corresponding to cell sizes of 6.25×10^{-3} m to 7.8125×10^{-4} m. It is performed in 'quarter-space' i.e. assuming two symmetry planes, the 'in-plane' symmetry plane corresponding to the structure centreline, and a 'back-plane' symmetry condition at the charge centre parallel with the barrier. Reflections from the back-plane symmetry condition would arrive too late to interfere with the presssure histories in the positive phase.

Density contours at 146 μs are shown in Figure 11.6 and compared with the results of Rice *et al.* Although there is generally good agreement in major flow features, there are still noticeable differences, especially near the symmetry axis. Rice's simulations use a much finer resolution, so current results do not resolve certain features as well. The diffracted shock behind the barrier is so weak that the adaptation criteria fail to refine it. In the axisymmetric solution, apparent numerical jetting along the axis is seen, but it is interesting to note that the shadowgraph results also show that detonation products above the charge have apparently been ejected ahead of the primary blast wave.

Density contours at 246 μs are shown in Figure 11.7. There are some noticeable differences, especially between the axisymmetric solutions. Unlike Rice's results the current solutions seem to be at a more advanced stage; they show the reflected shock from the structure already interacting with the vortex slip layer. Also, the reflections behind the blast barrier are so weak no grid adaptation is present there and thus features there are not well-resolved.

The apparent time-wise difference in solutions is also reflected in the pressure histories (Figure 11.8). Apart from this discrepancy, agreement in peak overpressure and positive phase wave behaviour with the axisymmetric solution is good, particularly for gauges 2 and 3. The three-dimensional result, because of the coarser grids and planar symmetry, has a noticeably lower peak pressure, and a delayed reflection in gauge 2. Some grid-dependence in the axisymmetric solutions can still be seen. The difficulty of obtaining mesh convergent solutions in three dimensions to this blast wall problem is noted in [171].

The discrepancy in arrival time, like in Section 11.1, is puzzling. There may again be a time offset in Rice's results. Perhaps the axisymmetric corner cell degeneracy encountered at the barrier (Appendix E.1) may affect the solution and arrival time, so it is worthwhile to perform two additional simulations – (a) one where the barrier dimensions are adjusted slightly to align exactly with the mesh lines (avoiding the obstructed corner cell degeneracy), and (b) one without the barrier. The arrival times at gauges 1 and 2 are affected by the presence of the barrier, but there is a direct 'line-of-sight' from the charge to gauge 3, so the arrival time at that sensor should be independent of the barrier's presence. This result is confirmed in Figure 11.8(d) which shows the arrival times of the actual barrier, grid-aligned barrier and no barrier cases to be nearly identical. Thus, it is likely that there is another explanation of the arrival time discrepancy – probably a misreporting of one or more of the modelling parameters.

11.2.1 Performance of the Simulations

The three-dimensional solution had a maximum of around 1.4 million cells with an elapsed time of 67.4 hours running on 4 processors. The finer resolution two-dimensional solution had a maximum of 79000 cells, running for 11.95 hours on 2 processors. Clearly, significant savings in computation time can be made if the problem can be solved in

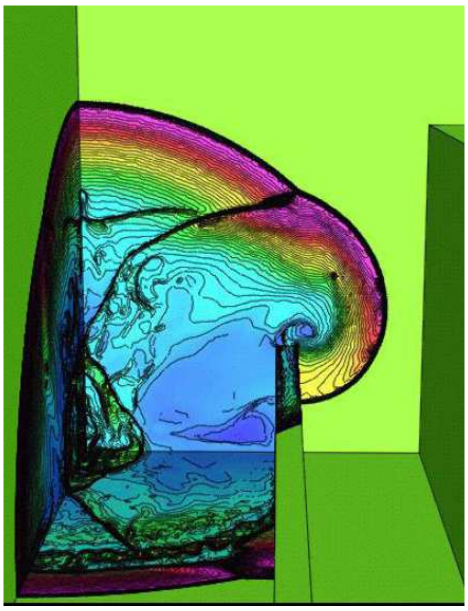
(a) Rice 3D (from [123])

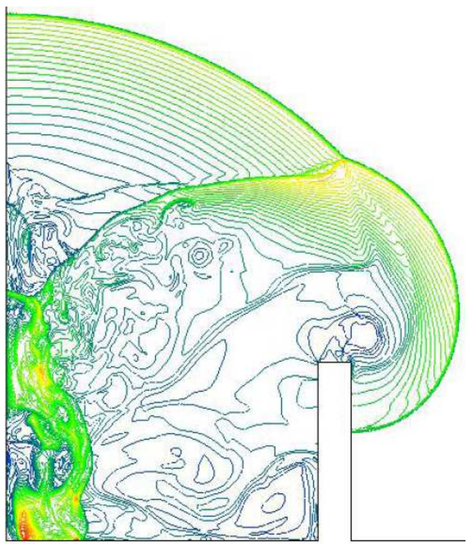
(b) Rice 2D (from [123])

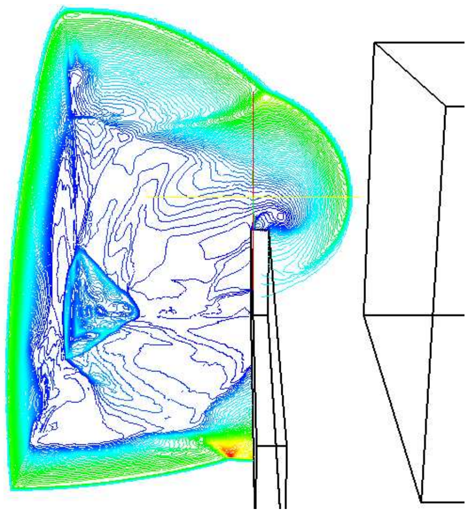
(c) 3D contours

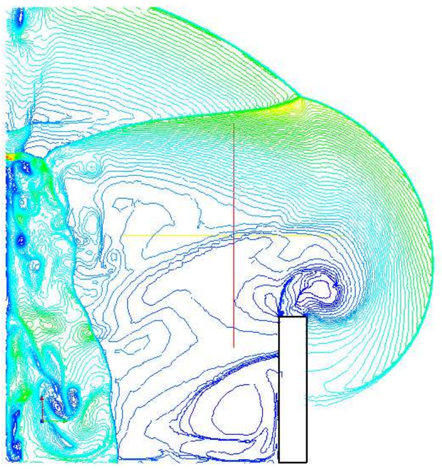
(d) 2D contours

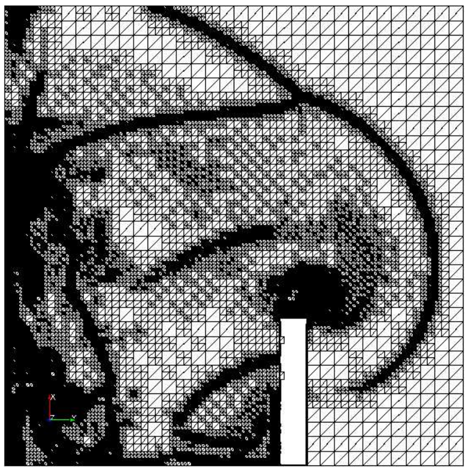
(e) 2D grid

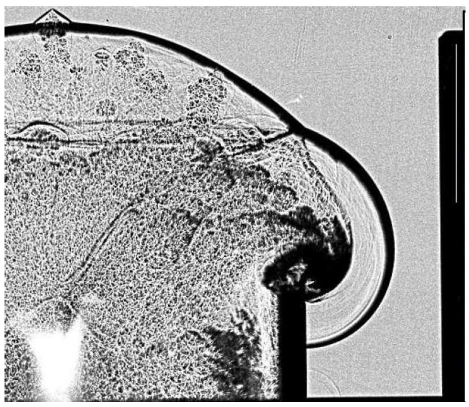
(f) Shadowgraph (from [123])

Figure 11.6: Solution to Rice's [123] blast wall problem at 146 μs

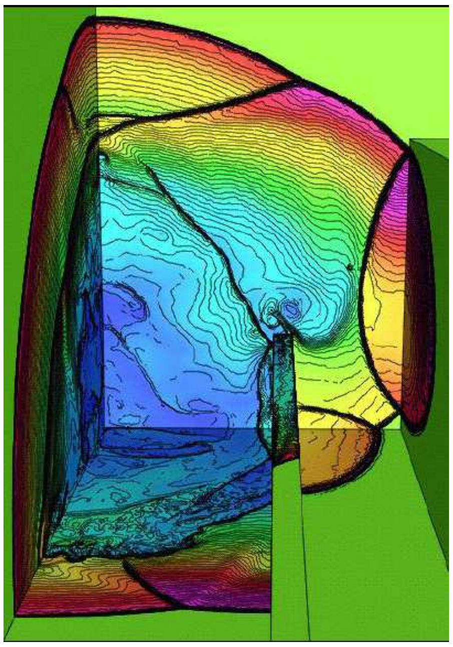
(a) Rice 3D (from [123])

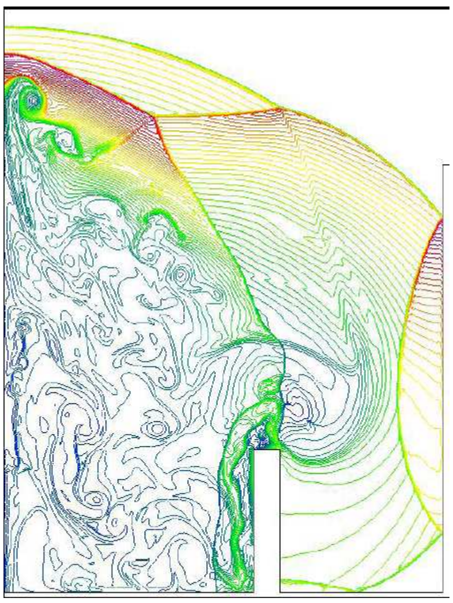
(b) Rice 2D (from [123])

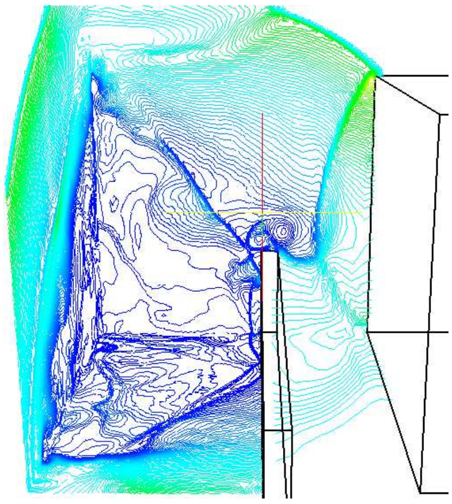
(c) 3D contours

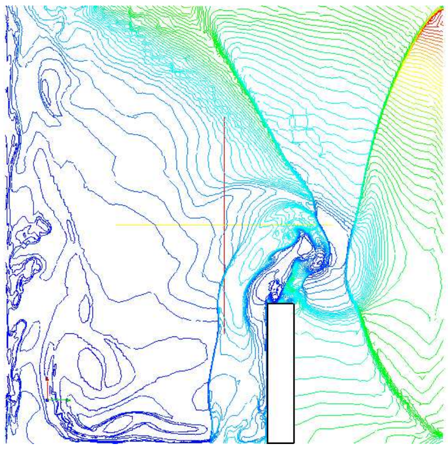
(d) 2D contours

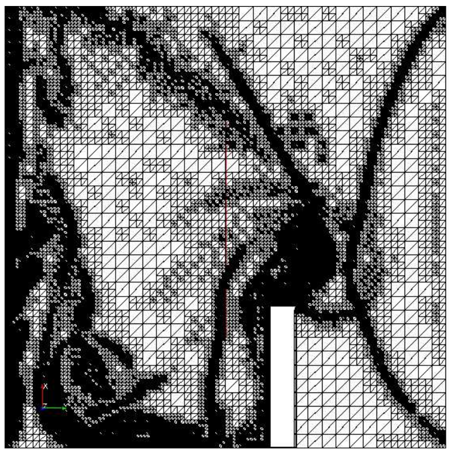
(e) 2D grid

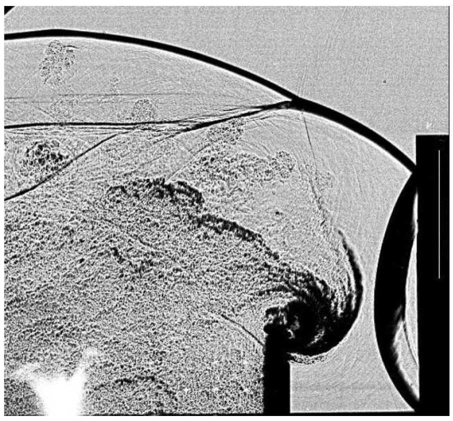
(f) Shadowgraph (from [123])

Figure 11.7: Solution to Rice's [123] blast wall problem at 246 μs

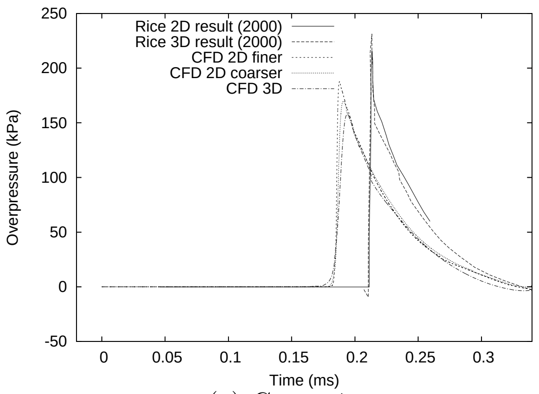

(a) Gauge 1

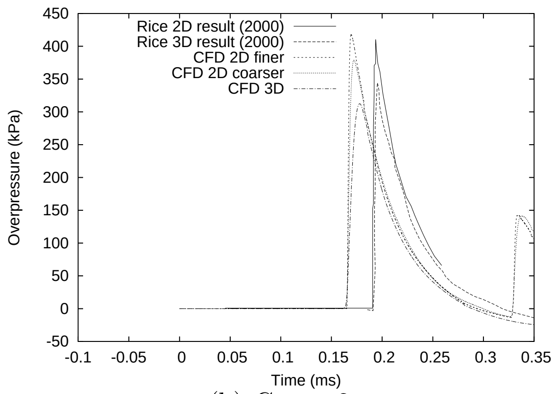

(b) Gauge 2

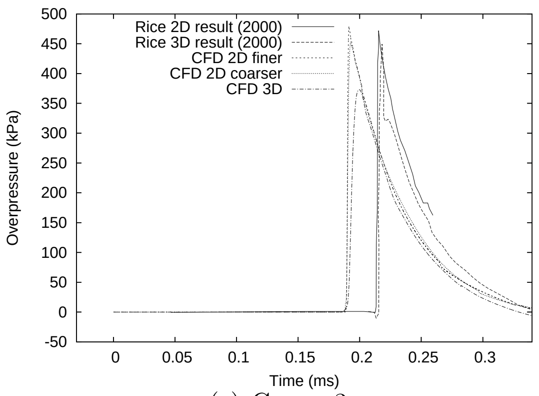

(c) Gauge 3

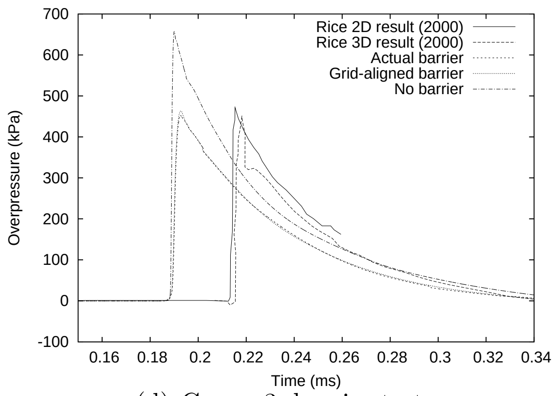

(d) Gauge 3, barrier test

Figure 11.8: Pressure histories for blast wall scenario 2

axisymmetric geometry.

11.3 Blast Wave Clearing Simulation

As further validation, the blast wave clearing simulation from Rose [171, 176] is performed. This is a fully three-dimensional problem, and strictly not a blast wall simulation as there is only one structure in the blast environment. Details of the problem geometry are shown in Figure 11.9 and taken from [176]. The charge is equivalent in energy to 27.26 g of TNT, detonated at a height of 0.1 m and 0.15 m from the structure. The charge energy density is 4.52×10^6 J/kg, and in the simulation is assumed to be composed of high density air. In Rose's simulation, the charge is initially simulated in a one-dimensional spherical calculation and remapped to two and three dimensions before the wave reaches the structure. A uniform mesh cell size of 1 cm was used, with a numerical domain of $2.5 \times 0.5 \times 0.4$ m.

In the simulations here, an adaptive mesh is used with four working levels corresponding to cell sizes of 0.0172 to 0.1375 m. This mesh is so coarse it could only represent the initial charge with 3 cells. Another simulation is also performed with an additional refinement level (cell size of 8.59×10^{-3} m) to observe grid dependence and similarity with Rose's result due to closeness of the cell sizes. Like Section 11.2 quarter-space symmetry is used. A combined adaptation criterion is used with the density-based adaptation indicator (Equation 3.4) of 0.3, 0.1 and 0.025 for the refinement, coarsening and noise thresholds respectively, and 0.005 for the velocity difference indicator (Equation 3.3). An adaptive flux solver is used with EFM at shocks and AUSMDV elsewhere. The number of area and volume subcells is 32 and 16 respectively.

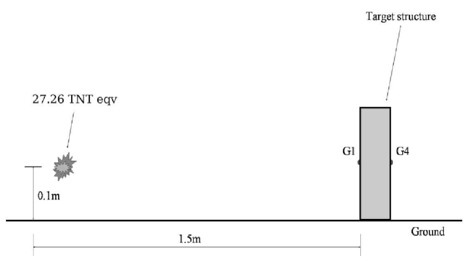

(a) Clearing geometry. Source [176]

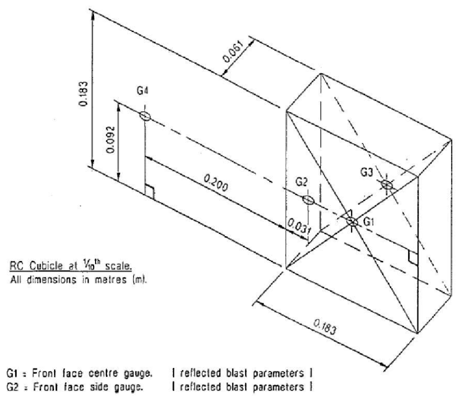
0.183
0.061
G4
0.092
0.200
G2
G3
G1
0.031
RC Cubicle at 1/10th scale.
All dimensions in metres (m).
0.183
G1 = Front face centre gauge. | reflected blast parameters |
G2 = Front face side gauge. | reflected blast parameters |

(b) Clearing structure. Source [176]

Figure 11.9: Blast wave clearing geometry and structure

The pressure histories at gauges 1 and 3 are shown in Figure 11.10. Agreement is generally good, especially for the higher resolution simulation. Note that the arrival times correspond well with Rose's results, strengthening the suspicion of a time offset in the simulations of Sections 11.1 and 11.2. Grid independence in solutions has not been fully achieved. Rose's numerical result is still probably more accurate due to its use of the remapping method and fine uniform mesh. Both Rose's and the present simulations do not seem to capture some peaks recorded in the experimental histories, which suggests that the experimental results might be in error at those locations.

11.3.1 Performance of the Simulations

Both simulations were performed on 4 processors on the SGI Altix. The lower resolution simulation ran for 2.27 hours (maximum of around 220000 cells), and the higher resolution simulation for 28.78 hours (maximum of around 1051000 cells). Memory requirements work out to be about 2.6 kB per cell (it is difficult to calculate the exact memory cost per cell as there are numerous data structures associated with an adaptive mesh that may not always be allocated).

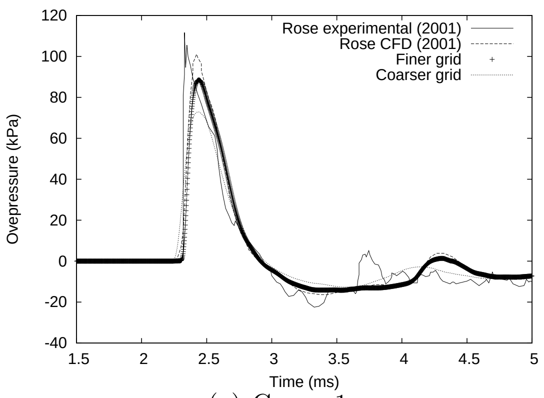

(a) Gauge 1

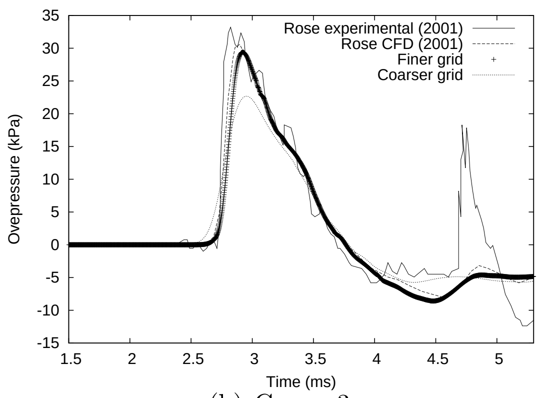

(b) Gauge 3

Figure 11.10: Blast wave clearing trace results

This is much larger compared to Rose's `ftt_air3d` code of around 0.25 kB per cell [175], but an adaptive grid necessitates larger storage, and this code also stores neighbour cell pointers and various list structures. This figure has also not fared well with the move to 64-bit computer architectures, as pointers are used frequently in the cell and vertex data structures (see Appendix K), so storage has doubled with respect to the older 32-bit computers. Certainly more work can be done to reduce costs e.g. by using the fully threaded tree structure [118] instead of storing neighbour connectivities. This will also boost performance.

Chapter 12

Validation - Explosion in Axisymmetric Container

This section attempts to reproduce the results of Lind *et al* [129] in simulating explosions in a containment facility. This facility is used for safe disposal of unwanted munitions via partially confined open-air burning and detonation. Lind's axisymmetric simulations also used VCE to represent the facility geometry, but they did not specify how the extra axisymmetric terms were accounted for (Appendix D). They also used a uniform, structured grid. Figure 12.1 shows a schematic of the containment facility. It consists of two spherical endcaps, a cylindrical section, and a neck and lip section on the top. The simulations here draw from two of Lind's simulations [129], (a) the R4 run (with a spherical charge) and (b) the R7 run (cylindrical charge). This validation exercise is thus also a useful test of the usefulness of the balloon analogue model (Section 4.6) in representing different initial charge shapes.

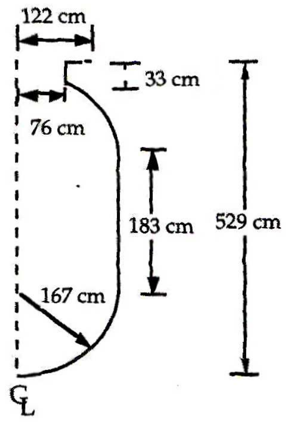

Figure 12.1: Containment facility schematic. Source [129]

In the R4 run the charge is composed of RDX explosive (assumed to have a yield of 2×10^6 J/kg) with a mass of about 22.68 kg (50 lb) and detonated at a height of 1.82 m above the bottom endcap. Like in Lind's simulation, perfect gas air is used for the charge with an assumed density of 1000 kg/m^3. In the R7 run the cylindrical charge is 1.22 m in length, 0.26 m in radius and has twice the masss at 45.36 kg, with a detonation height also at 1.82 m. The energetic yield is the same. Air at standard atmospheric conditions is assumed for the ambient gas.

Both adaptive-mesh simulations use four working mesh levels (level 5 to 8), but a higher resolution simulation (levels 5 to 9) is also performed to observe grid dependence. These correspond to cell sizes of 0.0137 m to 0.21875 m for the finer resolution simulation, which has a minimum cell size around the nominal fine-grid cell size in Lind's simulations (1 cm). The density-based adaptation indicator (Equation 3.4) is used with 0.3, 0.1 and 0.04 for the refinement, coarsening and noise filter thresholds respectively. An adaptive flux solver is implemented with EFM at shocks and AUSMDV elsewhere, and 64 subcells are used.

As the code cannot handle thin wall degeneracies, the facility's walls are set with a wall thickness larger than the maximum distance within a cell (the diagonal spanning a cell's corners). Thus at no point will a cell be split by the container walls and thus 'leak' some gas to the exterior. This is unlikely to affect the results much, since the focus is on loads on the internal walls of the facility. However, cells at the walls are kept at the highest permissible level both to increase resolution and reduce wall thickness. Non-reflecting boundary conditions are placed on domain boundaries.

12.1 Explosion in Containment Facility – R4 Run

Pressure contours for the R4 run at selected times are shown in Figure 12.2, and may be compared with Lind's snapshots. A transparent outline of the adapted mesh is overlaid on top of the contours. Note the complex shock interactions, reflections and focussing that occur in these plots. The top non-reflecting boundary condition also seems to work well in supressing reflections, as in Section 11.

The pressure as a function of time and distance along the wall for both grids is shown in Figure 12.3 and is qualitatively comparable to Lind's result (Figure 12.4) in terms of shock trajectories and locations of maxima. Note the presence of fairly noisy contours even prior to the arrival of the primary shock. These pressure variations stem from a perturbed flowfield because of the degeneracies associated with obstructed axisymmetric cells discussed in Appendix E.1. However, they are relatively very small, and do not seem to have a debilitating effect on the contours above the primary shock.

Nonetheless, there is a considerable difference in the maximum values between the grids, indicating grid independence has not yet been fully achieved. However Lind's runs also did not aim for grid-independent solutions as, somewhat curiously, their coarser resolution simulations were more conservative in terms of overpressure.

It is possible to give a more accurate estimate to the peak overpressure by using Richardson-extrapolation [163, 164] (Equation 6.1). In this case, with an assumed order

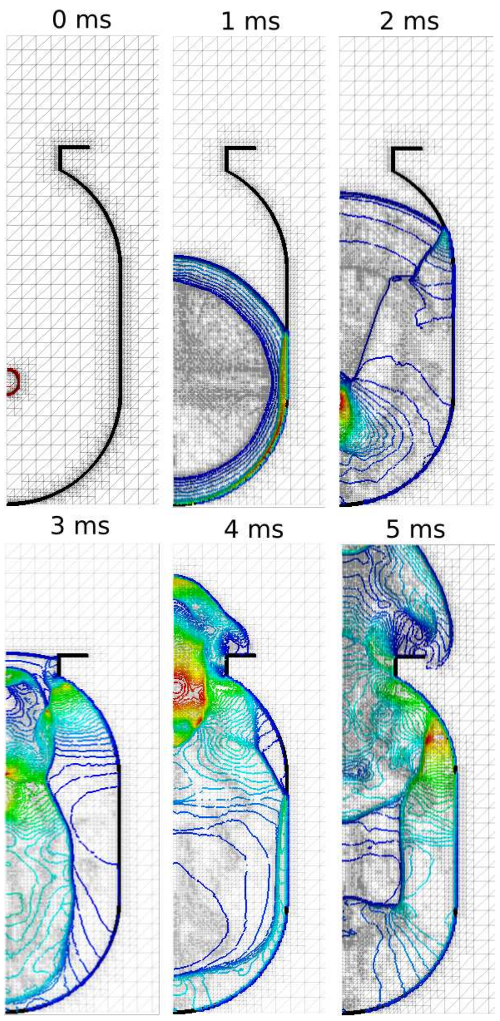

Figure 12.2: Pressure contours for R4 simulation of explosion in containment facility

of accuracy of 1 (as the scheme reverts to first-order at shocks) and a grid refinement factor of 2, the estimated true solution f_e is simply $f_e = 2f_1 - f_2$, where f_1 and f_2 are the finer and coarser resolution solutions respectively. Thus the estimated true peak overpressure for this simulation is 81.55 atm, which is quite close to Lind's fine-grid result of 83.3 atm. This is a good indication that the code can give reasonably accurate solutions in complex geometry even with all the attendant problems involved with axisymmetric VCE surface representation.

The local maximum near the bottom end of the lower endcap is due to shock focussing there. The pressure at focus points is a particularly grid-dependent result [54] as according to analytic theory the pressure is actually infinite at these locations [52]. Thus this pressure is an averaged value in the vicinity of focus, which in turn depends on grid resolution. However the fine grid result of 48.45 atm is fairly close to Lind's coarse grid result of 55.4 atm. Simulations for the R4 run were run on 2 processors in parallel; the lower resolution simulation had an elapsed time of 25 minutes (maximum

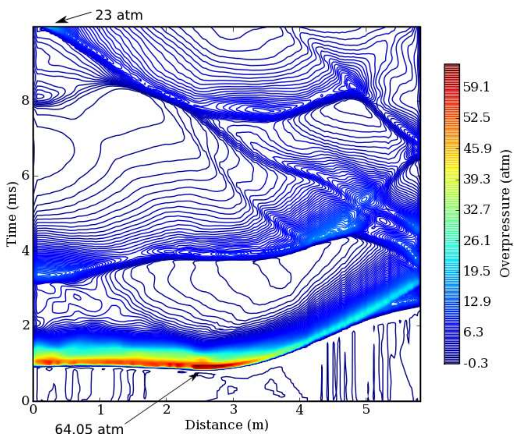

(a) Coarser resolution

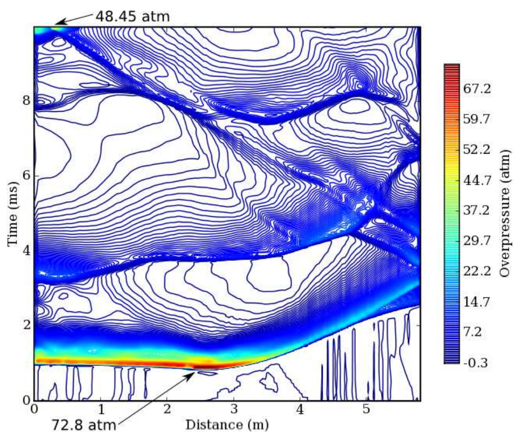

(b) Finer resolution

Figure 12.3: Pressure contours in the s-t plane for R4 simulation of explosion in containment facility

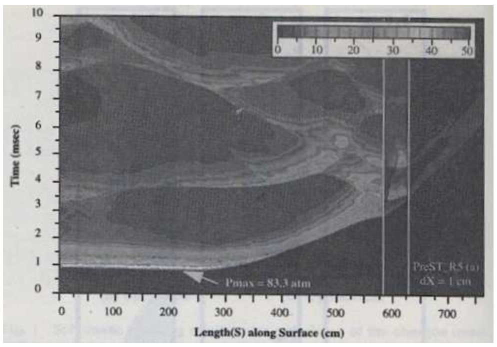

Figure 12.4: Lind's pressure contours in the s-t plane for the R4 simulation [129]

9700 cells), the higher resolution run had an elapsed time of 58 minutes (maximum of 21000 cells).

12.2 Explosion in Containment Facility – R7 Run

The pressure-time history along the wall for the cylindrical charge case is seen in Figure 12.5. These results are again qualitatively comparable to Lind's result (Figure 12.6), although slight differences can be observed. Nonetheless the location of peak overpressures is predicted well. The magnitude of the peak overpressures again varies significantly between the two resolution simulations. They all seem to occur at the bottom of the endcap due to shock focussing there, which is sensitive to the grid resolution, as mentioned in Section 12.1.

Via the same Richardson-extrapolation procedure the estimated actual peak overpressures for the peaks at around 2.5 ms and 9 ms are 188 atm and 489 atm respectively, which are quite close in value to Lind's result (186 atm and 496 atm respectively). The initial peak pressure at this focus point is the most problematic result; the extrapolated peak pressure there is only 162 atm, which is much lower than Lind's result of 340 atm. It is not known why this disagreement is so severe when compared to the other peaks. Apart from the issues at focus points, it is also possible that Lind's uniform grid may have better preserved the peak pressure than the adapted grid given its sensitivity to charge shape.

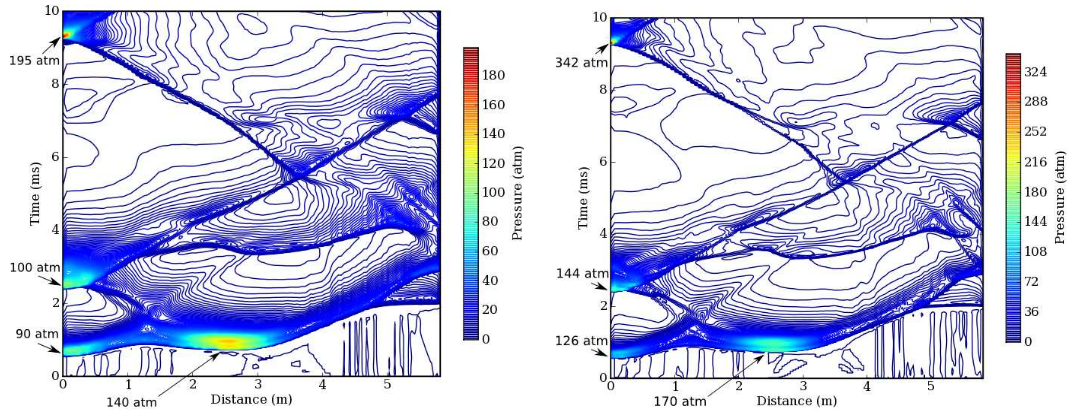

(a) Coarser resolution

(b) Finer resolution

Figure 12.5: Pressure contours in the s-t plane for R7 simulation of explosion in containment facility

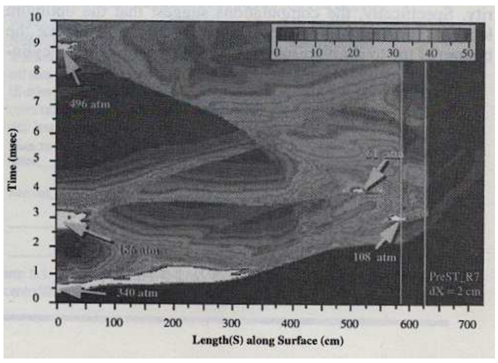

Figure 12.6: Lind's pressure contours in the s-t plane for the R7 simulation [129]

The simulations show that `OctVCE` seems able to give comparably accurate results to Lind's results [129]. It is possible, like with Lind [129], to feed the pressure-time data from Figures 12.3 and 12.5 into a simplified structural loading model to yield the wall tension. Simulations for the R7 run were run on 1 processor; the lower resolution simulation had an elapsed time of 86 minutes (maximum 10200 cells), the higher resolution run had an elapsed time of 285 minutes (maximum of 25000 cells). This is significantly longer than the R4 run (even accounting for the 1 processor), but it is likely due to a consistently larger number of cells over a longer time.

Chapter 13

Validation - Blast in Simple Street and Obstacle Geometries

This section tests the ability of OctVCE to model the three-dimensional blast environment in simple street and obstacle geometries, which are essentially arragements of two or more (typically grid-aligned) rectangular prismatic bodies. In the case of street geometries, the obstacles are arranged and scaled to represent buildings in realistic street layouts. Manually gridding the computational domain can still be tedious if the arrangement of objects is complicated. The resulting flow-field can be quite complex with multiple shock interactions and reflections, and formulation of simple semi-empirical rules is difficult [194], and can lead to drastic under- or over-predictions of pressures and impulses.

Blast channeling and shielding in various street configurations has been the subject of numerous investigations [74, 160, 172, 193, 195]. Significant enhancement (as much as a factor of four) to both peak overpressure and peak positive phase impulse was observed, and sometimes the effect of shielding can be reduced considerably by blast channeling. Reference [194] provides a good overview of these studies. In two-building simulations, overpressure amplification in the rear wall of the front structure (due to shock reflection) of more than two times the incident value was observed [160, 191].

Simulations of two different obstacle scenarios are performed here. The first is a scaled street configuration with a right angle bend which is taken from the blast simulations of Rose and Smith [173]. The basic layout, dimensions and charge and gauge locations can be seen in Figure 13.1. Further detail on this simulation is provided in Section 13.1.

The second simulation is the three-obstacle scenario by Sklavounos and Rigas [190]. The basic geometry is shown in Figure 13.2, and further details on the dimensions are provided in Section 13.2.

13.1 Blast in Street with Right Angle Bend

This simulation is based on the one performed by Rose and Smith [173] where a blast propagates around a right angle bend in a street. The basic plan layout of the street

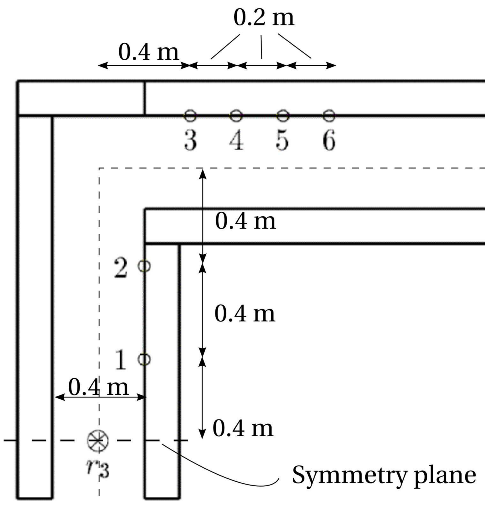

Figure 13.1: Right angle bend street layout. Source [173]

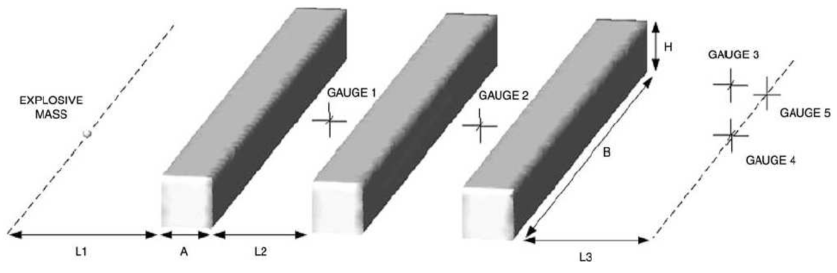

Figure 13.2: Three-obstacle layout. Source [190]

is given in Figure 13.1. The street is at 1/40$^{\text{th}}$ scale with a constant width of 0.4 m. The charge has a mass of 15.625 g TNT and is located at the r_3 point in Figure 13.1 at 37.5 mm height of burst. Each of the street buildings are 0.6 m high and 0.15 m thick. Gauges 1–6 are all 75 mm high up the buildings.

From the results in Reference [173] the size of the computational domain is chosen so that any reflections from the boundary would arrive too late to influence peak positive impulse results. The adaptive-mesh simulation uses four working mesh levels (level 4 to 7) corresponding to cell sizes of 18.75 mm to 156.25 mm. Cells at surfaces had to be kept at least at level 6 to avoid thin wall degeneracies. A higher resolution simulation with level 8 cells is also performed to observe grid dependence, and also because the minimum cell size (9.375 mm) roughly corresponds to the nominal uniform mesh cell size (10 mm) employed by Rose and Smith [173].

The AUSMDV flux solver is used. A combined adaptation criterion is used with the density-based adaptation indicator (Equation 3.4) of 0.3, 0.03 and 0.015 for the refinement, coarsening and noise filter thresholds respectively, and 0.005 for the velocity difference indicator (Equation 3.3). The number of interface area and volume subcells is 32 and 16 respectively. Because all surfaces are rectangular and grid-aligned, a 'stair-cased' wall representation (Section 2.4.3) is used.

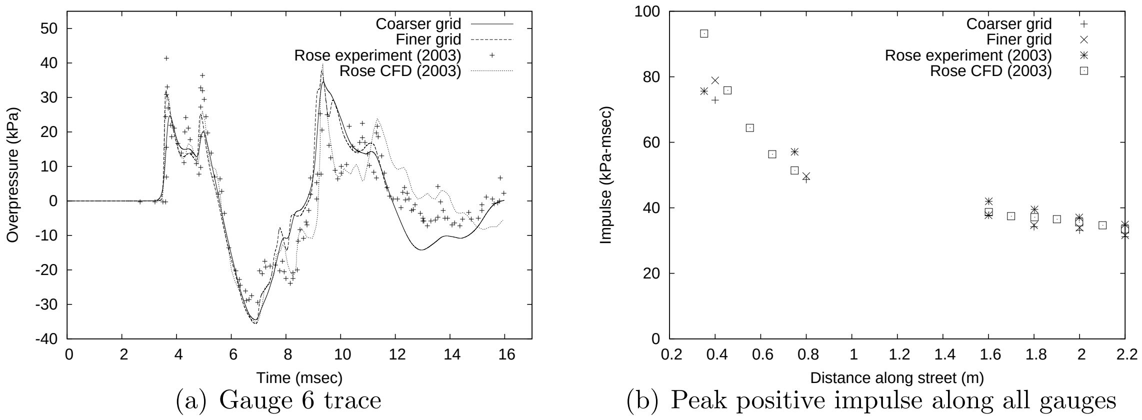

(a) Gauge 6 trace (b) Peak positive impulse along all gauges

Figure 13.3: Results for blast in street with right angle bend

The pressure history at gauge 6 is shown in Figure 13.3(a) and compared with Rose's results. The comparison is quite good, especially for the finer grid in the positive phase region (3–6 ms). Rose's results are probably more accurate due to their employment of a multi-dimensional solution remapping technique in the early stages of the blast (Section 4.6) and a uniform grid. The multiple reflections in the later time period from 8 to 14 ms are weaker and are not always refined about at the maximum cell level, so differences with Rose's solution are more prominent. The finer grid result was terminated prematurely because of computer system maintenance.

The peak positive impulse at each gauge location is shown in Figure 13.3(b). The 'distance along the street' is the distance along the centreline of the street (from the charge) to a location directly opposite the gauge. The comparison is fairly good, and there appears to be more grid-independence of results at larger distances. At gauge 1 there is a noticeable discrepancy between the coarser and finer grids, but that is likely due to initial charge shape effects. At gauges after 1.6 m the current results underestimate slightly the impulse. It is likely the uniform grids used by Rose and Smith is still superior to the adaptive scheme even when the minimum cell size is similar to the uniform grid size.

13.2 Blast in Three-Obstacle Environment

This simulation is taken from Sklavounos and Rigas [190], who modelled blast wave propagation over three successive obstacles. The basic layout of their experiment is shown in Figure 13.2. The dimensions are $L1 = 1.7$ m, $A = H = 0.6$ m, $L2 = 1.2$ m,

$B = 8.5$ m and $L3 = 1.8$ m. The charge is detonated at the midpoint of the obstacles. Gauges 1 to 4 are positioned 0.3 m above ground along this central axis (except for gauge 3 at 0.9 m height) and gauge 5 is at 0.3 m height, but offset 2.215 m to the side. The total energy of the charge is 1908 kJ, with an explosive mass of about 325 g. High pressure and density air is used to model the charge.

The boundaries are placed at a sufficiently far distance to ensure reflections do not intefere with pressure histories. The simulation utilized quarter space symmetry to improve performance, with a symmetry plane parallel to the central axis, and another symmetry plane parallel to the obstructions passing through the charge centre. A minimum cell size was not specified in [190], so the focus of this test case is on matching Skavounos' experimental result. Here the adaptive mesh simulation uses four working mesh levels (levels 4 to 7) corresponding to cell sizes of 78.125 mm to 625 mm. A higher resolution simulation with level 8 cells (39.0625 mm) is also performed.

An adaptive flux solver is used with EFM at shocks and AUSMDV elsewhere. A combined adaptation criterion is used with the density-based adaptation indicator (Equation 3.4) of 0.3, 0.035 and 0.02 for the refinement, coarsening and noise filter thresholds respectively, and 0.005 for the velocity difference indicator (Equation 3.3). A plot of the contours and grid along the ground and two symmetry planes is shown in Figure 13.4. These results were also presented by the author in Reference [202].

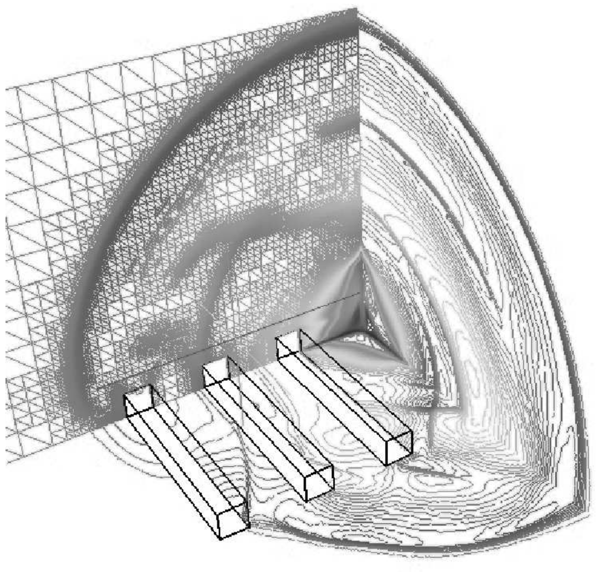

Figure 13.4: Contours for blast in three-obstacle environment

Pressure histories at the five gauge locations are shown in Figure 13.5 and compared with Sklavounos' results. At gauge 1, the agreement between the current computational and experimental results (especially with the finer grid) is quite good, and seems to be better than Sklavounos' own computational results at times. The coarser grid fails to resolve the distinct peaks in the positive phase period. There is also good agreement between computation and experiment at gauge 2.

Gauge 3 exhibits an overly high peak experimental pressure which may be due to amplification by ground shock and/or gauge vibration. This is a possibility because (a) ground shock is also seen in the gauge 4 trace and (b) this peak seems isolated from the pressures in the rest of the positive phase period. There is also some apparent drift in experimental results prior to the arrival of the blast. In other respects agreement between current computational and experimental results is good, and Sklavounos' computational result seems to be relatively poor as it has a pronounced finite rise time to peak pressure (suggesting coarser grids) and a delayed arrival time.

Agreement between the current results and Sklavounos' experimental result is poorest at gauge 4. The positive phase duration seems to be underestimated. Interference from ground shock may be partly to blame, but the more pronounced finite rise time to peak overpressure suggests grid refinement is no longer working as well here due to the lower wave strength, and thus the positive phase is not represented so well. However, arrival time seems to be calculated well. Note an apparent glitch at about 23 ms that is too sharp (compared to the initial pulse) to be a shock. The reason for this artifact is discussed below. Gauge 5 is at about the same horizontal distance as gauge 4, but the computational results do agree better with experiment here. This suggests that the more marked disagreement in gauge 4 might not be mainly due to poor mesh adaptation there. Note again a sharp glitch at about 23 ms.

The reason for this glitch in Figures 13.5(d) and 13.5(e) is probably due to the cell coarsening process. The cell adaptation method as discussed in Chapter 3 is only conservative in density, momentum and energy. Thus there will be a discontinuity in cell pressure between children cells and their just-coarsened parent cell, which will be more pronounced for larger cells. At gauges 4 and 5 the mesh refinement is no longer as fine as it was closer to the charge due to weaker shock strength, and cells here are quite coarse, on the order of the obstacle dimensions.

This phenomenon can also be observed in simulations of free-field TNT burst (as in Chapter 10). For example, Figure 13.6 shows the free-field pressure history at a gauge location some distance from the charge, comparing a uniform mesh with an adapted mesh. A glitch is present at about 16.4 ms in the adaptive mesh solution, but not seen in the uniform mesh solution. In this case the glitch is not so noticeable as the adaptive mesh has higher resolution. As long as cells are kept sufficiently fine, the glitch can be minimized.

The coarser resolution simulation had a maximum of 1.61×10^5 cells (running for 18.5

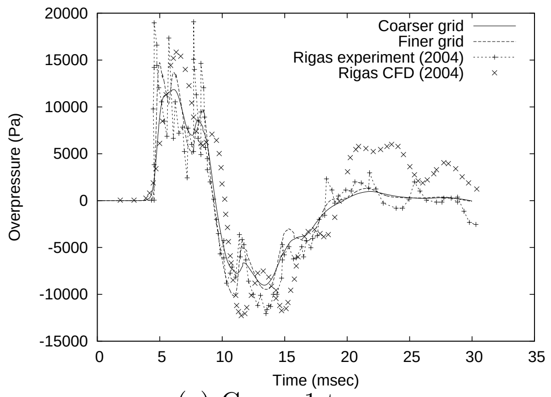

(a) Gauge 1 trace

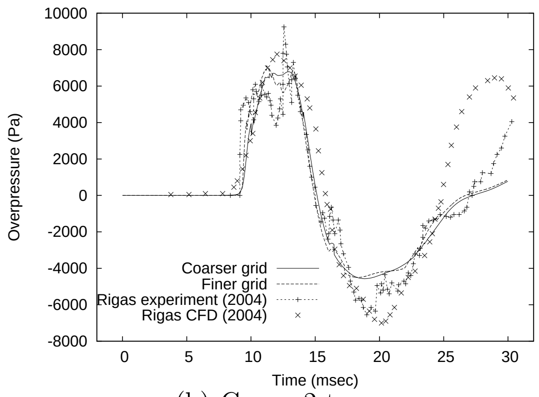

(b) Gauge 2 trace

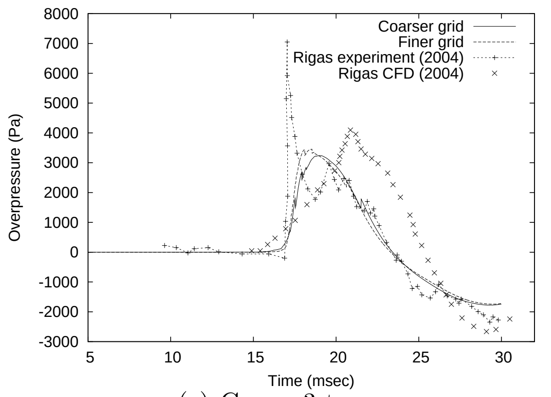

(c) Gauge 3 trace

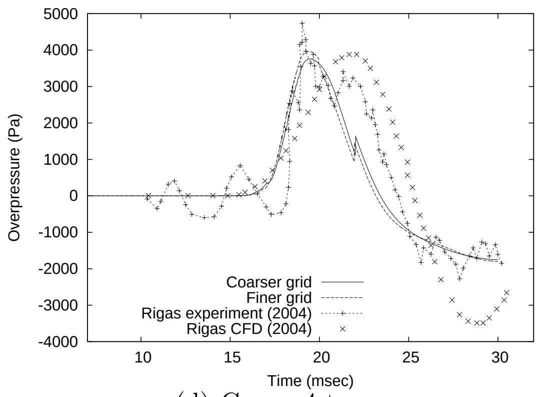

(d) Gauge 4 trace

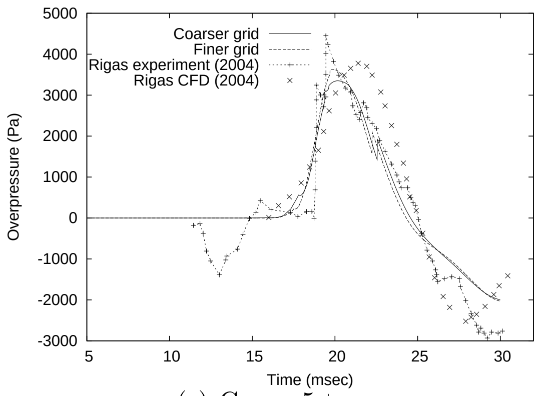

(e) Gauge 5 trace

Figure 13.5: Results for blast in three-obstacle environment

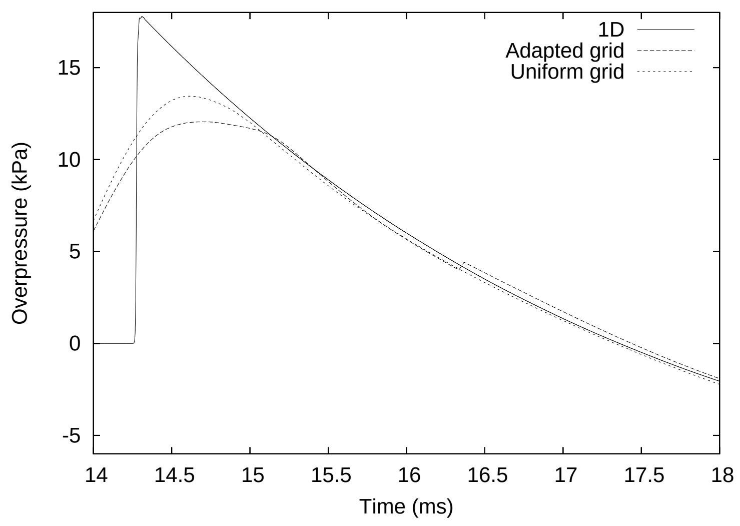

Figure 13.6: Example of adaptation-generated noise in pressure trace

hours) and the finer resolution simulation had a maximum of 6.25×10^5 cells (running for 100.75 hours). The elapsed times for these simulations are not a reliable indicator of computational effort as they were run on a shared interactive Altix cluster with disabled cpusets.

Chapter 14

Validation - Explosion in Complex Cityscape

The ultimate goal of `OctVCE` is to simulate explosions in complex three-dimensional geometries. Brittle *et al* have investigated in detail an explosion in a complex cityscape geometry with both scaled experiments and the Cartesian-cell `ftt_air3d` code [39, 175, 194], making this an ideal validation test case. This test case was also performed by the present author in Reference [203]. The plan geometry of the cityscape at 1/50th scale is taken from Brittle [39] and shown in Figure 14.1 with some annotations. The 16 g spherical TNT charge is detonated at the `EC1` location. Coordinates are given relative to the origin at the lower left corner. The angle α can be computed from the dimensions of building 1.

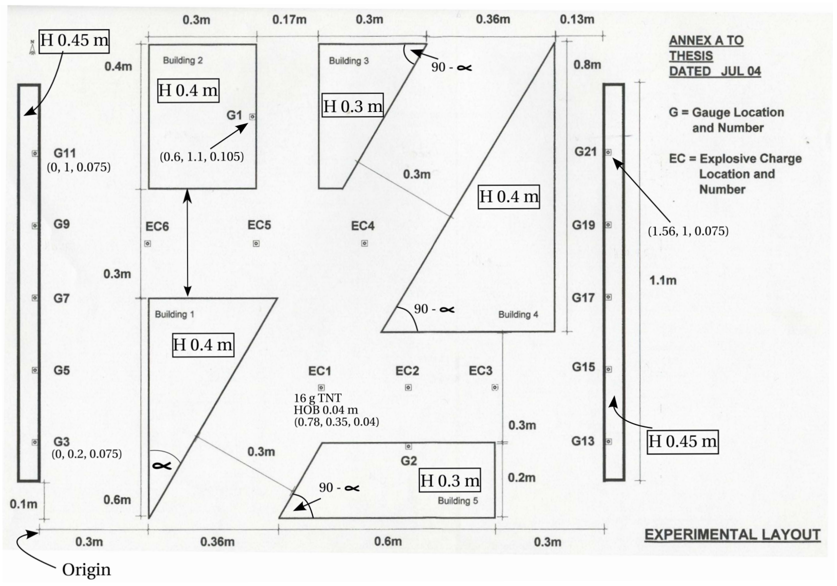

Figure 14.1: Complex cityscape geometry. From [39]

The domain size is the same as Rose's [175] at 2.56 m × 2.56 m × 2.56 m, and three different, increasingly finer meshes are used to observe grid dependence. The coarsest resolution is a uniform mesh level 6 (40 mm cells), the next finer grid is an adaptive mesh with level 6 and 7 cells, and the finest grid has level 6 to 8 cells (10 mm minimum cell size). These mesh levels are the same ones used by Brittle and Rose [39, 175].

The coarsest mesh represents the charge as a cube because of the relatively large cell sizes. Due to computational resource constraints, a level 9 mesh simulation could not be performed.

The assumed specific energy of the charge is 4520 kJ/kg, which is represented with the ballon analogue model (Section 4.6), and thus its pressure and density is modified to represent correct blast energy and mass depending on the grid resolution. The ambient gas is air at standard conditions (density of 1.2 kg/m^3 and pressure 101.325 kPa). A combined adaptation criterion is implemented with the density-based adaptation indicator (Equation 3.4) of 0.3, 0.05 and 0.03 for the refinement, coarsening and noise filter thresholds respectively, and 0.01 for the velocity difference indicator (Equation 3.3). An adaptive flux solver is used (Section 4.4) with EFM at shocks and AUSMDV elsewhere. The number of interface area and volume subcells is 32 and 16 respectively.

14.1 Results

Pressure histories at gauge locations 1, 3, 11 and 21 are shown in Figure 14.2 and compared with the results of Brittle and Rose [39, 175]. There is generally good agreement, especially for the finest resolution mesh in the positive phase. Agreement in peak overpressure is poorest at gauge 11. These results demonstrate that the balloon analogue model of charge representation can produce acceptable pressure histories, although the remapping procedure implemented by `ftt_air3d` [177] which remaps an initial highly resolved one-dimensional solution to multidimensions would still produce more accurate results.

In less major details there are more noticeable differences with Rose's result, like the poorer resolution of secondary waves e.g. for gauge 21 where the train of waves at around 6 ms are not captured well. This is probably partly due to the cruder balloon analogue model, but also because of the time-dependent cell size at surfaces. Intersected or partially obstructed cells were kept at the maximum level in Rose's simulation, but this was not enforced in `OctVCE`, which allows a varying cell size at surfaces for faster results. If the resolution of secondary details is not a priority, the current methodology seems sufficient.

Increments between the coarse, finer and finest mesh solutions in peak pressure and impulse are shown in Tables 14.1 to 14.6; increasingly smaller differences suggest convergent behaviour. Gauge 1 (Table 14.1), being the gauge least shielded from the blast, appears to demonstrate the best convergent behaviour in both pressure and impulse. Coarser resolutions in fact overpredict the peak impulse, a result also observed by Brittle [39], which might be a useful result if conservatism is desired.

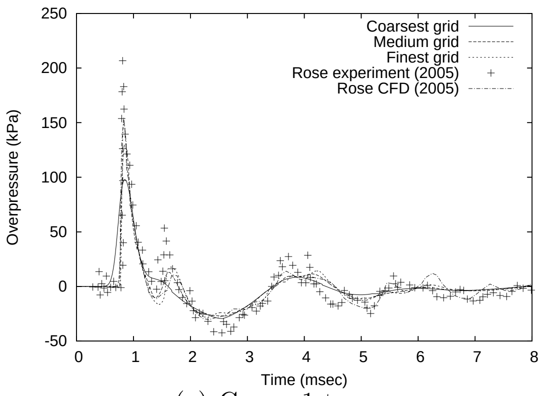

(a) Gauge 1 trace

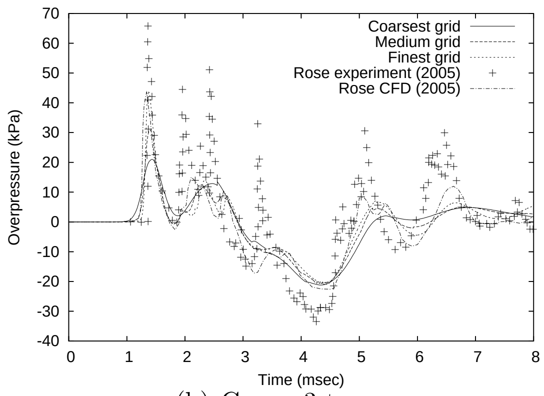

(b) Gauge 3 trace

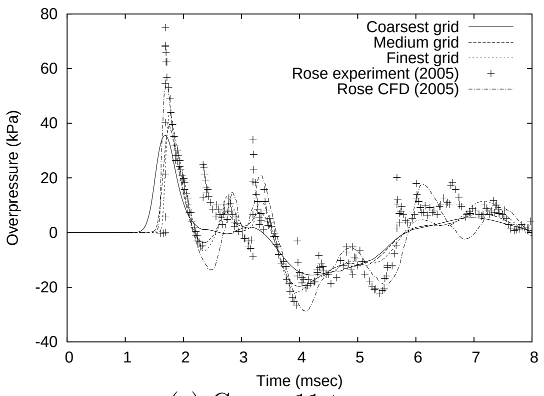

(c) Gauge 11 trace

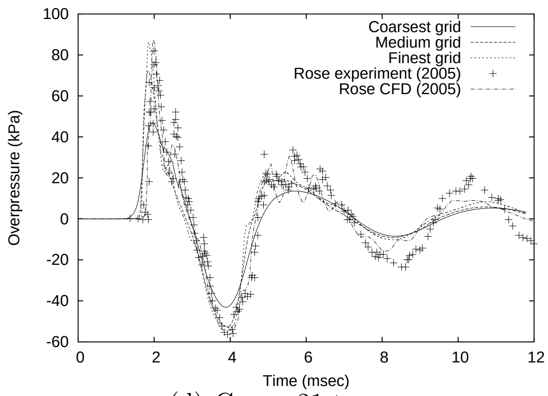

(d) Gauge 21 trace

Figure 14.2: Pressure histories for blast in complex cityscape

Gauge 3 (Table 14.2) does not appear to demonstrate convergent behaviour in pressure, and the increments in impulse actually change sign. This behaviour is also repeated for gauges 11 and 21 (Tables 14.3 and 14.5), however gauge 21 has convergent pressure. Rose's data [175] for gauges 11 and 21 are shown in Tables 14.4 and 14.6. Rose's gauge 21 results also show apparent lack of convergence in overpressure and also impulse.

It is clear that mesh convergence is not always easy to demonstrate, and depends on the gauge location and quantity under consideration. Convergence may be hampered by the adaptive mesh and complex nature of the wave interactions [175], or perhaps only consistently demonstrable on very fine meshes. In the simulations here, constant cell size at surfaces is also not enforced, which may hinder convergence. It may be particularly difficult to observe convergence in peak pressure as it is a shock-dependent quantity and thus quite sensitive to grid resolution and flux limiters. Perhaps the coarsest mesh is too coarse to be in the asymptotic convergence range. Nonetheless, correspondence with Rose's experimental results still seems reasonably good, even if mesh convergence has not been fully attained everywhere.

Figures 14.3(a) and 14.3(c) show the peak pressure and impulse contours respectively on the entire surface of the left-end wall (on which is placed gauges 3 to 11). They

Table 14.1: Complex cityscape, gauge 1 peak quantities

No. levels	Pressure (kPa)	Impulse (kPa-msec)	Inc. pressure (kPa)	Inc. impulse (kPa-msec)
1	98	35.58	-	-
2	130	29.89	31.9	-5.694
3	149	28.94	19.07	-0.949

Table 14.2: Complex cityscape, gauge 3 peak quantities

No. levels	Pressure (kPa)	Impulse (kPa-msec)	Inc. pressure (kPa)	Inc. impulse (kPa-msec)
1	21	17.12	-	-
2	30.8	14.85	9.845	-2.27
3	43.6	15	12.7	0.1503

Table 14.3: Complex cityscape, gauge 11 peak quantities

No. levels	Pressure (kPa)	Impulse (kPa-msec)	Inc. pressure (kPa)	Inc. impulse (kPa-msec)
1	35.5	16.91	-	-
2	39.4	16.07	3.83	-0.84
3	43.84	18.02	4.47	1.96

Table 14.4: Complex cityscape, Rose's gauge 11 peak quantities [175]

No. levels	Pressure (kPa)	Impulse (kPa-msec)	Inc. pressure (kPa)	Inc. impulse (kPa-msec)
1	30.2	16.2	-	-
2	44.3	19.3	14.1	3.1
3	53.9	19.7	9.6	0.4

Table 14.5: Complex cityscape, gauge 21 peak quantities

No. levels	Pressure (kPa)	Impulse (kPa-msec)	Inc. pressure (kPa)	Inc. impulse (kPa-msec)
1	46.9	38.4	-	-
2	72.1	38.49	25.16	0.997
3	86.2	40.08	14.17	1.584

Table 14.6: Complex cityscape, Rose's gauge 21 peak quantities [175]

No. levels	Pressure (kPa)	Impulse (kPa-msec)	Inc. pressure (kPa)	Inc. impulse (kPa-msec)
1	47.6	40.4	-	-
2	66.5	40.9	18.9	0.5
3	88.1	40.2	21.6	-0.7

were obtained by distributing about 1000 trace points over the wall, and are shown for the finest resolution mesh. These contours are compared with Rose's result [175] in Figures 14.3(b) and 14.3(c). There is generally good agreement in the magnitude and location of the various 'hot spots', some of which are due to wave coalesence. Rose compared these contours to unshielded CONWEP data to demonstrate the inadequacy of simple line-of-sight methods for blast problems in complex geometries due to multiple shock reflection and diffraction [175].

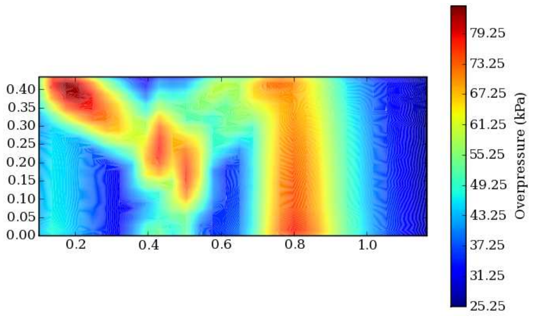

(a) Peak pressure contours

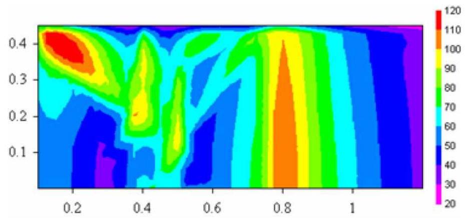

(b) Rose's peak pressure contours [175]

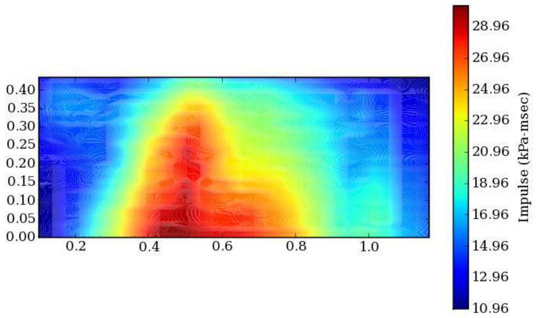

(c) Peak impulse contours

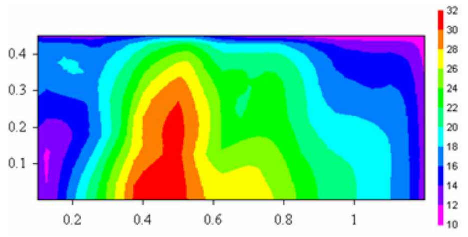

(d) Rose's peak impulse contours [175]

Figure 14.3: Contours on left-end wall of blast in complex cityscape

Although a mesh convergence analysis was performed for individual gauge results, it is also interesting to perform it for these pressure and impulse contours. The incrementals in peak pressure and impulse are computed for each sensor on the face and compared with the next higher level mesh to yield an absolute relative error for the sensor. This quantity is then summed over all sensors to yield an *average relative error per sensor point* on this face. A decreasing error might indicate convergence. These errors are shown in Table 14.7. Convergence in impulse is observed but apparently not in pressure, although the difference is by less than 1%. This demonstrates again the difficulty of obtaining convergence consistently for all quantities for the meshes used in this simulation. Note also that impulse errors are substantially smaller than pressure errors, sometimes by an order of magnitude.

Table 14.7: Complex cityscape, average relative error for left-end wall

No. levels	Avg. pressure error	Avg. impulse error
1–2	0.154	0.0347
2–3	0.163	0.0123

14.2 Performance

The performance for the various mesh resolution simulations are shown in Table 14.8 and compared to Rose's `ftt_air3d` results [175]. The current simulations were all conducted on four processors in parallel, and elapsed times cannot be directly compared with Rose's results. Thus in the second major column of Table 14.8 the elapsed time is normalized by the coarsest resolution elapsed time.

`OctVCE` seems to exhibit slightly poorer scaling in relative time. Rose's simulation also used less cells especially for the finest mesh simulation. The most significant difference is in memory consumption, with the current code using as much as 15 times more memory. Some of this overhead comes from explicit neighbour connectivities and also additional data structures for parallel processing e.g. lists. This larger memory consumption undoubtedly affects performance.

Table 14.8: Performance statistics for different mesh levels

	Max no. cells		Relative time		Max memory (GB)	
No. levels	`OctVCE`	`ftt_air3d`	`OctVCE`	`ftt_air3d`	`OctVCE`	`ftt_air3d`
1	2.57×10^5	2.62×10^5	1	1	0.528	0.058
2	5.8×10^5	4.3×10^5	3.42	3.29	1.33	0.088
3	2.06×10^6	1.44×10^6	23.15	18.67	4.65	0.317

A single processor simulation using the finest resolution (3 levels) was performed for analysis of parallel performance, and this took 234.78 CPU hours, which is much larger than Rose's equivalent simulation at 12.47 hours. Even allowing for the greater number of cells with the current simulation, the code is still slower than `ftt_air3d` by around a factor of 10. The single processor simulation could only be performed on the Altix cluster using a cpuset of at least two memory nodes, as the memory consumption exceeded the capacity of one node. Thus a considerable number of memory requests would not be to local memory, which can degrade performance as the Altix system is fairly 'NUMA-heavy', as mentioned in Section 5.5.3. Rose's simulation was also run on a single 2 GHz Pentium 4 personal computer, which is slightly faster than an individual Altix processor (an Intel Itanium 2) – this performance was measured on a similar workstation and compared with the Altix installed at the University of Queensland.

Clearly more work needs to be done to improve performance of the current code. For example, many of the efficiency-boosting techniques used by `ftt_air3d` [177] can be implemented, like variable timestepping, a less conservative timestep, fully threaded tree structure [118], solution remapping from lower dimensions, pressure-based refinement criteria and better memory management. More attention should be given to reducing storage requirements, which was originally not a high priority as it was thought that explicit storage e.g. of mesh connectivity would be more efficient. These performance gains might be outweighed by the performance losses due to memory overhead e.g. increased cache misses.

14.2.1 Parallel Performance

Parallel performance data is obtained for the finest resolution simulation on 1, 2, 4 and 8 processors. These simulations were done on the Altix 3700 cluster. Speedups are shown in Figure 14.4, and are similar to those of the three-dimensional simulations in Section 10.4.1. In this case the 2 processor speedup seems close to the ideal limit, but as mentioned above the 1 processor simulation may have suffered a performance degradation due to spreading its memory usage over two nodes . The relative differences between the 2, 4 and 8 processor jobs are more reliable.

Performance statistics like those in Section 7.3 can be obtained from speedup data and also the code profiler (the Intel compiler's `-openmp-profile` flag), and are shown in Table 14.9. The effective serial fraction is obtained from the Karp-Flatt metric (Section 5.4), but as in Section 10.4.1 it could not be extrapolated to estimate the true serial fraction (on 1 processor) because it did not monotonically increase with increasing processors.

An explanation, also given in Section 10.4.1, is that the increased memory resources of the 8 processor simulation enabled better performance, but this may also be explain-

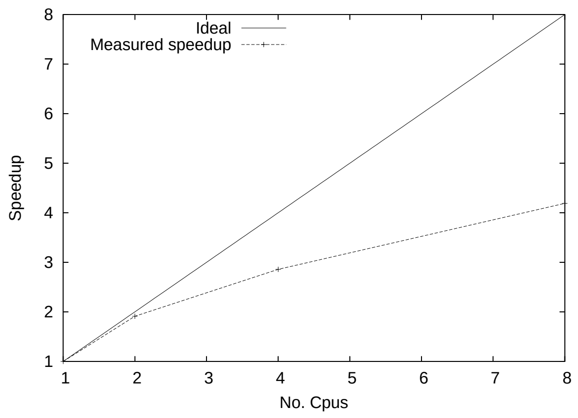

Figure 14.4: Parallel speedups for blast in cityscape simulations

able from variations in memory access due to operation on the NUMA system. The 2 processor effective serial fraction is also probably too low from the discussion above. Like in Section 10.4.1 the minimum fraction, 0.0466 (a considerably lower bound) is used, and performance statistics are then relative to the 2 processor performance.

Table 14.9: Parallel performance statistics for complex cityscape simulations

No. processors –	1	2	4	8
Single processor time (hrs)	234.78			
Max no. cells	2.063×10^6			
‘Effective’ serial fraction		0.0466	0.133	0.13
Extrapolated serial fraction	0.0466*			
Barrier fraction		0.0174	0.052	0.0391
Overhead fraction		0.0174*	0.0864	0.0834
Barrier/overhead		1	0.602	0.469
Max imbalance time/elapsed		0.008	0.02701	0.02763

Many of the trends seen in Table 10.4 can also be observed here. In some cases the values have similar magnitudes, but there are also noticeable discrepancies. Some of these are due to the lower estimate of the serial fraction. Although the overhead fraction should be defined to be zero for the 2 processor simulation, the barrier fraction can still be obtained from the Intel profiler and thus for the 2 processor simulation is set identical to the overhead fraction. The imbalance fractions are quite low, indicating fairly good load balancing.

Note that the barrier/overhead fraction decreases with more processors indicating that communication overhead becomes increasingly important. A reasonable estimate for the code serial fraction is around 10% given upper bounds of 13% (the 8 processor effective fraction in Table 14.9) and lower bounds of 4.7% (Table 14.9) and 9.2% (Table 10.4) respectively. This is fairly good given the relatively crude parallelization method (Section 5.5).

As a final demonstration that the code parallelization method is functioning properly, the pressure histories at gauges 1, 3, 11 and 21 from the 1, 2, 4 and 8 processor simulations are shown in Figure 14.5. The parallelization should not affect the solution and thus the pressure histories for all simulations should align exactly, which is observed. There is a very small discrepancy in solutions at gauge 1. The best explanation for this might be from slightly divergent numerical roundoff errors because the compiled code is different with and without the `-openmp` flag. Other traces exhibit exact alignment. The code was analyzed with the Valgrind memory checker application [67] and no memory faults were apparent.

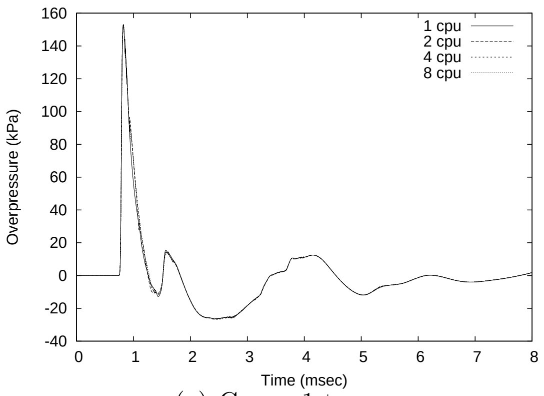

(a) Gauge 1 trace

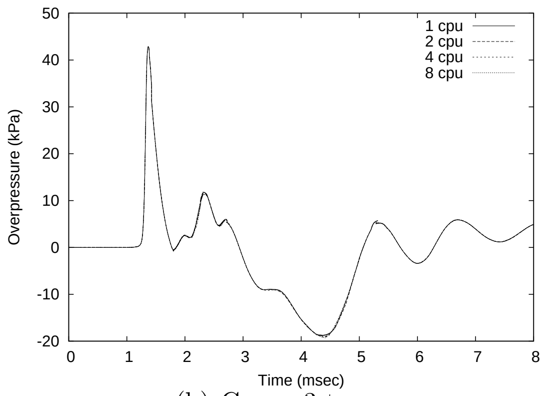

(b) Gauge 3 trace

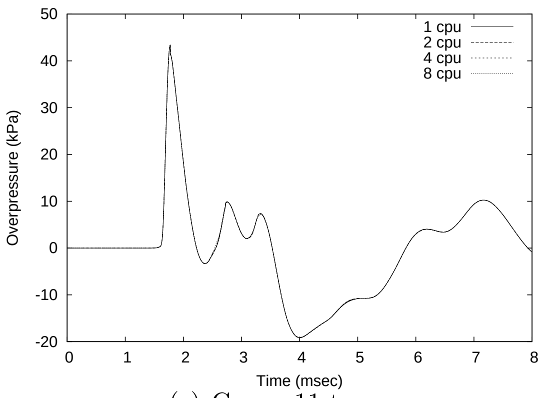

(c) Gauge 11 trace

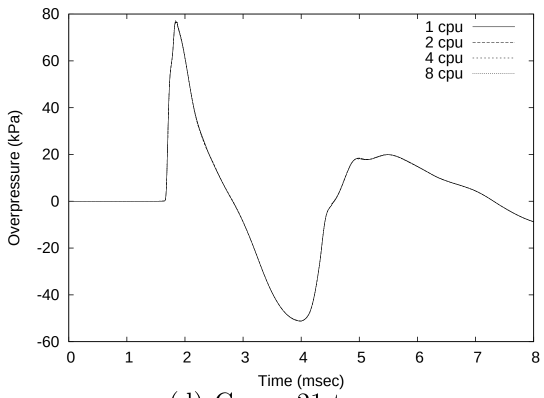

(d) Gauge 21 trace

Figure 14.5: Pressure histories from parallel simulations (blast in complex cityscape)

14.3 Effect of Adjusting Adaptation Criteria

It was discovered that the adaptation criteria used resulted in prolonged, needless and excessive cell refinement near the explosion centre, as shown in Figure 14.6(a) which plots the schileren and overlaid grid for the medium resolution mesh at an early stage of the explosion (on the ground). This obviously has a significant effect on the simulation performance. The adjustment of the adaptation parameters is experimented with to observe the effect on the solution and its elapsed time. As it is known from Appendix A.1 that the density-based refinement criterion usually refines around the turbulent explosion centre, only the simple velocity-difference based criterion (Equation 3.3) is used.

Figures 14.6(b) to 14.6(d) show the effect on the grid refinement density as this parameter is varied from 0.01 to 0.1 respectively. The schlieren and overlaid grids are for the finest resolution. The degree of refinement clearly decreases as this parameter is increased, and is virtually non-existent for a value of 0.1. For a value of 0.01 the primary blast wave is still well-captured, but there appears still to be a considerable degree of refinement near the explosion centre, probably due to the multiple shock reflections occuring there. However, this is still less than the original simulation using the density-based criterion (Figure 14.6(a)).

The speedup (relative to the original grid), memory usage and maximum number of cells for these simulations are shown in Table 14.10. It is clear that significant reductions in storage and time can be made if the adaptation criteria are selected properly. However, this is a difficult exercise *a priori*. A value of 0.01 for the velocity-difference criterion seems to give a maximum number of cells more consistent with Rose's simulation. However, the absolute solution time is still much larger.

Table 14.10: Performance for different refinement criteria (complex cityscape)

	Original grid	VD: 0.01	VD: 0.03	VD: 0.1
Speedup	1	1.76	5.81	12.8
Max memory (GB)	4.625	3.624	1.753	0.791
Max. no. cells	2.063×10^6	1.431×10^6	6.64×10^5	3.49×10^5

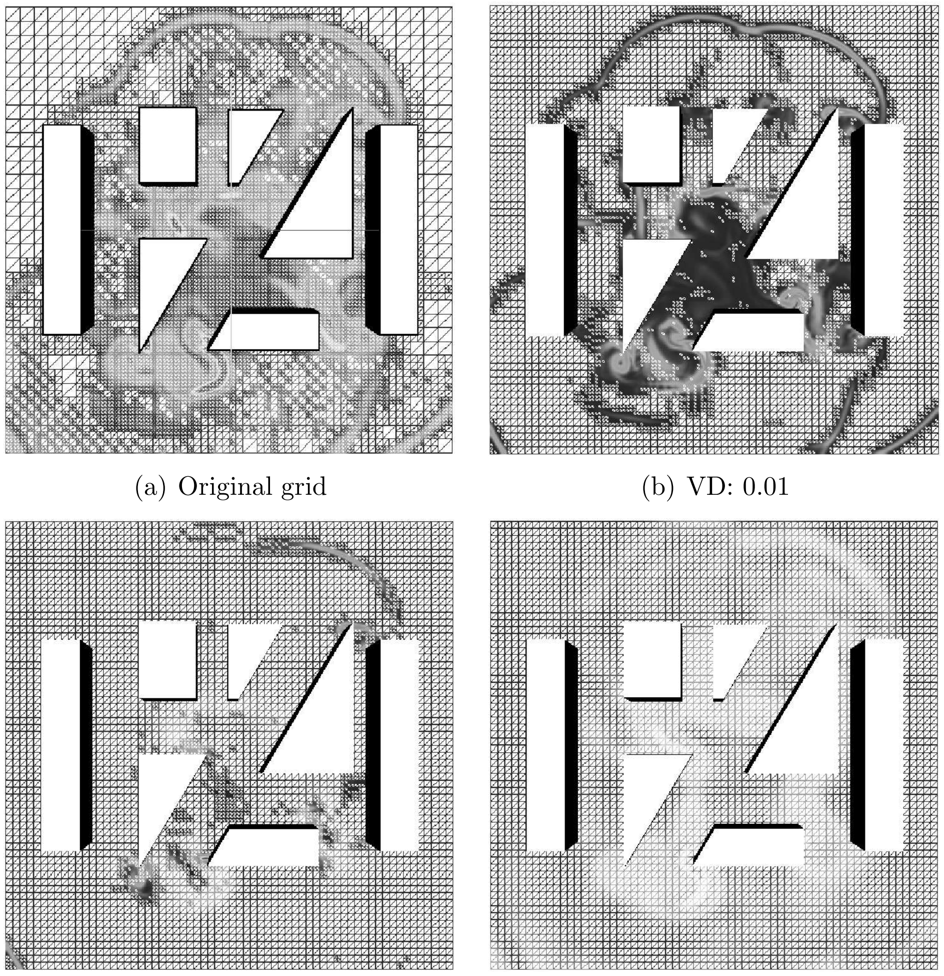

Figure 14.6: Grids for different adaptation criteria

The pressure histories at gauges 1, 3, 11 and 21 for these simulations are shown in Figure 14.7 and compared with the original simulation. The lesser refinement causes a deterioration in the solution quality, especially for secondary features after the positive phase. However it is surprising that all solutions give good peak overpressure at gauges 1 and 21, even for the very coarse grid with 0.1 as the velocity-difference indicator. Gauges 3 and 11 show how resolution of the peak overpressure becomes poorer as the indicator is enlargened, and is particularly bad for the 0.1 indicator (as little cell refinement occurs for this gauge location at this stage).

It appears that a value of 0.01 for the indicator produces results quite close to the original simulations; some secondary peaks are not captured so well but these are not so important. Fine-tuning this value between 0.01 and 0.03 may result in further savings with comparably low deterioration in accuracy, but this is a costly exercise. Except in special circumstances, this velocity-difference based criterion seems the most cost-

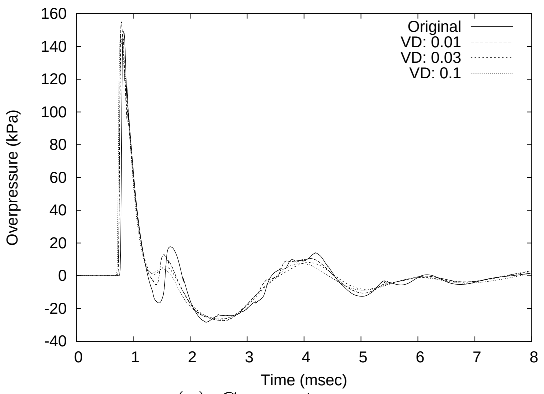

(a) Gauge 1 trace

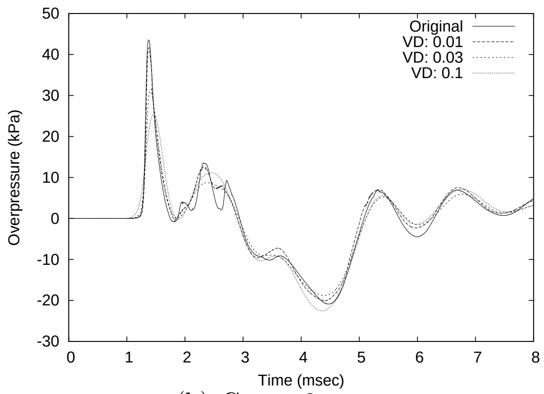

(b) Gauge 3 trace

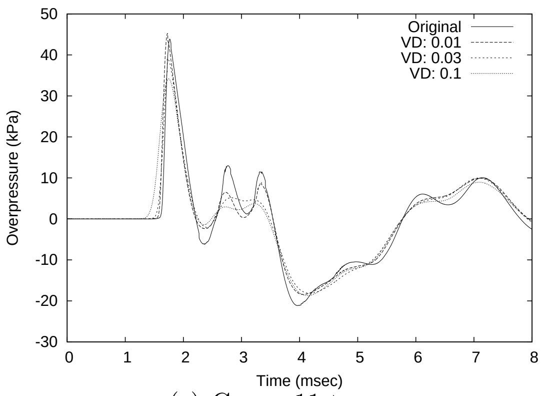

(c) Gauge 11 trace

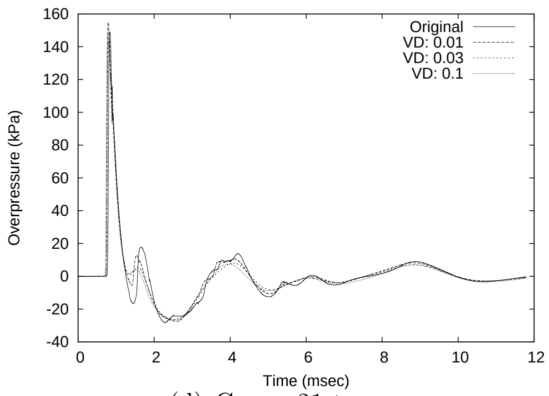

(d) Gauge 21 trace

Figure 14.7: Pressure histories from different adaptation criteria

effective, and for such blast simulations is preferrable. There is still some unnecessary refinement near the explosion centre, so perhaps an additional pressure-difference criterion (used in `ftt_air3d` [177]) might be useful.

Chapter 15

Application Study – Modelling Explosion in Shipping Container Geometries

This application study was originally reported by the author in Reference [203] and models an explosion in an internal geometry resembling a shipping container. The stems from the recent consideration by the Centre of Hypersonics (The University of Queensland) into the possibility of testing rocket motors in a confined facility, which is a modified shipping container with roof vents for the inlet and outlet. Open-air rocket testing is not preferred because the noise generated from the turbulent plume is quite high at 120-130 decibels. This section presents a very simplified numerical simulation of the worst-case scenario when the mainly nondetonable rocket propellant explodes, with the goal of obtaining contours of peak overpressures and impulses on the (assumed rigid) internal walls. This is essentially a design study and no opportunity for a supplemental experimental study could be performed.

The propellant for the proposed Wagtail rocket [35] weighs 20 kg and is predominantly composed of ammonium perchlorate, which is normally very difficult to detonate [158]. In light of this fact and the inability of the code to model propellant burning, a conservative TNT equivalence value of 1 to 1 is assumed, and thus the charge in the simulation consists of 20 kg of TNT. Although an explosion of this mass of TNT within a shipping container with only 5 mm thick walls will result in failure of the facility, the simulation can be thought to model the explosion in any rigid structure with the same internal geometry, and it will still be interesting to observe the magnitude of peak pressures. This study is thus a study into blast confinement effects.

A diagram of the testing facility is shown in Figure 15.1. The walls are modelled as smooth, flat surfaces. The explosive source is located along the container centerline, 3 m from the intake end and 1 m off the floor. However, a plane of symmetry along the container centerline is not used. An energy density of 4520 kJ/kg of TNT is assumed [19]; the charge is initialized with the balloon analogue model (Section 4.6). It is assumed to be composed of perfect gas air.

Three minimum adaptive grids are used to observe grid dependence. The coarsest resolution uses four working levels (level 4 to 7) with cell sizes 0.2344 m to 1.875 m, and is denoted the L7 mesh. Like in Section 12 the cells are kept at level 7 at walls as the

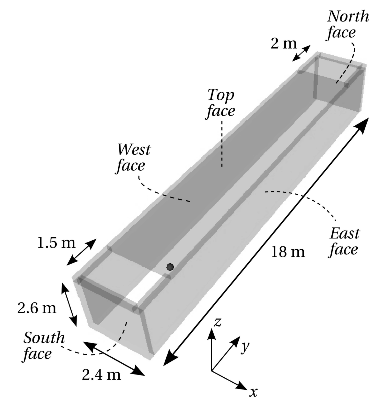

Figure 15.1: Diagram of rocket motor testing facility

code cannot handle thin wall degeneracies; the walls are themselves set with a thickness larger than the diagonal spanning the cell corners. Computational resource constraints prevent additionally finer grids to be used. The medium resolution uses five working mesh levels (levels 4 to 8) and is denoted the L8 mesh. The finest resolution has six working levels (levels 4 to 9, 0.0586 m the minimum cell size) and is denoted the L9 mesh. The domain size (30 m) is chosen to ensure the primary blast wave can exit all vents without any boundary effects on the pressure histories.

A combined adaptation criterion is used with the density-based adaptation indicator (Equation 3.4) of 0.3, 0.1 and 0.09 for the refinement, coarsening and noise thresholds respectively, and 0.02 for the velocity difference indicator (Equation 3.3). An adaptive flux solver is used with EFM at shocks and AUSMDV elsewhere. The number of interface area and volume subcells is 32 and 16 respectively. 225 sensor points are distributed uniformly over each interior wall to obtain peak impulse and pressure contours.

As this is an internal blast scenario, it is expected that the high degree of confinement will cause multiple wave reflections and coalesence and produce enhancements in corners, edges and other local constrictions [193]. Depending on the geometry and explosive, quasi-static gas pressure can persist for a long time (compared to the wave length of the initial pulse) due to buildup of hot gas from the detonation products, and can have a singificant impact on structural loading.

15.1 Results

15.1.1 Selected Pressure Histories

Some pressure histories at different wall locations are shown in Figure 15.2. They illustrate that convergence in peak pressure is not always attainable depending on the sensor location. Figures 15.2(a) to 15.2(d) are examples of sensors located at either corners or edges in the geometry. These histories do not show convergence in peak overpressure; however Figure 15.2(c) apparently shows convergence in the second peak. Figures 15.2(e) and 15.2(f) show pressure histories away from edges, and convergence in peak overpressure is more demonstrable.

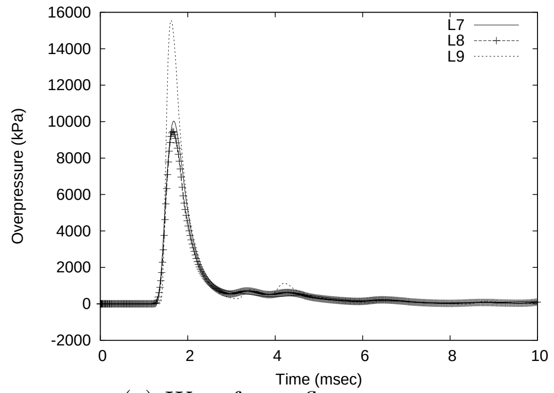

(a) West face - floor, corner

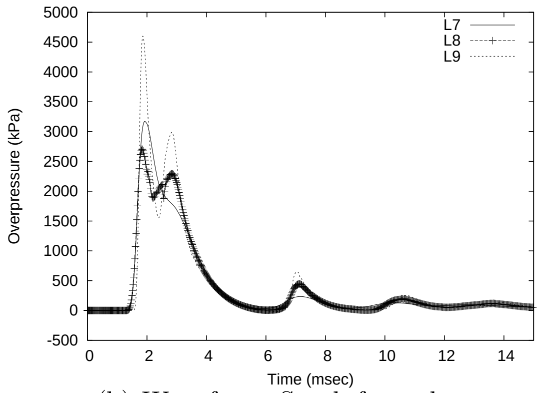

(b) West face - South face edge

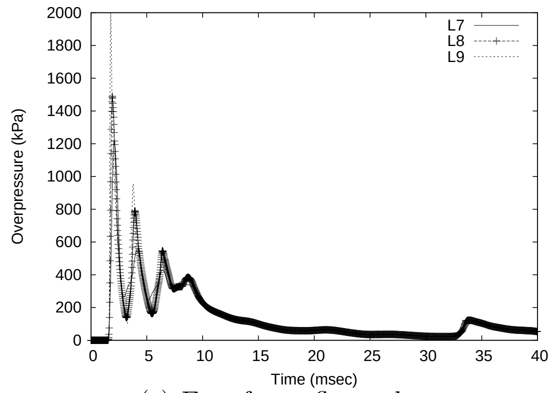

(c) East face - floor edge

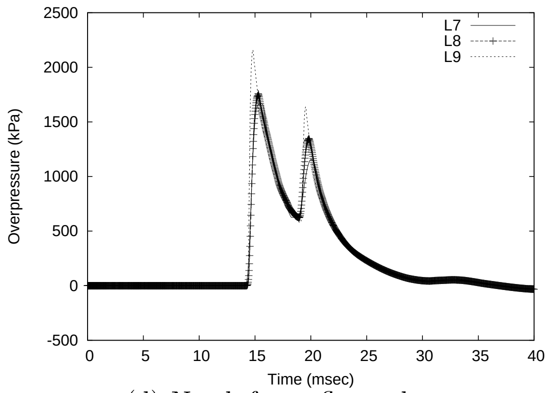

(d) North face - floor edge

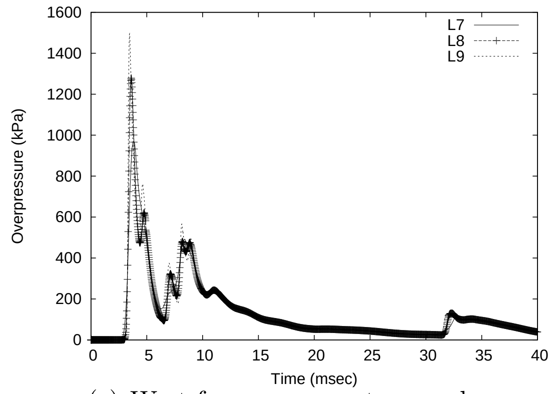

(e) West face convergent example

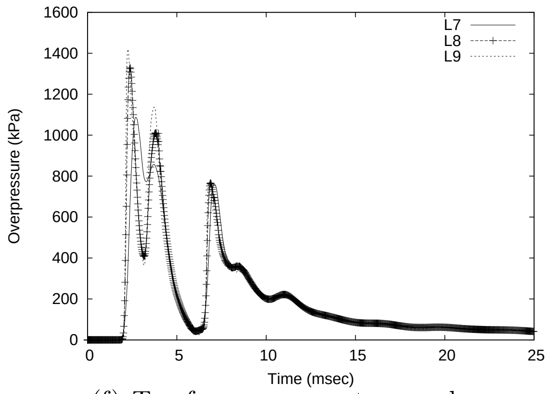

(f) Top face convergent example

Figure 15.2: Selected traces for explosion in shipping container problem

Numerical convergence in peak overpressure was also found to be difficult in previous simulations [175] (see also Section 14.1), and particularly with gauge readings at structural corners in an internal geometry [136]. Rose *et al* [175] state that convergence may be difficult to demonstrate when initial pulses are comprised of several (previously) distinct waves, although secondary pulses might be easier to converge. In this case, the inconsistent convergent behaviour might be because a shock wave travelling into an edge or corner geometry is analogous to shock focussing, due to symmetry of the solid boundary condition. As discussed in Section 12.1 the pressure at such focus points is a particularly grid-dependent result and difficult to resolve [54].

Hence convergence is more readily expected for sensors away from edges, which is observed. Another factor influencing non-convergence at edges is that the finest cell sizes are not always used at surfaces; depending on the geometry and adaptation criteria the grid may not be adapted to the finest level at some sensor points, especially those far from the charge. The range of grid sizes for this study may not be in the asymptotic convergence range, which may need to be quite fine. Also VCE 'rounds off' corners unless a staircased representation is used. The existence of 'small cells' (Section 2.4.2) at edges and corners, and a locally first-order scheme, may also contribute to the deterioration of accuracy.

15.1.2 Impulse and Pressure Wall Contours

Contours of peak overpressure and impulse along the facility's interior walls are shown in Figures 15.3 to 15.5. Figure 15.3 shows peak quantities along the south face, or inlet-end wall. This figure gives an example of the different peak overpressure solutions on different resolutions, which do differ noticeably, although general features are preserved. These differences are used in computing average wall errors in Section 15.1.3. Peak overpressures are of the order of tens of megapascals. Maximum values increase with increasing resolution, and the solution is symmetrical about the centreline. It is interesting that the local maxima in the higher resolution simulations are slightly away from the corners and do not correspond to the height of burst. The maximum impulse occurs along the floor edge due to the shock focussing there and the charge height of burst.

Figure 15.4 shows the peak quantities along the east face or long side wall for the L9 grid. Note that peak values occur at the charge location, and are greatest at corners and edges due to focussing. The impulse is nearly constant along the wall section from the charge to the outlet vent. The peak pressures and impulse increase at the north face (or outlet-end wall) due to shock reflection there.

Figure 15.5 shows contours for the L9 grid along the north face, or outlet-end wall, which is farthest from the charge. By this stage there might have been much coalesence of waves, and some numerical diffusion has occured, so the contours are more smoothly

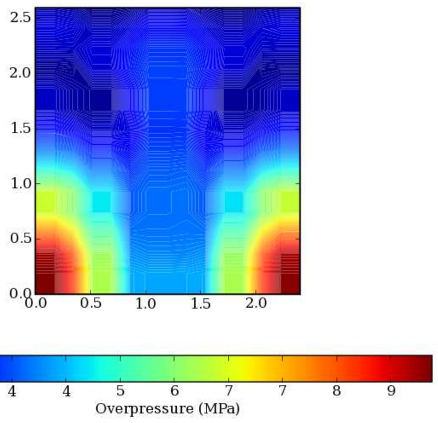

(a) Peak ovepressure, L7 grid

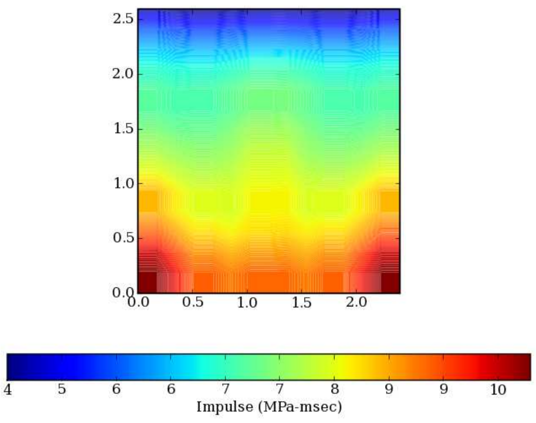

(b) Peak impulse, L7 grid

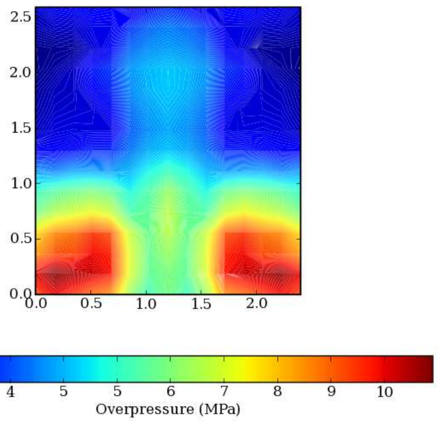

(c) Peak ovepressure, L8 grid

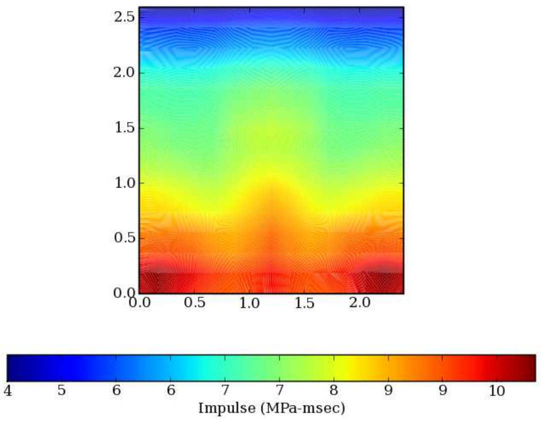

(d) Peak impulse, L8 grid

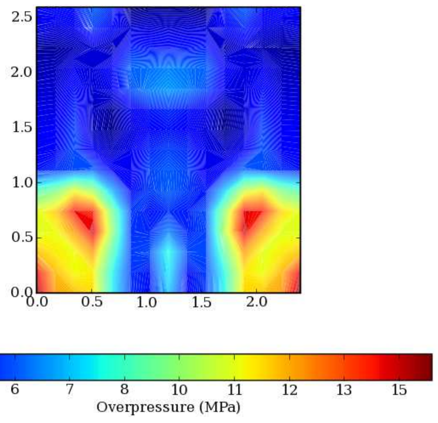

(e) Peak overpressure, L9 grid

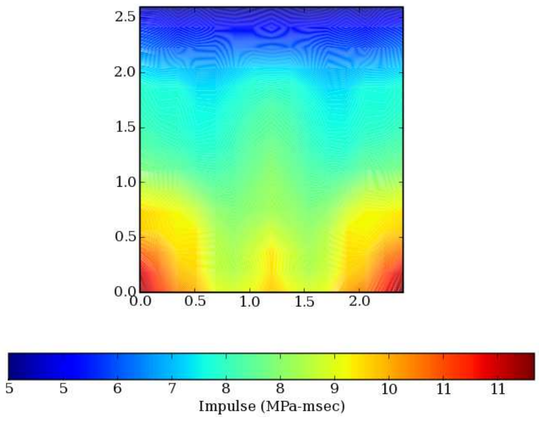

(f) Peak impulse, L9 grid

Figure 15.3: South face contours for explosion in shipping container problem

varying. Peak pressure occurs at the facility floor and has attenuated to the order of megapascals. Impulse values are also greatest at the floor.

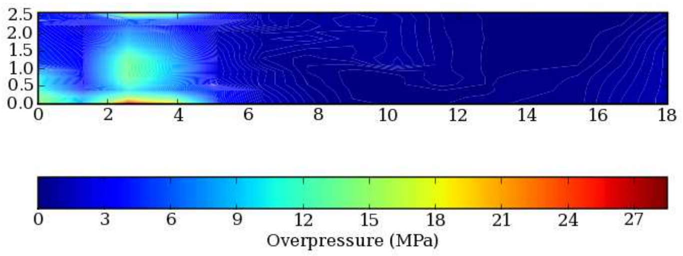

(a) Peak ovepressure

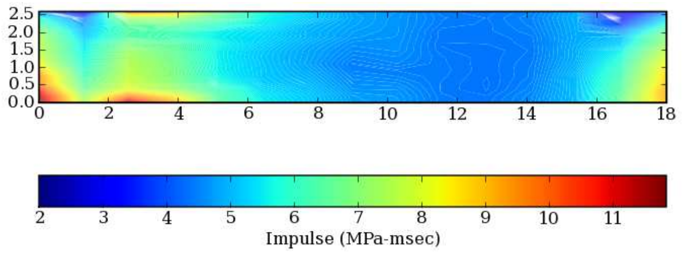

(b) Peak impulse

Figure 15.4: East face contours (L9 grid) for explosion in shipping container problem

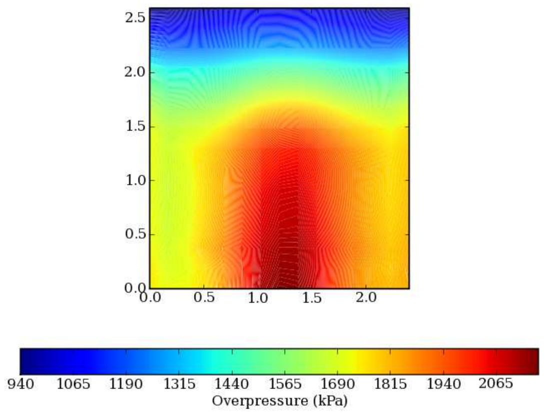

(a) Peak ovepressure

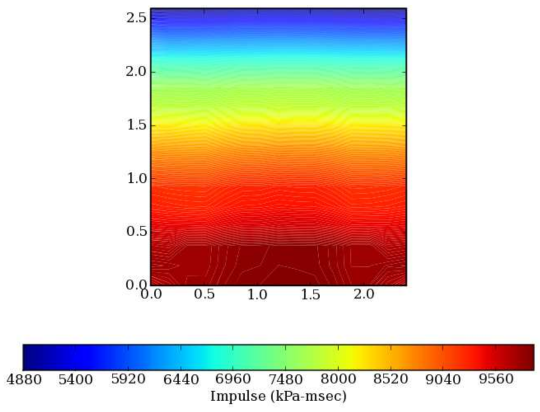

(b) Peak impulse

Figure 15.5: North face contours (L9 grid) for explosion in shipping container problem

Figure 15.6 plots peak values for the L9 grid along the interior ceiling, or top face. There exists a local maximum in pressure directly above the charge itself, although peak values occur at edges (at the charge location) due to focussing. The effect of venting on reducing peak values can be seen on the impulse plot where a marked decrease can be observed. The impulse is nearly constant along the section from the charge to the outlet vent.

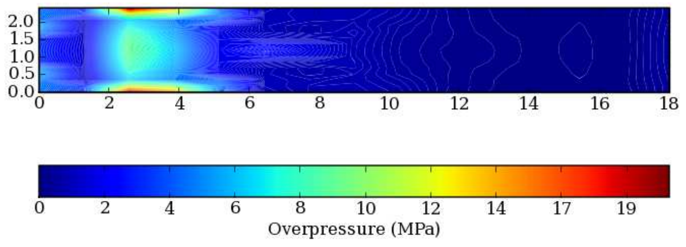

(a) Peak ovepressure

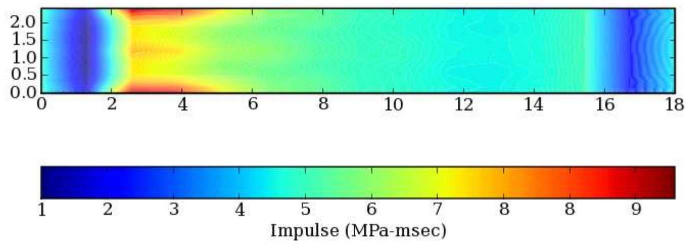

(b) Peak impulse

Figure 15.6: Top face contours (L9 grid) for explosion in shipping container problem

15.1.3 Average wall errors

Like in Table 14.7 an average error for the whole wall can be estimated by calculating the relative error between grids to obtain an average relative error per sensor point. This relative error is identical to the Richardson-extrapolated error if the refinement factor and solution order are 2 and 1 respectively. Decreasing errors for higher resolutions indicate convergence. These errors are shown in Table 15.1. Note that errors in pressure are quite high, and are as much as an order of magnitude higher than impulse errors. This behaviour is also seen in Tables 10.1 and 10.2 and 14.7. Although impulse errors are quite low, convergence has not been achieved either in impulse or pressure (except for the top face pressure).

As the greatest sources of error typically lie at corners and edges, it might be interesting to calculate this error *excluding* those sensors at corners/edges. The results are tabulated in Table 15.2. It is noteworthy that more wall faces do display convergent behaviour, although not always consistently in both the impulse and pressure. Convergence seems to depend on what quantity is computed, and even how it is computed. Pressure errors have been reduced by at least a factor of 2 compared to Table 15.1 and no impulse error exceeds 0.4%. The north face, being located farthest from the charge and more affected by wave coalesence, interaction, focussing and numerical diffusion, does not converge in either impulse or pressure.

As a final exercise, a simulation is performed on a series of much finer grids by reducing the domain size to only encompass the inlet-end (south) wall and the charge

Table 15.1: Estimated average relative errors for each face

Face	Impulse error	Pressure error
East face (L7-L8)	0.00764954	0.139601
East face (L8-L9)	0.0086392	0.149198
South face (L7-L8)	0.00735129	0.169336
South face (L8-L9)	0.0102446	0.247718
North face (L7-L8)	0.00840221	0.0288078
North face (L8-L9)	0.0120841	0.150225
Top face (L7-L8)	0.00899833	0.17061
Top face (L8-L9)	0.0124166	0.140126

Table 15.2: Estimated average relative errors (excluding edges) for each face

Face	Impulse error	Pressure error
East face (L7-L8)	0.00322188	0.075768
East face (L8-L9)	0.0031481	0.0710504
South face (L7-L8)	0.00212314	0.0719346
South face (L8-L9)	0.00175235	0.0649372
North face (L7-L8)	0.00289666	0.00655631
North face (L8-L9)	0.00440226	0.0627783
Top face (L7-L8)	0.00308275	0.0817211
Top face (L8-L9)	0.00315627	0.0409477

(with a symmetry boundary condition at the charge). Thus up until an early time (around 5 ms) the solution on this wall can be compared with the larger domain runs, until effects from the boundary cause divergences in the solution. Minimum cell sizes used in these adaptive-mesh simulations are 0.00732 m, 0.0146 m and 0.0293 m. Average facial errors between these solutions are shown in Table 15.3. In this case convergence for both impulse and pressure is observed, showing that these finer resolutions appear to be within the asymptotic convergence range.

Table 15.3: Smaller domain error estimates on south face

Grid	Impulse error	Pressure error
Medium-coarsest grid	0.00951	0.143
Finest-medium	0.00533	0.0964

A better estimate of the larger-domain errors can be thus computed by comparing the solution to the finest smaller-domain grid (up until 5 ms). The results are in Table 15.4 and the estimated errors for the south face in Table 15.1 are reproduced here. These better error estimates show that the larger-domain peak impulse errors are around 3% (even for the coarsest mesh), which is quite good, but peak overpressure errors are no smaller than 23%. The pressure errors do in fact converge on this calculation, but impulse does not converge monotonically.

Table 15.4: Better estimate of larger domain errors on south face

	Better estimate		Previous estimate	
Grid level	Impulse error	Pressure error	Impulse error	Pressure error
L7	0.0329	0.353	-	-
L8	0.0345	0.33	0.00735	0.169
L9	0.0226	0.232	0.01	0.248

These simulations demonstrate the difficulty of obtaining convergence for this problem, which is also noted in Section 14.1 and in Reference [171]. The simplest means to obtain convergent solutions is to employ finer meshes, but this can result in excessive resource usage (time and storage) for the current code. It is still encouraging that impulse errors have been shown to be quite low (no larger than 3.5%).

15.1.4 Pressure Amplification and Failure on the Outlet Wall

The effect of confinement can be quantified by observing how much larger the overpressures are at the far-end outlet wall and outlet vent compared to a free-field air burst. It is found that on the finest resolution mesh (L9 mesh) the average peak overpressure on the outlet wall (north face) and outlet vent is 1.66 MPa and 0.5 MPa respectively. The peak overpressure at the vent corresponds to a reflected shock from the outlet wall. Using scaled spherical TNT free-field data from Kinney [119], at the same straight-line scaled distance to the outlet wall the overpressure is around 0.024 MPa. Assuming a shock with this overpressure undergoes normal reflection, the reflected overpressure is calculated via the Rankine-Hugoniot relations to be 0.053 MPa. This means amplification factors at the outlet wall and vent of *at least* 31 and 9.4 respectively.

Approximating the outlet wall as a simply-supported flat plate of thickness 5 mm subject to the uniform load of 1.66 MPa, it is possible to calculate the maximum wall stress (located at the wall center) by a simple formula obtainable from a standard solid mechanics text [227]. As the wall is a nearly square section, the stress is simply

$0.2874q(L/t)^2$ where q is the load, L and t are the length and thickness respectively. It is computed to be 110 GPa; this is clearly much higher than the tensile strength of the steel wall (which is on the order of hundreds of megapascals), making failure a certainty.

If wall failure alone is being investigated, it is unnecessary to use numerical simulation as hand calculation via Kinney's free-field scaled data [119] is sufficient to demonstrate this. As the reflected overpressure is calculated to be 0.053 MPa (based on Kinney's curve), the computed stress is 3.5 GPa, which is still too high. In reality the walls are corrugated, effectively raising stiffness, and are not simply supported at their edges. More detailed modelling of the wall response is best obtained via a finite element simulation.

15.1.5 Performance

All simulations for the longer-domain simulations (used to generate Tables 15.1 and 15.2) were run in parallel on the SGI Altix cluster using 8 processors. The L7 mesh had a maximum of about 106,000 cells, running for 2.5 hours and required about 0.3 GB of memory. The L8 mesh had a maximum of 452,000 cells, elapsed time 9.6 hours and required 1.2 GB memory. The L9 mesh had a maximum of 2,120,000 cells, elapsed time of 69.13 hours and required 5.6 GB memory. Based on these figures the memory requirements are at most 2.95 kB per cell, which is slightly more than the value of 2.6 calculated in Section 11.3.

15.2 Explosion in a More Complex Facility

A more complicated geometry for the motor testing facility was considered in which the facility is partially buried on a hill side, with the outlet being a duct to enclose the rocket plume to reduce noise. A simulation was briefly performed mainly to test how well the code can handle this more complex geometry. A diagram of this geometry is shown in Figure 15.7. Also shown are the density contours and the superimposed grid on the vertical plane along the duct. The charge in this case is equivalent to 60 kg of TNT (a larger motor size) and three adaptive mesh simulations were performed with a minimum cell size of about 20 cm (level 7), 10 cm (level 8) and 5 cm (level 9).

The results show that no 'leakage' of the gas from inside of the duct to the surrounding atmosphere has occured, because the cells are refined to the highest level at the walls. The focussing of the shock in the duct has resulted in a stronger blast wave at the duct exit, evident from the better mesh adaptation compared to the blast escaping from the inlet and entryway. It appears from Figure 15.8 that the overpressure directly above the duct can be aligned with the standard free-field overpressure curve obtained from Kinney's data [119]. In this case the free-field curve is scaled to the charge weight and offset by 2.9 m (or 0.74 kg/m$^{1/3}$). This means that the blast exiting from the duct outlet can be treated essentially like a free-field blast, but offset by 2.9 m (a relatively small distance, indicating strong confinement). The behaviour of this offset free-field curve might be worth exploring for different explosives and geometries.

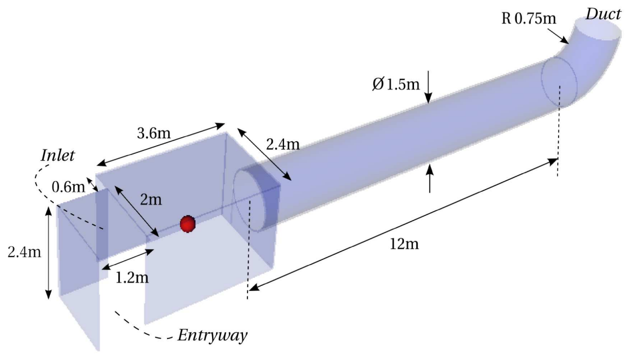

(a) Initial geometry

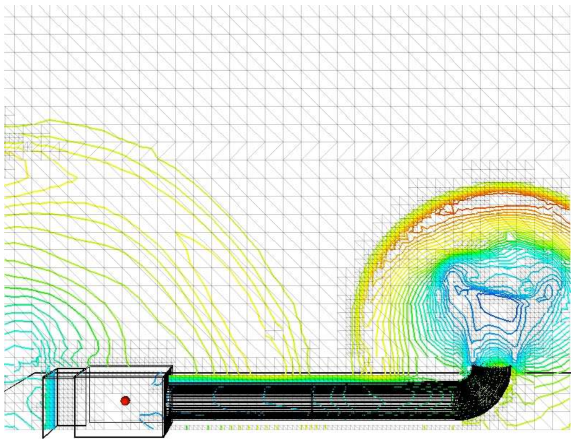

(b) Density contour on 2D plane

Figure 15.7: Initial geometry and contours for more complex motor testing facility

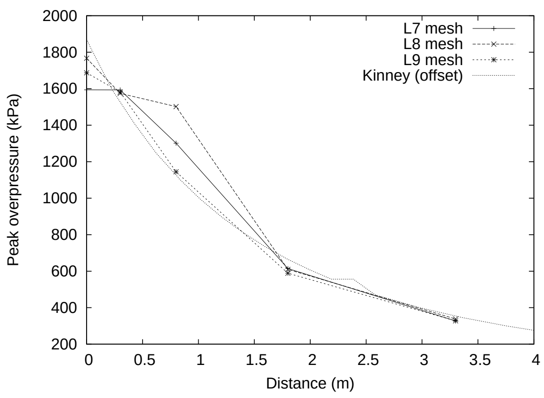

Figure 15.8: Overpressure above duct exit of motor testing facility

Chapter 16

Summary, Conclusions and Future Work

This thesis has described the design and testing of the CFD code `OctVCE` to model the problem of blast propagation in complex geometries. The main design intent behind this code is reliable prediction of blast loading in complex environments which is fast enough to be used in a design process. This in turn can aid assessment of critical damage zones and improve design of public spaces and structures. The code validation process has led to a better insight into its accuracy and limitations and has helped identify a number of areas and problems with the code that can be improved as future work.

Chapter 1 gave reasons why numerical simulation is in many cases the superior or even necessary approach, compared to empiricial or semiempirical methods, for solving this problem. An overview of previous attempts and codes also used in modelling blast propagation in realistic geometries was provided, and the basic characteristics of explosive blasts was discussed. Chapter 2 then presented different CFD methods which could be used to simulate flows in complex geometries, concluding with a discussion on different Cartesian cell methods and their advantages. A detailed discussion was provided of the VCE method and its associated shortcomings.

Chapter 3 then discussed the octree data structure and how it could be utilized as the basis for mesh adaptation in the code. Some algorithms in the form of pseudo-code were presented to demonstrate the recursive nature of the mesh adaptation process. Some measures that could be taken to increase speed (by sacrificing memory) and handle degeneracies were also discussed, and the two different adaptation indicators used in the code (based on velocity and density differences) were presented.

Chapter 4 centered on the numerical methodology of the code. The governing equations being solved, their method of discretization and integration, flux solvers used (the AUSMDV [221] and EFM [150] schemes), reconstruction method and equations of state were described. This section also reviewed the boundary conditions used in the code and described how initial explosions or charges are represented in the numerical simulation using the 'balloon analogue' or isothermal bursting sphere approach. Some point-inclusion query methods were also reviewed.

Chapter 5 provided a review of parallel computing, parallel programming methods and parallel performance measures, like Amdahl's law [8] and its inverse (the useful

Karp-Flatt metric [113]). Section 5.5 described the shared-memory parallel implementation of the code.

Chapter 6 proceeded to the verification stage of code testing to establish the reliability of the code programming in its implementation of the numerical methodology. Four different test cases were considered. The first case, the Method of Manufactured Solutions (Section 6.1), demonstrated higher-order behaviour of the code (between 1 and 2). In the second case (Section 6.2), the code was shown to provide solutions in good agreement with the classic Sod shock tube problem, and an adaptive mesh solution had a factor of savings of up to 3 in time and storage compared to the uniform grid result. The non-reflecting boundary conditions were also tested with this problem and shown to work well.

Section 6.3 demonstrated convergence as both subcell and grid resolution increased for supersonic flow over simple wedge and cone geometry. Importantly, the surface solution noise arising from the approximative nature of the VCE method (discussed in Section 2.4.4) was shown not to be significant for practical engineering purposes e.g. if integrated pressure forces are desired. Adaptive mesh solutions resulted in savings of up to 9 times in storage and 7 times in time compared to comparable uniformly-refined mesh solutions, demonstrating the large gains in efficiency obtainable from mesh adaptation. Section 6.4, which dealt with supersonic vortex flow, demonstrated very good grid convergence (sometimes as high as the formal order of accuracy) of the numerical result to the analytic solution.

Chapters 7 to 14 then described the numerous validation tests undergone by the code to establish how well it can solve realistic blast and shock propagation problems. In Chapter 7 the shock diffraction over a wedge was simulated, and good agreement with previous experimental and numerical data was shown. The code performance was also profiled for this simulation. Serial profiling showed that reconstruction-related operations dominated the calculation, suggesting that future work should target this area to improve efficiency. However, fairly good efficiency in the adaptation procedure was achieved. Parallel profiling (using the Karp-Flatt metric) showed a serial fraction for this calculation of approximately 10-20%, and significant overheads due to execution of the code on a NUMA system and the non-local nature of parallelization and work distribution among threads. This suggests that if any future development of the code is to occur, it should focus on more complex parallel implementations and importantly on improving the code's memory efficiency.

Chapter 8 presented a simulation of shock interaction with cylindrical geometry which showed good agreement with previous numerical work on this problem. Chapter 9 validated the one-dimensional spherical solver and demonstrated the accuracy of the isothermal bursting sphere solution with previous experimental and numerical data. It confirmed the findings of previous studies [166, 171] that the initial energy release is the most important factor when peak overpressure or postive impulse in the mid- to far-field regimes is desired. Non-reflecting boundary conditions were also tested for this problem and shown to work well. Chapter 10 proceeded to simulate spherical TNT blast for both the one-, two- and three-dimensional solvers. Convergence of the two- and three-dimensional solvers to the one-dimensional result was demonstrated, and the errors due to discretization and staircasing of the charge were measured. Parallel profiling of the simulations showed large parallel overhead, but around 10% serial fraction to the code.

Chapter 11 concerned simulations of blast near single barrier structures. Good agreement with previous data was shown, although there was a puzzling discrepancy in blast arrival times. Simulations employing the non-reflecting boundary conditions performed well when compared with larger-domain simulations. Savings of up to 5 times in time were observed between adaptive and uniformly-refined mesh solutions. However, the code was shown to be quite memory inefficient, which can impact performance considerably. Chapter 12 demonstrated the code's ability to simulate well explosions in complex axisymmetric containers. The current results were somewhat inferior to previous numerical results of commensurate resolution, but comparable accuracy was obtained when Richardson extrapolation [163, 164] of the results was performed using solutions from different meshes.

Chapter 13 tested the code in simulations of blast in three-dimensional environments consisting of simple grid-aligned rectangular-prismatic geometries, and the results compared well with previous experimental and numerical data. Chapter 14 focussed on simulations of blast in a more complex urban environment, and fairly good agreement with past results was achieved without the need for multi-dimensional remapping of an initial one-dimensional spherical result [171]. Parallel profiling of the code showed a serial portion of around 10% as before, and significant parallel overheads.

It was also observed that for this simulation, unnecessary and excessive refinement of the mesh occured near the fireball due to the adaptation criteria employed, and future work might also consider using a pressure-difference based indicator to prevent needless refinement in this region. It is difficult to know *a priori* what values of the adaptation indicators are optimum for the simulation; only guidelines can be provided. Convergence of solutions was not always demonstrable, although there were reliable trends. The previous data for this problem was supplied from Rose's `ftt_air3d` code [174], which is also an octree adaptive mesh, Cartesian cell code developed concurrently with `OctVCE`. Comparison of the codes' performance for this problem showed that `ftt_air3d` is much more efficient time-wise and storage-wise.

Chapter 15 focussed on an application study of the code in simulations of internal blast in a shipping container geometry. Regrettably there was no opportunity for experimental work to supplement the numerical study, but the work was part of a design process which helped in the evaluation of options for the rocket test facility. Convergence of solutions was not always easy to demonstrate due to the coarseness of the grids, and shock focussing at the edges and corners of the geometry. Nonetheless the simulations demonstrated very large amplification of pressures and positive impulses within the structure due to confinement of the blast.

Many of the validation simulations demonstrated that acceptable (but still somewhat inferior) solutions can be obtained without the need for first remapping a one-dimensional result before the blast passes the nearest surface feature. It would appear that the `OctVCE` code has been shown to be a reliable tool in simulating blast propagation in complex geometries, as per the aims of the thesis, and more generally that the VCE method and octree mesh adaptation appears suitable for such problems.

16.1 Comparison with a Similar Code

The `ftt_air3d` code of Rose *et al* [174] is similar to, more advanced than and developed at about the same time as the `OctVCE` code, and has greater time and memory efficiency. It may be instructive to compare and contrast the two codes in case future work in improving or extending `OctVCE` is undertaken.

The `ftt_air3d` code [174, 177] is written in FORTRAN and due to implementation of the Fully Threaded Tree (FTT) structure [118] (discussed in greater depth in Section 3.1) is much more memory-efficient than `OctVCE`, which stores mesh connectivity, geometric data and other information explicitly. Lower memory requirements contribute to overall better performance due to fewer cache misses. `ftt_air3d` also appears to use a one-dimensional form of reconstruction whilst `OctVCE` uses multi-dimensional reconstruction requiring inversion of matricies. In `OctVCE` this forms a significant portion (50%) of the calculation code (as mentioned above) and given the success of `ftt_air3d`, it may be that multi-dimensional reconstruction is not required for such problems.

Another very significant time-saving strategy used in `ftt_air3d` is the use of local but interleaved timestepping (depending on cell level) and an apparently less conservative timestep. `ftt_air3d` seems to use a timestep based on the expression

$$\Delta t = \frac{\Delta x}{max\,(a + |u_i|)} \tag{16.1}$$

with the maximum taken over the three directions $i = x, y, z$ [176]. If this expression is compared with Equation 4.7 and assuming the $(a+u)$ term is constant, Equation 4.7 gives a timestep which is 6 times smaller than Equation 16.1 in three dimensions. As it is very simple in `OctVCE` to increase the timestep e.g. by increasing the CFL or adopting Equation 16.1, this might be worth exploring for future simulations. To ensure stability and proper shock tracking, the mesh adaptation frequency can be increased and more aggressive cell merging undertaken to ensure large cells everywhere. Also, a less conservative CFL "cut-back" procedure (Section 4.8.1, page 37) might be used e.g. setting a larger value of ϵ_{cut}.

The adaptation indicators in `OctVCE` were chosen because of past success [148, 155, 211], capability to refine cells about other discontinuities like slip layers and provision of some refinement in the positive phase region of the blast. This can sometimes result in excessive refinement about relatively unimportant regions like the explosive products. This problem may not be present in `ftt_air3d`, which uses a simple pressure difference indicator. It also provides for some degree of refinement behind the blast by testing if the number of times a cell is considered for coarsening reaches some threshold value. `ftt_air3d` also allows specification of regions where mesh refinement can be switched off, which is not implemented in `OctVCE`.

Unlike `OctVCE`, `ftt_air3d` also supports remapping of one-dimensional spherical solutions to multi-dimensions, which can produce well-resolved blast profiles and save save solution time in the early stages of the explosion. Compared to `OctVCE` which allocated or deallocated memory (corresponding to refining or coarsening respectively) on a per cell basis, `ftt_air3d` appears to be more efficient in its handling of memory by allocating or deallocating stacks of cells. Codes that frequently allocate or deallocate memory do suffer from performance ineffiencies due to memory management overhead [105, 174], and the memory in `OctVCE` might become more fragmented over time than with `ftt_air3d` [177].

However, `OctVCE` does have parallel processing capability, unlike `ftt_air3d`, and it can handle geometry constructed of arbitrary surface polygons instead of just convex polygons (required by `ftt_air3d`) due to the generality of the VCE method. A disadvantage is possibly more time spent in computing geometrical operations like point-inclusion queries. Due to the axisymmetric extension to the VCE method, `OctVCE` can also simulate axisymmetric flows in complex geometry in addition to the simple height-of-burst problem. A parallel `OctVCE` solution conjoined with a less conservative timestepping strategy discussed above might be competitive with a `ftt_air3d` run. The parallel implementation (Section 5.5) seems to perform well given the inherently serial portion of the code, but still could be more efficient, due to the large memory requirements and locality issues when executed on a NUMA machine (as discussed above).

Further work might thus first focus on reducing memory usage without comprimising the basic numerical methodology. It may still be possible to achieve performance competitive with `ftt_air3d` despite the relatively simple parallelization method, explicit storage of neighbouring connectivity and use of list structures to access cells. For example, some relatively simple improvements to the `cell` data structure (Figure K.4 in Appendix K) can be made without requiring too much alterations to the code.

The `gradient` and `limiters` structures could be combined into a single limited gradient quantity, as in `ftt_air3d`, and geometric data like interface areas, volumes and surface normals really only require storage for intersected cells, being easily derived for unobstructed cells based on cell level. These additional complexities arise because intersected cells in `OctVCE` are not always at the finest level (unlike `ftt_air3d`), which require more storage to handle these special cases. Given the accuracy of the method, it may also be sufficient to use a single interface flux vector, even if the interface is shared by two or more cells at finer level.

16.2 Access to the Source Code

The `OctVCE` program source code and user manual can be found in
`http://www.mech.uq.edu.au/staff/jacobs/cfcfd/`.

Bibliography

[1] M J Aftosmis. Solution adapative Cartesian grid methods for aerodynamics flows with complex geometries, 1997. 28th Computational Fluid Dynamics Lecture Series, VKILS 1997-02.

[2] M J Aftosmis, G Adomavicus, and M J Berger. A parallel multilevel method for adaptively refined cartesian grids with embedded boundaries. In *38th Aerospace Sciences Meeting and Exhibit*, 2000. AIAA 2000–0808.

[3] M J Aftosmis, M J Berger, and J E Melton. Adaptation and surface modeling for Cartesian mesh methods, 1995. AIAA–95–1725–CP.

[4] M J Aftosmis, M J Berger, J E Melton, and M D Wong. 3D applications of a Cartesian grid Euler method. In *33rd Aerospace Sciences Meeting and Exhibit*, 1995. AIAA 95–0853.

[5] M J Aftosmis, D Gaitonde, and T Sean Tavares. On the accuracy, stability and monotonicity of various reconstruction algorithms for unstructured meshes. In *32nd Aerospace Sciences Meeting and Exhibit*, 1994. AIAA 94–0415.

[6] M J Aftosmis, D Gaitonde, and T S Tavares. Behaviour of linear reconstruction techniques on unstructured meshes. *AIAA Journal*, 33(11):2039–2049, 1995.

[7] Daniel Ambrosini, B Luccioni, A Jacinto, and R Danesi. Location and mass of explosive from structural damage. *Engineering Structures*, 27:167–176, 2005.

[8] G Amdahl. The validity of the single processor approach to achieving large scale computing capabilities. In *AFIPS Conference Proceedings*, pages 483–485, 1967.

[9] J D Anderson. *Computational Fluid Dynamics: the Basics with Applications.* McGraw-Hill, New York, 1995.

[10] J D Anderson. *Modern Compressible Flow: With Historical Perspective.* McGraw-Hill Higher Education, New York, 3rd edition, 2003.

[11] J G Anderson, G Katselis, and C Caputo. Analysis of a Generic Warhead Part I: Experimental and Computational Assessment of Free Field Overpressure, 2002. DSTO Weapons Systems Division, Australia, DSTO-TR-1313.

[12] B J Armstrong, D D Rickman, J T Baylot, and T L Bevins. Code Validation Studies for Blast in Urban Terrain. In *Proceedings of 2002 HPC User's Group Conference*, 2002.

[13] U.S. Army. The Antiterrorist Planner Software – A Tool for Vulernability Assessment of Facilities and Force Protection Planning, 1988. U.S. Army Engineer Waterways Experiment Station, 3909 Halls Ferry Road, Vicksburg, MS 39180-6199.

[14] M Arora and P L Roe. A Well-Behaved TVD Limiter for High-Resolution Calculations of Unsteady Flow. *Journal of Computational Physics*, 132(1):3–11, 1997.

[15] L S Avila. *The VTK user's guide.* Kitware, Inc., Clifton Park, NY, 2004.

[16] A Bagabir and D Drikakis. Numerical experiments using high-resolution schemes for unsteady, inviscid, compressible flows. *Computer Methods in Applied Mechanics and Engineering*, 193:4675–4705, 2004.

[17] E L Baker. An Explosives Products Thermodynamic Equation of State Appropriate for Material Acceleration and Overdriven Detonation: Theoretical Background and Formulation, 1991. ARAED-TR-911013, U.S. Army Armament Research, Development and Engineering Center, Picatinney Arsenal, New Jersey.

[18] E L Baker and D L Littlefield. Implementation of a High Explosive Equation of State into an Eulerian Hydrocode. In *AIP Conference Proceedings*, volume 706, pages 375–378, 2004.

[19] W E Baker, P A Cox, P S Westine, J J Kulesz, and R A Strehlow. *Explosion Hazards and Evaluation.* Elsevier, New York, 1983.

[20] T J Barth. On Unstructured Grids and Solvers, 1990. von Karman Institute for Fluid Dynamics, Lecture Series 1990–03.

[21] J D Baum, L Hong, E Mestreau, and C Deel. Assessment of the terrorist attack on the US Embassy in Nairobi, Kenya. In *Proceedings of the 10th International Symposium on Interaction of the Effects of Munitions with Structures, San Diego*, 2001.

[22] J D Baum and R Löhner. Numerical simulation of a shock interaction with a modern main battlefield tank, 1991. AIAA-91-1666.

[23] J D Baum, H Luo, and R Löhner. Numerical simulation of a blast inside in the world trade center, 1995. AIAA 95-0085.

[24] J Bell, M Berger, J Saltzman, and M Welcome. Three-dimensional adaptive mesh refinement for hyperbolic conservation laws. *SIAM Journal of Scientific Computing*, 15(1):127–138, 1994.

[25] G Ben-dor, O Igra, and T Elperin. *Handbook of Shock Waves*, volume 2. Academic Press, San Diego, 2001.

[26] M J Berger. Adaptive Mesh Refinement for Hyperbolic Partial Differential Equations. *Journal of Computational Physics*, 53:484–512, 1984.

[27] M J Berger and R J LeVeque. An Adaptive Cartesian Mesh Algorithm for the Euler Equations in Arbitrary Geometries, 1989. AIAA 89–1930–CP.

[28] R Berrendorf and G Nieken. Performance characteristics for OpenMP constructs on different parallel computer architectures. *Concurrency: Practice and Experience*, 12:1261–1273, 2000.

[29] R Biswas and R Strawn. Tetrahedral and hexahedral mesh adaptation for CFD problems. *Applied Numerical Mathematics*, 26(1–2):135–151, 1998.

[30] T Blacker. Meeting the challenge for automated conformal hexahedral meshing. In *9th International Meshing Roundtable, New Orleans*, 2000.

[31] T Blacker. Auotmated Conformal Hexahedral Meshing Constraints, Challenges and Opportunities. *Engineering with Computers*, 17:201–210, 2001.

[32] T D Blacker and R J Meyers. Seams and Wedges in Plastering: A 3-D Hexahedral Mesh Generation Algorithm. *Engineering with Computers*, 9:83–93, 1993.

[33] BLASTX, 1996. U.S. Army Engineer Waterways Experiment Station, Mississippi.

[34] OpenMP Architecture Review Board. OpenMP C and C++ Application Program Interface, 2002. Version 2.0.

[35] D Bond, B Trinh, and D Fox. Wagtail Solid Rocket Project, 2007. University of Queensland MECH4552 Design Project Report.

[36] J Bonet and J Peraire. An Alternating Digital Tree (ADT) algorithm for 3D geometric searching and intersection problems. *International Journal for Numerical Methods in Engineering*, 31:1–17, 1991.

[37] J P Boris. The threat of chemical and biological terrorism: preparing a response. *Computing in Science and Engineering*, 4(2):22–32, 2002.

[38] S Børve, M Omang, and J Trulsen. Regularized smoothed particle hydrodynamics with improved multi-resolution handling. *Journal of Computational Physics*, 208:345–367, 2005.

[39] M A Brittle. Blast propagation in a geometrically complex urban environment. Master's thesis, Royal Military College of Science Engineering Systems Department, 2004.

[40] H L Brode. Numerical Solutions of Spherical Blast Waves. *Journal of Applied Physics*, 26:766–775, 1955.

[41] H L Brode. Blast Wave from a Spherical Charge. *Physics of Fluids*, 2:217–229, 1959.

[42] A E Bryson and R W F Gross. Diffraction of Strong Shocks by Cones, Cylinders, and Spheres. *Journal of Fluid Mechanics*, 10:1–16, 1961.

[43] P S Bulson. *Explosive Loading of Engineering Structures.* E and FM Spon, UK, 1997.

[44] J L Cambier, S Tokarcik, and D K Prabhu. Numerical simulations of unsteady flow in a hypersonic shock tunnel facility. In *AIAA 17th Aerospace Ground Testing Conference*, Nashville, TN, 1992.

[45] R S Cant, W N Dawes, and A M Savill. Advanced CFD and Modeling of Accidental Explosions. *Annual Review of Fluid Mechanics*, 36:97–119, 2004.

[46] Y A Çengel and M A Boles. *Thermodynamics: an engineering approach.* McGraw Hill, New York, 4th edition, 2002.

[47] R Chandra, L Dagum, D Kohr, D Maydan, J McDonald, and R Menon. *Parallel Programming in OpenMP.* Academic Press, USA, 2001.

[48] T C Chapman, T A Rose, and P D Smith. Blast wave simulation using AUTODYN2D: a parametric study. *International Journal of Impact Engineering*, 16(5/6):777–787, 1995.

[49] T C Chapman, T A Rose, and P D Smith. Reflected blast wave resultants behind cantilever walls: A new prediction technique. *International Journal of Impact Engineering*, 16(3):397–403, 1995.

[50] E F Charlton. *An Octree Solution to Conservation–laws over Arbitrary Regions (OSCAR) with Applications to Aircraft Aerodynamics.* PhD thesis, The University of Michigan, 1997.

[51] E F Charlton and K G Powell. An Octree Solution to Conservation-laws over Arbitrary Regions, 1997. AIAA 97-0198.

[52] R F Chisnell. An analytic description of converging shock waves. *Journal of Fluid Mechanics*, 354:357–375, 1998.

[53] T J Chung. *Computational fluid dynamics*. Cambridge University Press, Cambridge, 2002.

[54] S Cieslak, S B Kheil, I Choquet, and A Merlen. Cut cell strategy for 3-D blast waves numerical simulations. *Shock Waves*, 10:421–429, 2001.

[55] J F Clarke and M McChesney. *The dynamics of real gases*. Butterworths, London, 1964.

[56] J K Clutter. A reduced combustion model for vapor cloud explosions validated against full-scale data. *Journal of Loss Prevention in the Process Industries*, 14:181–192, 2001.

[57] J K Clutter, J T Mathis, and M W Stahl. Modeling environmental effects in the simulation of explosion events. *International Journal of Impact Engineering*, 34:973–989, 2007.

[58] W J Coirier. *An Adaptively-Refined, Cartesian, Cell-Based Scheme for the Euler and Navier-Stokes Equations*. PhD thesis, The University of Michigan, 1994.

[59] W J Coirier and K G Powell. An Accuracy Assessment of Cartesian-Mesh Approaches for the Euler Equations, 1993. AIAA 93–3335–CP.

[60] P Colella and H M Glaz. Efficient Solution Algorithms for the Riemann Problem for Real Gases. *Journal of Computational Physics*, 49:264–289, 1985.

[61] T Colonius. Modeling Artifical Boundary Conditions for Compressible Flow. *Annual Review of Fluid Mechanics*, 36:315–345, 2004.

[62] R Courant, K Friedrichs, and H Lewy. On the Partial Difference Equations of Mathematical Physics. *IBM Journal*, 11(2):215–234, 1967.

[63] G Cybenko. Dynamic load balancing for distributed memory multiprocessors. *Journal of Parallel and Distributed Computing*, 7:279–301, 1989.

[64] A Dadone. Cartesian grid computation of inviscid flows about multiple bodies. In *41st Aerospace Sciences Meeting and Exhibit*, 2003. AIAA 2003-1121.

[65] A Dadone and B Grossman. An Immersed Body Methodology for Inviscid Flows on Cartesian Grids. In *40th Aerospace Sciences Meeting and Exhibit*, 2002. AIAA 2002–1059.

[66] D De Zeeuw and K G Powell. An Adaptively Refined Cartesian Mesh Solver for the Euler Equations. *Journal of Computational Physics*, 104:56–68, 1993.

[67] Valgrind developers. Valgrind. ¡http://www.valgrind.org/¿, accessed May 2008.

[68] Maxima development team. Maxima, a computer algebra system. ¡http://maxima.sourceforge.net/¿, accessed May 2008.

[69] K D Devine, E G Boman, R T Heaphy, B A Hendrickson, J D Teresco, J Faik, J E Flaherty, and L G Gervasio. New challenges in dynamic load balancing. *Applied Numerical Mathematics*, 52:133–152, 2005.

[70] J M Dewey and A van Netten. Calculating Blast-Effects Distances in Urban Environments. In *17th International Symposium on Military Aspects of Blast and Shock*, Las Vegas, Nevada USA, 2002.

[71] D Drikakis, F Grinstein, and D Youngs. On the computation of instabilities and symmetry-breaking in fluid mechanics. *Progress in Aerospace Sciences*, 41:609–641, 2005.

[72] J A Edwards and T Ren. Vortex Interaction with an Aerofoil Using Chimera and the *AMR* algorithm. In *AIAA Atmospheric Flight Mechanics Conference and Exhibit*, volume AIAA 2002–4806, 2002.

[73] H El-Rewini and M Abd-El-Barr. *Advanced Computer Architecture and Parallel Processing*. John Wiley and Sons, Inc, Hoboken, New Jersey, 2005.

[74] G E Fairlie, N F Johnson, and K C Moran. Validated Numerical Simulations of Blast Loads on Structures. In *16th International Symposium on Military Aspects of Blast and Shock*, Oxford, England, 2000.

[75] F R Feito and J C Torres. Inclusion test for general polyhedra. *Computers and Graphics*, 21(1):23–30, 1997.

[76] J E Flaherty, R M Loy, M S Shephard, B K Szymanski, J D Teresco, and L H Ziantz. Adaptive Local Refinement with Octree Load-Balancing for the Parallel Solution of Threee-Dimensional Conservation Laws. *Journal of Parallel and Distributed Computing*, 47:139–152, 1997.

[77] H Forrer and R Jeltsch. A higher order boundary treatment for cartesian-grid methods. *Journal of Computational Physics*, 140:259–277, 1998.

[78] C E Fothergill, S Chynoweth, P Roberts, and A Packwood. Evaluation of a CFD porous model for calculating ventilation in explosion hazard assessments. *Journal of Loss Prevention in the Process Industries*, 16:341–347, 2003.

[79] P J Frey and P L George. *Mesh generation : application to finite elements*. Hermes Science Publishing, Paris, 2000.

[80] N T Frink. Upwind Scheme for Solving the Euler Equations on Unstructured Tetrahedral Meshes. *AIAA Journal*, 30(1):70–77, 1992.

[81] B Fryxell, K Olson, P Picker, F X Timmes, M Zingale, D Q Lamb, P MacNeice, R Rosner, J W Truran, and H Tufo. FLASH: An adaptive mesh hydrodynamics code for modeling astrophysical thermonuclear flashes. *The Astrophysical Journal Supplement Series*, 131:273–334, 1999.

[82] C F Gerald and P O Wheatley. *Applied Numerical Analysis*. Pearson, Boston, 7th edition, 2004.

[83] R Gollan. Verification Exercises for a Compressible Flow Code. In *10th International Workshop on Shock-Tube Technology*, Brisbane, Australia, 2006.

[84] R J Goozee. *Simulation of a Complete Shock Tunnel Using Parallel Computer Codes*. PhD thesis, The University of Queensland, 2003.

[85] J J Gottlieb and C P T Groth. Assessment of Riemann Solvers for Unsteady One-Dimensional Inviscid Flows of Perfect Gases. *Journal of Computational Physics*, 78(2):437–458, 1988.

[86] J A Greenough and J W Jacobs. A Numerical Study of Shock-Acceleration of a Diffuse Helium Cylinder. In *Proceedings of the Fifth International Workshop on Comrpessible Turbulent Mixing*, 1996.

[87] W Gropp, E Lusk, and A Skjellum. *Using MPI: Portable Parallel Programming with the Message-Passing Interface*. The MIT Press, Cambridge, Massachusetts, 1994.

[88] M E Hayder, F Q Hu, and M Y Hussaini. Toward Perfectly Absorbing Boundary Conditions for Euler Equations. *AIAA Journal*, 37(8), 1999.

[89] M Held. Blast Waves in Free Air. *Propellants, Explosives, Pyrotechnics*, 8:1–7, 1983.

[90] A Henderson and J Ahrens. *The ParaView guide.* Kitware, Clifton Park, NY, 2004.

[91] B Hendrickson. Graph partitioning and parallel solvers: Has the emperor no clothes, 1998. Lecture notes in Computer Science, 1457: 218–225.

[92] J Henrych. *The Dynamics of Explosion and Its Use.* Elsevier Scientific Publishing Company, Czechoslovakia, 1979.

[93] E Hertel, J Bell, M Elrick, A Farnsworth, G Kerley, J McGlaun, S Petney, S Silling, P Taylor, and L Yarrington. CTH: A Software Family for Multi-Dimensional Shock Physics Analysis. In *Proceedings of the 19th International Symposium on Shock Waves*, pages 377–382, France, 1993.

[94] S Hikida and S Needham. *Low Altitude Multiple Burst (LAMB) Model, Volume 1: Shock Description.* S-Cubed, Albuquerque, New Mexico, 1981.

[95] M D Hill and J R Larus. Cache considerations for multiprocessor programmers. *Communications of the ACM*, 33(8):97–102, 1990.

[96] C Hirsch. *Numerical Computation of Internal and External Flows. Volume 1: Fundamentals of Numerical Discretization*, volume 1. Wiley, England, 1988.

[97] C Hirsch. *Numerical Computation of Internal and External Flows. Volume 2: Computational Methods for Inviscid and Viscous Flows*, volume 2. Wiley, England, 1988.

[98] K Hormann and A Agathos. The point in polygon problem for arbitrary polygons. *Computational Geometry*, 20:131–144, 2001.

[99] W P Horn and D L Taylor. A Theorem to Determine the Spatial Containment Point in a Planar Polyhedron. *Computer Vision, Graphics and Image Processing*, 45:106–116, 1989.

[100] C W Huang and T Y Shih. On the complexity of point-in-polygon algorithms. *Computers and Geosciences*, 23(1):109–118, 1997.

[101] W K E Huntington-Thresher and I G Cullis. TNT blast scaling for small charges. In *19th International Symposium of Ballistics*, pages 647–654, 2001.

[102] M Y Hussaini and T A Zang. Spectral Methods in Fluid Dynamics. *Annual Review of Fluid Mechanics*, 19:339–367, 1987.

[103] D W Hyde. *CONWEP: Conventional Weapons Effects Program.* Waterways Experiment Station, Vicksburg, MS, USA, 1991.

[104] Century Dynamics Inc. Autodyn user's manual-version 4.2, 1997.

[105] Silicon Graphics Inc. Linux Application Tuning Guide, 2005. SGI Manual 007-4639-005.

[106] D M Ingram, D M Causon, and C G Mingham. Developments in cartesian cut cell methods. *Mathematics and Computers in Simulation*, 61(3–6):561–572, 2003.

[107] M M Ismail and S G Murray. Study of the Blast Wave Parameters from Small Scale Explosions. *Propellants, Explosives, Pyrotechnics*, 18:11–17, 1993.

[108] M M Ismail and S G Murray. Study of the Blast Waves from the Explosion of Nonspherical Warheads. *Propellants, Explosives, Pyrotechnics*, 18:132–138, 1993.

[109] P A Jacobs. MB_CNS: A computer program for the simulation of transient compressible flows, 1996. Department of Mechanical Engineering Report 10/96, The University of Queensland, Australia.

[110] I A Johnston. *Simulation of Flow Around Hypersonic Blunt–Nosed Vehicles for the Calibration of Air Data Systems.* PhD thesis, The University of Queensland, 1999.

[111] Y E Kalay. Determining the Spatial Containment of a Point in General Polyhedra. *Computer Graphics and Image Processing*, 19:303–334, 1982.

[112] G E Karniadakis and R M Kirby. *Parallel Scientific Computing in C++ and MPI.* Cambridge University Press, United Kingdom, 2003.

[113] A H Karp and H P Flatt. Measuring parallel processor performance. *Communications of the ACM*, 33(5):539–543, 1990.

[114] G Karypis and V Kumar. METIS - a Software Package for Partitioning Unstructured Graphs, Partitioning Meshes, and Computing Fill-Reducing Orderings of Sparse Matrices. Version 4.0, 1998. University of Minnesota Report.

[115] G Karypis, K Schloegel, and V Kumar. ParMETIS - Parallel Graph Partitioning and Sparse Matrix Ordering Library. version 3.1, 2003. University of Minnesota Report.

[116] K Kato, T Aoki, S Kubota, and M Yoshida. A numerical scheme for strong blast wave driven by explosion. *International Journal for Numerical Methods in Fluids*, 51:1335–1353, 2006.

[117] M P Kerry, B J Bibby, A J Martin, and R Garforth. Engineering level coupled blast flow and damage module with rapid input scene generator for multibuilding environments. In *17th International Symposium on Military Aspects of Blast and Shock*, Las Vegas, Nevada USA, 2002.

[118] A M Khokhlov. Fully Threaded Tree Algorithms for Adaptive Refinement Fluid Dynamics Simulations. *Journal of Computational Physics*, 143:519–543, 1998.

[119] G F Kinney. *Explosive Shocks in Air.* Springer-Verlag Berlin Heidelberg, 2nd edition, 1985.

[120] H Kleine, J M Dewey, K Ohashi, T Mizukaki, and K Takayama. Studies of the TNT equivalence of silver azide charges. *Shock Waves*, 13:123–138, 2003.

[121] A Klomfass. A Cartesian grid finite-volume method for the simulation of gasdynamic flows about geometrically complex objects. In *26th International Symposium on Shock Waves*, 2007.

[122] A L Kuhl. Mixing in Explosions, 1993. Lawrence Livermore National Laboratory Report UCRL-JC-115690.

[123] Rice D L, Giltrud M E, Luo H, Mestreau E, and Baum J. Experimental and Numerical Investigation of Shock Diffraction About Blast Walls. In *Proceedings of the 16th International Symposium of the Military Aspects of Blast and Shocks*, pages 335–342, Oxford, 2000.

[124] A M Landsberg and J P Boris. The Virtual Cell Embedding method: a simple approach for gridding complex geometries, 1997. AIAA–97–1982.

[125] A M Landsberg, J P Boris, T R Young, and R J Scott. Computing Complex Shocked Flows Through the Euler Equations. In *Shock waves at Marseille: Proceedings of the 19th International Symposium on Shock Waves*, pages 421–426, 1993.

[126] E Lee, M Finger, and W Collins. JWL Equation of State Coefficients for High Explosives, 1973. Lawrence Livermore Laboratory Report No. UCID-16189.

[127] E L Lee, H C Horning, and J W Kury. Adiabatic Expansion of High Explosive Detonation Products, 1968. University of California Report No. UCRL–50422.

[128] W Lin and C J Chen. Automatic grid generation of complex geometries in Cartesian co–ordinates. *International Journal for Numerical Methods in Fluids*, 28:1303–1324, 1998.

[129] C A Lind, J P Boris, and E S Oran. The Effect of Charge Shape on Partially Confined Detonations. *Journal of Pressure Vessel Technology*, 120:313–318, 1998.

[130] J Linhart. A quick point-in-polyhedron test. *Computers and Graphics*, 14(3/4):445–447, 1990.

[131] R Löhner, J D Baum, C Charman, and D Pelessone. Fluid–structure interaction simulations using parallel computers, 2003. Lecture notes in Computer Science, 2565: 3–23.

[132] H Luo, J D Baum, and R Löhner. A hybrid Cartesian grid and gridless method for compressible flows. *Journal of Computational Physics*, 214(2):618–632, 2006.

[133] C L Mader. *Numerical modeling of explosives and propellants.* CRC Press, Boca Raton, 1998.

[134] A Masud, M Bhanabhagvanwala, and R A Khurram. An adaptive mesh rezoning scheme for moving boundary flows and fluid-structure interaction. *Computers and Fluids*, 36:77–91, 2007.

[135] T Minyard and Y Kallinderis. Octree partitioning of hybrid grids for parallel adaptive viscous flow simulations. *International journal for numerical methods in fluids*, 26:57–58, 1998.

[136] A Miura, A Matsuo, T Mizukaki, T Shiraishi, G Utsunomiya, K Takayama, and I Nojiri. Reflection and Diffraction Phenomena of Blast Wave Propagation in Nuclear Fuel Cycle Facility. *JSME International Journal, Series B*, 42(2):287–292, 2004.

[137] J J Monaghan. Smoothed Particle Hydrodynamics. *Reports on Progress in Physics*, 68:1703–1759, 2005.

[138] C Needham, K Potter, and S Hikida. Structure load calculations for a full-scale office building. In *16th International Symposium on Military Aspects of Blast and Shock*, pages 129–136, Oxford, England, 2000.

[139] C E Needham. Blast Loads and Propagation around and over a Building. In *26th International Symposium on Shock Waves*, 2007.

[140] M Nemec, M J Aftosmis, and T H Pulliam. CAD–Based Aerodynamic Design of Complex Configurations Using a Cartesian Method. In *42nd AIAA Aerospace Sciences Meeting and Exhibit*, 2004. NAS Technical Report NAS–04–001.

[141] P Nithiarasu and O C Zienkiewicz. Adaptive mesh generation for fluid mechanics problems. *International Journal for Numerical Methods in Engineering*, 47:629–662, 2000.

[142] W L Oberkampf and T G Trucano. Verification and validation in computational fluid dynamics. *Progress in Aerospace Sciences*, 38:209–272, 2002.

[143] M Omang, S Børve, and J Trulsen. Numerical simulations of shock wave reflection phenomena in non-stationary flows using regularized smoothed particle hydrodynamics (rsph). *Shock Waves*, 16:167–177, 2006.

[144] M Omang, S Børve, and J Trulsen. Modelling High Explosives using Smoothed Particle Hydrodynamics. In *26th International Symposium on Shock Waves*, 2007.

[145] P B Pember, J B Bell, P Colella, W Y Crutchfield, and M L Welcome. An Adaptive Cartesian Grid Method for Unsteady Compressible Flow in Irregular Regions. *Journal of Computational Physics*, 120:278–304, 1995.

[146] P Person and J Lee. *Rock blasting and explosives engineering.* CRC Press, Boca Raton, Fla, 1994.

[147] W P Petersen and P Arbenz. *Introduction to Parallel Computing: A Practical Guide with Examples in C.* Oxford University Press, USA, 2004.

[148] P R Petrie. *Numerical Simulation of Diaphragm Rupture.* PhD thesis, The University of Queensland, 1997.

[149] J R Pilkington and S B Baden. Dynamic partitioning of non-uniform structured workloads with space filling curves. *IEEE Transactions on Parallel and Distributed Systems*, 7(3):288–300, 1996.

[150] D I Pullin. Direct Simulation Methods for Compressible Inviscid Ideal-Gas Flow. *Journal of Computational Physics*, 34(2):231–244, 1980.

[151] M J Quinn. *Parallel programming in C with MPI and OpenMP.* McGraw-Hill, Dubuque, Iowa, 2004.

[152] J J Quirk. *An Adaptive Grid Algorithm For Computational Shock Hydrodynamics.* PhD thesis, Cranfield Institute of Technology College of Aeronautics, 1991.

[153] J J Quirk. An alternative to unstructured grids for computing gas dynamic flows around arbitrarily complex two–dimensional bodies. *Computers Fluids*, 23(1):125–142, 1994.

[154] J J Quirk. A Contribution to the Great Riemann Solver Debate. *International Journal for Numerical Methods in Fluids*, 18(6):555–574, 1994.

[155] Löhner R, Yang C, Baum J D, Luo H, Pelessone D, and Charman C M. The Numerical Simulation of Strongly Unsteady Flow with Hundreds of Moving Bodies. *International Journal for Numerical Methods in Fluids*, 31:113–120, 1999.

[156] S Rahman, E Timofeev, H Kleine, and K Takayama. On pressure measurements in blast wave flow fields generated by milligram charges. In *26th International Symposium on Shock Waves*, 2007.

[157] B Rajkumar. *High Performance Cluster Computing: Architectures and Systems.* Prentice Hall, NJ, USA, 1999.

[158] J W Reed. Analysis of the Accidental Explosion at Pepcon, Henderson, Nevada, 1988. Sandia National Laboratories Report SAND88–2902 UC–70.

[159] A M Remennikov. A review of methods for predicting bomb blast effects on buildings. *Journal of Battlefield Technology*, 6(3):5–10, 2003.

[160] A M Remennikov and T A Rose. Modelling blast loads on buildings in complex city geometries. *Computers and Structures*, 83:2197–2205, 2005.

[161] A M Remennikov and T A Rose. Predicting the effectiveness of blast wall barriers using neural networks. *International Journal of Impact Engineering*, 34(12):1907–1923, 2007.

[162] S K Richards, X Zhang, X X Chen, and P A Nelson. The evaluation of non-reflecting boundary conditions for duct acoustic computation. *Journal of Sound and Vibration*, 270:539–557, 2004.

[163] L F Richardson. The Approximate Arithmetical Solution by Finite Differences of Physical Problems Involving Differential Equations, with an Application to the Stresses in a Masonry Dam. *Transactions of the Royal Society of London*, 210:307–357, 1908. Series A.

[164] L F Richardson. The Deferred Approach to the Limit. *Transactions of the Royal Society of London*, 226:229–361, 1927. Series A.

[165] R C Ripley, B Rosen, D V Ritzel, and D R Whitehouse. Small-scale modelling of explosive blasts in urban scenarios. In *21st International Symposium on Ballistics*, pages 885–892, Adelaide, South Australia, 2004.

[166] D V Ritzel and K Matthews. An adjustable explosion–source model for CFD blast calculations. In *21st International Symposium on Shock Waves*, 1997. Paper 6590.

[167] P J Roache. Quantification of uncertainty in computational fluid dynamics. *Annual Review of Fluid Mechanics*, 29:123–160, 1997.

[168] P J Roache. *Verification and Validation in Computational Science and Engineering*. Hermosa Publishers, Albuquerque, New Mexico, 1998.

[169] P J Roache. Verification of Codes and Calculations. *AIAA Journal*, 36(5):696–701, 1998.

[170] P Roe. A Survey of Upwind Differencing Techniques, 1988. Lecture notes in Physics, 323:69–78.

[171] T A Rose. *An Approach to the Evaluation of Blast Loads on Finite and Semi-Infinite Structures*. PhD thesis, Cranfield University, Engineering Systems Department, 2001.

[172] T A Rose and P D Smith. Influence of the principal geometrical parameters of straight city streets on positive and negative phase blast wave impulses. *International Journal of Impact Engineering*, 27:359–376, 2002.

[173] T A Rose and P D Smith. The influence of street junctions on blast wave impulses produced by vehicle bombs. In *Proceedings of the 11th International Symposium on Interaction of the Effects of Munitions with Structures, New Orleans, USA*, 2003.

[174] T A Rose and P D Smith. Development of an adaptive mesh CFD code for high explosive blast simulation. In *Proceedings of the 12th International Symposium on Interaction of the Effects of Munitions with Structures, New Orleans, USA*, 2005.

[175] T A Rose, P D Smith, and M Brittle. Analysis of a generic cityscape using an adaptive mesh CFD code. In *Proceedings of the 12th International Symposium on Interaction of the Effects of Munitions with Structures, New Orleans, USA*, 2005.

[176] T A Rose, P D Smith, and S A Forth. *A Computational Tool for the Evalulation of Blast-Structure Interactions, Air3d version 9 users' guide*. Engineering Systems Department, Cranfield University, UK, 2006.

[177] T A Rose, P D Smith, and S A Forth. *A Computational Tool for the Evaluation of Blast-Structure Interactions, ftt_3d users' guide.* Engineering Systems Department, Cranfield University, UK, 2006.

[178] T A Rose, P D Smith, and J H May. The interaction of oblique blast waves with buildings. *Shock Waves*, 16:35–44, 2006.

[179] C J Roy. Grid Convergence Error Analysis for Mixed-Order Numerical Schemes. *AIAA Journal*, 41(4):595–604, 2003.

[180] C J Roy, Nelson C C, T M Smith, and C C Ober. Verification of Euler/Navier-Stokes codes using the method of manufactured solutions. *International Journal for Numerical Methods in Fluids*, 44:599–620, 2004.

[181] H Samet. *The design and analysis of spatial data structures.* Addison–Wesley Publishing Company Inc, Massachusetts, 1990.

[182] H Schardin. *Stossrohre [Shock Tubes]*, pages 716–720. Springer Verlag, New York, 1966. Edited by Oertel H.

[183] R Schneiders. A Grid-based Algorithm for the Generation of Hexahedral Element Meshes. *Engineering with Computers*, 12:168–177, 1996.

[184] A Sharma and L N Long. Numerical simulation of the blast impact problem using the Direct Simulation Monte Carlo (DSMC) method. *Journal of Computational Physics*, 200(1):211–237, 2004.

[185] A Sharma, L N Long, and T Krauthammer. Using the Direct Simulation Monte Carlo approach for the blast–impact problem. In *17th International Symposium on the Effects of Blast and Shock*, 2002.

[186] Y Shi, H Hao, and Z X Li. Numerical simulation of blast wave interaction with structure columns. *Shock Waves*, 17:113–133, 2007.

[187] H Simon. Partitioning of unstructured problems for parallel processing. *Computing Systems in Engineering*, 2:135–148, 1991.

[188] J L Sims. Tables for Supersonic Flow Around Right Circular Cones at Zero Angle of Attack, 1964. NASA SP-3004.

[189] S Sivier, E Loth, J Baum, and R Löhner. Vorticity produced by shock wave diffraction. *Shock Waves*, 2:31–41, 1992.

[190] S Sklavounos and F Rigas. Computer simulation of shock waves transmission in obstructed terrains. *Journal of Loss Prevention in the Process Industries*, 17:407–417, 2004.

[191] J E Slater, D V Ritzel, and P A Thibault. Development of computational methods and conduct of experimental tests for blast loading analysis. In *Proceedings of the 3rd International Conference on Structures under Shock and Impact*, pages 383–392, 1993.

[192] P D Smith and J G Hetherington. *Blast and Ballistic Loading of Structures.* Butterworth and Heinemann Ltd., Oxford, 1994.

[193] P D Smith and T A Rose. Blast loading and building robustness. *Progress in Structural Engineering and Materials*, 4:213–223, 2002.

[194] P D Smith and T A Rose. Blast wave propagation in city streets – an overview. *Progress in Structural Engineering and Materials*, 8:16–28, 2005.

[195] P D Smith, G P Whalen, L J Feng, and T A Rose. Blast loading on buildings from explosions in city streets. *Structrues and Buildings*, 146(1):47–55, 2001.

[196] G A Sod. A survey of several finite difference methods for systems of nonlinear hyperbolic conservation laws. *Journal of Computational Physics*, 27(1):1–31, 1978.

[197] D Sridar and N Balakrishnan. An upwind finite difference scheme for meshless solvers. *Journal of Computational Physics*, 189:1–29, 2003.

[198] M L Staten, S J Owen, and T D Blacker. Unconstrained plastering – a new all hexahedral mesh generation algorithm. In *International Conference on Adaptive Modeling and Simulation*, Barcelona, 2005.

[199] J L Steger and R Warming. Flux Vector Splitting of the Inviscid Gasdynamic Equations with Application to Finite-Difference Methods. *Journal of Computational Physics*, 40(2):263–293, 1981.

[200] M Sun and K Takayama. A solution–adaptive technique using unstructured hexahedral grids. In *15th AIAA Computational Fluid Dynamics Conference*, 2001. AIAA–2001–2656.

[201] M M Jr. Swisdak. Explosion Effects and Properties, Part 1: Explosion Effects in Air, 1975. NSWC/WOL/TR 75-116, Naval Surface Weapons Center, White Oak, USA, 1975.

[202] J Tang. Another alternative method for blast wave simulation in complex geometries using Virtual Cell Embedding. In *10th International Workshop on Shock-Tube Technology*, Brisbane, Australia, 2006.

[203] J Tang. CFD simulation of blast in an internal geometry using a Cartesian cell code. In *16th Australasian Fluid Mechanics Conference*, Gold Coast, Australia, 2007.

[204] J Tang. A simple axisymmetric extension to virtual cell embedding. *International Journal for Numerical Methods in Fluids*, 55(8):785–791, 2007.

[205] J Tang. User guide for shock and blast simulation with the OctVCE code (version 3.5+), 2007. University of Queensland Mechanical Engineering Report 2007/13.

[206] J Tang. Free-field blast parameter errors from cartesian cell representations of bursting sphere-type charges. *Shock Waves*, 18:11–20, 2008.

[207] T Tautges, T Blacker, and S Mitchell. The Whisker Weaving Algorithm: A connectivity-based method for constructing all-hexahedral finite element meshes. *International Journal for Numerical Methods in Engineering*, 39:3327–3349, 1996.

[208] G I Taylor and J W Maccoll. The air pressure on a cone moving at high speed I. *Proceedings of the Royal Society of London Series A*, 139:278–311, 1933.

[209] K W Thompson. Time-Dependent Boundary Conditions for Hyperbolic Systems. *Journal of Computational Physics*, 68(1):1–24, 1987.

[210] K W Thompson. Time-Dependent Boundary Conditions for Hyperbolic Systems, II. *Journal of Computational Physics*, 89(2):439–461, 1990.

[211] E Timofeev, P Voinovich, and K Takayama. Adaptive Unstructured Simulation of Three–Dimensional Blast waves with Ground Surface Effect. In *36th Aerospace Sciences Meeting and Exhibit*, 1998. AIAA 98–0544.

[212] E V Timofeev, P A Voinovich, A O Galyukov, T Saito, and K Takayama. On the adaptive unstructured simulations of blast wave propagation and attenuation in complex geometries and various media: an illustrated view. *Computational Fluid Dynamics Journal*, 12(22):171–177, 2003.

[213] TM5-1300. Design of Structures to Resist the Effects of Accidental Explosions, 1991. U.S. Department of the Army Technical Manual TM 5-1300.

[214] E F Toro. *Riemann Solvers and Numerical Methods for Fluid Dynamics, A Practical Introduction.* Springer-Verlag, Berlin, 1997.

[215] N Touheed, P Selwood, P K Jimack, and M Berzins. A comparison of some dynamic load-balancing algorithms for a parallel adaptive flow solver. *Parallel Computing*, 26:1535–1554, 2000.

[216] S Tsynkov. Numerical solution of problems on unbounded domains. *Applied Numerical Mathematics*, 27:465–532, 1998.

[217] B Van Leer. Flux Vector Splitting for the Euler Equations. In *Proceedings of the 8th International Conference on Numerical Methods in Fluid Dynamics*, Berlin, 1982.

[218] V Venkatakrishnan. Convergence to Steady State Solutions of the Euler Equations on Unstructured Grids with Limiters. *Journal of Computational Physics*, 118:120–130, 1995.

[219] V Vidwans, Y Kallinderis, and V Venkatakrishnan. Parallel dynamic load-balancing algorithm for three-dimensional adaptive unstructured grids. *AIAA Journal*, 32(3):497–505, 1994.

[220] P A Voinovich, E V Timofeev, T Saito, K Takayama, Y Yodo, and A O Galyukov. An adaptive shock-capturing method in real 3-D applications. In *22nd International Symposium on Shock Waves, Imperial College, London, UK*, 1999.

[221] Y Wada and M S Liou. An Accurate and Robust Flux Splitting Scheme for Shock and Contact Discontinuities. *SIAM Journal of Scientific Computing*, 18(3):633–657, 1997.

[222] C Walshaw, M Cross, and M G Everett. Parallel dynamic graph partitioning for adaptive unstructured meshes. *Journal of Parallel and Distributed Computing*, 47:102–108, 1997.

[223] H Wu, J Gong, D Li, and W Shi. An algebraic algorithm for point inclusion query. *Computers and Graphics*, 24(4):517–522, 2000.

[224] G Yang, D M Causon, and D M Ingram. Calculation of compressible flows about complex moving geometries using a three-dimensional Cartesian cut cell method. *International Journal for Numerical Methods in Fluids*, 33:1121–1151, 2000.

[225] J Y Yang, Y Liu, and H Lomax. Computation of Shock Wave Reflection by Circular Cylinders. *AIAA Journal*, 25:683–689, 1987.

[226] T Ye, R Mittal, H Udaykumar, and W Shyy. An accurate Cartesian grid method for viscous incompressible flows with complex immersed boundaries. *Journal of Computational Physics*, 156:209–240, 1999.

[227] W C Young. *Roark's Formulas for Stress and Strain.* McGraw-Hill Book Company, USA, 6th edition, 1989.

[228] S J Zhang, J Liu, and Y S Chen. Adaptation for hybrid unstructured grid with hanging node method. In *15th AIAA Computational Fluid Dynamics Conference*, 2001. AIAA 2001–2657.

[229] Z C Zhang, S T Yu, and S C Chang. A Space-Time Conservation Element and Solution Element Method for Solving the Two- and Three-Dimensional Unsteady Euler Equations Using Quadrilateral and Hexahedral Meshes. *Journal of Computational Physics*, 175:168–199, 2002.

[230] J Zóltak and D Drikakis. Hybrid upwind methods for the simulation of unsteady shock-wave diffraction over a cylinder. *Computer Methods in Applied Mechanics and Engineering*, 162:165–185, 1998.

Appendix A

Mixing at the Explosion Core

As discussed in Section 1.2 the contact surface between the detonation products and air can be very unstable. In multi-dimensional simulations, this instability is triggered numerically due to the perturbed (radially asymmetric) charge representation on a Cartesian mesh [122] when initiated using the balloon gas approach. Very early in the explosion this uneven contact surface is swept outwards from lighter to heavier gas, resulting in Rayleigh-Taylor type instabilities also observed in other simulations of blast propagation [71, 139]. Implosion of the secondary shock results in further mixing of this surface.

A typical spherical explosion simulation is performed by `OctVCE` and the schlieren of the early stages of the process is shown in Figure A.1, which shows the instability at the contact surface before and after implosion of the secondary shock. In this simulation, the balloon gas is perfect gas helium with a pressure of 30,000 atmospheres. Note the asymmetry of the mixing.

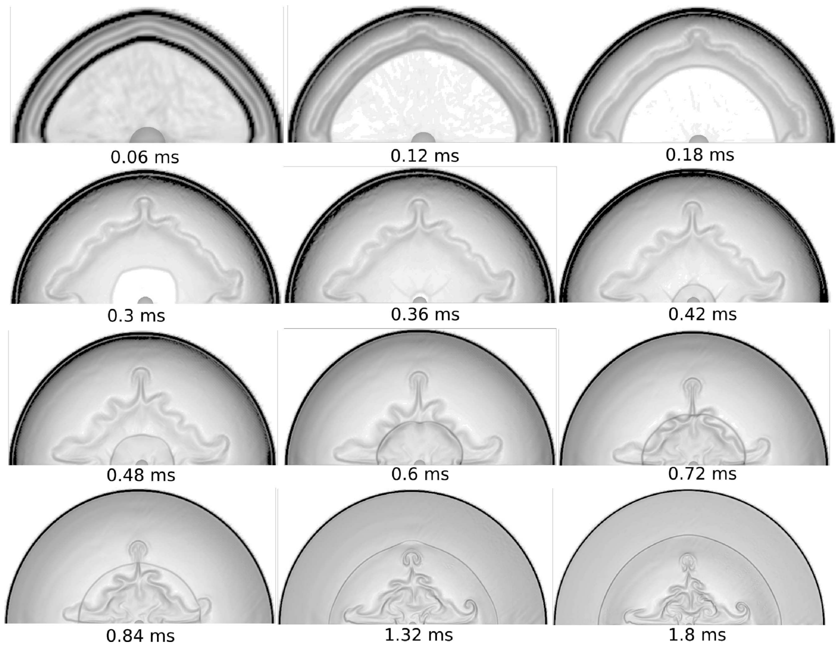

Figure A.1: Schlieren of 2D axisymmetric blast in its early stages

This instability has the unfortunate effect of triggering excessive refinement in that region for density-based adaptation indicators (Section 3.5), but it does not significantly affect the blast wave and positive phase (Section 1.2). It may be advantageous to use a pressure-based indicator to avoid this needless refinement.

A.1 Adaptation Parameters for Blast Simulation

As discussed in Section 3.5, `OctVCE` implements two types of adaptation indicators – (a) a density-based indicator and (b) velocity-based indicator. Default values for the refinement threshold are 0.3 and 0.01 for indicators (a) and (b) respectively. Lowering these thresholds allow better shock-capturing at larger distances from the blast, but at the cost of excessive cell refinement nearer the explosion. Indicator (a), which can also refine the positive phase behind the shock, require coarsening and noise filter thresholds to be set, and a small test of different values for these thresholds is shown in Figure A.2, which simulates the same blast problem above.

Five adaptive mesh levels are used. The numbers beside the letters `R`, `C` and `F` stand for refinement, coarsening and noise filter thresholds respectively. The primary shock is at a scaled distance of about 13.3 m/kg$^{1/3}$ and it is difficult to refine about the secondary shock without resulting excessive refinement elsewhere. The resolution of the positive phase was not found to be so dependent on the refinement threshold, so only the coarsening and noise filter values were varied.

Note the turbulent core region is always refined about, which can be wasteful. The degree of refinement shows a dependence on the noise filter threshold and coarsening threshold. Decreasing the coarsening threshold is more likely to confine refinement to the positive phase behind the blast, whilst decreasing the noise filter also tended to result in more refinement in the core region. For this problem, the simulation with a coarsening and noise filter threshold of 0.03 and 0.005 respectively seems to produce the best degree of refinement at the shock and positive phase, which persisted until a scaled distance of around 25 m/kg$^{1/3}$. Selection of optimal adaptation parameters requires some trial and error, but this is characteristic of any adaptive method. In the simulations of this thesis, the coarsening threshold ranges from 0.01 to 0.1 and the noise filter threshold from 0.001 to 0.1.

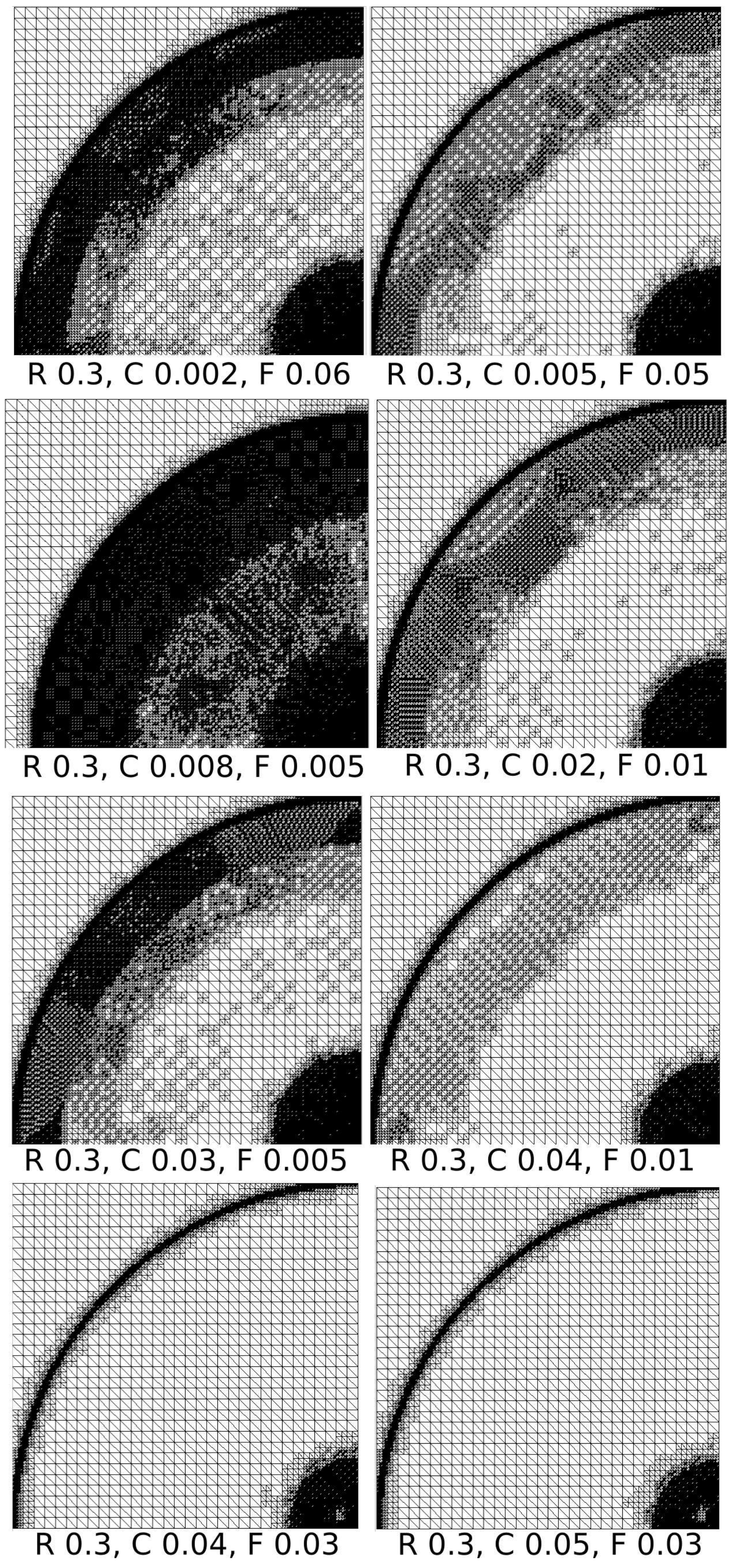

Figure A.2: Experimentation with adaptation parameters for blast simulation

Appendix B

One-dimensional Spherical Code

This section briefly describes key features of the simple one-dimensional code written for validating `OctVCE` for those test cases with radial symmetry (e.g. chapters 9 and 10). This code allows an accurate fine-grid spherically symmetric one-dimensional solution to be obtained with little cost. The spherical integral Euler equations can be expressed as

$$\frac{\partial}{\partial t}\int_V \mathbf{U}r^2 dr + \int_S r^2 \mathbf{F}\cdot\widehat{\mathbf{n}} = \mathbf{Q} \tag{B.1}$$

where $\mathbf{U} = [\rho, \rho u, \rho E, \rho_p]^T$ and the vector of fluxes is

$$\mathbf{F} = \begin{bmatrix} \rho u \\ \rho u^2 + P \\ \rho E u + P u \\ \rho_p u \end{bmatrix} \widehat{\mathbf{r}} \tag{B.2}$$

where $\widehat{\mathbf{r}}$ is the unit vector in the radial direction, in reality a one-dimensional vector like the interface outward-normal $\widehat{\mathbf{n}}$. The source term is $Q = [0, 2PrL, 0, 0]$ where L is the cell length. The cell-centered finite volume discretization is simply

$$\frac{d\mathbf{U}_c}{dt} r_c^2 L = -\sum_{if} r_{if}^2 \mathbf{F}_{if}\cdot\widehat{\mathbf{n}}_{if} + \mathbf{Q} \tag{B.3}$$

The solution marching procedure is essentially the same that used by `OctVCE` (Section 4.2) reduced to one dimension. Hence a second-order Runge-Kutta time integration procedure and the AUSMDV flux solver is used (Appendix F.1). In performing these simulations care must be taken to have the correct charge radius (represented by the balloon gas) and have an integral number of cells within the charge to obtain exact correspondence in blast energy.

Rose recommends around 50 computational cells through the explosive charge for grid-independent solutions [171]. The initial time might also be offset by the detonation time (time for the detonation wave, starting from the charge centre, to engulf the whole constant-volume charge). As the detonation speed is usually very high (of the order of $O(10^3)$ m/s), this offset is normally very small and noticeable only for trace points close to the charge.

The CFL cutback procedure (Section 4.8.1) is also used to prevent instability, and thus the solution order 'switching-time' scheme described in Section 4.8.1 is unnecessary. The one dimensional code employs an upwind biased third-order interpolation scheme with MINMOD-type limiter [110, 148] and also in the `MB_CNS` code [109]. This scheme should be suitable for unsteady one-dimensional blast wave problems and is summarized below.

Suppose reconstruction of a quantity Q is desired for interface value $Q_{i+1/2}$. On this reconstruction scheme cell-centered values from four cells are required, Q_{i-1}, Q_i, Q_{i+1} and Q_{i+2}. Let $\Delta_i^- = Q_i - Q_{i-1}$ and $\Delta_i^+ = Q_{i+1} - Q_i$. To reconstruct Q to the *left* side of the interface, the formula is used –

$$Q^L_{i+1/2} = Q_i + \frac{1}{4}\left[(1-\kappa)\,MINMOD\left(\Delta_i^-, b\Delta_i^+\right) + (1+\kappa)\,MINMOD\left(b\Delta_i^-, \Delta_i^+\right)\right] \tag{B.4}$$

where b is a biasing parameter and κ a blending parameter. To reconstruct Q to the *right* side of the interface the formula is

$$Q^R_{i+1/2} = Q_{i+1} - \frac{1}{4}\left[(1-\kappa)\,MINMOD\left(\Delta_{i+1}^-, b\Delta_{i+1}^+\right) + (1+\kappa)\,MINMOD\left(b\Delta_{i+1}^+, \Delta_{i+1}^-\right)\right] \tag{B.5}$$

Default values of $b = 2$ and $\kappa = 1/3$ are used. The MINMOD function is given by

$$MINMOD\,(x, y) = sign\,(x)\, max\,(0, min\,[|x|\,, y \cdot sign\,(x)]) \tag{B.6}$$

Reflecting (solid wall) boundary conditions are used for the ghost cells at the left and right ends of the domain. Two ghost cells are used, and the outermost ghost cell uses reflected conditions from the cells adjacent to the border cells.

Appendix C

Finite Energy Release in Cylindrical Charges

An extension to the code was considered in this thesis to incorporate a finite rate of energy release from ignition points within the charge in a very simplified model of detonation, much like the approach of Timofeev *et al* [211, 212]. In this 'finite-rate-release' model, detonation proceeds radially at a preset speed from specified ignition points until all the explosive is consumed. This can be readily implemented in the code as it already represents the initial charge as a group of high pressure cells. Thus, cells representing the charge are essentially treated as solid objects until activation to appropriate gas conditions when the detonation wave passes their centroids.

With this approach an additional degree of realism in modelling the blast waveform and overpressures may be obtainable for near-field modelling, although this extension may prove inadequate as the complex chemistry of the explosive detonation and afterburning is not taken into account. It would probably be more suitable for cheaper two-dimensional simulations as this increased realism may only be noticeable on highly-resolved meshes.

To observe the differences in solution compared to the 'instantaneous-release' detonation model where all cells are initially active and filled with high pressure gas, an axisymmetric simulation of cylindrical warhead detonation is performed. This draws from the experimental and numerical study of Anderson *et al* [11], whose axisymmetric simulations also assumed perfect gas, instantaneous energy release of the explosion, but incorporated a simple afterburning model. Because of the radially asymmetrical charge shape, free-field overpressure and energy distribution near the charge is dependent on charge orientation and even location of initiation [108] and thus makes an interesting test case for this study.

A diagram of the numerical domain and pressure sensor locations is shown in Figure C.1. The warhead is positioned at a height of 2015 mm. This domain and minimum cell size (10 mm) is chosen to be the same as Anderson's [11] but an adaptive mesh simulation is used with coarsest allowable cell size of 160 mm. Actual sensor locations are given in Table C.1.

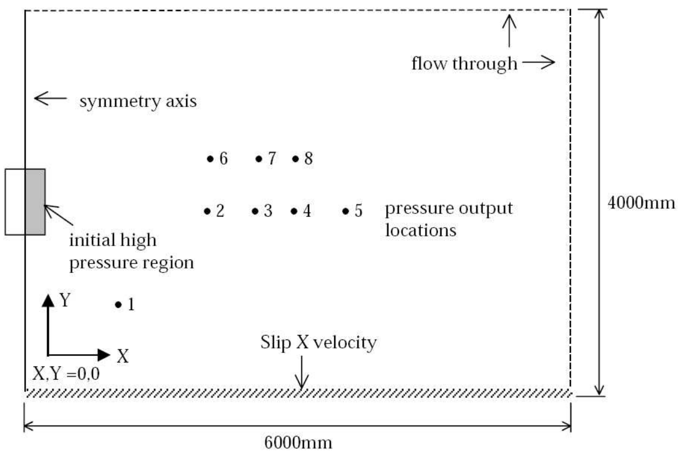

Figure C.1: Cylindrical warhead numerical domain and sensor locations (from [11])

Table C.1: Sensor locations for cylindrical warhead explosion (from [11])

Sensor number	X location (mm)	Y location (mm)
1	1010	1000
2	1980	2010
3	2520	2000
4	2950	2040
5	3550	2000
6	2010	2610
7	2560	2600
8	2960	2590

The initial conditions for the charge are given in Table C.2 and have also been taken from Anderson [11]. The simulation applies the JWL equation of state to the explosion products (Composition B explosive, like in Anderson's experiments) with JWL parameters provided by Reference [127]. As the charge is discretized by finite-volume cells its actual diameter and length are slightly different from the reported nominal values, but the density and pressure of the cells is adjusted to give the correct energy. The simulation is performed with an adaptive flux solver (EFM at shocks, AUSMDV elsewhere) and density-based adaptation indicator (Equation 3.4) of 0.3, 0.1 and 0.013 for the refinement, coarsening and noise thresholds respectively.

Figure C.2 shows a progression of temperature and grids in the early stages of the explosion when initiated from three points along the charge centreline (which can be seen in the initial plot, Figure C.2(a)). These points at located at heights of 1939 mm, 2015 mm (charge centre) and 2091 mm. The consumption of the explosive is nearly complete at about 14.4 ms (Figure C.2(d)).

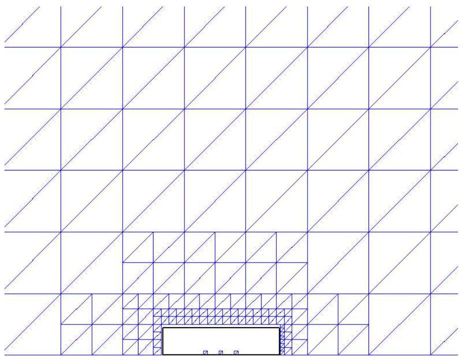

(a) 0 ms

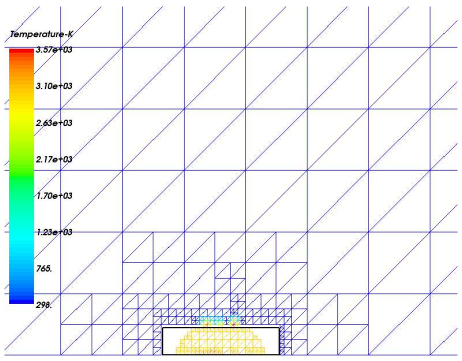

(b) 9.48 ms

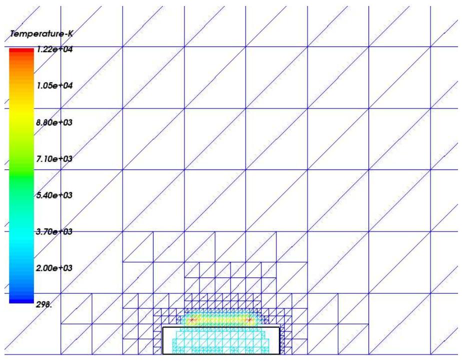

(c) 11.5 ms

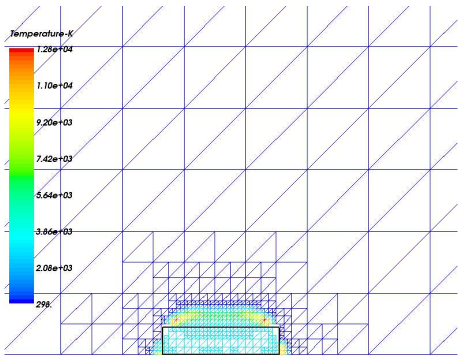

(d) 14.4 ms

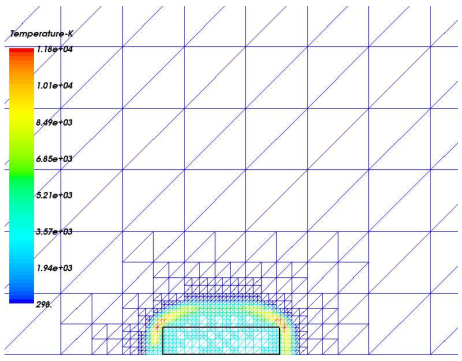

(e) 17.8 ms

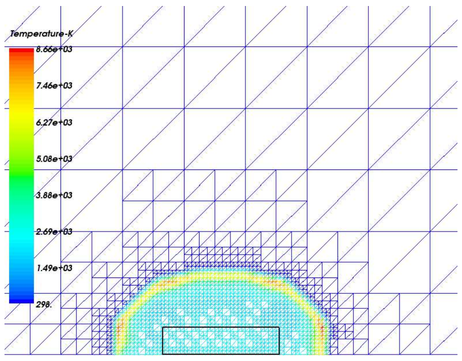

(f) 35.5 ms

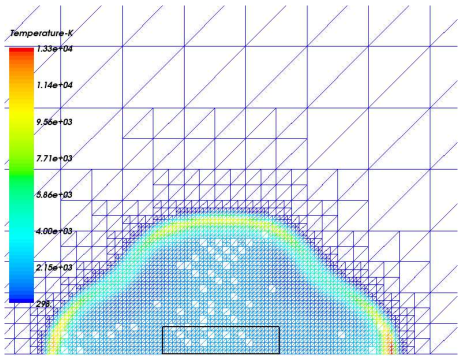

(g) 64.9 ms

Figure C.2: Temperature and grid for cylindrical warhead detonation

Table C.2: Initial conditions for cylindrical warhead (taken from [11])

Diameter	360 mm
Length	720 mm
Blast energy	4.00925×10^7 J
Ambient Pressure	101.325 kPa
Ambient Temperature	298 K

Pressure histories from the various sensor locations are shown in Figure C.3 and compared with Anderson's results. A simulation is also performed assuming the instantaneous detonation model for comparison. The results show that observable differences exist between the finite-rate-release and instantaneous detonation solutions, which in turn differ with Anderson's pressure histories. This is to be expected as Anderson took into account afterburning which was not implemented here.

There is also a lag in blast wave arrival time relative to the experimental results. Modelling accurately the actual detonation process might yield better arrival time results, but this is not so important. Except for sensor 1, the finite-rate-release model has an arrival time either earlier than or equal with the instantaneous model. The detonation speed through the charge is too rapid relative to the scale of the waveforms to make much difference in arrival time here. At sensors 6 to 8, arrival times from both solutions are nearly coincident.

At sensors 1, 3 and 8 the finite-rate-release model seems to give slightly better peak overpressures relative to experimental results compared to the instantaneous detonation model. However, the decay rate for the initial pulse is much sharper for the finite-rate-release model than the instantaneous one. It is also interesting that the current results seem on the whole to yield better peak overpressures (and comparably good positive phase) as Anderson's numerical results, compared to experiment. However, in some cases the experimental pressure histories are not very good (particularly with sensor 6), presumably because of sensor vibration. Also, in many cases the numerical simulations display secondary shocks which are not clearly distinguishable in the experimental pressure histories.

The results show that whilst there is a notable difference between finite-rate-release and instantaneous detonation models, the finite-rate-release approach does not produce consistently better solutions (when compared to experimental results) in either peak overpressure or positive phase waveform, at least for this problem. It may still be a useful option to have in some cases, but here the instantaneous detonation model seems to yield fairly good results even in the near-field (discounting the arrival time discrep-

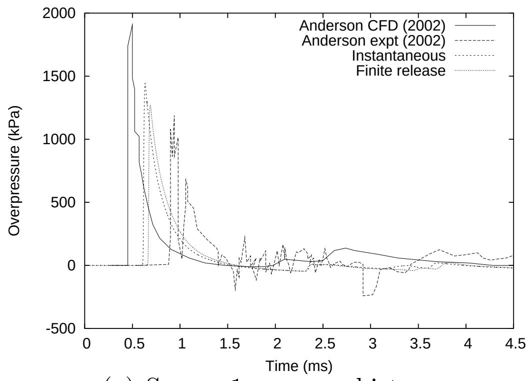

(a) Sensor 1 pressure history

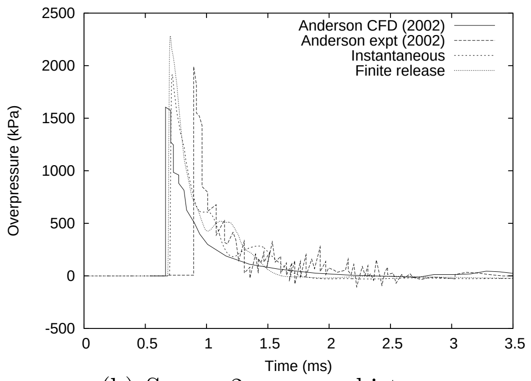

(b) Sensor 2 pressure history

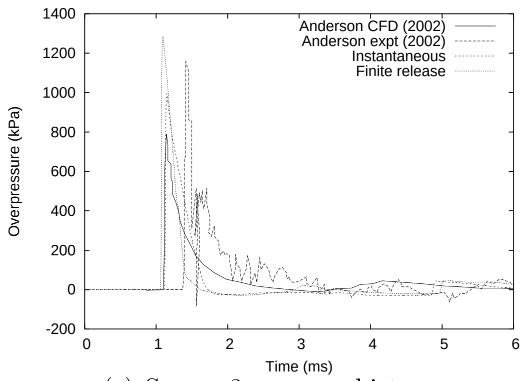

(c) Sensor 3 pressure history

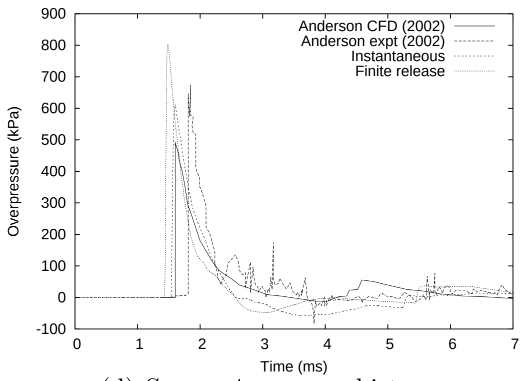

(d) Sensor 4 pressure history

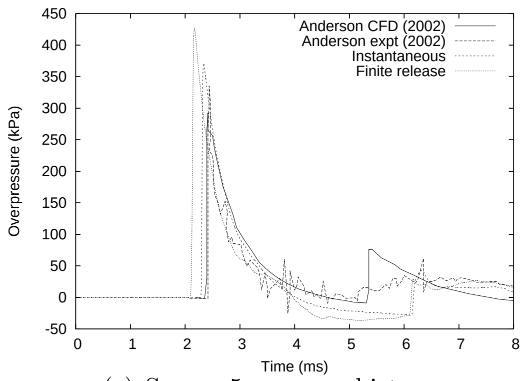

(e) Sensor 5 pressure history

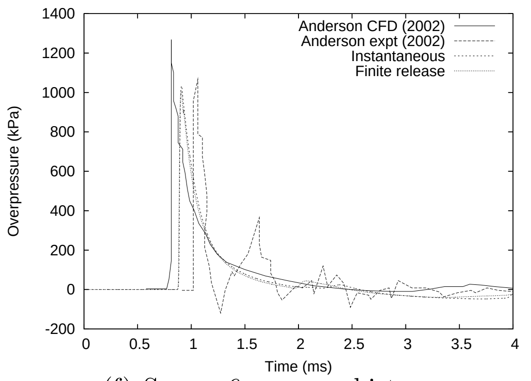

(f) Sensor 6 pressure history

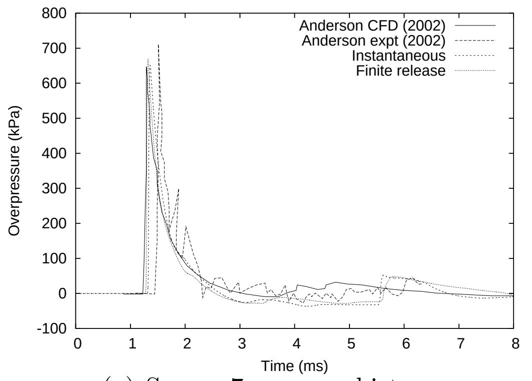

(g) Sensor 7 pressure history

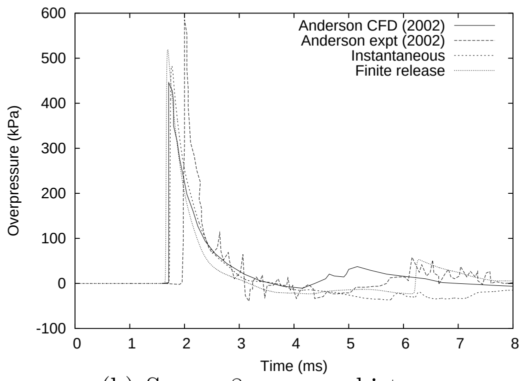

(h) Sensor 8 pressure history

Figure C.3: Pressure histories for cylindrical warhead detonation

ancy). Better correspondence with experimental results is probably only achievable in the near-field through detailed modelling of the chemistry of the detonation process. This extension to the code requires further development and exploration.

Appendix D

Axisymmetric Virtual Cell Embedding (VCE) method

The base VCE scheme (Section 2.4) is unsuitable for axisymmetric flow as the axisymmetric Euler equations (Equation 4.8) require additional information – the radial co-ordinates of the cell center r_c and its fluid interfaces i.e. the unobstructed side lengths r_l and wall surface r_w. How these quantities are calculated has been described in Reference [204] (a derivative paper from the current thesis) and is repeated below.

D.1 Obtaining cell-centre and interface radial co-ordinates

The VCE subcell division can be used to calculate r_c (the cell's average radial co-ordinate) and r_l (the average radial co-ordinate of its unobstructed interfaces) if the radial co-ordinates of each subcell are stored and then averaged in the summation i.e. $r_{c/l} = \sum_N r_{s_{c/l}}/N$, where r_s is the radial co-ordinate of a subcell and N the total number of fluid subcells i.e. unobstructed subcells.

D.2 Obtaining the wall radial co-ordinate

The wall radial co-ordinate r_w can be found by noting that VCE always gives straight surface representations. With the help of Figure 2.1(b) (page 14), first shift the origin to the lower left cell corner, and assume the cell is square of length l_c. In a similar manner to finding r_l now the average *obstructed* radial coordinates on the east and west faces r_{xr} and r_{xl} respectively are found.

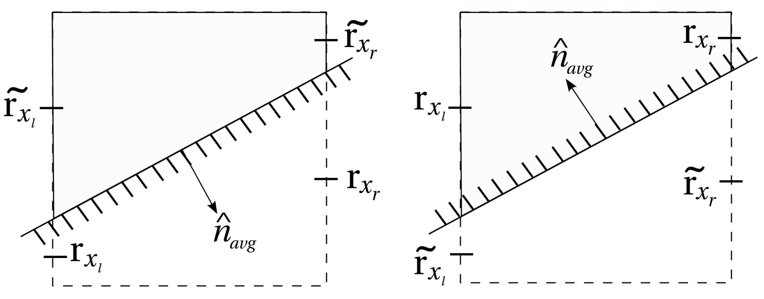

(a) Downward surface normal (b) Upward surface normal

Figure D.1: Two surface normal configurations

Now consider two cases – (1) when the surface normal is pointing downward or sideways (i.e. its radial co-ordinate is negative or zero respectively) and (2) when it is pointing upward.

1. *Downward or sideways surface normal*

   With the help of Figure D.1(a), note that r_{xr} and r_{xl} represent the midpoint of obstruction on a side, so that very simply $r_w = r_{xr} + r_{xl}$.

2. *Upward surface normal*

   With the help of Figure D.1(b), this case can also been seen as case (1) if the origin is shifted to the top right cell corner and the transformation $r' = l_c - r$ is applied. However if either r_{xr} or r_{xl} are zero, then likewise r'_{xr} or r'_{xl} respectively are zero (no obstruction is present). Then $r'_w = r'_{xr} + r'_{xl}$, and finally transforming back, $r_w = l_c - r'_w$.

   Thus

$$r'_{x(l/r)} = \begin{cases} 0 & \text{when } r_{x(l/r)} = 0 \\ l_c - r_{x(l/r)} & \text{when } r_{x(l/r)} > 0 \end{cases}$$

   Then $r_w = l_c - (r'_{xr} + r'_{xl})$.

It should be noted from Figures D.1(a) and D.1(b) that it is equally possible to use the average unobstructed radial coordinates $\widetilde{r}_{xr}$ and $\widetilde{r}_{xl}$ instead of r_{xr} and r_{xl}. This extended VCE scheme can now handle complex axisymmetric geometry, and has an accuracy consistent with and limited by the basic VCE paradigm [204].

D.3 Euler Equations in Axisymmetric Geometry

The axisymmetric Euler equations (Equation 4.3) and the axisymmetric VCE method (Appendix D) assume that for the axisymmetric cell –

1. The volume per radian $A_c = Ar_c$, where A is the cell's area and r_c the cell's average radial co-ordinate
2. The area per radian of each interface can be given by $r_{if}l_{if}$, where r_{if} is the average radial co-ordinate of the interface, and l_{if} is the interface length

These expressions will be derived more fully below, with the help of the axisymmetric cell illustration in Figure D.2. Note this is a partial view of the axisymmetric cell as it in reality extends a full circle around the axis of symmetry. The red surface is an example surface e.g. of a cone cutting through the cell.

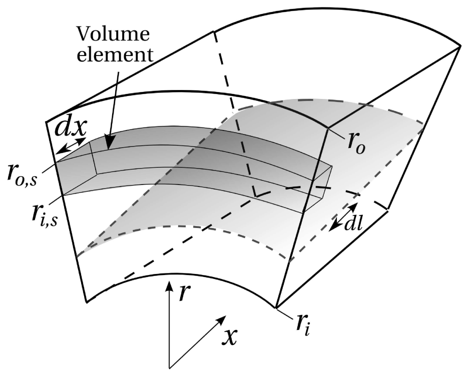

Figure D.2: Axisymmetric cell illustration

D.4 Volume per radian expression

Consider a volume element of the axisymmetric cell of Figure D.2. In reality it is an annulus with a length dx, with an inner radius of $r_{i,s}$ and outer radius of $r_{o,s}$. The volume elements are chosen are such that $dx = r_{o,s} - r_{i,s}$. This annulus has a volume of

$$V_e = \pi \left({r_{o,s}}^2 - {r_{i,s}}^2\right) dx = \pi dx \left(r_{o,s} + r_{i,s}\right)\left(r_{o,s} - r_{i,s}\right) = \pi dx^2 \left(r_{o,s} + r_{i,s}\right) \tag{D.1}$$

Note that the two-dimensional area of the volume element, $A_e = dx^2$. With N elements, the area of the cell can be expressed as $A = NA_e$. The sum of these volume elements gives the total volume of the axisymmetric cell –

$$V = \pi dx^2 \sum_{i=1}^{N} \left(r_{o,s} + r_{i,s}\right) \tag{D.2}$$

The volume per radian of the axisymmetric cell is then

$$\frac{V}{2\pi} = A_c = dx^2 \sum_{i=1}^{N} \frac{\left(r_{o,s} + r_{i,s}\right)}{2} = A_e \sum_{i=1}^{N} r_{avg} \tag{D.3}$$

where r_{avg} is the average radial co-ordinate of the volume element. Assuming the volume per radian of the cell is its area $A = NA_e$ multipled by some radial value r, then

$$Ar = NA_e = A_e \sum_{i=1}^{N} r_{avg} \tag{D.4}$$

which means that $r = \sum r_{avg}/N = r_c$ i.e. the average radial co-ordinate of the cell from the volume elements.

D.5 Area per radian of interfaces

D.5.1 Interfaces normal to radial axis

For any unobstructed interfaces normal to (i.e. pierced by) the radial axis, the interface area is simply that of the cylindrical area of the annulus (the cell length). This is $A = 2\pi rl$, where r is the annulus radius, and l is the (axial) length of the cell. Thus the area per radian is $A/(2\pi) = rl$. Thus for example the top face of the cell is $r_o l$.

D.5.2 Interfaces normal to axial axis

The interfaces normal to the axial axis are the cross-sectional area of the cell annulus. Thus the area is

$$A = \pi \left({r_2}^2 - {r_1}^2\right) = \pi \left(r_2 + r_1\right)\left(r_2 - r_1\right) = \pi l_{if}\left(r_2 + r_1\right) \tag{D.5}$$

where r_2 and r_1 is the outer and inner radius of the annulus. The interface length $l_{if} = r_2 - r_1$. In the case of an unobstructed interface like the axisymmetric cell of Figure D.2 the front and back interfaces have area of $\pi\left({r_o}^2 - {r_i}^2\right)$. Thus the area per radian is

$$A/(2\pi) = l_{if}\left(r_2 + r_1\right)/2 = l_{if} r_{avg} \tag{D.6}$$

where r_{avg} is the average radial co-ordinate of the interface.

D.5.3 Wall interface

An example wall interface of a conical surface can be seen by the red surface in Figure D.2. An area element of this interface is $dA = 2\pi r dl$ where r and dl are the radius and length of area element respectively. In VCE the variation of the interface radius can be described by the linear relation $r = r_1 + mx$ (recall VCE only represents planar surfaces). Thus if $dl = \sqrt{dr^2 + dx^2} = dx\sqrt{m^2+1}$. Thus

$$dA = 2\pi\left(r_1 + mx\right)\sqrt{m^2+1}dx \tag{D.7}$$

The area elements are integrated from x_1 to x_2 (the axial length of the cell is $x_2 - x_1$) to give the total area –

$$\begin{aligned}
\int_{x_1}^{x_2} dA &= 2\pi\sqrt{m^2+1}\int_{x_1}^{x_2}\left(r_1+mx\right)dx && \text{(D.8)}\\
&= 2\pi\sqrt{m^2+1}\left[r_1x+\frac{mx^2}{2}\right]_{x_1}^{x_2} && \text{(D.9)}\\
&= 2\pi\sqrt{m^2+1}\left(x_2-x_1\right)\left[r_1+m\frac{x_1+x_2}{2}\right] && \text{(D.10)}\\
&= 2\pi\sqrt{m^2+1}\left(x_2-x_1\right)\left(r_1+mx_{avg}\right) && \text{(D.11)}\\
&= 2\pi\sqrt{m^2+1}\left(x_2-x_1\right)r_{avg} && \text{(D.12)}
\end{aligned}$$

where r_{avg} is radial midpoint of the interface line length. Note that the slant length of the interface $l = \left(x_2 - x_1\right)\sqrt{m^2+1}$. Thus $A = 2\pi l r_{avg}$. The area per radian is thus $A/\left(2\pi\right) = l r_{avg}$. Thus for all interfaces the area per radian is $r_{if}l_{if}$.

Appendix E

Integrated Pressure Force Over a Cone

The force on a portion of the cone surface is calculated from the integral $\int P_s dA$, where P_s is the pressure on the surface and A the area. As $dA = 2\pi r dl$, where r is the radius and dl the length increment along the cone surface(Figure E.1), the force per radian is

$$F = \int P_s r dl \tag{E.1}$$

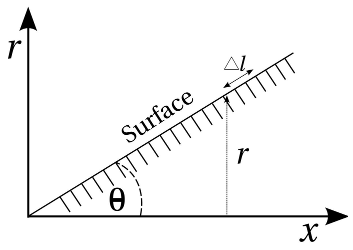

Figure E.1: Diagram of cone

Now dl can be computed in terms of x and the gradient of the line m ($m = tan\theta$) –

$$dl = \sqrt{dr^2 + dx^2} = \sqrt{m^2 dx^2 + dx^2} \tag{E.2}$$

Thus from Equations E.1 and E.2 the force per radian F is

$$F = \int P_s r \sqrt{m^2 + 1} dx = P_s m \sqrt{m^2 + 1} \left[\frac{x^2}{2} \right]_{x_0}^{x_1} \tag{E.3}$$

where x_0 and x_1 are starting and ending points of integration. By the same reasoning the force per unit length along a wedge surface is

$$F = \int P_s \sqrt{m^2 + 1} \, [x]_{x_0}^{x_1} \tag{E.4}$$

Note also that for CFD simulations, the approximate form of Equation E.1 can be used to obtain the force for each cell i.e. if P_s, r and Δl is known for each intersected cell, then the surface force in that cell is $F = P_s r \Delta l$.

E.1 Degeneracies with the Axisymmetric Code

There are some problems associated with the axisymmetric VCE method. To illustrate, consider an initially quiescent state in a square corner cell shown in Figure E.2. All flux terms would be zero, except for pressure in the momentum fluxes in the x and r directions. The VCE method (Section 2.4) constructs a single planar surface from the two obstructed interfaces with an radial coordinate of r_c.

However the cell is in fact unobstructed and thus the source term Q for the radial direction in the axisymmetric equation (Equation 4.3), P/r also uses a value of $r = r_c$. In the cell update for axisymmetric flow (Equation 4.8) this means that Q does not entirely cancel with the sum of flux terms $(1/A)\sum_{if} r_{if}\mathbf{F}_{if} \cdot \widehat{\mathbf{n}}_{if} l_{if}$ leading to production of momentum in the radial direction proportional to $P/(2r)$. This production of momentum arises from this basic mathematical or geometrical inconsistency between the radial values of the cell interfaces and cell volume.

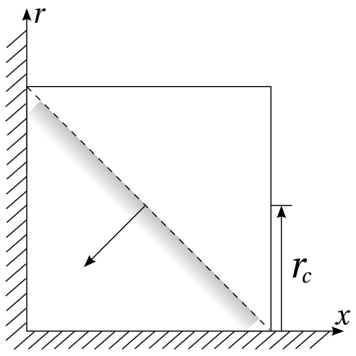

Figure E.2: Axisymmetric corner cell

This problem is not present in the planar situation as there is no source term and interfacial and cell radial coordinates are not used. This degeneracy is avoided if the corner cell is represented correctly i.e. with two obstructed interfaces. This is basically the staircased surface representation (Section 2.4.3) and is implemented in the code for axisymmetric corner cells. Unfortunately, if a corner cell does have some of its volume obstructed, it is difficult apart from visual inspection to identify it as such as only cell area and volume fractions are stored. Thus this degeneracy is not always treated.

Also, inconsistencies between cell interfacial and volume radial coordinates will exist even for non-corner cells. Consider Figure E.3 where an axisymmetric cell with 64 subcells is obstructed by a conical surface. There will still be a slight geometrical inconsistency between the cell radial coordinate r_c (obtained by averaging, $r_c = \sum_N r_s/N$ where r_s is the radial coordinate of a subcell) and the computed wall radial coordinate r_i computed from the interface obstruction (Section 4.2.1). r_c is computed only

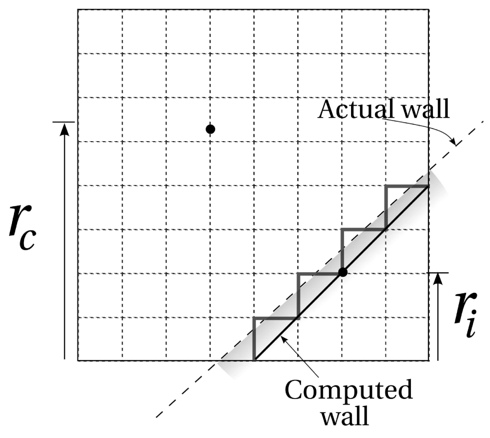

Figure E.3: Axisymmetric cell cut by cone

from wholly unobstructed subcells, but for consistency the contributions of partially obstructed subcells to this value are also needed. Momentum in the radial direction is still produced.

To investigate the severity of this problem a simulation is first conducted of initially quiescent air at standard conditions (with a fairly coarse grid) in an obstructed corner cell situation as shown in Figure E.4. The domain is a simple square with walls on the left and bottom border, and non-reflecting outflow boundary conditions on the right and top border. It was found that due to the boundary conditions steady-state behaviour was apparently produced, and Figure E.4 shows the solution at steady-state.

The solutions show that a very strong wind can be produced at this corner cell, although effects seem localized there. As there is production of radial momentum some wind is produced in the radial direction, which is mainly confined to the vertical wall. A strong inflow into the corner cell along the horizontal wall is also induced to replace mass lost in the radial direction. Clearly, the solution at this corner is very different from the ambient condition.

The flow of initially quiescent air over a conical surface is also simulated. This simulation uses the geometry and grid of the supersonic conical flow study in Section 6.3. It was simulated to the same time that produced steady-state behaviour in the simulations of Section 6.3, but steady-state behaviour was not observed here, even long after this time. Figure E.5 shows the solution at this late time. Extrema in the solution seem to increase in magnitude.

Clearly the radial momentum generated along the numerically roughened surface (Section 2.4.4) leads to a very complicated and noisy solution. The density and pressure solutions seem to behave best, as there is overall small deviation from ambient values. Significant velocity is produced, although it very low compared to the supersonic ve-

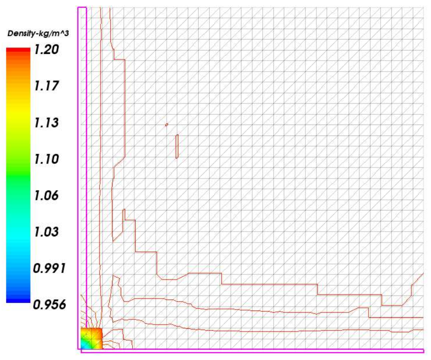

(a) Density

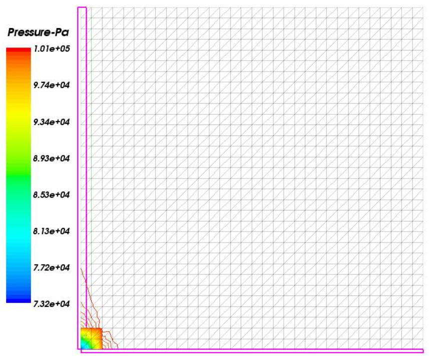

(b) Pressure

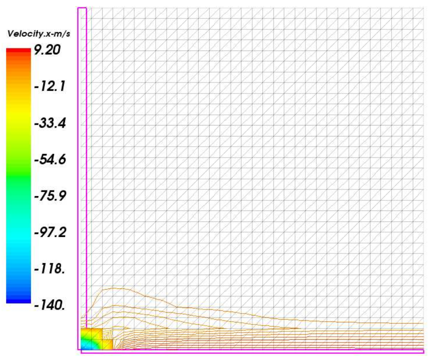

(c) x velocity

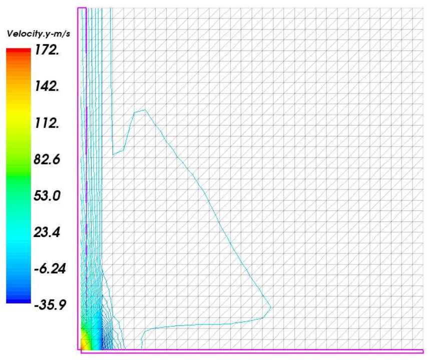

(d) y velocity

Figure E.4: Axisymmetric corner cell degeneracy

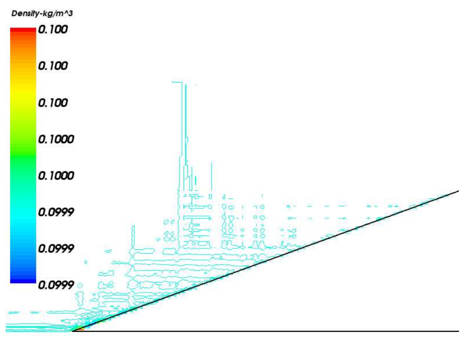

(a) Density

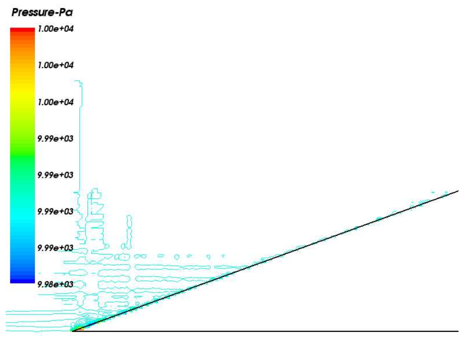

(b) Pressure

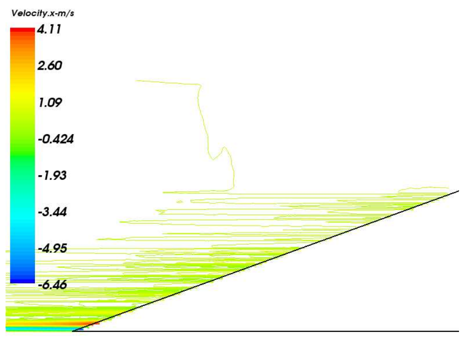

(c) x velocity

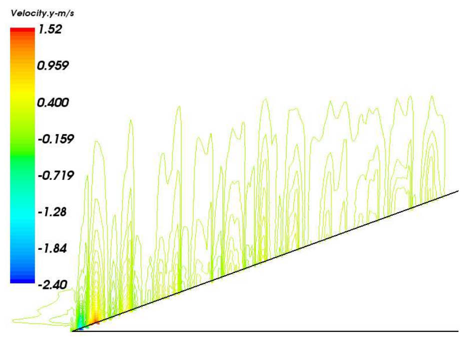

(d) y velocity

Figure E.5: Axisymmetric conical degeneracy

locities studied in Section 6.3. A vortex-like feature also appears present at the cone tip, and this is where the extrema in velocity occur; it may have initially risen with the inducing of horizontal flow into an obsturcted cell at the cone tip to replace mass loss in the radial direction.

The effects of this axisymmetric degeneracy on solutions with initial quiescent state (in addition to numerical surface roughening) can be quite significant. Divergent or convergent solutions seem to both be possible depending on the boundary condition and geometry. It is difficult to predict the effect this degeneracy has on flows with more interesting initial conditions. However, these effects may not always prove detrimental to solutions in simulations of practical interest. For example, it is shown in Section 6.3 that convergent and accurate solutions of supersonic conical flow can nonetheless be produced. In the axisymmetric blast wall simulations of Section 11, good overpressure traces can be computed despite the presence of problematic corner cells. Perhaps relative to much stronger or sudden features like a blast or shock wave, the effect on the flow produced by such degeneracies (which do not increase so fast) is minimal.

Appendix F

Flux Calculation Schemes

This section summarizes the algorithms for the AUSMDV and EFM schemes to calculate the interface flux $\mathbf{F}_{if} \cdot \widehat{\mathbf{n}}_{if}$ in Equation 4.4. More detailed descriptions of the schemes can be found in References [110, 148, 150, 221].

F.1 AUSMDV Scheme

This scheme combines flux differencing and vector splitting. At an interface the left state has flow parameters density ρ_L, explosion products density $\rho_{p,L}$, velocity $\mathbf{u}_L$, pressure P_L and total enthalpy H_L, and the right state ρ_R, $\mathbf{u}_R$, P_R and H_R. To begin, the normal velocity components at the left and right of an interface are obtained (in an interface frame of reference) –

$$u_L = \mathbf{u}_L \cdot \widehat{\mathbf{n}}_{if} \tag{F.1}$$

$$u_R = \mathbf{u}_R \cdot \widehat{\mathbf{n}}_{if} \tag{F.2}$$

Tangential velocity vectors relative to the interface are

$$\mathbf{v_L} = \mathbf{u}_L - u_L \mathbf{n}_{if} \tag{F.3}$$

$$\mathbf{v_R} = \mathbf{u}_R - u_R \mathbf{n}_{if} \tag{F.4}$$

Functions α_L and α_R are designed to avoid dissipation at contact discontinuities –

$$\alpha_L = \frac{2P_L/\rho_L}{P_L/\rho_L + P_R/\rho_R} \tag{F.5}$$

$$\alpha_L = \frac{2P_R/\rho_R}{P_L/\rho_L + P_R/\rho_R} \tag{F.6}$$

Define the interface sound speed at the interface a_m as

$$a_m = max\left(a_L, a_R\right) \tag{F.7}$$

and individual splitting terms

$$u_L^+ = \begin{cases} \alpha_L \left[\frac{(u_L+a_m)^2}{4a_m} - \frac{u_L+|u_L|}{2}\right] + \frac{u_L+|u_L|}{2} & \text{, if } \frac{|u_L|}{a_m} \leq 1 \\ \frac{u_L+|u_L|}{2} & \text{otherwise} \end{cases} \tag{F.8}$$

$$u_R^- = \begin{cases} \alpha_R \left[\frac{-(u_R-a_m)^2}{4a_m} - \frac{u_R-|u_R|}{2}\right] + \frac{u_R-|u_R|}{2} & \text{, if } \frac{|u_R|}{a_m} \leq 1 \\ \frac{u_R-|u_R|}{2} & \text{otherwise} \end{cases} \tag{F.9}$$

Second-order pressure splittings are given by

$$P^{\pm}_{L/R} = \begin{cases} \frac{1}{4}P_{L/R}\left(\frac{u_{L/R}}{a_m} \pm 1\right)^2\left(2 \mp \frac{u_{L/R}}{a_m}\right) & \text{, if } \frac{u_{L/R}}{a_m} \leq 1 \\ P_{L/R}\frac{u_{L/R} \pm \left|u_{L/R}\right|}{2u_{L/R}} & \text{otherwise} \end{cases} \tag{F.10}$$

and the interface pressure term is

$$P_{1/2} = P^+_L + P^-_R \tag{F.11}$$

The switching factor s is based on the pressure difference across the interface –

$$s = \frac{1}{2}min\left[1, \frac{K\left|P_R - P_L\right|}{min\left(P_L, P_R\right)}\right] \tag{F.12}$$

with sensitivity constant K set to 10. The mass flux is given by the vector splitting

$$G = u^+_L\rho_L + u^-_R\rho_R \tag{F.13}$$

For explosion products the mass flux of the explosion products would similar be $G_p = u^+_L\rho_{p,L} + u^-_R\rho_{p,R}$. The AUSMV momentum flux (vector splitting) is

$$L_V = \rho_L u_L u^+_L + \rho_R u_R u^-_R \tag{F.14}$$

and the AUSMD momentum flux (flux differencing) is

$$L_D = \frac{1}{2}\left[G\left(u_L + u_R\right) - \left|G\right|\left(u_R - u_L\right)\right] \tag{F.15}$$

and the normal momentum flux is a mixture of the AUSMV and AUSMD momentum fluxes

$$L_n = \left(\frac{1}{2} + s\right)L_V + \left(\frac{1}{2} - s\right)L_D + P_{1/2} \tag{F.16}$$

The tangential component of the momentum flux is

$$\mathbf{L}_t = \frac{1}{2}\left[G\left(\mathbf{v}_L + \mathbf{v}_R\right) - \left|G\right|\left(\mathbf{v}_R - \mathbf{v}_L\right)\right] \tag{F.17}$$

and thus the interface momentum flux is

$$\mathbf{L} = L_n\widehat{\mathbf{n}}_{if} + \mathbf{L}_t \tag{F.18}$$

The total enthalpy flux is

$$H = \frac{1}{2}\left[G\left(H_L + H_R\right) - \left|G\right|\left(H_R - H_L\right)\right] \tag{F.19}$$

Thus the flux $\mathbf{F}_{if} \cdot \widehat{\mathbf{n}}_{if}$ is

$$\mathbf{F}_{if} \cdot \widehat{\mathbf{n}}_{if} = \begin{bmatrix} G \\ \mathbf{L} \\ H \\ G_p \end{bmatrix} \tag{F.20}$$

The glitch at the sonic expansion point is fixed by modifying the flux for two cases (1) when $u_L - c_L < 0$ and $u_R - c_R > 0$ and (2) when $u_L + c_L < 0$ and $u_R + c_R > 0$. For case (1)

$$\mathbf{F}_{if} \cdot \widehat{\mathbf{n}}_{if} = \begin{bmatrix} G - C\Delta(u-a)\Delta\rho \\ \mathbf{L} - C\Delta(u-a)\Delta(\rho\mathbf{u}) \\ H - C\Delta(u-a)\Delta(H) \\ G_p - C\Delta(u-a)\Delta(\rho_p) \end{bmatrix} \tag{F.21}$$

where $\Delta() = ()_R - ()_L$ and the constant parameter C has a value of 0.125. For case (2)

$$\mathbf{F}_{if} \cdot \widehat{\mathbf{n}}_{if} = \begin{bmatrix} G - C\Delta(u+a)\Delta\rho \\ \mathbf{L} - C\Delta(u+a)\Delta(\rho\mathbf{u}) \\ H - C\Delta(u+a)\Delta(H) \\ G_p - C\Delta(u+a)\Delta(\rho_p) \end{bmatrix} \tag{F.22}$$

F.2 EFM Scheme

As with the AUSMDV scheme, at the interface left state the flow parameters are ρ_L, explosion products density $\rho_{p,L}$ with mass fraction f_L, velocity $\mathbf{u}_L$, pressure P_L, total enthalpy H_L, specific heat $C_{v,L}$ and temperature T_L. The right state similarly has parameters ρ_R, $\rho_{p,R}$, f_R, $\mathbf{u}_R$, P_R, H_R, $C_{v,R}$ and T_R. To begin, the gas 'constants' are derived for each state –

$$R_L = \frac{P_L}{\rho_L T_L} \tag{F.23}$$

$$R_R = \frac{P_R}{\rho_R T_R} \tag{F.24}$$

The normal velocity components at the left and right of an interface u_L and u_R are obtained from Equation F.1 and F.2. An averaging function is defined

$$\alpha = \frac{\sqrt{\rho_L}}{\sqrt{\rho_L} + \sqrt{\rho_R}} \tag{F.25}$$

The averaged gas constants for the interface are

$$C_v = \alpha C_{v,L} + (1-\alpha) C_{v,R} \tag{F.26}$$

$$R = \alpha R_L + (1-\alpha) R_R \tag{F.27}$$

$$C_p = C_v + R \tag{F.28}$$

$$\gamma = C_p / C_v \tag{F.29}$$

Now define the values

$$C = \frac{1}{2}\frac{\gamma+1}{\gamma-1} \tag{F.30}$$

$$C_L = \sqrt{2R_LT_L} \tag{F.31}$$

$$C_R = \sqrt{2R_RT_R} \tag{F.32}$$

$$W_L = \frac{1}{2}\left(1 + erf\left(u_L/C_L\right)\right) \tag{F.33}$$

$$D_L = \frac{1}{2\sqrt{\pi}}e^{-u_L^2} \tag{F.34}$$

$$W_R = \frac{1}{2}\left(1 - erf\left(u_R/C_R\right)\right) \tag{F.35}$$

$$D_R = -\frac{1}{2\sqrt{\pi}}e^{-u_R^2} \tag{F.36}$$

The mass flux from the left state is

$$m_L = W_L\rho_Lu_L + D_LC_L\rho_L \tag{F.37}$$

and the mass flux from the right state

$$m_R = W_R\rho_Ru_R + D_RC_R\rho_R \tag{F.38}$$

The total interface mass flux is thus

$$G = m_L + m_R \tag{F.39}$$

For the explosion products the mass flux G_p depends on which direction the wind is blowing, and is f_Lm if $m > 0$, else f_Rm otherwise. The momentum flux is

$$\mathbf{L} = m_L\mathbf{u}_L + m_R\mathbf{u}_R + \widehat{\mathbf{n}}_{if}\left(W_LP_L + W_RP_R\right) \tag{F.40}$$

and the enthalpy flux is

$$H = W_L\rho_Lu_LH_L + W_R\rho_Ru_RH_R + D_LC_L\rho_L\left(\frac{|\mathbf{u}_L|^2}{2} + C\frac{P_L}{\rho_L}\right) + D_RC_R\rho_R\left(\frac{|\mathbf{u}_R|^2}{2} + C\frac{P_R}{\rho_R}\right) \tag{F.41}$$

The flux $\mathbf{F}_{if}\cdot\widehat{\mathbf{n}}_{if}$ is the same expression as given by Equation F.20.

Appendix G

Mixture Equation of State

A combined equation of state is required for cells close to the fireball with a mixture of explosion products (when modelled by the JWL equation of state, Section 4.5.2) and ambient gas (modelled by the ideal gas equation of state). However given the insensitivity of the blast wave in mid- to far-field on initial condition (Section 4.6) it is not always necessary to obtain a fully realistic thermodynamic model of this mixture.

A common, simple approach is to obtain an average ratio of specific heats from the two gases, γ_{avg}, to be used in a 'γ-law' ideal equation of state $P = \rho e\left(\gamma_{avg} - 1\right)$ [24, 86, 177]. A harmonic average is used to calculated γ_{avg} –

$$\gamma_{avg} = 1 + \frac{1}{\frac{f_1}{\gamma_1 - 1} + \frac{f_2}{\gamma_2 - 1}} \tag{G.1}$$

where f_1 and f_2 are the mass fractions of the two gases, $f_2 = 1 - f_1$ and γ_1 and γ_2 their respective ratio of specific heats. A different harmonic average may be used for the sound speed formula [24] $a = \sqrt{\Gamma_a P/\rho}$ where

$$\Gamma_a = \frac{1}{f_1/\gamma_1 + f_2/\gamma_2} \tag{G.2}$$

The harmonic average for the gas γ is used in multifluid volume-of-fluid algorithms [86] which are designed to track interfaces and treat different species as thermodynamically distinct entities. Pressure and internal energy within a cell is assumed to be at equilibrium amongst the species. For the JWL equation of state the gas γ of the explosion products may be approximated as an effective value [177] based on comparison with the ideal gas law

$$\gamma_p = \gamma_p\left(\rho_p, e\right) = \frac{P\left(\rho_p, e\right)}{\rho_p e} + 1 \tag{G.3}$$

where $P\left(\rho_p, e\right)$ is the JWL equation of state (Equation 4.18) for pressure and e the internal energy. Additive partial pressure is not assumed; the JWL equation of state in Equation G.3 is used just to obtain an appropriate γ value. Brode [40] notes that a constant γ assumption is also reasonable because of a fairly low range of γ behaviour [60]. Another simple analytical expression for the adiabatic JWL γ is also derived by Baker [17].

Another, perhaps more thermodynamically consistent approach is to assume thermal equilibrium and Dalton's law of additive partial pressures of each species. This is approximate for real gases due to intermolecular forces, but can be used with reasonable accuracy when combined with a real gas equation of state [46]. This approach is simple due to the linear dependence of pressure on temperature for both the JWL and ideal gases. In a mixture the pressure consists of the sum of the partial pressures for the ambient gas P_a and explosion products P_p –

$$P = P_a\left(\rho_a, T\right) + P_p\left(\rho_p, T\right) \tag{G.4}$$

The combined internal energy is the mass-fraction weighted average of each species' internal energies

$$e = f_a e_a\left(\rho_a, T\right) + f_p e_p\left(\rho_p, T\right) \tag{G.5}$$

Given the equation of state expressions in Section 4.5.1 and Equations 4.19 and 4.20 the mixture pressure is

$$P = Ae^{-R_1\widetilde{v}} + Be^{-R_2\widetilde{v}} + \left(\frac{\omega C_{v,p}}{v_0\widetilde{v}} + \rho_a R_a\right) T \tag{G.6}$$

and the mixture internal energy is

$$e = f_p\left(\frac{Av_0}{R_1}e^{-R_1\widetilde{v}} + \frac{Bv_0}{R_2}e^{-R_2\widetilde{v}}\right) + C_{v,mix}T \tag{G.7}$$

where the relative volume of the explosion products $\widetilde{v} = \rho_{0,p}/\rho_p$, f_a and f_p are the mass fractions of the ambient gas and explosion products respectively, and the mixture specific heat $C_{v,mix} = f_a C_{v,a} + f_p C_{v,p}$. A derivation of sound speed based on this mixture equation of state is given in Appendix G.1.

To minimize JWL equation of state evaluations, the strategy of Löhner *et al* [131, 155] is used to treat as ambient gas those mixtures with only a small amount of explosive products. If ρ_p is small (or v_p large) $\omega/\left(R_i\widetilde{v}\right) \approx 0$ which appear in the JWL equation (Equation 4.18). Then the term with the lowest value of R is chosen (given this vanishes last) and ambient gas is assumed when $Ce^{-R_l\widetilde{v}} < \delta$ where δ is a small threshold value of order $O\left(10^{-3}\right)$ and C the JWL constant corresponding to the exponential term in the JWL equation with the lowest value of R, R_l. When this occurs, pressure has linear dependence on density, as in an ideal gas.

G.1 Sound Speed

In this section, the sound speed a of a mixture of detonation products and ambient gas will be derived given the equation of state for JWL and ideal gases in Appendix G assuming additive partial pressures. This expression would be particularly simple if an averaged gas γ_{avg} were used ($a = \gamma_{avg} P/\rho$), and for mixtures of ideal, calorically perfect gases this is obtained from the mass-fraction weighted average of the specific heats. For the more complicated case, the derviation uses thermodynamic principles. The general expression for a in either real or ideal gases [55] is

$$a^2 = \left.\frac{\partial P}{\partial \rho}\right|_{s,f_i} \tag{G.8}$$

where subscripts s and f_i means entropy and mass fractions are held constant, thus $\partial\rho_i/\partial\rho = f_i$. It is common to eliminate entropy in the expression by using the energy form of the equation of state, $e = e(\rho, P)$, taking its differential, $de = \frac{\partial e}{\partial \rho}|_P \, d\rho + \frac{\partial e}{\partial P}|_\rho \, dP$ and for an isentropic process (as in an infinitely weak sound wave) $de = -Pdv$, thus after further derivation

$$a^2 = \frac{v^2\left(P - \rho^2 \frac{\partial e}{\partial \rho}|_P\right)}{\rho^2 \frac{\partial e}{\partial P}|_\rho} \tag{G.9}$$

Thus it is necessary to derive the quantities $\frac{\partial e}{\partial \rho}|_P$ and $\frac{\partial e}{\partial P}|_\rho$ for the mixture.

Now the mixture internal energy is the mass-fraction weighted average of each species' internal energy, $e = \sum_i f_i e_i$, thus

$$\left.\frac{\partial e}{\partial \rho}\right|_P = \sum_i f_i \left.\frac{\partial e_i}{\partial \rho}\right|_P \tag{G.10}$$

Now assuming an energy form of the equation of state with temperature as a variable for each species, $e_i = e_i(\rho_i, T)$, the chain rule for partial differentiation gives

$$\left.\frac{\partial e_i}{\partial \rho}\right|_P = \left.\frac{\partial e_i}{\partial \rho_i}\right|_T \left.\frac{\partial \rho_i}{\partial \rho}\right|_P + \left.\frac{\partial e_i}{\partial T}\right|_{\rho_i} \left.\frac{\partial T}{\partial \rho}\right|_P \tag{G.11}$$

But the specific heat of each species $C_{v,i} = \partial e_i/\partial T\,|_{\rho_i}$ by definition and $\partial e_i/\partial \rho_i\,|_T$ can be derived from each species' equation of state. It remains for the derivative $\partial T/\partial \rho\,|_P$ to be found.

Using a pressure form of the equation of state with temperature dependency and additive pressures from each species, $P = \sum_i P_i = \sum_i P_i(\rho_i, T)$ where temperature equilibrium is assumed. Fortunately for many real gas equations of state like the van der Waals, virial and JWL equation of state the temperature dependency is often linear and hence inversion of the pressure summation is usually possible, with $T = T(P, \rho_1, \rho_2, ..., \rho_n)$. Thus

$$\left.\frac{\partial T}{\partial \rho}\right|_P = \sum_i f_i \left.\frac{\partial T}{\partial \rho_i}\right|_P \tag{G.12}$$

Hence the final expression for $\partial e/\partial\rho\,|_P$ is

$$\left.\frac{\partial e}{\partial \rho}\right|_P = \sum_i {f_i}^2 \left.\frac{\partial e_i}{\partial \rho_i}\right|_T + C_v \sum_i f_i \left.\frac{\partial T}{\partial \rho_i}\right|_P \tag{G.13}$$

where C_v is for the mixture, $C_v = \sum_i f_i C_{v,i}$. Given the energy and pressure forms of the mixture and JWL equation of state in Section 4.5.2, the derivatives $\partial e_p/\partial\rho_p\,|_T$ and $\partial T/\partial\rho_p\,|_P$ can be analytically derived and are

$$\left.\frac{\partial e_p}{\partial \rho_p}\right|_T = \frac{A}{{\rho_p}^2} e^{-R_1\tilde{v}} + \frac{B}{{\rho_p}^2} e^{-R_2\tilde{v}} \tag{G.14}$$

$$\left.\frac{\partial T}{\partial \rho_p}\right|_P = -\left(\rho_a R_a + \omega\rho_p C_{v,p}\right)^{-1} \left(\frac{AR_1\rho_0}{{\rho_p}^2} e^{-R_1\tilde{v}} + \frac{BR_2\rho_0}{{\rho_p}^2} e^{-R_2\tilde{v}} + \omega T C_{v,p}\right) \tag{G.15}$$

For the ambient, calorically perfect and ideal gas, $e_a = e_a(T)$, $\partial e_a/\partial\rho_a\,|_T = 0$, and easily $\frac{\partial T}{\partial \rho_a}\,|_P = -TR_a/\left(\rho_a R_a + \omega\rho_p C_{v,p}\right)$.

As before the mixture internal energy $e = \sum_i f_i e_i$, thus

$$\left.\frac{\partial e}{\partial P}\right|_\rho = \sum_i f_i \left.\frac{\partial e_i}{\partial P}\right|_\rho \tag{G.16}$$

In this case as ρ is held constant then given the assumption in Equation G.8 that f_i is constant, all ρ_i are also constant. Thus $\partial\rho_i/\partial\rho\,|_\rho = 0$ and with $e_i = e_i(\rho_i, T)$ the chain rule for partial differentiation gives

$$\left.\frac{\partial e_i}{\partial P}\right|_\rho = \left.\frac{\partial e_i}{\partial T}\right|_{\rho_i} \left.\frac{\partial T}{\partial P}\right|_\rho \tag{G.17}$$

Note again that $\partial e_i/\partial T\,|_{\rho_i} = C_{v,i}$, and once more assuming the mixture temperature $T = T(P, \rho_i)$ then

$$\left.\frac{\partial e}{\partial P}\right|_\rho = C_v \left.\frac{\partial T}{\partial P}\right|_\rho \tag{G.18}$$

The derivative $\partial T/\partial P\,|_\rho$ is readily obtained from the mixture equation of state (Appendix G) since all ρ_i are held constant, and for a mixture of JWL and ideal gases is $\frac{\partial T}{\partial P}\,|_\rho = \left(\omega\rho_p C_{v,p} + \rho_a R_a\right)^{-1}$.

Appendix H

Non-reflecting Boundary Conditions

This section briefly describes the implementation of the non-reflecting boundary conditions of Thompson [210] for subsonic flow. Along a given co-ordinate axis x_i the non-reflecting conditions are implemented slightly differently depending on whether the boundary is the left face A or right face B, illustrated in Figure H.1.

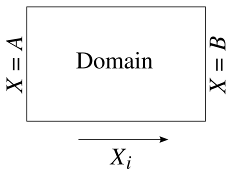

Figure H.1: Diagram for non-reflecting BC illustration

H.1 Outflow

For outflow at the left face A, the following condition must be satisfied –

$$\frac{\partial P}{\partial x_i} + \rho a \frac{\partial u_i}{\partial x_i} = 0$$

where a is the cell sound speed. For outflow at right face B, the condition is

$$\frac{\partial P}{\partial x_i} - \rho a \frac{\partial u_i}{\partial x_i} = 0$$

This condition can be implemented by giving the extrapolated pressure on the boundary a value consistent with the non–reflecting boundary condition given above (other flow quantities can just be extrapolated). For example, through the right face

$$P_b = P_c + \Phi \rho_c a_c \frac{\partial u_i}{\partial x_i} \Delta x_i \tag{H.1}$$

where Δx_i is half a cell length (from the cell centre to the border face), P_b is the extrapolated boundary pressure, and subscript c denotes the cell-centred values. Φ is the limiter for the velocity component u_i and its inclusion is necessary in Equation H.1 as the extrapolated pressure P_b can sometimes go negative (if $\Phi = 1$ always) if there is a strongly negative gradient e.g. when a shock crosses the boundary.

H.2 Inflow

Subsonic inflow is a rarely-used boundary condition for the type of simulations considered in this thesis as outflow boundary conditions are typically enforced at domain boundaries for exiting blast waves. For inflow at the left face A, these conditions must be satisfied –

$$\begin{aligned} a^2\frac{\partial \rho}{\partial x_i} - \frac{\partial P}{\partial x_i} &= 0 \\ \frac{\partial u_2}{\partial x_i} &= 0 \\ \frac{\partial u_3}{\partial x_i} &= 0 \\ \frac{\partial P}{\partial x_i} + \rho a\frac{\partial u_i}{\partial x_i} &= 0 \end{aligned}$$

For inflow at the right B, the conditions become

$$\begin{aligned} a^2\frac{\partial \rho}{\partial x_i} - \frac{\partial P}{\partial x_i} &= 0 \\ \frac{\partial u_2}{\partial x_i} &= 0 \\ \frac{\partial u_3}{\partial x_i} &= 0 \\ \frac{\partial P}{\partial x_i} - \rho a\frac{\partial u_i}{\partial x_i} &= 0 \end{aligned}$$

These four equations mean that four extrapolated flow variables must be set to satisfy the non-reflecting boundary condition.

Appendix I

Alternating Digital Tree (ADT) structures

This section describes the Alternating Digital Tree (ADT) structure, which is a spatial binary tree data structure like the octree but designed especially to speed up geometric searching and intersection problems [1, 36]. *Geometric searching* refers here to obtaining from a set of n points those that lie within a given hyper–rectangular (i.e. rectangular or hexahedral) region of space, whilst *geometric intersection* refers to obtaining from a set of hyper–rectangular *n objects* those that intersect with a given hyper–rectangular object. Sequential geometric searching is of $O(n)$ complexity; ADT searching reduces this to $O\left(log(n)\right)$ tests, which is significant when there are many bodies.

As an example of geometric searching, consider a set of points A–E in 2D space, as in Figure I.1. The first point A corresponds to the root of the binary tree and the whole space. The next point B is placed as either the left or right child of A depending on whether it is to the left or right of the bisector of the region on the x^0 axis. The corresponding region of B is thus the right half of A's domain.

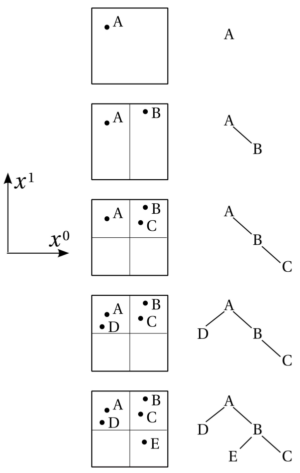

Figure I.1: Constructing an ADT

Point C then tests if it lies to the left or right of the bisector of the x^0 axis. It lies to the right, but since B has already been assigned to this region, point C tests if it should be the left or right child of B by now testing if it lies to the left or right of the bisector along the x^1 axis of B's region. This procedure is repeated for the other points D and E.

The ADT is thus recursively built up by traversing through the list of all points and cyclically partitioning the axes to test if a given point P lies to the left or right of the bisector of the subregion on this axis which a previous point P' is associated with. P will then be assignd the left or right child depending on this outcome, but if a child already exists corresponding to another point P'', the same bisection test is now applied on the subregion corresponding to P'', and so forth until P is finally assigned a partitioned subregion of its own. The cyclical axis bisection is given by

$$j = mod(l, N) \tag{I.1}$$

Thus the x^jth axis is bisected where N is the space dimension and l is the level of the node on the ADT (the root is level 0) corresponding to the subregion currently being bisected. For example, point C above would be B's child, and B is a level 1 point/node and $N = 2$, so the x^1 axis should be bisected for the subregion corresponding to B. These subregions are hyper-rectangular because of the axial bisection. The general algorithm for adding a point to a node on the ADT is given in Figure I.2.

```
build_ADT(point p, ADT node) {
  if(node is NULL) {
    Allocate p to node
    Calculate region corresponding
      to p
  }
  else {
    if(point lies in left subregion
       of node)
      build_ADT(p, left child of
                ADT node)
    elseif(point lies in right subregion
           of node)
      build_ADT(p, right child of
                ADT node)
  }
}
```

Figure I.2: ADT building algorithm

As points are uniquely assigned subregions of their own it is not necessary to linearly test each point to see if it lies within a hyper–rectangular region of space. A whole branch of points lying within a subregion on the ADT can be discarded if the subregion does not lie within the given space. To obtain a fully balanced ADT, the bisection of a given region can be done through the median of points [1], but this requires sorting the points along each axis. This has not been implemented in the code.

The intersection of hyper-rectangular regions (i.e. bounding boxes) is a simple test. Referring to Figure I.3 if the bounding box of one region k is given by $[\mathbf{x}_{k,min}, \mathbf{x}_{k,max}]$ and the bounding box of another region o is given by $[\mathbf{x}_{o,min}, \mathbf{x}_{o,right}]$, the regions will intersect if and only if

$$\begin{aligned} x^i_{k,min} &\leq x^i_{o,max} \\ x^i_{k,max} &\geq x^i_{o,max} \end{aligned} \tag{I.2}$$

where x^i are the vector components of the verticies and $i = 0, \ldots, N-1$

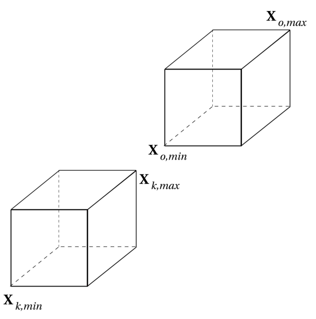

Figure I.3: Bounding box illustration

The general algorithm for using the ADT for geometric searching can be written simply and recursively as shown in Figure I.4.

```
search_ADT(node n) {
  test if n lies inside region R
  if(n is inside R)
    flag n or add it to count

  if(n has right child) {
    test if right subregion of n lies in R
    if(right subregion lies in R)
      search_ADT(right child of n)
  }

  if(n has left child) {
    test if left subregion of n lies in R
    if(left subregion lies in R)
      search_ADT(left child of n)
  }
}
```

Figure I.4: General geometric searching algorithm for ADTs

Geometric intersection problems can also be handled using ADTs via a mapping of Equation I.2 into $2N$ hyperspace. Note that Equation I.2 can be written as

$$\begin{gathered}
x^0_{min} \le x^0_{k,min} \le x^0_{o,max} \le x^0_{max} \\
\vdots \\
x^{N-1}_{min} \le x^{N-1}_{k,min} \le x^{N-1}_{o,max} \le x^{N-1}_{max} \\
x^0_{min} \le x^0_{o,min} \le x^0_{k,max} \le x^0_{max} \\
\vdots \\
x^{N-1}_{min} \le x^{N-1}_{o,min} \le x^{N-1}_{k,max} \le x^{N-1}_{max}
\end{gathered} \tag{I.3}$$

Note $[\mathbf{x}_{min}, \mathbf{x}_{max}]$ denotes the bounding box of the whole domain. Let $[\mathbf{x}_{k,min}, \mathbf{x}_{k,max}]$ be an object whilst $[\mathbf{x}_{o,min}, \mathbf{x}_{o,max}]$ be the target object. Then represent object k as a point in $2N$ space by writing its co–ordinates in a single array –

$$\mathbf{x_k} = \left[x^0_{k,min}, \ldots x^{N-1}_{k,min}, x^0_{k,max}, \ldots x^{N-1}_{k,max}\right]^T \tag{I.4}$$

Then intersection condition of Equation I.3 becomes

$$a^i \leq x^i_k \leq b^i, \; i = 0, \ldots, 2(N-1) \tag{I.5}$$

with

$$\begin{aligned} \mathbf{a} &= \left[x^0_{min}, \ldots, x^{N-1}_{min}, x^0_{o,min}, \ldots, x^{N-1}_{o,min}\right]^T \\ \mathbf{b} &= \left[x^0_{o,max}, \ldots, x^{N-1}_{o,max}, x^0_{max}, \ldots, x^{N-1}_{max}\right]^T \end{aligned} \tag{I.6}$$

Therefore, the geometric intersection problem of Equation I.2 can be equivalently thought of as a geomeric searching problem in Equations I.5 and I.6, where now $\mathbf{x_k}$ is tested for lying within the $2N$ space region $[\mathbf{a}, \mathbf{b}]$ described in Equation I.6. The bounding box of the hypercube corresponding to the whole domain likewise becomes

$$\begin{aligned} \mathbf{l} &= \left[x^0_{min}, \ldots, x^{N-1}_{min}, x^0_{min}, \ldots, x^{N-1}_{min}\right]^T \\ \mathbf{u} &= \left[x^0_{max}, \ldots, x^{N-1}_{max}, x^0_{max}, \ldots, x^{N-1}_{max}\right]^T \end{aligned} \tag{I.7}$$

For intersection problems where out of k objects those that intersected a region o need to be returned, each individual object $\mathbf{x_k}$ is thus placed on the ADT using the same general algorithm as in Figure I.2, and this binary search tree is again traversed and the objects flagged if they are inside the region given by Equation I.6.

For intersection problems involving more complex geometry, the bounding boxes of the bodies (the lower and upper verticies which uniquely define the bounds on each axes which the body occupies) are placed in the ADT. This still speeds up the searching problem as it quickly obtains candidates for the more expensive intersection test. For point-inclusion problems, the body facets can be further placed in a separate ADT to more quickly identify candidates for the ray intersection test, which is important for complex bodies with many surface panels.

Appendix J

Linhart's Point-inclusion Queries

J.1 Polygon Query

Linart's polygon inclusion test [130] is quite simple. With the help of Figure J.1, a *halfline* from any given point is drawn (here the lines go downward to some very large negative number). A line *enters* an edge if the dot product between the unit vector in the line's direction and the outward normal to the edge is negative, and conversely it leaves when the dot product is positive.

Let there be a sum S, such that if the line enters the polygon count -1 else count $+1$. If the line meets a vertex, count $\pm 1/2$ for each of the 2 edges sharing the vertex depending on whether the line is leaving or entering. This way $S = 0$ if and only if the point lies outside the polygon, else the point is inside or on the polygon. If the halfline is collinear with an edge the edge is ignored, since the halfline will meet a vertex.

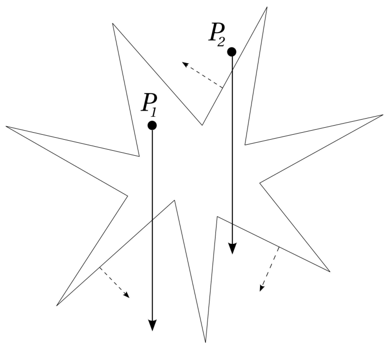

Figure J.1: Polygon halfline illustration

J.2 Polyhedron Query

To demonstrate Linhart's polyhedron query [130], use is made of Figure J.2 where a halfline is also drawn from the point in question. To each polyhedral face F met by the halfline a number s is assigned. The sum of each of these numbers S will then 0 if and only if the point lies outside the polyhedron, else the point is inside or on it.

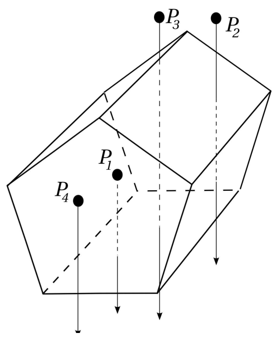

Figure J.2: Polyhedron halfline illusration

Let $\mathbf{u}$ be the unit vector in the direction of the halfline H, and F a face intersecting H in a point X. Let $\mathbf{v}$ be the outward normal of F. To determine if H intersects F, the polygon query of Appendix J.1 must be utilized. First project F onto a plane perpendicular to H, as in Figure J.3. Then H will intersect F if and only if it intersects the projection of F (ignoring the cases where F is in the plane of H).

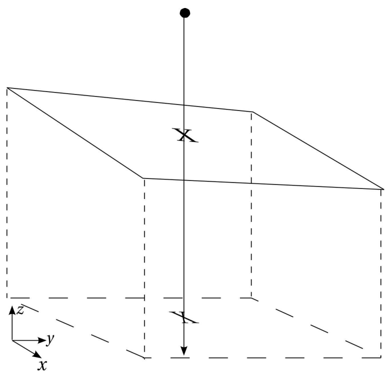

Figure J.3: Polygon projection

Depending on whether H intersects the interior of F, an edge or a vertex, s is defined as follows:

1. If X is in the interior of F:–

   $s = sign\left(\mathbf{u} \cdot \mathbf{v}\right)$

2. If X lies on an edge of F:–

   $s = \frac{1}{2} sign\left(\mathbf{u} \cdot \mathbf{v}\right)$

3. If X coincides with a vertex of F:–

   Let α be the inner angle of the normal projection of F in the direction of the halfline at this vertex ($0 < \alpha < 2\pi$). Then

   $s = \frac{\alpha}{2\pi} sign\left(\mathbf{u} \cdot \mathbf{v}\right)$

To illustrate how the algorithm works, first consider point P_1 in Figure J.2. It is inside the polyhedron, and the halfline intersects only one face. Thus $S = 1$ and P_1 is indeed inside. Point P_2 intersects two faces, but enters one and leaves another. Thus the individual numbers s for each face respectively are -1 and $+1$, and $S = 0$ i.e. P_2 is outside.

P_3 intersects the bottom face and an edge formed from two upper faces. Thus $s = -1/2$ for the two upper faces and for the bottom face $s = 1$, so the sum $S = 0$ i.e. P_3 is outside. Finally P_4 actually lies on face in the plane of its halfline, but this face is ignored, since the halfline will eventually intersect an edge or vertex, in this case the bottom face's. Thus $S = 1/2$ and P_4 is inside (technically *on*) the polyhedron.

In the case where the halfline intersects a vertex, consider Figure J.4. There are three faces sharing this vertex. These faces are projected onto onto the plane normal to the halfline; the right diagram shows the faces from the point's 'point of view'. The inner angles on these *projected faces* are α_1, α_2 and α_3, but given the algorithm, the numbers s associated with each face are thus $-\alpha_1/2\pi$, $-\alpha_2/2\pi$ and $+\alpha_3/2\pi$. But $\alpha_3 - \alpha_2 - \alpha_1 = -2\pi$, thus the sum of these three numbers give -1. As the line also leaves a face 'behind' the vertex the final sum $S = -1 + 1 = 0$ indicates the point is outside.

Note the special case in Figure J.5 where the algorithm will give a final sum $S = k$, where $0 < k < 1$. Hence the general rule that if $S = 0$ the point is outside, but if S is anything else it will be inside or on the polyhedron. As far as VCE is concerned though, both 'on' or 'inside' the polyhedron can be regarded as 'inside'.

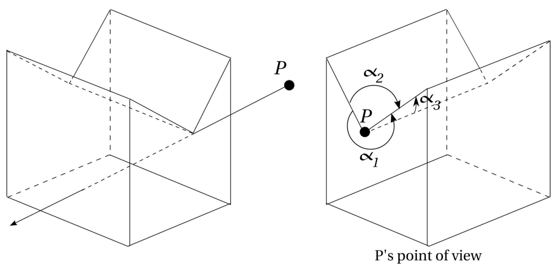

Figure J.4: Halfline passing through polyhedron vertex

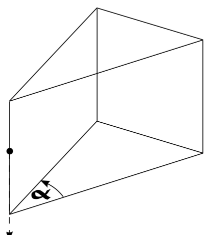

Figure J.5: Halfline passing through edge and vertex

Appendix K

OctVCE Data Structures

This section briefly discusses important data structures in the `OctVCE` code. Basic flow-related data strucutres can be seen in Figure K.1. The state vector structure also stores the explosion products density `rho_products`. Limiters for each flow variable are stored in the `limiters` data structure. The mass flux of the explosion products also constitute the `flux_vector` structure.

```
struct state_vector {
  double rho, u, v, w, e;
  double p, T, rho_products;
}

struct gradient {
  double grad_rho[3], grad_u[3];
  double grad_v[3], grad_w[3];
  double grad_e[3];
}

struct limiters {
  double rho_lim, u_lim, v_lim;
  double w_lim, e_lim;
}

struct flux_vector {
  double mass_flux;
  double x_momentum_flux;
  double y_momentum_flux;
  double z_momentum_flux;
  double e_flux;
  double mass_flux_prod;
}
```

Figure K.1: Basic flow-related data structures

The `list` data structure (Figure K.2), mentioned in Section 3.1 is a generic list structure that stores pointers to cells (the `cart_cell` structure) or verticies (the `vertex` structure). It is a doubly-linked list that points to previous and next list nodes (which are NULL if empty) in a recursive definition of the structure. There is also a `thread_num` variable to identify which thread the this list node belongs to in parallel processing (Section 5.5).

The `vertex` (Figure K.3) structure stores the position of the vertex and a vertex number that is needed for parallel solution output (Section 5.5.1). It contains pointers to the cells sharing the vertex (as many as 8), and also a pointer to its location on the list of verticies (the `vertex_list_loc` pointer).

```
struct list {
  struct cart_cell * cell;
  struct vertex * vtx;
  int thread_num;
  struct list *prev;
  struct list *next;
};
```

Figure K.2: List data structure

```
struct vertex {
  double position[3];
  int * vertex_number;
  struct cart_cell * leaf_cells[8];
  struct list * vertex_list_loc;
};
```

Figure K.3: Vertex data structure

The Cartesian cell data structure is shown in Figure K.4. This shows only a portion of the entire `cart_cell` structure. It stores the flow-related variables (from Figure K.1), but only pointers to the flux vectors, as not every interface needs a flux vector.

In a recursive definition that defines the octree data structure, a `cart_cell` points to its parent, children and potentially 24 neighbours (6 faces, 4 quadrants per face), and stores pointers to its 8 verticies. It also points to its location on the list of cells, and the list of merged cells (if part of a merged cluster of cells). There are some necessary extra variables storing geometric properties and adaptation flags.

```
struct cart_cell {
  struct state_vector State_vector;
  struct gradient Grads;
  struct limiters Lim;
  struct flux_vector * Fluxes[6][4];

  struct cart_cell * parent;
  struct cart_cell * children[8];
  struct cart_cell * face_neighbours[6][4];
  struct vertex * Verticies[8];

  struct list * List;
  struct list * List_merge;

  double volume;
  double interface_areas[6][4];
  double wall_normal[3];

  char adapt_flag;
}
```

Figure K.4: Cell data structure

In total, the cell data structure has a size of 988 bytes, and in actual practice (because of memory allocation of list, flux, vertex etc. structures) the effective memory per cell can range from 3 to 4 kilobytes. This is substantial and much larger than an equivalent cell size in Rose's `ftt_air3d` code [174, 177]. Large memory overheads do lead to performance inefficiencies such as cache misses. Explicit storage of neighbouring cells contributes to this overhead, and further work may be to make `OctVCE` more memory-efficient e.g. with the fully threaded tree structure [118] like that used by `ftt_air3d`.